
Doctoral Dissertations


Student Theses and Dissertations

Spring 2020

Transition metal chalcogenide hybrid systems as catalysts for energy conversion and biosensing

Siddesh Umapathi

Follow this and additional works at: https://scholarsmine.mst.edu/doctoral_dissertations

 Part of the [Inorganic Chemistry Commons](#), and the [Materials Science and Engineering Commons](#)
Department: Chemistry

Recommended Citation

Umapathi, Siddesh, "Transition metal chalcogenide hybrid systems as catalysts for energy conversion and biosensing" (2020). *Doctoral Dissertations*. 3044.
https://scholarsmine.mst.edu/doctoral_dissertations/3044

This thesis is brought to you by Scholars' Mine, a service of the Missouri S&T Library and Learning Resources. This work is protected by U. S. Copyright Law. Unauthorized use including reproduction for redistribution requires the permission of the copyright holder. For more information, please contact scholarsmine@mst.edu.

TRANSITION METAL CHALCOGENIDE HYBRID SYSTEMS AS CATALYSTS
FOR ENERGY CONVERSION AND BIOSENSING

by

SIDDESH UMAPATHI

A DISSERTATION

Presented to the Graduate Faculty of the
MISSOURI UNIVERSITY OF SCIENCE AND TECHNOLOGY

In Partial Fulfillment of the Requirements for the Degree

DOCTOR OF PHILOSOPHY

in

CHEMISTRY

2020

Approved by:

Manashi Nath, Advisor
Philip Whitefield
Vadym Mochalin
Risheng Wang
Sutapa Barua

© 2020

Siddesh Umapathi

All Rights Reserved

DEDICATED TO

My Guru Sri. Ramakrishna Paramahansa and my beloved son Pranav.

PUBLICATION DISSERTATION OPTION

This dissertation consists of the following five articles, formatted in the style used by the Missouri University of Science and Technology:

Paper I: Iron phosphide nanoparticles as an efficient electrocatalyst for OER in alkaline solution, found on pages 45-61, has been published in *Journal of Materials Chemistry A*, 2016, 4, 9750-9754.

Paper II: FeNi₂Se₄-Reduced Graphene Oxide Nanocomposite: Enhancing Bifunctional Electrocatalytic Activity for Oxygen Evolution and Reduction through Synergistic Effects, found on pages 62-109, has been published in *Advanced Sustainable Systems*, 2017, 1, 1700086.

Paper III: High efficiency electrochemical dopamine sensor based on transition metal chalcogenides, found on pages 110- 151 has been submitted to *Microchimica Acta*.

Paper IV: Porous copper selenide as an ultrasensitive and selective non enzymatic glucose biosensor, found on pages 152-172 has been submitted to *Journal of Materials Chemistry B*.

Paper V: FeCo₂Se₄- Functionalized onion like carbon as an efficient catalyst for oxygen evolution and oxygen reduction reaction, found on pages 173-191, is intended to be submitted to *Chemical Communications*.

ABSTRACT

Generation of hydrogen and oxygen through catalyst-aided water splitting which has immense applications in metal air batteries, PEM fuel cells and solar to fuel energy production, has been one of the critical topics in recent times. The state of art oxygen evolution reaction (OER), oxygen reduction reaction (ORR), hydrogen evolution reaction (HER) catalysts are mostly comprised of precious metals. The current challenge lies in replacing these precious metal-based catalysts with non-precious earth-abundant materials without compromising catalytic efficiency.

This research explores mixed metal selenides containing Fe-Ni, Fe-Co and RhSe which were hydrothermally synthesized and/or electrodeposited and tested for OER and ORR catalytic activity in alkaline medium. This spinel class of compounds generically referred to as AB_2Se_4 where A and B are divalent and trivalent cations respectively. Interestingly, $FeCo_2Se_4$ and $FeNi_2Se_4$, both showed highly efficient catalytic activity with low overpotential. Increase in performance was observed when these two spinel compositions were mixed with conducting carbon matrix, which decreased the overpotential significantly and increased the stability.

Finally, the metal selenides were also applied towards electrochemical bio sensing of dopamine and glucose. Electrodeposited and hydrothermally synthesized CuSe was studied towards detection of ultralow concentrations of dopamine in neutral phosphate buffer solution. The electrodeposited CuSe was also active towards detection of glucose in alkaline electrolyte. CuSe showed low detection limit, high sensitivity and selectivity towards these biomolecules.

ACKNOWLEDGMENTS

I would like to express my heartfelt thanks to my advisor, Prof. Manashi Nath, for the opportunity she provided to work in her lab. It has been a great honor to work with her and with the group, and for her continuous guidance throughout my stay at Missouri S&T. I would also like to thank my committee members, Prof. Philip Whitefield, Prof. Vadym Mochalin, Prof. Rishing Wang, and Prof. Sutapa Barua, for their perceptive suggestions during my study and research. Dr. Eric W. Bohannon and Brian Porter for exceptional assistance in X-Ray diffraction and X-Ray Photoelectron spectroscopy measurements. Thanks go to all the faculty and staff at the Chemistry department as well for their efforts to create an efficient and friendly working environment. I would like to thank all my friends and my lab mates: Dr. Jahangir Masud, Dr. Abdurazag Swesi, Dr. Wipula Liyanage, Dr. Xi Cao, Umanga de Silva, Maalavan, Holly Coleman, Prashanth, Bhushan, Srikanth, Harish and Apurv. I would like to thank Dr. Masud for teaching me the basics of electrochemistry and sharing his valuable inputs during my Ph.D.

I would like to thank my parents, Mr. Umapathi and Mrs. Dakshayani, for their belief in me and encouragement. Also special thanks to my inlaws, Mr. Nagaraj and Mrs. Shobha for their affection and support. Finally, I would like to deeply thank my wife Nagashree and my son Pranav for their unconditional love and encouragement. I owe them a lot and they have been constant support to me throughout this journey.

TABLE OF CONTENTS

	Page
PUBLICATION DISSERTATION OPTION	iv
ABSTRACT.....	v
ACKNOWLEDGMENTS	vi
LIST OF ILLUSTRATIONS.....	xii
LIST OF TABLES.....	xvi
NOMENCLATURE	xvii
 SECTION	
1. INTRODUCTION.....	1
1.1. SYNOPSIS.....	1
1.2. BACKGROUND	3
1.3. WATER ELECTROLYSIS	4
1.3.1. Oxygen Evolution Reaction.....	4
1.3.2. Oxygen Reduction Reaction.....	8
1.3.3. Mechanism of OER at the Catalytic Site and Effect of Surface Atom...10	
1.3.4. Mechanism of ORR at the Metal Chalcogenide Surface.....11	
1.4. METAL OXIDE BASED CATALYSTS FOR OER AND ORR	12
1.4.1. Ni-Fe/Co Based Catalysts for OER.....	13
1.4.2. Ni-Fe Reduced Graphene Oxide as a Hybrid Catalyst for Full Water Splitting.....	17
1.4.3. Nobel Metal Based Catalysts for ORR.....	18

1.4.4. Transition Metal Oxide Based Catalyst for ORR.....	19
1.4.5. Non-Metal Doped Carbon as ORR Catalyst.....	20
1.4.6. Motivation to Use Transition Metal Chalcogenides for OER and ORR.....	22
1.5. ELECTROCHEMICAL BIOSENSORS.....	25
1.6. ELECTROCHEMICAL OXIDATION OF DOPAMINE.....	26
1.6.1. Dopamine Sensing and Challenges.....	26
1.6.2. Theory of Square Wave Voltammetry.....	28
1.6.3. Graphene Based Dopamine Sensors.....	29
1.6.4. Metal and Semiconductor Nanoparticles Based Dopamine Sensors.....	30
1.6.5. Challenges in Real Sample Analysis.....	31
1.6.6. Future of Dopamine Sensors Based on Non-Enzyme Electrodes.....	32
1.7. ELECTROCHEMICAL NON-ENZYMATIC GLUCOSE SENSOR.....	33
1.7.1. History of Glucose Sensors.....	33
1.7.2. Advantages of Non-Enzymatic Glucose Sensors.....	35
1.7.3. Redox Mechanism of Glucose on Metal Surfaces.....	36
1.7.4. Metal/Metal Oxide Based Nano Composites as Glucose Sensors.....	38
1.7.5. Carbonaceous Materials for Glucose Sensors.....	40
1.7.6. Future Prospect in Glucose Sensing.....	41
1.7.7. Motivation to Use Transition Metal Chalcogenides as Biosensors.....	42
1.8. SUMMARY.....	43

PAPER

I. IRON PHOSPHIDE NANOPARTICLES AS AN EFFICIENT ELECTROCATALYST FOR OER IN ALKALINE SOLUTION	45
---	----

ABSTRACT.....	45
1. INTRODUCTION	46
2. RESULTS AND DISCUSSION	47
3. CONCLUSION.....	53
SUPPORTING INFORMATION.....	54
REFERENCES	59
II. FeNi ₂ Se ₄ - REDUCED GRAPHENE OXIDE NANOCOMPOSITE: ENHANCING BIFUNCTIONAL ELECTROCATALYTIC ACTIVITY OXYGEN EVOLUTION AND REDUCTION THROUGH SYNERGISTIC EFFECTS	62
ABSTRACT.....	62
1. INTRODUCTION	63
2. RESULT AND DISCUSSION	68
2.1. COMPOSITION AND MORPHOLOGY CHARACTERIZATION	68
2.2. ELECTROCHEMICAL CHARACTERIZATION AND CATALYTIC ACTIVITIES.....	73
2.3. EFFECT OF NANOSCOPIC INTERACTION BETWEEN GRAPHENE AND FeNi ₂ Se ₄ NANOPARTICLES ON OER CATALYTIC ACTIVITY	76
2.4. EFFECT OF STRUCTURE AND COVALENCY ON OER CATALYTIC ACTIVITY	77
2.5. ANALYZING THE EVOLVED GAS AND ESTIMATION OF FARADAIC EFFICIENCY	80
2.6. INVESTIGATING STABILITY OF THE CATALYSTS AND POST CATALYTIC CHARACTERIZATION	81
2.7. FeNi ₂ Se ₄ NrGO AS AN ORR CATALYST	85
3. CONCLUSION.....	87

SUPPORTING INFORMATION.....	88
REFERENCES	105
III. HIGH-EFFICIENCY ELECTROCHEMICAL DOPAMINE SENSOR BASED ON TRANSITION METAL SELENIDES	110
ABSTRACT.....	110
1. INTRODUCTION	111
2. MATERIALS AND METHODS.....	115
2.1. REAGENTS AND CHEMICALS.....	115
2.2. CHARACTERIZATION.....	115
2.3. SYNTHESIS OF CuSe BY HYDROTHERMAL METHOD.....	116
2.4. SYNTHESIS OF CuSe BY ELECTRODEPOSITION.....	117
2.5. ELECTROCHEMICAL MEASUREMENTS.....	117
3. RESULT AND DISCUSSION.....	119
3.1. ELECTROCHEMICAL OXIDATION OF DOPAMINE.....	124
3.2. DOPAMINE DETECTION IN PHYSIOLOGICAL SAMPLE.....	135
4. CONCLUSION.....	136
SUPPORTING INFORMATION.....	138
REFERENCES	146
IV. NANOSTRUCTURED COPPER SELENIDE AS AN ULTRASENSITIVE AND SELECTIVE NON- ENZYMATIC GLUCOSE BIOSENSOR	152
ABSTRACT.....	152
1. INTRODUCTION	153
2. RESULT AND DISCUSSION	155
3. CONCLUSIONS	164

SUPPORTING INFORMATION.....	166
REFERENCES	169
V. FeCo ₂ Se ₄ - FUNCTIONALIZED ONION LIKE CARBON AS AN EFFICIENT CATALYST FOR OXYGEN EVOLUTION AND OXYGEN REDUCTION REACTION	173
ABSTRACT.....	173
1. INTRODUCTION	173
2. RESULT AND DISCUSSION	176
3. CONCLUSION.....	184
SUPPORTING INFORMATION.....	184
REFERENCES	190
SECTION	
2. CONCLUSIONS.....	192
REFERENCES	195
VITA.....	205

LIST OF ILLUSTRATIONS

SECTION	Page
Figure 1.1. Process of photocatalytic water splitting and application in fuel cell	4
Figure 1.2. Schematic representation of a fuel cell.....	9
Figure 1.3. Typical LSV obtained during oxygen reduction reaction.	9
Figure 1.4. The OER polarization curves of pristine and 2-cycle NiFeO _x /CFP in 1M KOH.....	15
Figure 1.5. Polarization curves of bulk and exfoliated LDH.....	16
Figure 1.6. Possible nitrogen positions in the structure of graphitic sheet.	21
Figure 1.7. A qualitative band diagram showing the comparative valence band and conduction alignment between few transition metal oxides, selenides and sulfides.	23
Figure 1.8. Comparison of nickel oxidation peak in Ni ₃ Te ₂ , Ni ₃ Se ₂ , Ni ₃ S ₂ , Ni(OH) ₂	24
Figure 1.9. Structures of DOPA, dopamine, noradrenaline and adrenaline.	28
Figure 1.10. Schematic of the flow of voltage varies with time in SWV.	29
Figure 1.11. First generation enzyme glucose sensor.	34
Figure 1.12. Second generation enzyme glucose sensor.....	34
Figure 1.13. Schematic of third generation enzyme electrode glucose sensor.	35
Figure 1.14. The general mechanism of glucose oxidation in aqueous solution and the possible mechanism of electron transfer and coupled reactions.....	37
Figure 1.15. Redox process at the catalyst surface.	38
Figure 1.16. Prototype of continuous glucose monitoring system.	42

PAPER I

- Figure 1. (a) TEM images of FeP and particle size histogram (b) HRTEM image and corresponding selected-area electron diffraction pattern. (c) Pxrd of FeP and d. XPS spectra of Fe 2p and P 2p (inset)..... 48
- Figure 2. (a) LSVs of the various FeP nanostructured based catalyst coated electrodes measured in N₂ saturated 1.0 M KOH solution at a scan rate of 10 mV s⁻¹ and (b) the Tafel plot of catalysts... 50
- Figure 3. Stability study of catalyst under continuous O₂ evolution (at 10 mA/cm²) for 4 h studied through chronopotentiometry. Inset shows the LSVs of catalyst measured in N₂ saturated 1 M KOH before and after chronopotentiometry for 4h.... 51

PAPER II

- Figure 1. PXRD pattern of FeNi₂Se₄-NrGO nanocomposite and FeNi₂Se₄ nanoparticles along with reference FeNi₂Se₄ (PDF # 04-006-5240). Inset shows the crystal structure of FeNi₂Se₄ created from structure files corresponding to PDF # 04-006-5240. Color coded: black – Fe, red – Ni, grey – Se... 69
- Figure 2. Deconvoluted XPS spectra of the as prepared FeNi₂Se₄-NrGO nanocomposite showing the (a) Fe 2p, (b) Ni 2p and (c) Se 3d signals. (d, e) TEM images of FeNi₂Se₄-NrGO and FeNi₂Se₄, respectively. (f, g) HRTEM images of FeNi₂Se₄-NrGO nanocomposite and FeNi₂Se₄ nanoparticles. (h, i) SAED patterns collected from FeNi₂Se₄-NrGO nanocomposite and FeNi₂Se₄ nanoparticle ensemble... 70
- Figure 3. (a) LSVs measured for different catalysts coated on CFP substrate in N₂ saturated 1.0 M KOH solution at a scan rate of 10 mV s⁻¹. (b) Tafel plots of FeNi₂Se₄-NrGO... 74
- Figure 4. (a) Pxd of as-synthesized FeNi₂O₄ and FeNi₂O₄-NrGO compared with standard FeNi₂O₄ (PDF# 54-0964). (b) Comparison of LSV of FeNi₂Se₄-NrGO, FeNi₂O₄-NrGO and FeNi₂O₄ showing the enhanced OER catalytic activity of the ternary selenide... 80
- Figure 5. (a) Chronoamperometric stability study for FeNi₂Se₄-NrGO nanocomposite under continuous O₂ evolution for 12 h. Inset shows comparison of LSVs of the catalyst before and after chronoamperometry for 12 h. (b) 100 CV cycles of FeNi₂Se₄-NrGO in N₂ saturated 1.0 M KOH... 82

Figure 6. (a) PxrD spectra of FeNi_2Se_4 before and after 12 h of chronoamperometry on Au-glass. (b) Ni and (c) Fe XPS after chronoamperometry for 12 h. (d) XPS spectra of Se before and after chronoamperometry study... 84

Figure 7. ORR catalytic activity of FeNi_2Se_4 -NrGO nanocomposite. a) Linear sweep voltammograms of FeNi_2Se_4 -NrGO nanocomposite at different rotation rates. b) K-L plots at different potentials. c) LSVs of nanocomposite before and after 500 cycles of ORR activity. Inset shows stability of the ORR onset potential for 500 cycles.... 86

PAPER III

Figure 1. Schematic of dopamine electrooxidation at CuSe electrode surface..... 115

Figure 2. (a) PXRD pattern and deconvoluted XPS spectra of Cu 2p from (b) electrodeposited and (c) hydrothermally synthesized CuSe.... 121

Figure 3. SEM images of (a) ED-CuSe and (c) HT-CuSe. TEM images of (b) ED-CuSe and (d) HT-CuSe. HR-TEM images of (e) ED- CuSe and (f) HT-CuSe..... 123

Figure 4. SWV plots of (a) ED-CuSe and (b) HT-CuSe in 0.1 M PBS solution in the presence of increasing concentrations of DA..... 126

Figure 5. Chronoamperometric responses of the (a) ED-CuSe and (b) HT-CuSe to successive additions of DA into stirring 0.1M PBS electrolyte. The working potential was set at 0.18 V vs Ag|AgCl, and the DA concentrations ranged from 50 pM to 320 μM for ED-CuSe and 50 nM to 1 mM for HT-CuSe for sequential addition. Inset shows magnified portion of the amperometric response for lower concentrations. (c) and (d) shows the peak current vs concentration of dopamine for ED and HT-CuSe respectively, leading to estimation of sensitivity of the device..... 128

Figure 6. Scheme illustrating catalytic conversion of dopamine to dopamine quinone on CuSe substrate..... 130

Figure 7. Amperometric responses of the (a) ED-CuSe and (b) HT-CuSe in various interferents..... 133

PAPER IV

Figure 1. (a) PXRD pattern of electrodeposited CuSe, compared with the reference pattern (PDF#00-006-0427) star denotes Au peaks. (b) Deconvoluted XPS spectra of Cu 2p CuSe. Inset in (b) shows the corresponding Se 3d signals (c) SEM images of CuSe and (d) TEM images of CuSe... 158

Figure 2. (a) CV curves of CuSe with 0.25 mM glucose and no glucose in 0.1 M NaOH solution (b) with scan rates ranging from 5 to 75 mV/s. (c) CV curves of CuSe with varying concentrations of glucose ranging from 0.25 mM to 4 mM..... 159

Figure 3. (a) Chronoamperometric responses of the CuSe to successive additions of glucose into stirring 0.1M NaOH electrolyte. The working potential was set at +0.15 V vs Ag|AgCl, and the glucose concentrations ranged from 100 nM to 2 mM for sequential addition. Inset shows magnified portion of the amperometric response for lower concentrations. (b) Amperometric responses of CuSe 0.1M NaOH with successive addition of glucose (0.1 mM), AA (0.5 mM), DA (0.5 mM), UA (0.5 mM), Sucrose (0.1 mM) Lactose (0.1 mM), NaCl (0.5 mM), KCl (0.5 mM) and glucose (0.1 mM) at an applied potential of +0.15 V vs Ag|AgCl..... 160

PAPER V

Figure 1. (a) XRD of FeCo₂Se₄- OLCPhNH₂ (b) TEM images of FeCo₂Se₄- OLCPhNH₂ (c) FeCo₂Se₄. Deconvoluted XPS spectra of (d) Co 2p (e) Fe 2p and (f) Se 3d.... 177

Figure 2. (a) OER comparison and (b) chronoamperometry at 1.53 V for 12 h, LSV before and after of 12 h stability (inset)... 180

Figure 3. (a) ORR comparison of FCS- OLCPhNH₂ with different ratios, FCS, OLCPhNH₂ and 5% Pt (b) ORR polarization curves of FCS- OLCPhNH₂ at different rotations (c) K-L plots at different potential (d) LSV comparison of FCS- OLCPhNH₂ for before and after 1000 cycles..... 183

LIST OF TABLES

PAPER I	Page
Table 1. Parameters describing the catalytic activity of the FeP-nanoparticle based catalysts reported in this study.	53
Table 2. Comparison of OER activity of different phosphide based electrocatalysts.	54
PAPER III	
Table 1. Comparison of analytical performance of ED and HT CuSe with previously reported carbon and metal nanoparticles based dopamine electrochemical sensors.	137
Table 2. DA determination in urine samples with ED-CuSe.	138
PAPER IV	
Table 1. Results of glucose detection human blood.	164
Table 2. Comparison of performance of various copper based nonenzymatic glucose sensors.	165

NOMENCLATURE

Symbol	Description
η	Overpotential
α	Transfer number
F	Faraday constant
n	Number of Electrons trasferred
I	Current in Amperes
j	Current density
C_{DL}	Double layer capacitance
C_s	Specific capacitance
ρ	Roughness factor
ω	Angular velocity
I_D	Disk current
I_R	Ring current

1. INTRODUCTION

1.1. SYNOPSIS

Water splitting is considered to be one of the most promising ways to generate hydrogen, which has been projected as one of the cleanest fuels for the foreseeable sustainable energy future since hydrogen on combustion does not lead to production of any greenhouse gases (GHG). Electrocatalytic water splitting involves two half-cell reactions: hydrogen evolution reaction (HER) occurring at the cathode and oxygen evolution reaction (OER) at the anode. Although conventional ways using natural gas and coal can produce H_2 in large quantities, electrocatalytic water splitting, on the other hand, can be truly fossil-fuel-free technique to produce copious quantities of hydrogen. However, the bottleneck for water splitting is oxygen evolution reaction, which is a sluggish process requiring high energy to overcome the activation barrier for the reaction to go forward. Typically, electrocatalysts are used to reduce the activation barrier which is reflected in the lowering of applied potential to initiate the catalytic reaction. Although traditionally, precious metals and precious metal oxides such as those of Ru, Ir and Pt were the most commonly used OER electrocatalysts, recently transition metal-based compounds have shown very promising catalytic activity outperforming the state of the art catalysts. In this dissertation we have attempted to replace precious oxides with transition metal selenides as facile OER electrocatalyst based on the hypothesis that increasing lattice covalency will lead to better OER catalytic activity. The first step of oxygen evolution reaction in alkaline medium is the attachment of hydroxyl ions on the active transition metal surface site. Hence, the coordination and ligand environment around the catalytically active metal site plays a

crucial role in determining the chemical potential and OER catalytic activity. In the case of metal selenides, the degree of covalency in the metal-selenium bond increases according to Fajans' rule and by increasing nucleophilicity of the surface sites, it facilitates efficient attachment of OH^- ions thereby promoting initiation of OER. This favorable property has been exploited for application of transition metal selenides as electrocatalysts for OER and oxygen reduction reaction (ORR) in this work. This catalytic performance could further be improved by introducing conductive carbon based materials into the catalyst making them as hybrid composites, which facilitates better electron transfer between catalytic grains, within the composite, and the electrode. Carbon based materials such as reduced graphene oxide, and functionalized onion like carbon has been combined with transition metal chalcogenides to improve catalytic performance through synergistic effect. Furthermore, the synergistic effect has also been utilized for enhancing the efficiency of oxygen reduction reaction (ORR) which is the primary reaction happening in fuel cell. Thereby, these transition metal chalcogenide hybrid systems has been designed to be bifunctional catalyst active towards OER and ORR in alkaline medium.

Additionally, the transition metal chalcogenide systems have been also utilized for electrochemical oxidation of biomolecules such as glucose and dopamine. Similar to OER, the adsorption of OH^- on the catalytically active metal site is the first step in electrocatalytic oxidation of these biomolecules occurring directly on the catalyst surface. Transition metal selenides has thus been used as non-enzymatic biosensors that can be potentially integrated into flexible, wearable technology. Efficiency of these sensors has been optimized by applying design principles to tune redox potential of the catalytic site, which can lead to selective oxidation of different clinically relevant biomolecules at low applied potentials.

1.2. BACKGROUND

Hydrogen is an important component in the renewable energy sector. It is considered one of the most important precursor for the production of hydrocarbon fuels and industrial chemicals, but also an ideal energy carrier for the renewable energy storage due to its high energy density and environmental friendliness^{1,2}. However, hydrogen does not exist in its pure state in nature, like other elemental gases, and has to be produced from hydrogen-containing resources such as natural gas, coal, biomass and water by various methods such as reforming, gasification, thermal decomposition or electrolysis. Presently, about 96% hydrogen is produced from fossil fuels.^{3,4} Excessive use of crude oil based products has led to global warming which is a major concern, where significant amounts of CO₂ is pumped into the environment. Hydrogen production from water splitting or electrolysis derived from renewable energy, such as solar energy also known as photovoltaic conversion and wind energy, is an environmentally-friendly pathway to contribute towards meeting the constantly growing demand for energy supply and storage. For example, conversion of intermittent or excess solar (photovoltaic, PV) electrical energy into chemical energy by water electrolysis into hydrogen fuels can be used to store excess solar energy during peak generation periods. During low generation periods, these H₂ fuels can then be used to efficiently re-generate electricity via fuel cells. Fuel cells where oxygen reduction reaction (ORR) occurs is energy conversion devices that electrochemically convert fuels such as hydrogen into electricity with high power density, high efficiency, and low greenhouse gas emissions as shown in Figure 1.1.⁵ Hence, this technology complements solar energy conversion by providing a source of useable energy in absence

of direct sunlight, and is becoming increasingly important in grid-based energy generation technology.

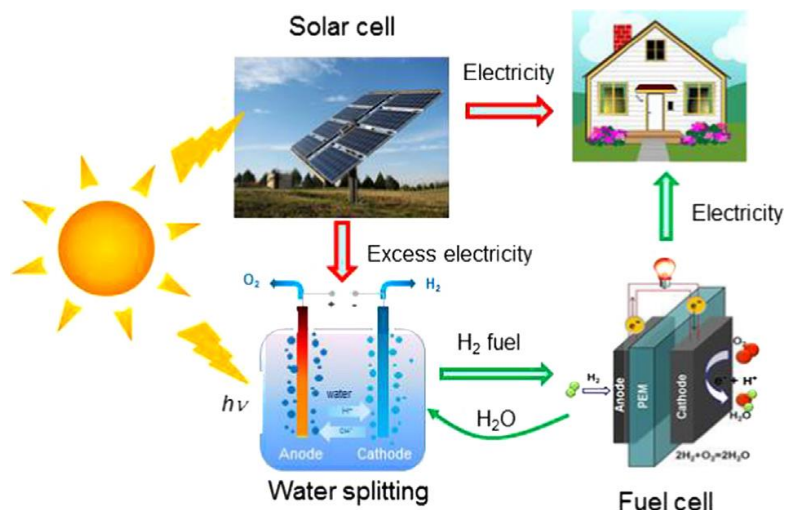
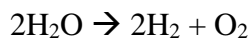


Figure 1.1. Process of photocatalytic water splitting and application in fuel cell.

1.3. WATER ELECTROLYSIS

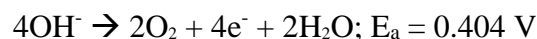
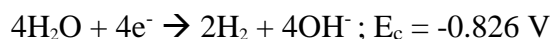
Electrolysis of water is the decomposition of water into oxygen and hydrogen gas due to the passage of an electric current. This technique can be used to make hydrogen which is a key component for hydrogen fuel production and oxygen gas. This technique is also called water splitting which requires an applied potential of 1.23 V vs RHE.

1.3.1. Oxygen Evolution Reaction (OER). The overall reaction of water splitting is can be described as follows,



Hydrogen is evolved at the cathode, (hydrogen evolution reaction, (HER)) while oxygen is evolved at the anode (oxygen evolution reaction, (OER)).

In the alkaline solution the corresponding cathodic and anodic reaction can be written as:⁶



The thermodynamic water splitting voltage is at 1.23V commensurate with the energy required for OER to take place. However, in practicality this reaction requires energy higher than 1.23 V to overcome the activation barrier for OER making the whole process kinetically slow. This is because OER is an energy intensive process, requiring a 4 e transfer pathway forming a double bond between two oxygen atoms in the dioxygen molecule (O₂).⁸ While the entire process is a multi-step electron transfer process, the rate of reaction is typically determined by the slowest electron transfer step, also referred to as the rate determining step (rds). Typically energy in the form of higher potential is applied to enhance rate of OER and potential that is applied in excess of 1.23 V (thermodynamic water splitting voltage) is called overpotential denoted by 'η'.

$$\eta = E_{\text{appl}} - 1.23 \text{ V} \quad (1)$$

where E_{appl} = applied potential. Extensive amount of research is going on to bring the overpotential as close as possible to 1.23 V by designing water splitting systems that can lower the overpotential. Bringing the overpotential close to thermodynamic value for OER during water splitting is crucial for large volume production of hydrogen which can be used in commercialization of alkaline fuel cells.⁹ Typically catalysts are utilized to reduce the

overpotentials and such catalysts are categorized either as electrocatalysts (activated by application of electric potential) or photocatalysts (activated by shining UV/visible light).

The other materials which complement electrocatalytic energy conversion are photoelectrochemical (PEC) catalysts. While both photocatalysts and photoelectrochemical catalysts can utilize solar energy for water splitting reaction, the photoelectrochemical systems decouple the solar absorption and electrocatalyst functionalities into separate photoabsorber and electrocatalyst layers. Such PEC systems has been projected as the most efficient solar-to-fuel energy conversion system since the performance of the device can be boosted by optimizing efficiency of each component. These systems mimic photosynthesis occurring in plants which has led to another branch in solar energy conversion research, generically referred to as artificial photosynthesis. Typically, current produced during OER process as a function of applied potential is normalized with respect to geometric electrode area and is reported as current density.¹⁰
¹¹ In both electrocatalysis and photoelectrocatalysis, a common denomination is used as a metric to benchmark the different catalysts, which is overpotential, η , measured at 10 mAcm^{-2} . Hence all the results presented in this dissertation has been reported as overpotential at 10 mAcm^{-2} and compared with other reported catalysts as presented in respective publications.

Further, to quantitatively compare the activity of various catalysts and correlate structure/composition/activity relationships, other metrics such as turn-over frequency (TOF) at steady state (i.e. after stabilization of the potential in response to an applied current) has been also used.¹² The TOF is defined as the number of times per second a single active site evolves an O_2 molecule (by accepting four electrons from solution).

Because TOFs are typically potential dependent, the overpotential at which the TOF is measured must be reported. TOF can be calculated using the following equation (2):

$$TOF = \frac{I}{4Fm} \quad (2)$$

where I is the current in Amperes, F is the Faraday constant and m is the number of moles of the active catalyst.

The kinetic activity of the electrocatalyst can be estimated using the Tafel's equation (3):

$$\eta = a + 2.3 \frac{RT}{\alpha n F} \log(j) \quad (3)$$

where η is the overpotential, j is the current density and the other symbols have their usual meanings. The Tafel equation as shown in eqn (3) is a fundamental equation which is acquired from the kinetically controlled region of OER, and relates the overpotential η with the log of current density, j , where the Tafel slope is given by $2.3RT/\alpha nF$.

Electrochemically active surface area (ECSA) was measured by varying from lower to higher scan rates. ECSA can be calculated using the equation 4:

$$ECSA = C_{DL} / C_s$$

where C_{DL} is the double layer capacitance and C_s is the specific capacitance. In this dissertation the value of C_s used was 0.04 mFcm^{-2} . (4)

The roughness factor (RF) can be calculated using the formula

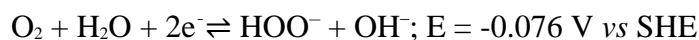
$$\rho = \frac{A_m}{A_g} \quad (5)$$

where A_m – actually accessible microscopic area and A_g - geometric area.

1.3.2. Oxygen Reduction Reaction. The standard reduction potential of O₂ to OH⁻ for a four electron reduction pathway is:¹³



On the other hand, if it is two electron pathway, O₂ is reduced to peroxide ion,



which can be further reduced to OH⁻



The schematic representation of fuel cell where oxygen reduction reaction occurs on the metal surface is shown in Figure 1.2. The powerful technique to evaluate the oxygen reduction at the electrodes is the rotating disk electrode (RDE), which is based on the convection/forced transport of the reactant molecules in the solution to enable the evaluation of ORR activity. Figure 1.3 gives the typical oxygen reduction reaction RDE polarization curve from which information such as the onset potential (E_{onset}), half wave potential ($E_{1/2}$), overpotential under a specific current density (η) and limiting current density (j_L) can be obtained.

To obtain information on the number of electrons transferred (n) and the rate constant (k), the electrochemical properties from RDE can be co-related to Koutecky – Levich (K-L) equation 6:

$$\frac{1}{j} = \frac{1}{j_k} + \frac{1}{n\omega^{1/2}} \quad (6)$$

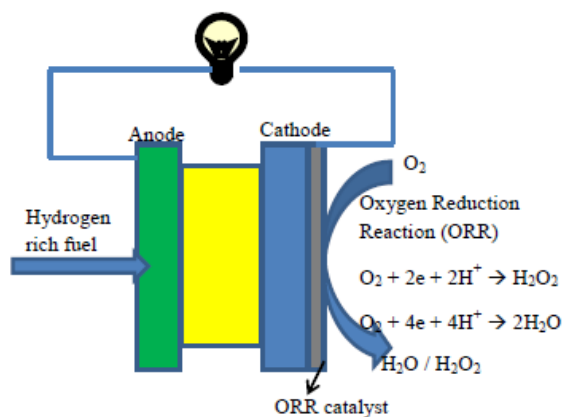


Figure 1.2. Schematic representation of a fuel cell.

where j_k is the kinetic-limiting current density, ω is the angular velocity in unit of rad/s, n is the number of transferred electrons, and k is the electron-transfer rate constant. n can be obtained from the slope and intercept of K-L equation.

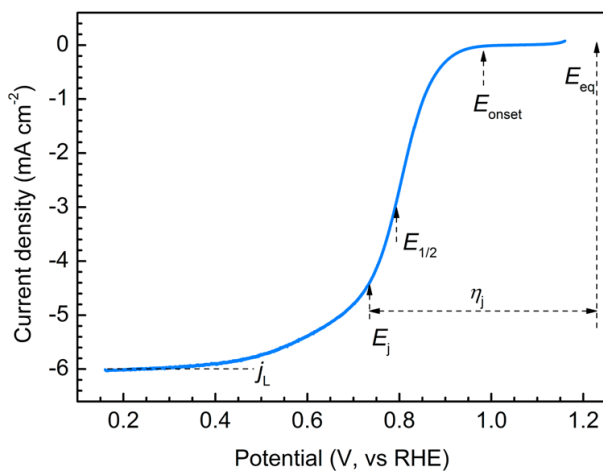


Figure 1.3. Typical LSV obtained during oxygen reduction reaction.

The extension of RDE is the rotating ring disk electrode (RRDE). In this method, ORR occurs on the disk and any unreacted species can be further reduced at the ring electrode. For example, Pt/C of different particle size can undergo a 2 or 4 electron ORR on the disk electrode and on the ring electrode any H₂O₂ produced during the reaction is further reduced to H₂O. This helps in deducing the reaction mechanism of the ORR as well as estimate amount of H₂O₂ produced.

The 2 electron reduction current is given by:

$$I_{2e^-} = I_R / N \quad (7)$$

where I_{2e^-} is the 2-electron reduction current during ORR on the disk electrode and N is the collection efficiency. The ORR current (I_D) on disk electrode can be expressed as:

$$I_D = I_{2e^-} + I_{4e^-} \quad (8)$$

where I_{4e^-} is the 4-electron ORR current.

Using the following equation (equation 9) we can calculate the percentage of H₂O₂ produced ($X_{H_2O_2}$) and number of electrons (n) utilized (equation 10) in ORR.

$$X_{H_2O_2} = \frac{\frac{200I_R}{N}}{I_D + \frac{I_R}{N}} \quad (9)$$

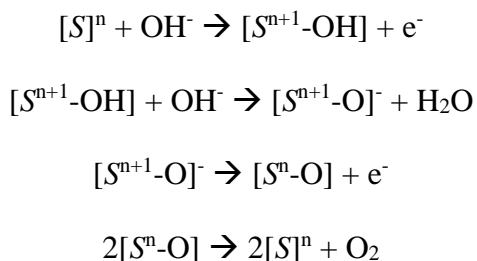
$$n = \frac{4I_D}{I_D + \frac{I_R}{N}} \quad (10)$$

where I_R is the ring current, I_D is the disk current, and N is the collection efficiency.¹⁴

1.3.3. Mechanism of OER at the Catalytic Site and the Effect of Surface Atom.

OER in alkaline medium is a multi-step 4 electron transfer process with each elementary step generating one electron. Each step comprises an unfavorable energy barrier leading to the sluggish kinetics of OER and large overpotential. A typical OER reaction on the

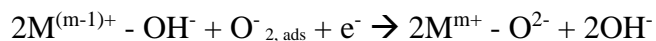
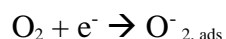
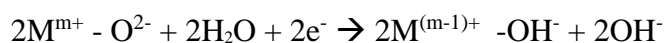
catalyst surface can be explained from the modified Krasilshchikov mechanism originally proposed for metallic anode OER catalysis which has been later adapted by several other researchers for metal oxidic and non-oxidic electrocatalyzed OER¹⁵⁻¹⁸ and the mechanism is as follows,



where $[S]$ is the catalytically active site in the anodic catalyst and n is average oxidation state of the active site. The first step in the attachment of the hydroxyl group to the active site of the catalyst $[S]$ which initiates the OER process. Catalytic activity of metals is different to that of the same metal oxides, hydroxides, oxyhydroxides or chalcogenides. Therefore, the oxidation state of the metal and its coordination with anions along with local geometries has a profound influence on the catalytic site which in turn the activity towards OER. It can be perceived from the above mechanism that the catalytic activity can be affected by any factor that can regulate the oxidation state, chemical potential and other factors of the catalytically active surface site.

1.3.4. Mechanism of ORR at the Metal Chalcogenide Surface. ORR mechanism pathway of metal chalcogenides/oxide follow a different rationale to those of the precious metal surfaces. The surface cations of transition metal oxides coordinate with the oxygen of H_2O in order to fulfill their full oxygen coordination. The hydrogen atoms of H_2O become distributed over the catalyst surface. To create OH^- species, the protonation of surface oxygen ligand is charge-compensated by the reduction of a surface cation M such

as Mn^{4+} , Co^{3+} , Fe^{3+} , and so forth. The M-OH^- species further interact with O_2 which adsorb on oxide surfaces. In 2011, the Shao- Horn group observed a volcano plot of the catalytic activities of perovskite oxides versus the e_g electrons on the transition metal site that peaked at e_g electrons ca. 0.8-1.0. A moderate e_g filling around 0.8-1.0 conferred the M-O_2 bonding that was neither too strong nor too weak. Hence, the presence of an e_g electron was proposed to destabilize the transition metal oxide bond and together with O_2 , and to facilitate the displacement of OH^- of M-O^- with M-O_2^{2-} ,^{19, 20}



1.4. METAL OXIDE BASED CATALYSTS FOR OER AND ORR

Electrocatalytic OER and ORR have attracted widespread attention because of the important role in various energy storage and conversion devices such as metal air batteries and water splitting devices. Metal oxides electrocatalysts has exhibited good catalytic activity and hold promise as materials for sustainable future. Presently RuO_2 and IrO_2 are considered as state of the art catalyst for OER while Pt is the best-performing catalyst for ORR. However, the expensive and scarcity of resources makes these catalysts non-feasible for practical usage, while Ir and Ru-oxides are also unstable for long-term OER. Pt, on the other hand gets poisoned in presence of methanol which causes its ORR catalytic activity to markedly reduce with time. Hence replacement of precious metal oxides with transition metal-based compositions has attracted significant attention in the energy research

community over the last several years. The following section gives an overview of the transition metal oxides for energy conversion.

1.4.1. Ni-Fe/Co Based Catalysts for OER. Transition metal oxides are known to possess wide bandgap and classify as insulators to wide-gap semiconductors, whereas transition metal chalcogenides with narrower bandgap could be considered as a semi-metals while few of them with zero bandgap are metallic.^{12, 21-29} First-row transition-metal oxides (or hydroxides), especially Co- and Ni-based metal oxides^{30, 31,32-37} have been researched for developing efficient water splitting catalysts in alkaline medium due to their unique electronic properties and variety of chemical compositions.³⁸⁻⁴³ Most of these transition metal oxide base catalysts exhibited compared OER activity to the precious metal oxides.

To understand the superior activity of Ni-based electrocatalysts several theoretical and experimental studies were carried out and the results of these investigations showed that this high activity can be attributed to the valence band edge- alignment and occupancy of the *d*-levels of the transition metal.⁴⁴⁻⁴⁶ It has been predicted that the transition metals having an *e_g* occupancy of 1e⁻ improves the catalytic activity manifolds.¹¹ The above discussed theories have been experimentally proven and it has been observed that the most influential factor to predict and optimize catalyst efficiency was the above molecular orbital descriptor.²³

Several published reports from various researchers have shown that Ni-based oxides and hydroxides which have a $t_{2g}^6 e_g^2$ electronic configuration for octahedral Ni²⁺, outperforms other metal-based oxides/hydroxides in terms of the overpotential required for oxygen evolution. It was observed after several experimental studies that NiOOH species

was the actual catalyst in the Ni-oxide-based systems, which is formed in situ by oxidation of Ni^{2+} to Ni^{3+} preceding the water oxidation reaction. In the linear sweep voltammograms (LSV), Ni oxidation from Ni^{2+} to Ni^{3+} shows up as a pre-oxidation peak before the actual water oxidation process. Ni^{3+} which is believed to be the catalytic site of OER achieves e_g^1 electronic configuration retaining the octahedral coordination, which explains the high catalytic activity of the NiOOH.

Dopants such as Fe has positive effects on Ni-based catalysts. Corrigan⁴⁷ et al. studied the OER behavior upon systematic doping of Fe impurities to nickel oxide. The decrease in OER overpotential and decrease in discharge capacity was reported even at an ultralow Fe concentration (0.01%), demonstrating the high sensitivity nature of OER on Ni-based electrodes to Fe impurities. By adjusting the Fe content, a composite NiFe hydrous oxide with >10% Fe showed intriguing activities toward OER electrocatalysis at low overpotential and smaller Tafel plot. However, some of the recently discovered non-oxidic electrocatalysts have outperformed oxide based catalysts opening up new directions of research.⁴⁸

Further nickel iron oxide, NiFe_2O_4 with spinel structure often has oxidation states of +2 and +3 for Ni and Fe respectively. The spinel structure type comprises cubic closed-packed oxide anions with Ni^{2+} occupying one-eighth of the tetrahedral holes and Fe^{3+} occupying half of the octahedral holes. This catalyst showed an overpotential of 362 mV with a low Tafel slope of less than 40 mV/dec as shown in Figure 1.4 outperforming the state of the art IrO_2 . Additionally, due to the crystalline nature of the nickel iron oxide, an impressive durability of over 7,000 hours was observed.⁴⁹

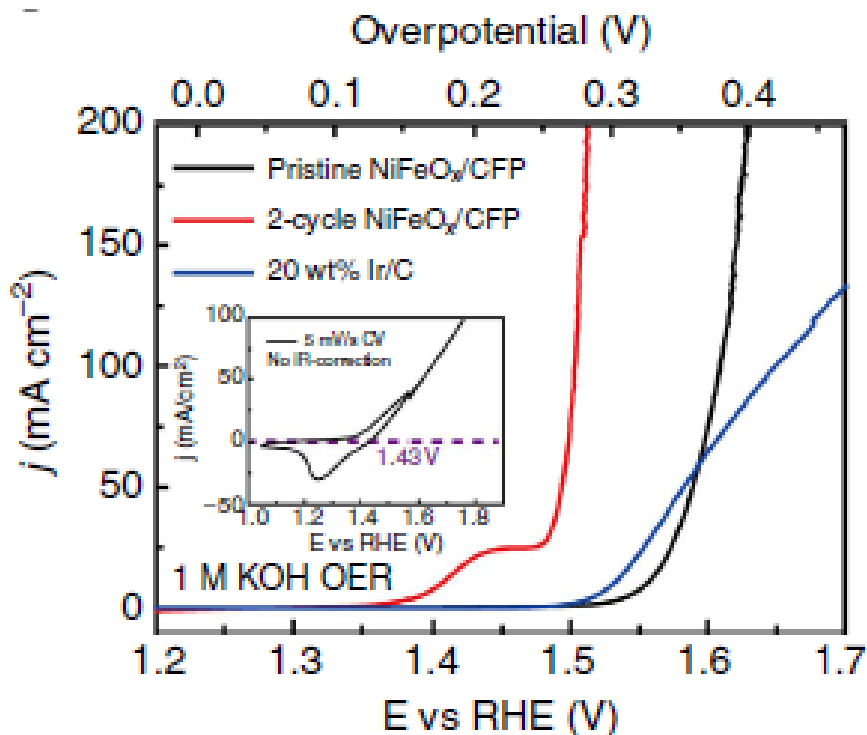


Figure 1.4. The OER polarization curves of pristine and 2-cycle $\text{NiFeO}_x/\text{CFP}$ in 1M KOH. (Reproduced with permission ⁴⁵).

Apart from the above, nickel iron layered double hydroxides (LDH's) and NiFe alloys have been studied towards OER.³⁸ In these type of LDH structures exfoliation of few layers was observed due to large interlayer spacing between the LDH structures. The authors proposed that there was increase in the active sites after exfoliation and observed dramatic improvement in OER activity with catalysts have similar ECSA as shown in Figure 1.5.

The other way of improving performance of metal oxides is by increasing the roughness factor of the catalyst surface. For example dissolution of the catalyst surface

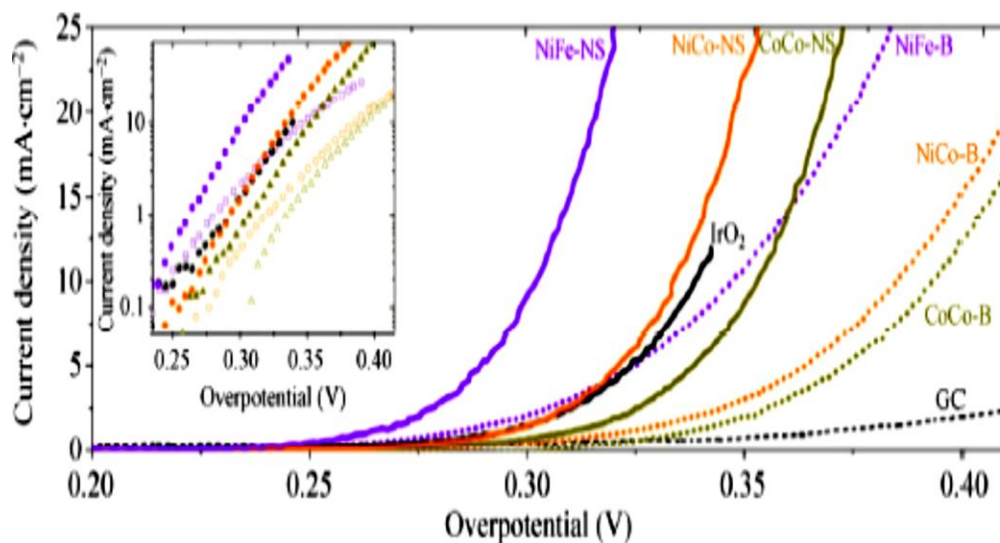


Figure 1.5. Polarization curves of bulk and exfoliated LDH. (Reproduced with permission⁵⁰).

which creates a highly textured porous catalyst surface has been shown to have a very large impact on the performance of the catalyst.⁵¹ Recently Yi Cui reported improvement of catalytic activity when transition metal oxide (iron, cobalt, nickel oxides and their mixed oxides) nanoparticles (20 nm) are electrochemically transformed into ultra-small diameter (2-5 nm) nanoparticles through lithium-induced conversion reactions.⁵¹

According to the studies corresponding to the molecular orbital descriptor, Co(II) based systems with a low spin octahedral coordination for Co should produce the best water oxidation catalyst. Cobalt oxides are highly active electrocatalysts for OER in alkaline solution.^{52, 53} Cobalt based catalysts with similar size and shape, regardless of their preparation methods and the nature of the supports, give approximately the same Tafel slope of around 60 mV dec⁻¹. Actually, organometallic complexes of Co do show high catalytic performance which has been researched extensively by many groups. Further

doping cobalt based electrocatalysts with iron and nickel has shown similar improvements as nickel based catalysts.⁵⁴⁻⁵⁶

1.4.2. Ni-Fe Reduced Graphene Oxide as a Hybrid Catalyst for Full Water Splitting. The low electronic conductivity of transition metal oxides is one reason for their depressed OER catalytic activity. The electronic conductivity of transition metal oxides can be improved by cation substitution or by integration with a conductive substrate. Spinel or perovskite-structured oxides are most amenable to modifications via cation substitution. For example, it has been shown that the resistivity of $Mn_{3x}Fe_xO_4$ spinel decreases with increasing x .^{57, 58} Transition metal oxides with good ORR activity may also be integrated with transition metal oxides with good OER activity to support bifunctionality in oxygen electrocatalysis. In comparison with perovskites, the spinel structure can be formed at lower temperatures and such materials are usually nanostructured. Metal oxides should additionally be integrated with a conductive substrate to decrease the contact resistance at the catalyst-electrode interface and film resistance within the catalyst composite. Graphene is a conductive material with high surface area and good stability under a wide range of environmental conditions and can be used as a conductive filler in such catalyst composites.⁵⁹

Graphene is more commonly synthesized as reduced graphene oxide (rGO) at some expense of electron transport properties. rGO can be nitrogenated to nitrogen-doped reduced graphene oxide (N-rGO) which recovers some of the lost electronic conductivity. The advantage of N-rGO nanosheets is ease of integration with many metal nanomaterials to improve the performance of the latter in catalysis.⁶⁰

NiFe-LDH on GO, Ni form, LDH and GO are all active towards OER. It is noteworthy that NiFe-LDH/rGO far outperforms the other catalysts in current density over the full potential window with lower overpotential value. The OER onset overpotential was achieved as low as 240 mV (~ 1.470 V vs. RHE), which is far smaller than the previous value for IrO₂ in 1.0 M KOH (290 mV, ~ 1.52 V vs. RHE).⁶¹

The group of Grätzel reported NiFe layered double hydroxide (LDH) as bifunctional electrocatalyst for overall water to approach a step closer to practical application.²⁷ This bifunctional catalyst delivers a 10 mA cm⁻² current density at a cell voltage of 1.7 V in alkaline medium. Indeed hybrid Ni- and Co-based oxides have shown great promise for water electrolysis in alkaline medium but the overpotential to reach 10 mAcm⁻² still remains a challenge.⁶²⁻⁶⁴

1.4.3. Noble Metal Based Catalysts for ORR. Pt is the best catalyst till date towards ORR both in acidic and alkaline medium. Research works on Pt/C in alkaline media attracts more and more attention because of the increasing interests on alkaline fuel cells and batteries. To reduce the use of high-cost Pt, core-shell structures with Pt as shell and less costly metal as core were developed, such as Pt@Au nanorods dispersed on pyridine cycloaddition of graphene (Pt@Au-PyNG) and Pt@Pd nanocubes enclosed with (100) planes.^{65, 66} Another approach is to use nonprecious metal oxides as the catalyst support for Pt. A novel Pt cluster loaded on CaMnO₃ as a noncarbon support was developed. It exhibited essentially competitive ORR kinetics of commercial Pt/Vulcan and outperforms Pt/C with better operating durability.⁶⁷ The catalytic activity and efficiency of ORR on the Pt surface in alkaline media is lower than in the acidic one, mainly due to the excessive HO₂⁻ species generated on the Pt surface in alkaline solutions.⁶⁸

Pd is also active for ORR in alkaline media. A combined electrochemical and topological analysis indicated that polycrystalline Pd surfaces underwent pronounced surface oxidation/reduction and morphology evolution due to the interaction of Pd with surface species.⁶⁹ A RDE study on the relationship between ORR activity and d-band center of noble metals (i.e., Au, Ag, Pd, Rh, Ir, Ru and Pt) indicated close d-band center value between Pd(111) and Pd/C with Pt(111) and Pt/C.⁷⁰ The specific activity of (100)-oriented Pd nanocubes with particle size of 27 nm was ~4 times of that of spherical Pd nanoparticles with particle size of 3 nm, highlighting the high activity of Pd(100) in alkaline media.⁷¹ Recently, 14 nm Pd nanocubes with (100) facets and with (111) facets at corners were synthesized. The adsorption of OH⁻ on the truncated Pd nanocubes in 1 M NaOH was more significant than in 0.1 M NaOH.

However, the future of Pt/C and Pd as feasible ORR catalysts is shadowed with high cost, scarcity, and the insufficient durability of Pt. Recent works have recognized some non-Pt metals and alloys for ORR.

1.4.4. Transition Metal Oxides Based Catalyst for ORR. In 2011, the Dai group revealed that Co₃O₄ nanoparticles grown on N-doped reduced and mildly oxidized graphene oxide (N-rmGO) exhibited superb activity for ORR, besides OER, in alkaline medium.⁷² After that seminal work, extensive studies for spinel/nanocarbon hybrid were carried out, where the transition metal spinel oxides includes Co₃O₄,^{73, 74} MnCo₂O₄,⁷⁵ NiCo₂O₄,⁷⁶ FeCo₂O₄,⁷⁷ CuCo₂O₄,⁷⁸ CoFe₂O₄,⁷⁹ Fe₃O₄,⁸⁰ CoMn₂O₄,⁸¹ Mn₃O₄,⁸² and various heterogeneous nanostructures based on these spinel oxides. Co₃O₄ is of normal spinel structure and is a p-type semiconductor with the fundamental band gap of 0.74 eV. The

small band gap of Co_3O_4 is due to a direct dipole forbidden d-d transition between tetrahedral-site Co^{2+} cations.⁸³

In Dai's seminal work, E_{onset} and $E_{1/2}$ of $\text{Co}_3\text{O}_4/\text{N-rmGO}$ was reported to be 0.93 and 0.82 V, respectively.⁸⁴ The measured HO_2^- of $\text{Co}_3\text{O}_4/\text{N-rmGO}$ was below 6%, and a gas-diffusion layer loaded with $\text{Co}_3\text{O}_4/\text{N-rmGO}$ exhibited negligible degradation in 0.1 M KOH solution. Slightly inferior performance was evident when the N-rmGO was replaced by CNT,⁸⁵ rGO,⁸⁶ mesoporous carbon,⁸⁷ and N-doped carbon.⁷⁴ The good ORR activity of $\text{Co}_3\text{O}_4/\text{N-rmGO}$ was attributed to the synergistic covalent coupling between Co_3O_4 and N-rmGO, as well as the unique property of N-rmGO. NiCo_2O_4 is a semiconductor with electronic transport based on the variable-range hopping and nearest-neighbor hopping mechanisms.⁸⁸ Su and Chen et al. reported a hydrothermal synthesis of urchin-like NiCo_2O_4 spheres.⁸⁹ Cao et al. prepared a 3D macro porous cubic spinel NiCo_2O_4 , consisting of numerous NiCo_2O_4 nanoparticles in size of 20–40 nm that further aggregated into slabs with thickness of 150 nm. The macroporous structure, with pore volumes of $0.23 \text{ cm}^3\text{g}^{-1}$, enabled facile mass transport of reactants to the active surface sites. The macroporous NiCo_2O_4 catalysts exhibited good ORR activity with E_{onset} of 0.89 and $E_{1/2}$ of 0.75 V.⁹⁰ Lou et al. developed a polyol synthesis of NiCo_2O_4 -rGO hybrid by refluxing metal acetates with ethylene glycol and subsequent annealing at a temperature as low as 300°C .⁷⁶ $\text{NiCo}_2\text{O}_4/\text{NrGO}$ and $\text{CuCo}_2\text{O}_4/\text{NrGO}$ synthesized by hydrothermal methods using NH_4OH as the precipitating and N-doping agent were also reported.⁹¹

1.4.5. Non-Metal Doped Carbon as ORR Catalyst. Carbon, including carbon black, graphene, and carbon nanotube (CNT), is conventionally used as catalyst support

because of its high electronic conductivity and large surface area. Recently, it was noticed that carbon doped with nonmetal heteroatoms exhibits good ORR activity, where the

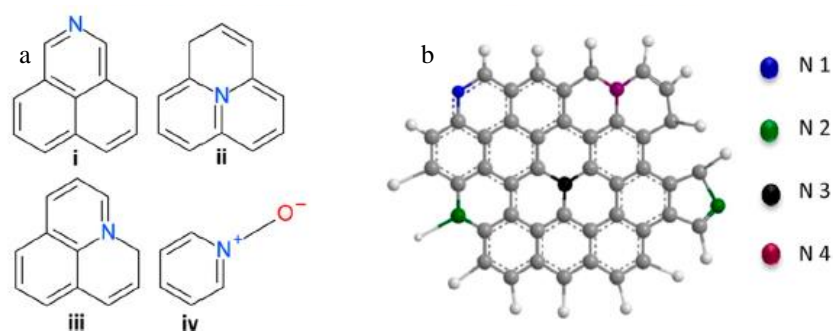


Figure 1.6. Possible nitrogen positions in the structure of graphitic sheet; (i) top-N, (ii) center-N, (iii) valley-N, and (iv) oxide-N. (b) different nitrogen functionalities in a graphitic sheet: pyridinic-N (N1), pyrrolic-N (N2), graphitic-N in center (N3, N-Q_{center}), and graphitic-N in valley (N4, N-Q_{valley}) (Reproduced with permission ⁹²).

nonmetal elements include N, B, S, P, F, and so forth of which N is the one of the attractive nonmetal studied extensively. N-sites of NC include pyridinic N, pyrrolic N, and quaternary N. Pyridinic N refers to N atoms at the edges of graphene planes, where each N is bonded to two carbon atoms and donates one p-electron to the aromatic π system. Pyrrolic N atoms are integrated into five membered heterocyclic rings, which are bonded to two carbon atoms and contribute two p-electrons to the π system. Quaternary N atoms are those substituting carbon atoms within the graphene layer.⁹³ As shown in Figure 1.6. the pyridinic and pyrrolic N are located at the graphitic edge, where quaternary N can be both “edge-N” and “bulk-like-N”. Quaternary N is further classified into quaternary N valley sites (N-Q_{valley}) and quaternary N center sites (N-Q_{center}).⁹⁴ The activity towards

ORR of N doped catalysts increases in the sequence of pyridinic N < pyrrolic N < quaternary N.

1.4.6. Motivation to Use Transition Metal Chalcogenides for OER and ORR.

Going forward, further reduction of overpotential is key in energy conversion through water splitting, and hence OER and ORR catalytic performance of the proposed catalysts needs to be improved either through compositional design or through forming hybrid materials modified with other foreign functional materials. We targeted transition metals selenides doped with different conductive carbons to synthesize hybrid catalyst prepared by electrodeposition and hydrothermal methods. This strategy shows that the combination of the over layers yields a cathodic shift in OER onset potential as compared to that observed for a pure metal selenides. The hybrid catalysts showed intriguing activities toward OER electrocatalysis with low overpotential at a current density of 10 mA cm^{-2} . This gives a new direction to design superior OER electrocatalysts with unprecedented catalytic efficiency surpassing other OER electrocatalysts reported till date including precious metal oxides.

Typically, it has been observed that while the transition metal oxides are wide bandgap and mostly insulating, transition metal chalcogenides have narrower bandgap, a semiconducting nature and some of them are even semimetal or metals with zero bandgap (Figure 1.7). For example, while NiO has a bandgap of 3.5 eV, NiS₂ and NiSe₂ have much smaller bandgaps of 0.35 eV and 0.0 eV, respectively.²¹ Typically in these transition metal oxides/chalcogenides in the simplest bonding scheme, the valence band edge is composed of the σ -bonding interaction with chalcogen s and p orbitals with the metal d-orbitals (e_g symmetric $d_{x^2-y^2}$ and d_{z^2}) while the bottom of the conduction band has more contribution

from the anti-bonding σ^* orbitals centered preferentially on the metal. The d-orbitals of the transition metal (forming the t_{2g} and e_g^* sets) lie in the inter-band region where the splitting between them is determined by simple consideration of ligand field theory.⁹⁵

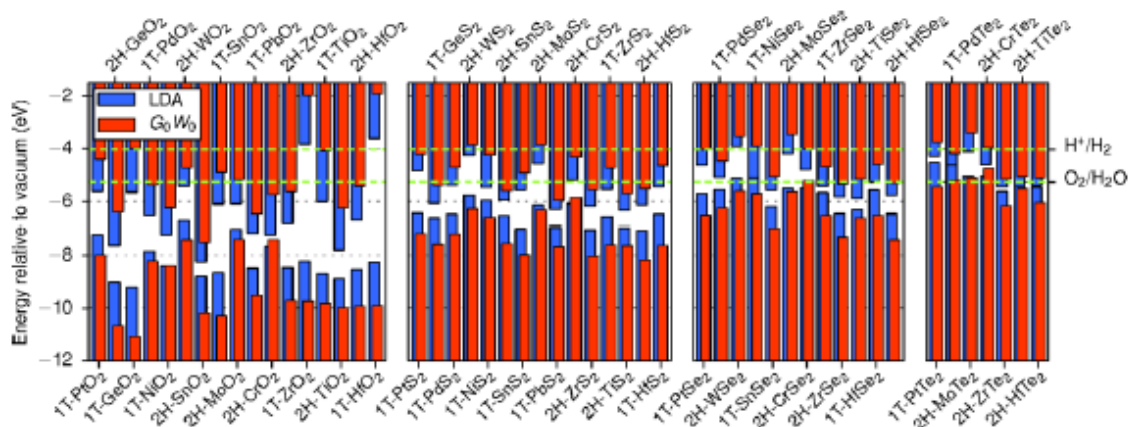


Figure 1.7. A qualitative band diagram showing the comparative valence band and conduction alignment between few transition metal oxides, selenides and sulfides. (Reproduced with permission²¹).

As the anions are changed from O to Te, i.e. down the chalcogen series, the valence band edge is expected to rise higher in energy due to decreasing electronegativity of the chalcogen atom and higher covalency shown in Figure 1.7. Additionally the crystal field splitting of the d-orbitals is also affected by changing the chalcogen atoms which changes the ligand field strength.⁹⁶ These changes in the orbital energy levels will directly influence their alignment with respect to the water oxidation and reduction levels, which in turn will affect the charge transfer between the catalyst and water. For the water splitting catalysts, one of the most influential factors in light of the electronic band structure is that water

oxidation-reduction levels are bracketed within the valence and conduction band edges of the catalyst. In these electrocatalytic systems charge transfer occurs at the semiconductor (catalyst)-electrolyte interface which will be influenced by the relative energy levels of the semiconductor and aqueous electrolyte. Efficient charge transfer will occur when these two levels are closer in energy.

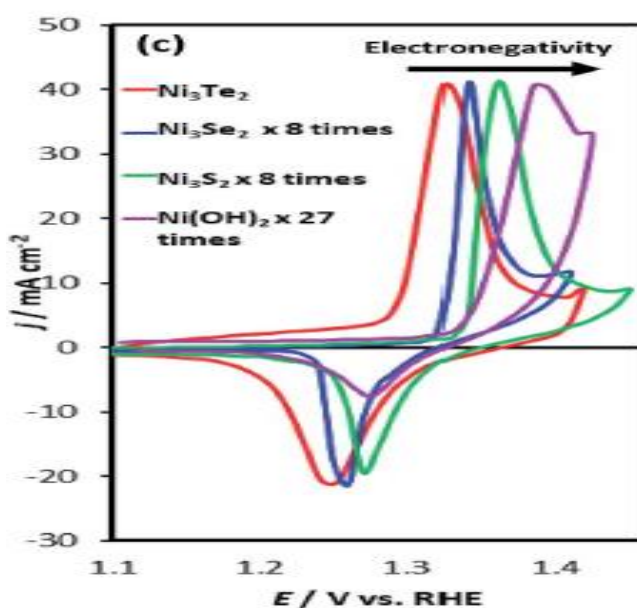


Figure 1.8. Comparison of nickel oxidation peak in Ni_3Te_2 , Ni_3Se_2 , Ni_3S_2 , $\text{Ni}(\text{OH})_2$ (Reproduced with permission ⁹⁷).

To prove this hypothesis that chalcogenides are better electrocatalyst than oxides towards OER, our group has measured the Ni(II)/Ni(III) oxidation peak in Ni_3E_2 ($E = \text{S}, \text{Se}, \text{Te}$) by collecting the CV in the range of 1.1 to 1.45 V and compared with that of $\text{Ni}(\text{OH})_2$. Indeed, it was observed that the Ni^{2+} oxidation peak showed a cathodic shift in

Ni_3R_2 indicating that the catalytically active Ni^{3+} was generated at a lower potential in Ni-chalcogenides compared to the oxide and hydroxides as shown in Figure 1.8.

In case of ORR, the drawbacks with Pt as ORR catalysts has led researchers to spend huge efforts towards developing low cost electrocatalysts with high ORR activity as an alternative to Pt.⁹⁸ In particular non-precious transition metal chalcogenides have gained signification reputation as ORR catalysts due to their high fuel tolerance, high catalytic activity, high stability and earth abundance. Among these, the chalcogenides of Fe and Co have gained special attention since their electrochemical redox potential is close to the potential required for reduction of oxygen to water. Thus, several chalcogenides of Ni, Co and Fe including Co_7Se_8 ,⁹⁹ Se-doped CoSe ,¹⁰⁰ iron and nickel doped CoS_2 ,¹⁰¹ W doped CoSe_2 ,¹⁰² $(\text{Co,Ni})\text{S}_2$, $(\text{Co,Fe})\text{S}_2$ ¹⁰³ has shown promising ORR activities. Nanoparticles of mixed metal chalcogenides like the Chevrel phase, $\text{Ru}_2\text{Mo}_4\text{Se}_8$ also exhibited high ORR activity.¹⁰⁴

1.5. ELECTROCHEMICAL BIOSENSORS

The development of the first electrochemical biosensor in 1962 by Leland Clark with the first glucose oxidase enzyme electrode. The first commercial glucose meters were available by the 1970s and have become the gold standard of the biosensor field. The main advantages of electrochemical biosensors are ease of miniaturization, low cost instrumentation, robustness, good detection limits, small sample volumes, and ability to work in turbid optically absorbing samples. The potential low cost of electrochemical biosensors combined with ease of miniaturization is the definitive advantage when used for point of care biosensors. The main drawbacks are that direct visual observation of

detection is usually not possible and multiplexing is less viable compared to optical methods.¹⁰⁵ Electrochemical biosensors are invaluable medical diagnostic tools and projects a capable method for detection of medically relevant analytes. Many electrochemical biosensor techniques have been developed to detect nucleic acids, proteins, and small molecules.¹⁰⁶ Studies have shown that electrochemical methods are robust and can accurately detect biomarkers in complex unpurified heterogeneous biological samples. Electrochemical biosensors have been applied to many cancer and infectious disease biomarkers which have illustrated the utility of electrochemical biosensors for future medical diagnostic applications. Electrochemical techniques are the foundation of electrochemical biosensors.¹⁰⁷

1.6. ELECTROCHEMICAL OXIDATION OF DOPAMINE

Dopamine (DA) is an important neurotransmitter in humans and any abnormal fluctuations in dopamine concentrations is associated with neurodegenerative diseases like Parkinson's, schizophrenia and Huntington's disease.^{108, 109} Therefore, continuous monitoring of neurotransmitter such as DA level is critical in patients with the above mentioned conditions.

1.6.1. Dopamine Sensing and Challenges. DA is electrochemically active and can be detected at low concentrations using electrochemical techniques. However, the following points briefly describes the challenges related to detection of DA.

1. Interference from compounds in biological samples such as ascorbic acid (AA) and uric acid (UA) is a challenge. For example UA is product of metabolism of urine and AA is a reducing agent and plays a vital role in maintaining a good health.

2. All three chemicals AA, UA and DA have very close oxidative potentials, thus making the detection of one compound very challenging at low concentrations.
3. UA and AA concentrations in body is several hundred times higher than DA
4. Oxidized products of these compounds absorb on the surface of electrode and reduce their reproducibility and reuse.¹¹⁰⁻¹¹³

The most widely used technique to detection of DA, UA and AA is electrochemical method. The major advantages include low cost associated with this technique, however, the low sensitivity and selectivity of this technique with real sample analysis is justifiable. Recently new materials have been developed with chemically modified surface for detecting DA in the presence of significant amounts of UA and AA. Reports of very low detection limits have been achieved with modified electrodes, while reaching such low limits was not possible with bare metal electrodes. Modified electrodes coated with carbon nanotubes,¹¹⁴⁻¹¹⁶ nanoparticles and nanocomposites¹¹⁷⁻¹²³ and polymeric composites¹²⁴⁻¹²⁷ have been used to fabricate novel sensors to detect DA.

Recent developments in dopamine sensors focus on the improvements in selectivity, sensitivity and compatibility. The other attempt is in the field of miniaturization with the objective of better spatial and resolution with multi analyte detection.

Dopamine is formed by decarboxylation of DOPA and is a precursor of two other neurotransmitters—adrenaline and noradrenalin as shown in Figure 1.9. The basis of electrochemical detection of dopamine is the $2e^-/2H^+$ redox reaction under physiological conditions. The current response in these reactions is linearly dependent on the concentration of the electroactive molecules in the extracellular medium, which enables to quantify dopamine. Apart from developing electrodes, new techniques have also been

attempted to solve the aforementioned problems, such as fast scan cyclic voltammetry (FSCV), square wave voltammetry (SWV), Differential pulse voltammetry (DPV) and relevant data treatments.

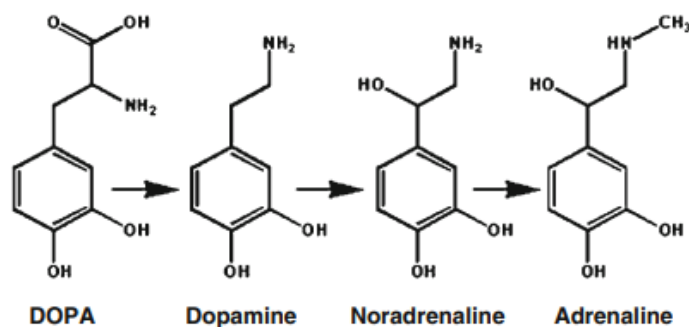


Figure 1.9. Structures of DOPA, dopamine, noradrenaline and adrenaline.

1.6.2. Theory of Square Wave Voltammetry. Square Wave Voltammetry (SWV) is a form of pulse voltammetry. Added to the staircase waveform is a square wave, so that as the voltage suddenly jumps with each step, the square wave is coincident with the jump. Halfway through the step, the square wave reverses polarity. This repeated series of staircase-plus-square-wave creates a characteristic voltage sequence applied to the sample as shown in Figure 1.10.

Cell current is measured over time between the counter and working electrodes. Cell voltage is measured between the working and reference electrodes.¹²⁸ Both square-wave cycle and length of a single step in the voltage series take a time τ . The inverse of the cycle length is the frequency, $1/\tau$. The scan rate for such an experiment is inversely dependent upon the time per step, τ .

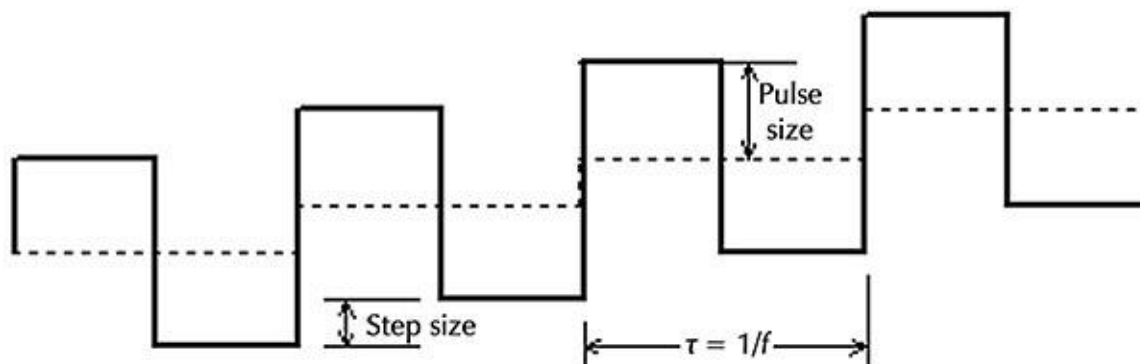


Figure 1.10. Schematic of the flow of voltage varies with time in SWV.

During the scan, the current is recorded at the end of the forward pulse and at the end of the reverse pulse, meaning it is sampled twice per cycle. Waiting till the end of the pulse to sample the current avoids involving the charging current.

The frequency, f , used in square-wave voltammetric experiments is generally from about 1 to 125 Hz. Such a high f means that square-wave voltammetry is usually much faster than other pulsed experiments.

1.6.3. Graphene Based Dopamine Sensors. Graphene is a considered as a promising material in electrochemical sensing because of the large surface area, large electrical conductivity and 2D surface. Electrodes can also be modified on graphene surfaces starting with graphene suspension, powder and graphene composites.¹²⁹⁻¹³¹ Using reduced graphene oxide (rGO) has been used for DA detection has been recently studied. It is been observed that oxygen containing groups increases the response to DA detection.¹³² The DA sensors with best detection limit (1-10 nmolL⁻¹) and good linear range was obtained using electrodes modified with graphene synthesized by modified

Hummers method.¹³³ The stability and reproducibility of electrodes modified with quercetin and polypyrrole^{134, 135} have been investigated and it showed a relative standard deviation to be lower than 2%.

1.6.4. Metal and Semiconductor Nanoparticles Based Dopamine Sensors.

Recently there has been an ample growth of research activities regarding applications of metal and semiconductor nanoparticles for electroanalysis.^{136, 137} These nanoparticles perform several important functions, which includes an increase of the sensing surface and facilitation of quick electron transfer. They also can be modified with different functional groups further to improve the performance. Conducting polymer [poly(3,4-ethylenedioxythiophene) polystyrene sulfonate- PEDOT] and inorganic Cu crystals are given here as an example towards DA sensing.¹³⁸ It was demonstrated sensing properties increase as the thickness of PEDOT, surface coverage by Cu in nano molar concentration range. This is because of Cu(II) – o- quinolate complex and its promotion of DA oxidation. There are numerous examples where metal nanoparticles are used in combination with some other metal nanoparticles (e.g. NPs of other metals or metal oxides) or other materials for modification of electrode surfaces. In such hybrid materials, metal nanoparticles are used to perform a certain function.¹³⁹ All the materials in combination are expected to contribute added or enhanced effects. For example, Au/Pt/Pd/TiO₂ NT electrodes showed synergistic effects of Au, Pt, and Pd NPs through enhanced conductivity and electrocatalytic activity. TiO₂ nanotubes are a better substrate for electrochemical deposition of metal NPs. Pd gives uniform modification on the surface of TiO₂ NTs, and AuNPs enhance sensitivity.¹⁴⁰ Pd-loaded amino group-functionalized mesoporous

Fe₃O₄ NPs (Pd@Fe₃O₄) have been reported to enhance electrochemical catalysis based on the synergistic effects.¹⁴¹

1.6.5. Challenges in Real Sample Analysis. Electrochemical detection of DA in urine or blood samples is difficult due to matrix effect of real samples. Along from major interferences such as uric and ascorbic acid there are other factors which could significantly increase or decrease the response of DA. The reported amounts of DA in real samples do not always represent the actual amount. Some of the ways to overcome the matrix effect in real samples are by using

1. Selective electrode surfaces by modifying the novel catalyst material
2. Dilution of the real sample to an optimal level
3. Extraction of DA or interferences by separation methods before analysis.

For example blood samples can be centrifuged followed by dilution while for urine samples it has to be diluted by several folds. The quantification of these samples is done by spiking with standard DA and applying standard addition method.

An electrochemical sensor was developed using amino- functionalized Fe₃O₄ on graphene to determine DA in urine samples. The sample was diluted with PBS to overcome the matrix effect. The results of this were comparable with existing techniques, and the linear range was also within the normal DA levels. Similarly graphitic carbon nitride nanosheets are also reported to have good response to DA levels in presence of AA and UA.

Further surface sensing analysis of real samples can be tried by the following merits

1. Using inexpensive electrodes for surface modifications
2. Simple to use and ready to modify with less number of steps

3. Stability of the modified electrode in harsh conditions
4. Reproducibility and reliability of modification
5. High sensitivity and low detection limit
6. Capacity to analyze the real sample directly

1.6.6. Future of Dopamine Sensors Based on Non-Enzymatic Electrodes. The sensitivity of electrochemical non enzymatic DA detection can be enhanced by accelerating the electron transfer at the surface of the electrode. Accumulation of the product at the catalyst surface decreases the sensitivity considerably. Preconcentration of the analyte at the electrode surface can be achieved through interaction between the functional groups and the sample. The other option to increase the sensitivity is physical adsorption of the analyte at the surface. Modification of the electrode surface is important factor as it helps the adsorption of analyte during preconcentration step and further it also aids in increase of the surface area with more functional moieties can be attached to increase the sensitivity of the DA detection.

In terms of selectivity of detection of DA in presence of other interfering bio molecules at physiological condition, two approaches can be employed. First, using the chemical moiety which at the electrode surface which can selectively bind the analyte which in this case DA. Secondly, selectively modify the electrode surface with functional groups or ions which can repel all the interference. In both the cases detection limit and sensitivity will be improved and the quantification of DA will be closer with actual value.

Electroanalytical methods involving modifications in electrodes shows a good improvement in real sample analysis and applications. However, these modified electrodes are still limited to proof of concept the question needs to be addressed. In this context, the

possibilities of such systems are still need to be further explored because of limited studies describing toxicity and biocompatibility of these modified materials. The other concern is the stability of these electrodes. For successful commercialization of these non-enzymatic sensors, technology that ensures production of large number of sensors with good reproducibility and at affordable cost for the consumer has to be developed. Special attentions should be given for facile synthesis of the electrodes, thorough characterization of the surface before and after the DA detection, electron kinetics, long term stabilities and application for real sample analysis are the challenges ahead.

1.7. ELECTROCHEMICAL NON-ENZYMATIC GLUCOSE SENSOR

1.7.1. History of Glucose Sensors. The historical advancement in electrochemical sensors can be summarized into three generations. The first generation glucose sensors is showed in Figure 1.11. Here oxygen plays an important role and acts as an electron mediator between glucose oxidase and surface of the electrode.¹⁴² Glucose oxidase reduces O_2 to H_2O_2 in presence of glucose. The oxygen reduction kinetics depends on the glucose concentration which can be determined by measuring the H_2O_2 concentration. The type of electrodes suffer from dependency of oxygen or interference by active redox species.

Figure 1.12 shows the second generation glucose sensor that uses artificial mediators to overcome the disadvantages related to first generation sensors. This mediator helps the electron transfer between enzyme and electrode surface.¹⁴⁴ Design of the redox systems is the important from high efficiency. Commonly used electron mediators are ferro/ferricyanide, ferrocene and other organic dyes.¹⁴⁵ The disadvantage with this generation sensor is oxygen competing with mediators that may lead to error.

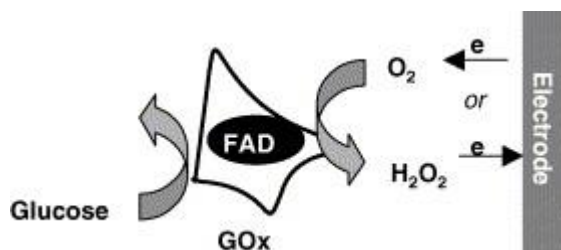


Figure 1.11. First generation enzyme glucose sensor (Reproduced with permission ¹⁴³).

The third generation glucose sensors are based on direct electron transfer where the electron is directly transferred from the enzyme to the surface of electrode as shown in Figure 1.13. If electrode and enzyme are electrically wired¹⁴⁶ the direct electron transfer transforms the events to an electric signal which is free of concentration of oxygen or redox mediators.¹⁴⁷ The advantage of these sensors are the elimination of possible interfering species.

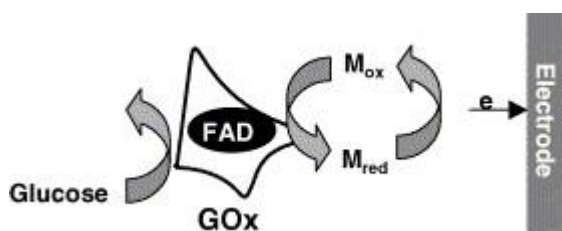


Figure 1.12. Second generation enzyme glucose sensor (Reproduced with permission ¹⁴³).

1.7.2. Advantages of Non-Enzymatic Glucose Sensors. Stability: Thermal and chemical instability of glucose oxidase prohibits enzymatic glucose sensors from using it continuously in human bodies. Additionally, humidity, temperature, pH and toxic chemicals affect the response of glucose sensors.¹⁴⁸ Optimal humidity is a significant criteria for these enzymatic glucose sensors to be store. Hence it is advantageous to use non enzymatic sensors, which is low cost, stable in highly alkaline and acidic environments. Further, they are not affected by drastic change in temperature and humidity.¹⁴⁹

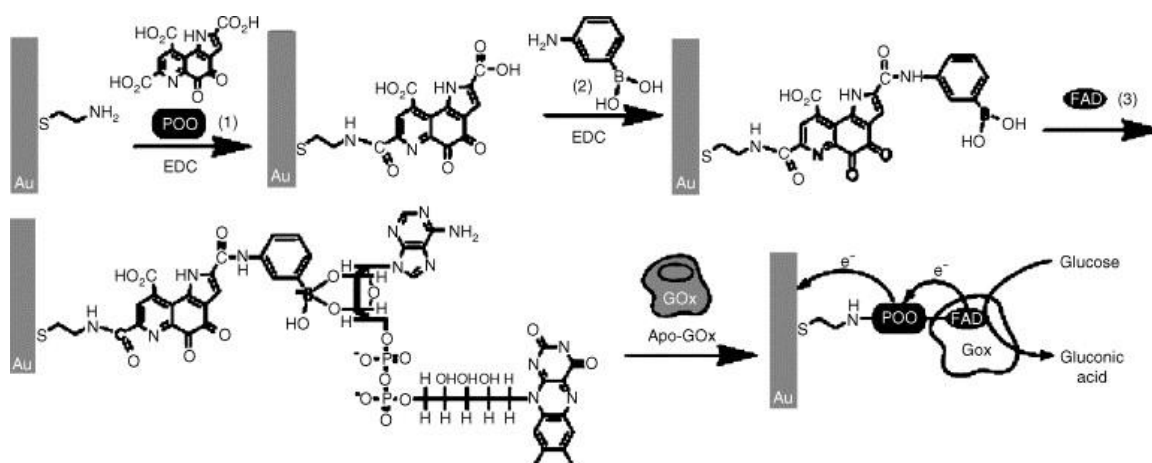


Figure 1.13. Schematic of third generation enzyme electrode glucose sensor. (Reproduced with permission ¹⁴³).

Free from oxygen and mediator limitations: The response of most enzyme electrodes depends on the oxygen concentration. Although some refined designs of quick electron transfer system can overcome the oxygen dependence effectively. However, even the best design is not completely free from oxygen. The other option to overcome the

oxygen mediation is the direct chemical oxidation of glucose on the surface of the electrode which occurs in non-enzymatic sensors. It should be noted that the reductive potential of oxygen is more positive than the glucose is oxidized. Hence such interference can be easily minimized in non-enzymatic sensors by finding an optimal potential for maximum current sensing region for glucose and sluggish reduction kinetics for oxygen molecule.^{150, 151}

1.7.3. Redox Mechanism of Glucose on Metal Surfaces. The two types of glucose (α - and β - glucose) are converted to glucono lactone through acid hydrolysis via γ – glucose (aldehyde glucose). Figure 1.14 shows the general reaction mechanism for glucose oxidation. For both α - and β - glucose, the hydrogen atom attached to C1 carbon is activated because hemiacetalic OH (pKa = 12.3) group is stronger than alcoholic OH (pKa = 16). The resultant product of this electrochemical oxidation of glucose is glucono- δ -lactone, which further oxidizes to gluconic acid which has a half-life of 10 mins and a rate constant of 10^{-3} s^{-1} at pH 7.2. In case of γ - glucose it oxidizes directly to gluconic acid. In all three cases (α -, β - and γ -glucose) the final stable product is gluconic acid which is a two electron process, regardless of the intermediate step of glucono- δ -lactone.¹⁵² The rate of mutarotation is acid base catalysed however, with alkaline solution shown to favor β -glucose in a 20:80 ratio of the anomers. As such, the pH of a solution is highly important when conducting glucose tests that are to reflect the whole blood glucose concentration, as the physiological ratio of α to β glucose can shift significantly. Furthermore, an anomeric effect has been observed for glucose in which β -glucose is oxidized at a faster rate than α -glucose, suggesting a preferred orientation for glucose adsorption on platinum electrodes. Similar mechanism is also proposed for Ni and Cu based catalysts. It was established, that

the catalytic component in these metals are the higher oxidation state (e.g.+3) and the oxidized partner which is the oxyhydroxide redox couple.¹⁵²

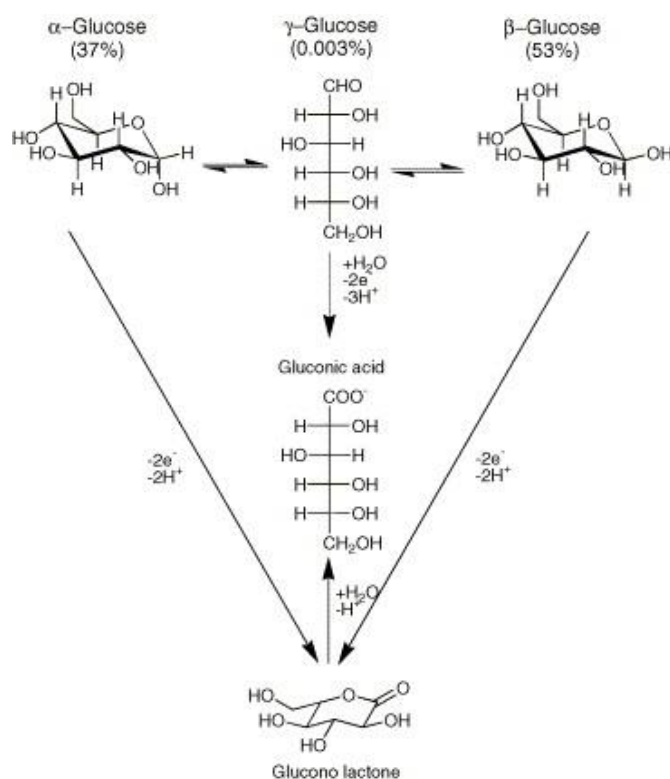


Figure 1.14. The general mechanism of glucose oxidation in aqueous solution and the possible mechanism of electron transfer and coupled reactions. (Reproduced with permission ¹⁵³).

A schematic illustration of Incipient Hydrous Oxide/ Adatom Mediator (IHOAM) model is depicted in Figure 1.15 where the metal is the adsorption site for $-OH$ attachment which forms $M[OH]_{ads}$ which is the oxidative hydroxide radical adsorbed on the metal. This scheme shows the redox process occurring at the catalyst surface. This was based on the observation that active surface metal atoms undergo a pre-monolayer oxidation step that

forms an incipient hydrous oxide layer of reactive OH_{ads} mediating oxidation and inhibiting reduction of kinetically slow electrode reactions. Considering this effect, both the activated chemisorption model and the IHOAM model will be important in explaining the reaction mechanism in non- enzymatic glucose sensors.

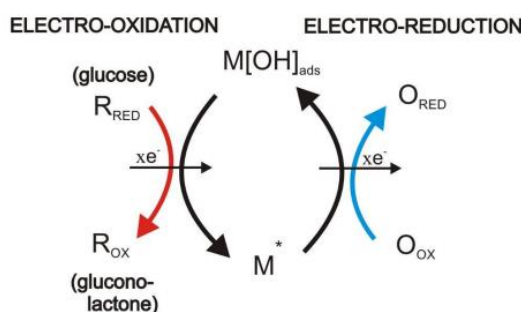


Figure 1.15. Redox process at the catalyst surface.

1.7.4. Metal/ Metal Oxide Based Nano Composites as Glucose Sensors. Metallic nanoparticles has been significantly incorporated as non-enzymatic biosensor fabrication. They show high surface area, good conductivity, compatibility, high chemical resistance and are nontoxic. Different metal nanoparticles such as Cu, Zn, Au, Ag, Pt, Zn and their alloys have been used for this purpose. They provide enhanced surface area and quick charge transfer from the analyte to the electrodes, which eventually improves the digital signal.¹⁵⁴ Moreover, by associating two or more metals in nano-hybrid, several favorable properties will be combined which leads to improved performance which cannot be attained by just one component. For example, the low catalytic activity of gold could be compensated by Pt alloys to enhance the catalytic properties by synergistic effect.¹⁵⁵

Additionally, incorporation of polymer films (nafion, chitosan or mesoporous silica) in metal nanoparticles have the effect to increase in structural stability, enzyme leakage and it retains the chiral confirmation if any.¹⁵⁶

The assembly of gold with silver nanoparticles has been reported as glucose sensor. The synergistic effect between Ag which has good catalytic properties and Au which is a good conductor has a major advantage to biosensing. The Ag-Au assemble has been synthesized using reverse micellar method where enzymes exhibits higher activity than in aqueous systems. Electrochemical studies has shown that Au-Ag nanoparticles is having enhanced electron transfer, stability, and sensitivity of glucose sensing.¹⁵⁷

Recently, nanohybrids based on one dimensional materials and nanoparticles of noble metals, with a synergistic effect have found many applications in biosensing. In comparison with spherical nanoparticles, nanowires possess a number of unique electronic and physical properties due to their anisotropic nature for electrochemical reactions at the surface of the electrode. Synergistic effect of lead nanowires and gold nanoparticles has improved electrochemical biosensing of glucose through excellent electrocatalytic activity. This is due to high loading efficiency and a compatible environment for biosensing.¹⁵⁸ Further 2D nanomaterials have also been explored for glucose sensing. For example MoS₂ nanosheets modified on glassy carbon electrode decorated with Au nanoparticles has a good catalytic behavior for sensing. This electrode showed excelled electrocatalytic activity and stability.

Finally, polymer nanocomposite films such as chitosan polypyrrole onto carbon electrode showed superior activity for glucose detection. The nanocomposites combined the electroconductive properties of polypyrrole, the film forming and the biocompatibility

with chitosan has surface area related advantage over monodispersed nanoparticles. Therefore this fabricated electrode shows faster amperometric response time (>5 s) a low LOD (15.5 μM) and wider linear range. Indeed higher biocompatibility and improved stability and reproducibility are key for biosensors.¹⁵⁹

1.7.5. Carbonaceous Materials for Glucose Sensors. It is clear that using carbon materials as a support to disperse metal nanoparticles (oxides or chalcogenides) improves the catalytic properties of the hybrid through the increase of surface area and relative conductivity. Apart from these improvement the physical properties of carbonaceous nanomaterials can also improve on their own as in the case of hybrids between graphene and the metal oxide/ chalcogenide nanoparticles. For example, when graphene-oxide hybrids are used as photocatalysts, there is extended absorption and fast electron transfer in graphene based hybrid when compared to oxide nanoparticles alone. Additionally, due to its 2D structure graphene is an excellent electron accepting and transporting material. When graphene is incorporated into semiconductor materials, it promotes photo-generated electron through pi-pi interactions and helps the material to overcome charge recombination. Similar effects of graphene addition is seen in electrocatalytic water splitting, where the overpotential is significantly reduced and closer to 1.23 V vs RHE. Without the addition of any conductive carbon these catalyst are active towards water splitting, but the overall performance is low.

Therefore use of these carbonaceous materials in sensing field is in use to improve the sensing properties. Cu nanoparticles on graphene sheets are reported as non-enzymatic glucose sensor by electrodeposition method. The Cu-graphene sheets shows much better activity for glucose detection compared to unmodified graphene sheets are Cu electrode as

such. The linear range up to 4.5 mM was achieved with a detection limit of 0.5 μM at an applied potential of 500 mV.¹⁶⁰ Similarly, a novel nanocomposite of reduced graphene oxide and gold-palladium bimetallic nanoparticles is reported as a non-enzymatic glucose sensor. The hybrid catalyst showed excellent biocompatibility, enhanced electron transfer because of large surface area, having high sensitivity and stable towards mediating species like oxygen. The resulting electrode had a sensitivity of 266.6 $\mu\text{A}/\text{mM}/\text{cm}^2$ with a linear range up to 3.5 mM.¹⁶¹

1.7.6. Future Prospect in Glucose Sensing. As researchers are trying to improve the sensor performance parameters, the future of bio sensing is to focus on improving the selectivity at practical levels. Stability is another important parameter in evaluating a sensor. The drift of sensors should also be considered which can be solved by calibration of equipment and data processing. New trends in sensor technology are beginning to emerge and new methodology is needed to garner more information from a single sensor. This goal can be achieved through developing an optimal electrode material combined with statistical tools. The development of best catalyst with high sensitivity, low energy consumption, low detection limit could facilitate precise measurements and has an enormous demand in chemistry, pharmaceuticals and materials science. With miniaturization using microelectronic technology and increase in the number of users the cost of device production is expected to lower and help the people in need for regular monitoring of blood glucose levels in the body.

Continuous glucose monitors allow a patient and clinician to more closely monitor glucose control by evaluating time in target range, time in hypoglycemia, and time in hyperglycemia. A continuous glucose monitor has a subcutaneous sensor that measures the

interstitial fluid glucose at a minimum of every five minutes, and the sensor's transmitter continuously sends data to its receiver (Figure 1.16).



Figure 1.16. Prototype of continuous glucose monitoring system.

1.7.7. Motivation to Use Transition Metal Chalcogenides as Biosensors. Since the first step of glucose oxidation is the adsorption of hydroxyl group on C1 atom, the principle of changing O to Se which increases the conductivity and also reduces the potential applied for charge transfer still applies in glucose sensing.

The objective of the two papers regarding biosensing, is about designing high-efficiency direct dopamine and glucose electrochemical sensors from transition metal chalcogenides using principles of materials chemistry described above, specifically, tuning the redox potential of the transition metal site. This thesis present CuSe as example of high-efficiency chalcogenide based dopamine and glucose sensors.

These chalcogenide based electrocatalysts show high activity for glucose oxidation at very low potential (~ 0.15 V vs Ag|AgCl) with high sensitivity (exceeding 19.41 mA/mM cm^2) and low limit of detection (LOD). Further metal chalcogenides can offer direct electron transfer pathways over a wide potential range leading to much higher sensor efficiency. Moreover, the sensing performance of these electrocatalysts were tested in presence of common interferents present in physiological samples such as uric acid, ascorbic acid, and lactose.

1.8. SUMMARY

This research focuses on synthesizing transition metal chalcogenide materials by hydrothermal and electrodeposition methods and their applications in energy conversion like oxygen evolution reaction, oxygen reduction reaction and electrochemical oxidation of biomolecules such as glucose and dopamine.

The first part describes designing electrocatalysts for oxygen evolution reaction and oxygen reduction reaction and controlling this composition for achieving bifunctional activity. These metal selenide based catalyst performance can be further improved by introducing carbon matrix such as reduced graphene oxide and functionalized onion like carbon where synergistic effect places a critical role. This research shows that activity of the catalyst can be altered by changing the environment around the metal, from oxide to selenide which raises the valance band edge close to water oxidation potentials. The catalysts reported in this work are also having good stability for long hours without any observable degradation. Further the catalyst retain there performance after the stability study which is confirmed by post catalytic characterization.

The second part describes the use of transition metal chalcogenides for electrooxidation of biomolecules such as glucose and dopamine which can be used as non-enzymatic biosensors. The catalyst reported in this research performs oxidation at low applied potentials with high sensitivity and low detection limit which makes these catalyst potential candidates for wearable devices. These chalcogenides can offer direct electron transfer pathways over a wide potential range leading to much higher sensor efficiency. Further, the sensing performance of these electrocatalysts were tested in presence of common interferents present in physiological samples such as uric acid, ascorbic acid, lactose, sucrose and common salt, where it showed that glucose/dopamine sensing was unaffected by interferents, which shows high selectivity of these metal chalcogenides.

PAPER

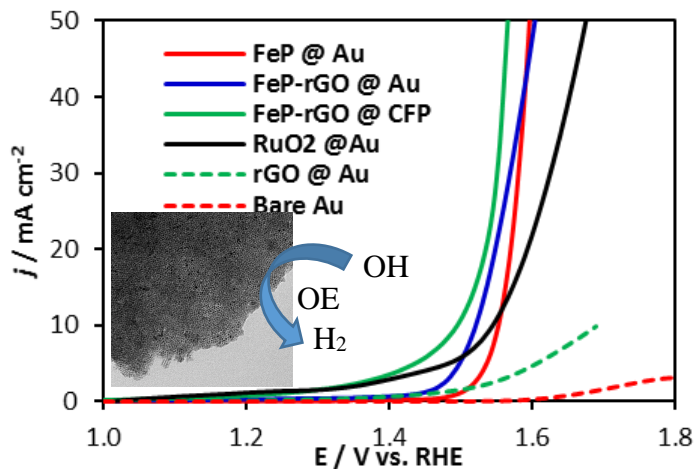
I. IRON PHOSPHIDE NANOPARTICLES AS AN EFFICIENT ELECTROCATALYST FOR OER IN ALKALINE SOLUTION

Jahangir Masud, Siddesh Umapathi, Nikitaa Ashokan and Manashi Nath

Department of Chemistry, Missouri University of Science & Technology, Rolla,
MO 65409-1170, USA

ABSTRACT

Ultrasmall iron phosphide nanoparticles has been reported as efficient electrocatalyst for oxygen evolution reaction in alkaline condition with low overpotential and Tafel slope. Mixing the FeP nanoparticles with reduced graphene oxide further reduces the overpotential to 260 mV at $10\text{mA}/\text{cm}^2$, which is one of the lowest reported for OER electrocatalyst.



1. INTRODUCTION

The development of renewable and clean energy technologies,¹⁻³ such as water splitting for hydrogen production, artificial photosynthesis and metal-air batteries, is hindered because of very sluggish oxygen evolution reaction (OER) kinetics. Several catalysts, generically referred to as OER catalysts, has been employed to facilitate the oxygen evolution reaction. Among these the catalysts based on noble metals including Pt, Ru, and Ir, show some of the best catalytic efficiency for OER.⁴⁻⁵ However, the prohibitive cost and scarcity of the noble metals have significantly impacted their large-scale application. Consequently, great efforts have been devoted to developing new OER electrocatalysts with both excellent activity and low cost.

Recently, transition metal oxides⁶⁻⁷ comprising earth-abundant elements have shown immense promise as OER electrocatalysts. In addition to oxides, transition metal chalcogenides⁸⁻⁹ have shown even better potential as OER electrocatalysts possibly due to their more compatible electronic structure.¹⁰ More recently, transition-metal phosphides (TMPs)¹¹⁻¹⁹ which are intrinsically metallic have been intensively studied as a electrocatalysts for OER as well as HER. For instance, FeP¹¹⁻¹², Ni₂P¹³, and CoP¹⁴, have already shown great potentials as HER catalysis at high current densities at low overpotentials. On the other hand, there has been some reports on CoP, NiP and recently MnCoP as OER catalyst in alkaline medium.^{16-17, 20-21} Although FeP has been shown to be active for HER, oxygen evolution with pure FeP has not been reported till date. Recently, Yan et. al¹⁹ has reported iron phosphide nanotubes coated with an iron oxide/phosphate layer grown on carbon cloth as full water splitting catalyst.

Herein, we report high catalytic efficiency for ultrasmall pure FeP nanoparticles synthesized from solution-based hot injection methods (see supporting information). These FeP nanoparticles can achieve a current density of 10 mA cm^{-2} at overpotentials as low as 290 mV for OER in strongly alkaline solution along with small Tafel slope (50.8 mV/dec). A hybrid electrode formed from these FeP nanoparticles mixed with reduced graphene oxide (rGO) lowers the overpotential at 10 mA.cm^{-2} even further to 260 mV making this the lowest reported in the family of transition metal phosphides. Electrodes prepared from FeP catalyst also show excellent stability with retention of full activity even after 4 h of constant current electrolysis.

2. RESULTS AND DISCUSSION

Figure 1a shows a typical TEM image and corresponding histogram analysis (inset of Figure. 1a) of the as synthesized catalyst. From extensive TEM analysis it was observed that the FeP nanoparticles had a narrow size distribution (3 – 7 nm), with an average size of ~ 5 nm based on counting about 200 randomly chosen particles from different regions of the TEM specimen grid. The high-resolution TEM (HRTEM) image, as shown in Figure. 1b, reveals the lattice fringes with interplanar spacings of 1.54, 2.42 and 2.73 Å, corresponding to $\langle 020 \rangle$, $\langle 111 \rangle$ and $\langle 011 \rangle$ planes of the FeP, respectively. The crystallinity of film was further confirmed by selected area electron diffraction (SAED) pattern shown as inset of Figure. 1b, where the diffraction spots can be indexed to the $\langle 111 \rangle$ and $\langle 211 \rangle$ planes of FeP, respectively. The energy dispersive spectra (EDS) of FeP collected in the TEM mode also showed the presence of Fe and P elements with the atomic

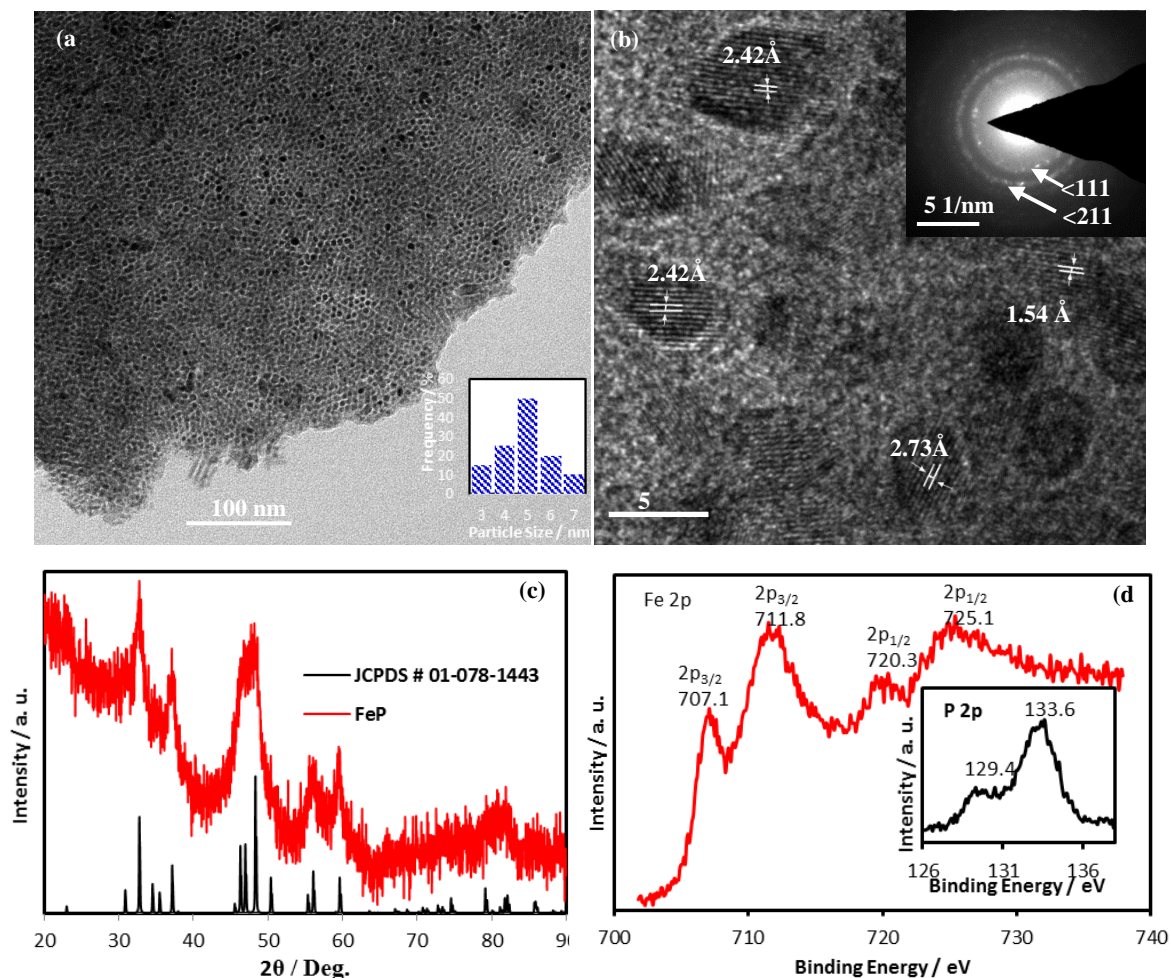


Figure 1. (a) TEM images of FeP and particle size histogram (b) HRTEM image and corresponding selected-area electron diffraction pattern (c) Pxrdd of FeP and d. XPS spectra of Fe 2p and P 2p (inset).

ratio close to 1:1 (Figure. S1). Powder X-ray diffraction (pxrd) of the as synthesized nanostructures was collected to further characterize the chemical composition and crystallinity of the catalyst. As shown in Figure 1c, all the diffraction peaks could be well indexed to FeP (JCPDS Card No.01-078-1443), with almost no detectable impurities. The average particle size was estimated to be 8.0 nm by using Scherrer equation (see supporting documents) which is in accordance with TEM observation. The X-ray photoelectron

spectroscopy (XPS) analysis of the as-prepared FeP shown in Figure. 1d also confirmed the composition of the catalyst. The doublet peaks for the binding energy (BE) of Fe 2p_{3/2} appear at 707.1 and 711.8 eV and P 2p peaks at 129.3 and 133.8 eV. The peak at 707.1 eV is associated with Fe in FeP,²² whereas that of 711.8 eV due to oxidized Fe,²³ resulting from the surface oxidation of FeP when exposed to air.²³ The P 2p XPS spectrum revealed two peaks at 133.6 and 129.4 eV, respectively. The lower energy peak is consistent with the binding energy for FeP (129.4 eV),²²⁻²³ and peak at 133.6 might due to the presence of oxidized phosphorus on the surface.

The FeP nanoparticles were coated on different electrodes following standard procedures as described in the supplementary information. In addition to standard electrodes, the FeP nanoparticles were also mixed with reduced graphene oxide (rGO) powder to increase the conductivity of the catalyst coating eventually enhancing catalytic performance. The rGO was synthesized separately following a protocol as described in supplementary information, and has been characterized by Raman spectroscopy and TEM imaging (Figure S1). In the following sections, the OER catalytic activity of Fe on Au-coated glass (FeP@Au), FeP-rGO on Au-coated glass (FeP-rGO@Au) and FeP-rGO on carbon fiber paper (CFP), [FeP-rGO@CFP] has been presented.

All the catalytic activities have been measured in alkaline solution in presence of 1M KOH and the results were compared with RuO₂ which is known as state-of-the-art OER catalyst. The RuO₂ was prepared in our laboratory by electrodepositing directly on the Au-coated glass electrodes (see supporting information). Figure 2a shows the polarization curves of FeP@Au, FeP-rGO@Au, FeP-rGO@CFP, rGO@Au, and bare Au-coated glass in N₂ saturated 1 M KOH at a scan rate of 10 mV s⁻¹. As expected, no obvious

current responses were obtained for the bare Au-coated glass substrate while very poor activity was observed at the rGO modified Au-glass electrodes. The FeP loaded Au-glass on the other hand, showed very efficient oxygen evolution activity. Specifically, the onset potential of FeP@Au was 1.48 V (vs. RHE) and yielded a current density of 10 mA cm⁻² at an overpotential of 320 mV. The hybrid electrode containing mechanically mixed rGO

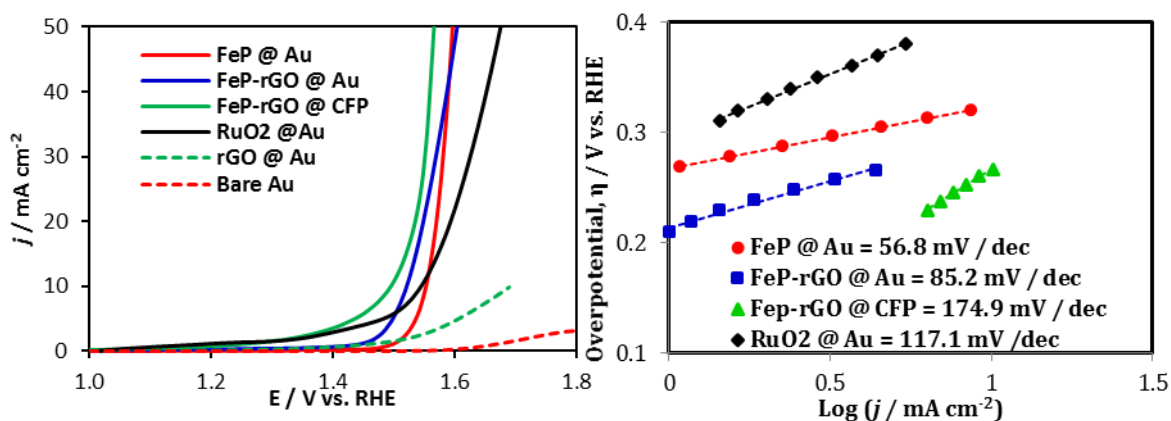


Figure 2. (a) LSVs of the various FeP nanostructured based catalyst coated electrodes measured in N₂ saturated 1.0 M KOH solution at a scan rate of 10 mV s⁻¹ and (b) the Tafel plot of catalysts.

with FeP nanoparticles showed even better OER catalytic activity. The onset potential for FeP-rGO@Au and FeP@CFP were 1.44 and 1.40 V vs. RHE, respectively. To achieve the OER current density at 10 mA cm⁻² FeP-rGO@Au requires 290 mV and for FeP-rGO@CFP only 260 mV, which is better than RuO2@Au (320 mV), IrOx (320 mV)²⁴ and other transition metal phosphide based catalysts. Figure 2b shows the Tafel plot, η vs. $\log(j)$, for FeP based catalysts. The Tafel slopes were obtained as 56.8, 85.2 and 174.9 mV dec⁻¹ for FeP@Au, FeP-rGO@Au and FeP-rGO@CFP, respectively which are comparable

with other phosphide based OER electrocatalysts.¹⁶⁻¹⁸ Based on the above observations it can be concluded that hybrid composite of FeP-rGO yields the best OER catalytic activity both in terms of overpotential @ 10 mA.cm⁻², exchange current density and low Tafel slope. Such enhancement of the catalytic activities in the rGO mixed hybrid composites can be explained by the possible synergistic effects of rGO with FeP which increases the conductivity of the matrix and facilitates charge transfer within the catalyst composite, thereby increasing the current density. The high electrical conductivity of FeP may also favor fast electron transport which enhances the catalytic activity.

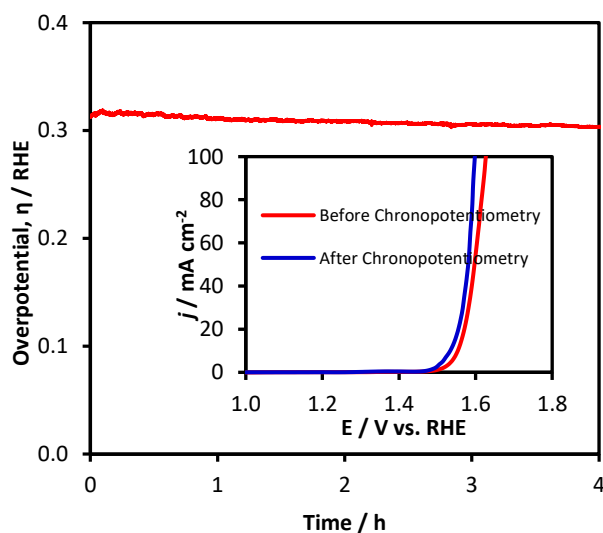


Figure 3. Stability study of catalyst under continuous O₂ evolution (at 10 mA/cm²) for 4 h studied through chronopotentiometry. Inset shows the LSVs of catalyst measured in N₂ saturated 1 M KOH before and after chronopotentiometry for 4h.

Stability of the FeP electrocatalyst was investigated through chronoamperometry studies where the voltage required to produce a constant current of 10 mA cm⁻² (i.e.

overpotential @ $10 \text{ mA}\cdot\text{cm}^{-2}$) was recorded for 4h and shown in Figure 3. Initially high overpotential was required to achieve 10 mA cm^{-2} . However, the overpotential was significantly reduced after 4 h of chronoamperometry (only 290 mV overpotential requires to get 10 mA cm^{-2}) indicating that the catalyst became more active on aging. The inset of Figure. 3 shows the comparison of LSVs before and after 4 h of chronopotentiometry indicating superior stability of catalyst as well as improving catalyst performance under conditions of continuous O_2 evolution. The SEM image collected after 4 h of chronoamperometry (Supplementary Figure S3) showed that the electrode surface remained unchanged while EDX line scan showed uniform distribution of Fe and P in the catalyst film. The FeP-rGO@Au hybrid electrode also shows very high stability under conditions of continuous O_2 evolution (Supplementary Figure. S4).

The turnover frequency (TOF) of the FeP catalyst was calculated at an overpotential of 330 mV in 1 M KOH, assuming all of the active metals in the catalyst are catalytically active for OER. The TOF value of FeP@Au, FeP-rGO@Au, and FeP-rGO@CFP were calculated as 0.004, 0.019 and 0.031 s^{-1} , respectively which are comparable with the previously reported TOF values of metal phosphide based catalyst¹⁸, and higher than well-known IrOx (0.0089 s^{-1})²⁵ OER catalyst, also indicating a better OER activity for FeP.

The enhanced catalytic activity of the FeP nanoparticles can be possibly explained by the very small size of the nanoparticles which increases the active functional surface area of the catalyst. Dispersing these ultrasmall particles in the rGO matrix further increases the functional surface area of the catalyst by de-coagulating the catalytically active particles. On the other hand, coating the planar Au-coated glass substrate with the

catalyst ink leads to possible aggregation of the catalyst particle, leading to lesser accessibility of the electrolyte to all the catalytically active sites.

3. CONCLUSION

In conclusion, we have reported a FeP nanoparticle-based efficient OER electrocatalyst containing earth-abundant elements. This catalyst requires comparatively lower overpotential to achieve 10 mA cm^{-2} which is significantly lower than the state-of-the-art IrOx catalysts and is one of the lowest for phosphide based electrocatalyst. Importantly, the FeP nanoparticles can be combined with reduced graphene oxide sheets which results in significantly improved catalytic activity owing to the synergistic effect. High catalytic activity along with the ease of synthesis of the nanoparticles, makes this system have high technological importance.

Table 1. Parameters describing the catalytic activity of the FeP-nanoparticle based catalysts reported in this study.

Catalysts	Onset potential/ V vs. RHE	η to achieve 10 mA cm^{-2} / mV vs. RHE	Tafel slope / mV dec^{-1}	TOF at $\eta=330 \text{ mV}$ / s^{-1}
FeP @ Au	1.48	320	56.8	0.004
FeP-rGO @ Au	1.44	290	85.2	0.019
FeP-rGO @ CFP	1.40	260	174.9	0.031
RuO ₂ @ Au	1.49	320	117.1	-

Table 2. Comparison of OER activity of different phosphide based electrocatalysts.

Catalyst	Electrolyte	Onset potential	η at 10 mA cm ⁻² / mV	Tafel / mV dec ⁻¹	TOF at 330 mV/s ⁻¹	References
(Co _{0.54} Fe _{0.46}) ₂ P	0.1 M KOH	1.46	370	-	-	14
Ni-P	1.0 M KOH	1.54	344	49	-	15
CoP	1.0 M KOH	1.56	345	47	-	16
CoP NPs	0.1 M NaOH	1.52	330	50	0.0287 at 370 mV	17
CoMnP	1.0 M KOH	1.52	330	61	-	20
FeP @ Au	1.0 M KOH	1.48	320	56.8	0.004	This work
FeP-rGO @ Au	1.0 M KOH	1.44	290	85.2	0.019	This work

SUPPORTING INFORMATION

Synthesis of Reduced Graphene Oxide (rGO)

Graphene oxide was synthesized by modified Hummers method. Typically, 1 g of graphite and 0.5 g of sodium nitrate were mixed together followed by the addition of 23 ml of conc. sulfuric acid under constant stirring. After 1 h, 3 g of KMnO₄ was added gradually to the above solution while keeping the temperature less than 20°C to prevent overheating and explosion. The mixture was stirred at 35 °C for 12 h and the resulting

solution was diluted by adding 500 ml of water under vigorous stirring. To ensure the completion of reaction with KMnO_4 , the suspension was further treated with 30% H_2O_2 solution (5 ml). The resulting mixture was washed with HCl and H_2O respectively and allowed to stand for 48 hrs, followed by centrifugation and drying.

To convert GO to reduced Graphene Oxide (rGO), 0.1 ml of hydrazine was added to 10 mg of GO in water. For further reduction of GO to rGO, this solution was transferred to Teflon lined autoclave, which was sealed and maintained at 145°C for 24 hrs.

Synthesis of FeP

All reagents used in this synthesis were purchased from Sigma Aldrich. In a typical experiment, 1.00 g of Trioctylphosphine oxide (TOPO) and 1.2 ml of Trioctylphosphine (TOP) were mixed and heated at 300°C for 30 mins in a three neck round bottom flask under vigorous stirring in N_2 medium. Subsequently, 0.3 ml of solution 1 (made from 0.2 ml of $\text{Fe}(\text{CO})_5$ and 0.8 ml TOP) was added into TOP/TOPO solution. Instantly, the solution changes to black and the temperature was constantly maintained at 300°C for 30 mins. The black solution is washed and centrifuged several times with hexane using ultrasonification to remove the reaction mixture. The black product is dried and characterized.

Preparation of FeP-rGO

FeP was mechanically mixed with reduced graphene oxide (rGO) in different ratio (1:1 and 7:3 w/w for FeP:rGO) by using agate pestle and mortar for 30 mins. A homogeneous black powder was obtained after such mixing.

Electrodeposition of RuO₂ on Au

Electrodeposition of RuO₂ on GC substrate was carried out from a mixture of RuCl₃ (0.452 g) and KCl (2.952 g) in 40 ml of 0.01M HCl by using cyclic voltammetry from 0.015 to 0.915 V (vs. Ag|AgCl) for 100 cycles at a scan rate of 50 mV s⁻¹. Finally heated at 200 °C for 3 h in presence of air.

Electrode Preparation

Au-coated glass used as substrates was purchased from Deposition Research Lab Incorporated (DRLI), Lebanon Missouri. . All solutions were prepared using deionized (DI) water with a resistivity of 18 MΩ·cm. Prior to electrodeposition, the substrates were cleaned by ultrasonic treatment in micro-90 followed by isopropanol rinse for three times and eventually rinsed with deionized water (15 min each step) to ensure the clean surface. FeP catalyst ink was prepared by ultrasonically dispersing 1.0 mg catalysts in 1.0 mL isopropyl alcohol (IPA) and ultrasonicated for 30 min. Au-coated glass plates was covered with a Teflon tape, leaving an exposed geometric area of 0.283 cm², served as an underlying conductive substrate of the working electrode. A quantity of 20 μL of the ink was pipetted out on the top of the Au. The catalyst layer was dried at room temperature. Then, an aliquot of Nafion solution (10 μL of 1 mg/mL solution in 50% IPA in water) was applied onto catalyst layer. The Nafion-coated working electrode was dried at room temperature and finally heated at 130 oC for 30 min. in air in an oven.

Characterizations

Transmission Electron Microscopy (TEM). FEI Tecnai F20 was used to obtain TEM, high resolution TEM images (HRTEM) and selected area electron diffraction (SAED) patterns of the catalyst.

Powder X-ray Diffraction. The electrodeposited substrates were studied as such without any further treatment. The product was characterized through powder X-ray diffraction (pxrd) with Philips X-Pert using $\text{CuK}\alpha$ (1.5418\AA) radiation. Pxd pattern was collected from the as-synthesized product spread on the growth substrate. Because the product formed a very thin layer on the substrate, the pxd was collected at grazing angles in thin film geometry (GI mode with Göbel mirrors).

X-ray Photoelectron Spectroscopy (XPS). XPS measurements of the catalysts were performed by KRATOS AXIS 165 X-ray Photoelectron Spectrometer using monochromatic Al X-ray source. The spectra were collected as is and after sputtering with Ar for 2 min which removes approximately 2 nm from the surface.

Electrochemical Characterization and Catalytic Studies. The OER catalytic performance was estimated from linear scan voltammetry (LSV) plots while the stability of the catalyst was studied by chronoamperometry. Electrochemical measurements were performed in a three-electrode system with an IvumStat potentiostat using Ag/AgCl and Pt mesh as reference and counter electrodes, respectively. All measured potentials vs the Ag/AgCl were converted to the reversible hydrogen electrode (RHE) scale via Nernst equation (eq. 1):

$$E_{\text{RHE}} = E_{\text{Ag/AgCl}} + 0.059 \text{ pH} + E_{\text{Ag/AgCl}}^{\circ} \quad (1)$$

where RHE is the converted potential vs. RHE, $E_{\text{Ag/AgCl}}$ is the experimentally measured potential against Ag/AgCl reference electrode, and $E_{\text{Ag/AgCl}}^{\circ}$ is the standard potential of Ag/AgCl at 25 °C (0.197 V). For most of the electrochemical characterizations, the electrode area of the film surface was kept constant at 0.283 cm^2 .

Turnover Frequency (TOF). The turnover frequency (TOF) was calculated from the following equation

$$\text{TOF} = \frac{I}{4 \times F \times m} \quad (2)$$

where I is the current in Amperes, F is the Faraday constant and m is number of moles of the active catalyst.

Tafel plots. The Tafel slope was calculated from the following equation

$$\eta = a + \frac{2.3 RT}{\alpha n F} \log(j) \quad (3)$$

where η is the overpotential, j is the current density and the other symbols have their usual meanings.

The Tafel equation as shown Eq. (3) is a fundamental equation which acquires from the kinetically control region of OER / HER, and relates the overpotential η with the current density j where the Tafel slope is given by $2.3RT/\alpha nF$. To calculate Tafel slopes, LSV plots were obtained with slow scan speed (2 mV s^{-1}) in non-stirred solution

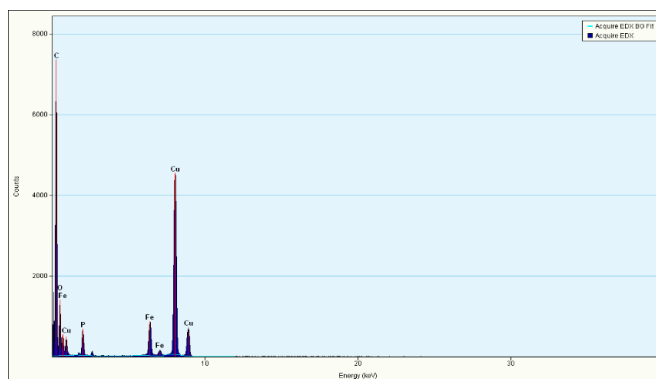


Figure S1. TEM EDS of FeP.

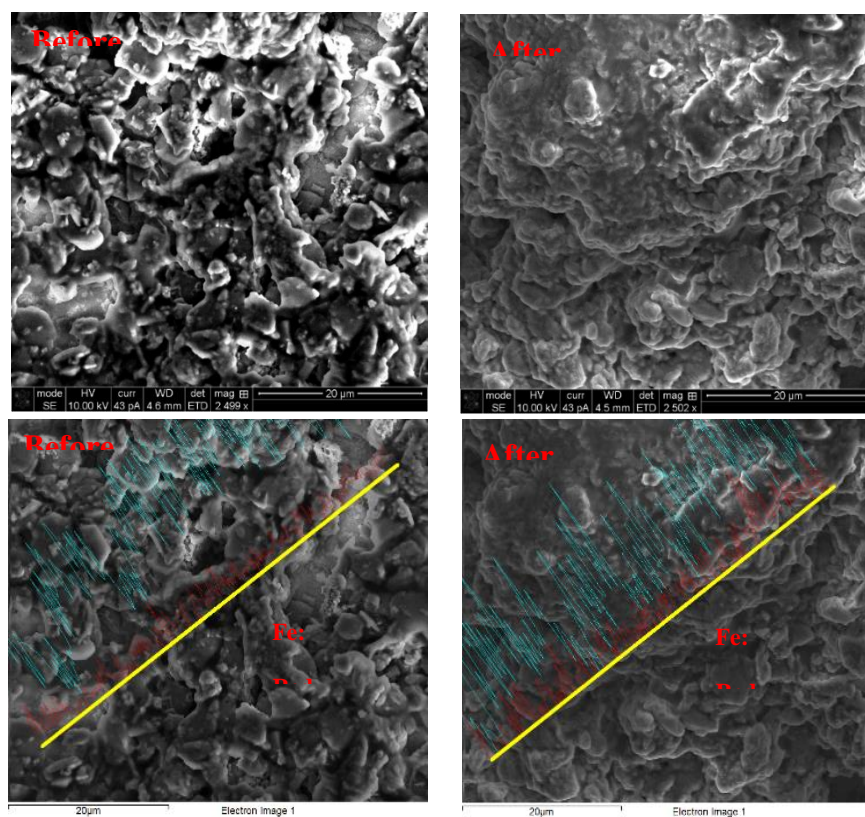


Figure S2. SEM images of electrodes (top two images) and EDS line scans of electrode (bottom).

REFERENCES

1. M. G. Walter, E. L. Warren, J. R. McKone, S. W. Boettcher, Q. Mi, E. A. Santori and N. S. Lewis, *Chemical Reviews*, 2011, **111**, 5815-5815.
2. J. R. McKone, N. S. Lewis and H. B. Gray, *Chemistry of Materials*, 2014, **26**, 407-414.
3. N. S. Lewis and D. G. Nocera, *Proceedings of the National Academy of Sciences*, 2006, **103**, 15729-15735.
4. Y. Lee, J. Suntivich, K. J. May, E. E. Perry and Y. Shao-Horn, *The Journal of Physical Chemistry Letters*, 2012, **3**, 399-404.

5. J. Jiang, A. Zhang, L. Li and L. Ai, *Journal of Power Sources*, 2015, **278**, 445-451.
6. W. T. Hong, M. Risch, K. A. Stoerzinger, A. Grimaud, J. Suntivich and Y. Shao-Horn, *Energy & Environmental Science*, 2015, **8**, 1404-1427.
7. F. Jiao and H. Frei, *Angewandte Chemie International Edition*, 2009, **48**, 1841-1844.
8. A. T. Swesi, J. Masud and M. Nath, *Energy & Environmental Science*, 2016, **9**, 1771-1782.
9. Y.-R. Zheng, M.-R. Gao, Q. Gao, H.-H. Li, J. Xu, Z.-Y. Wu and S.-H. Yu, *Small*, 2015, **11**, 182-188.
10. Y. Liu, H. Cheng, M. Lyu, S. Fan, Q. Liu, W. Zhang, Y. Zhi, C. Wang, C. Xiao, S. Wei, B. Ye and Y. Xie, *Journal of the American Chemical Society*, 2014, **136**, 15670-15675.
11. J. F. Callejas, J. M. McEnaney, C. G. Read, J. C. Crompton, A. J. Biacchi, E. J. Popczun, T. R. Gordon, N. S. Lewis and R. E. Schaak, *ACS Nano*, 2014, **8**, 11101-11107.
12. Z. Zhang, B. Lu, J. Hao, W. Yang and J. Tang, *Chemical Communications*, 2014, **50**, 11554-11557.
13. E. J. Popczun, J. R. McKone, C. G. Read, A. J. Biacchi, A. M. Wiltrout, N. S. Lewis and R. E. Schaak, *Journal of the American Chemical Society*, 2013, **135**, 9267-9270.
14. E. J. Popczun, C. W. Roske, C. G. Read, J. C. Crompton, J. M. McEnaney, J. F. Callejas, N. S. Lewis and R. E. Schaak, *Journal of Materials Chemistry A*, 2015, **3**, 5420-5425.
15. A. Mendoza-Garcia, H. Zhu, Y. Yu, Q. Li, L. Zhou, D. Su, M. J. Kramer and S. Sun, *Angewandte Chemie International Edition*, 2015, **54**, 9642-9645.
16. N. Jiang, B. You, M. Sheng and Y. Sun, *ChemCatChem*, 2016, **8**, 106-112.
17. N. Jiang, B. You, M. Sheng and Y. Sun, *Angewandte Chemie International Edition*, 2015, **54**, 6251-6254.
18. C.-C. Hou, S. Cao, W.-F. Fu and Y. Chen, *ACS Applied Materials & Interfaces*, 2015, **7**, 28412-28419.
19. Y. Yan, B. Y. Xia, X. Ge, Z. Liu, A. Fisher and X. Wang, *Chemistry – A European Journal*, 2015, **21**, 18062-18067.

20. M. Liu and J. Li, *ACS Applied Materials & Interfaces*, 2016, **8**, 2158-2165.
21. D. Li, H. Baydoun, C. N. Verani and S. L. Brock, *Journal of the American Chemical Society*, 2016, **138**, 4006-4009.
22. H. Du, S. Gu, R. Liu and C. M. Li, *International Journal of Hydrogen Energy*, 2015, **40**, 14272-14278.
23. J. Tian, Q. Liu, Y. Liang, Z. Xing, A. M. Asiri and X. Sun, *ACS Applied Materials & Interfaces*, 2014, **6**, 20579-20584.
24. C. C. L. McCrory, S. Jung, J. C. Peters and T. F. Jaramillo, *Journal of the American Chemical Society*, 2013, **135**, 16977-16987.
25. L. Trotochaud, J. K. Ranney, K. N. Williams and S. W. Boettcher, *Journal of the American Chemical Society*, 2012, **134**, 17253-17261.

**II. FeNi₂Se₄ – REDUCED GRAPHENE OXIDE NANOCOMPOSITE:
ENHANCING BIFUNCTIONAL ELECTROCATALYTIC ACTIVITY FOR
OXYGEN EVOLUTION AND REDUCTION THROUGH SYNERGISTIC
EFFECTS**

*Siddesh Umapathi, Dr. Jahangir Masud, Abdurazag T. Swesi and Prof. Dr. Manashi Nath**

Department of Chemistry, Missouri University of Science & Technology,
Rolla, MO 65409, USA.

*Email: nathm@mst.edu

ABSTRACT

Water splitting reaction using earth abundant and environmentally benign catalysts is critical for renewable energy technologies. Herein we report a hybrid composite, FeNi₂Se₄ nanoparticles supported on nitrogen doped reduced graphene oxide (FeNi₂Se₄-NrGO) as an efficient and dependable bifunctional electrocatalyst for oxygen evolution and oxygen reduction reactions (OER and ORR, respectively) under alkaline conditions. While FeNi₂Se₄ nanoparticles themselves showed good catalytic activity for water oxidation, the constructed hybrid nanocomposite with NrGO as the supporting matrix, showed enhanced catalytic activity with a small overpotential of 170 mV @ 10 mAcm⁻², small Tafel slope of 62.1 mV/decade, and high current density. The ORR catalytic activity of the nanocomposite was exceptionally good with an onset potential of 0.93 V, comparable to that of Pt. This is possibly due to the synergistic chemical coupling effects

between the FeNi_2Se_4 and NrGO matrix. Chronoamperometric studies showed that the catalyst is stable under conditions of continuous O_2 evolution and reduction with very less degradation. Apart from reporting highly efficient OER-ORR bifunctional catalyst, this study also provides more proof for the effect of anion coordination on the catalyst performance, as well as the synergistic role of nanoscale interactions between the catalyst particles and graphene matrix to enhance catalytic activity.

Keywords: Water splitting, Oxygen evolution reaction, Nitrogen doped reduced graphene oxide, synergistic chemical coupling, overpotential

1. INTRODUCTION

As the global energy consumption is expected to increase by mid-century, intense research is being carried out to discover environmentally benign, earth abundant and low cost materials for energy related applications.^{1,2} Production of oxygen and hydrogen through water splitting reaction is one such process which generates clean fuel as well as renewable energy and has been the central theme of several technologies including metal-air batteries, fuel cells, and solar-to-fuel energy generation.^{3,4} Electrolytic water splitting is composed of two half-cell reactions, oxygen evolution reaction (OER) and hydrogen evolution reaction (HER). Among these, OER being a four electron process has sluggish kinetics, and is considered to be the bottleneck for the entire process. For effective OER process, it is thus essential to reduce the overpotentials and increase the conversion rates.⁵⁻

¹² Till recent times, precious metal oxides such as RuO_2 and IrO_2 were known to be the

best OER electrocatalysts. However, since these precious metals are scarce, researchers continued to look for low cost alternatives for OER and HER electrocatalysts.^{13, 14}

Among the non-precious metal based catalysts, transition metal oxides including perovskites and layered double hydroxides,^{15,16} and more recently sulfides and selenides have shown tremendous promise for OER electrocatalysts over the last few years.¹⁷⁻²³ Among these the transition metal selenides deserves a special attention since they have outperformed most of the previously known OER electrocatalysts in alkaline medium including the transition metal and precious metal oxides.¹⁸⁻²³ Additionally, Ni₃S₂ nanorods synthesized by hydrothermal method on Ni form exhibited excellent OER activity in alkaline solutions with a low overpotential of -157 mV.¹⁷ In a separate study NiSe nanofiber assemblies showed good catalytic activities for the HER process.²¹ Recently our group reported Ni₃Se₂ electrodeposited on Au-coated glass substrate, which showed a low overpotential of 290 mV to achieve 10 mA cm⁻².²² Another nickel selenide, NiSe₂, showed even lower overpotential at 10 mA cm⁻² achieved in films grown with a preferred orientation.²³ Ni-based OER electrocatalysts have shown the best performance till date,^{24,25,26} and it has been attributed to the presence of a single electron in the *e_g* orbital of the octahedral metal center.²⁷ Typically, Ni(II) undergoes a pre-oxidation to Ni(III) in alkaline medium, and it is the Ni(III) center which initiates the OER reaction. Most of the Ni-based electrocatalysts reported till date contain Ni(II) and other lower oxidation states of Ni in the pristine state, and the Ni(II) → Ni(III) conversion precedes the catalytic activity. Oxidation of Ni(II) to Ni(III) in alkaline medium is followed by oxidative-attachment of OH⁻ to the metal site which is believed to be the initiation of the OER catalytic process and the Ni(II) → Ni(III) conversion is visible as a pre-oxidation peak in

the linear sweep voltammograms (LSVs) of the OER reaction before the onset of increasing current density signifying the OER process. However, the oxidation potential of a metal center depends on the ligand environment around the central metal atom it and varies from solid to solid.^{28,29} The effect of ligand substitution on the redox potential of the metal center has been observed more prominently in organometallic and coordination complexes. In fact, recently we have also observed that changing the ligand environment from oxide to selenide shifted the Ni(II) to Ni(III) oxidation peak to more cathodic potentials.³⁰ Such a shift can be explained by the decreasing electronegativity from oxide (3.5) to selenide (2.4) which leads to increased covalency of the metal-chalcogen bond.³¹ However, since Ni(III) has been proven to be the actual catalytically active site, it would be more optimal to start with a Ni(III)-based catalyst such that OER can proceed directly without the pre-oxidation step. Ni(III) species is less common and has been found in some organometallic complexes and some other mixed metal ferrites.³² In this article, we have intentionally synthesized nanoparticles of a Ni(III)-based mixed metal selenide, FeNi_2Se_4 with a vacancy-ordered spinel structure-type, and have investigated its catalytic activity towards OER in alkaline medium. The importance of mixed metal selenides, especially with Ni-Fe combination has been an attractive venture in the OER community attributed to the high OER electrocatalytic performance observed in the Fe-doped Ni-oxide and hydroxide class of compounds. As per our hypothesis, the selenides should show better catalytic performance than the oxides, and hence we have attempted to prepare a ternary iron-nickel selenide. Additionally, lesser anion electronegativity and higher degree of covalency makes the Ni(III) more stable in the selenide coordination compared to the oxide, thereby facilitating the catalytic activities. In this article we have reported efficient OER catalytic activity of

FeNi₂Se₄ nanoparticles for the first time, and have optimized the catalytic efficiency by forming a hybrid nanocomposite, FeNi₂Se₄ – NrGO [NrGO = N-doped reduced graphene oxide], which shows even better catalytic performance.

There are two approaches of enhancing the catalytic efficiencies of these electrocatalysts. While the first one deals with reducing the overpotential, the second one deals with increasing the current density. The latter one can be achieved by nanostructuring and increasing conductivity of the catalyst composite which also leads to synergistic effect, thereby enhancing its performance. In recent times, graphene sheets, has been identified for its outstanding electrical conductivity, high surface area,³³⁻³⁶ and as supporting matrix for foreign materials which leads to improvement in the electrocatalytic applications.^{37,38} Recently it has been observed by several researchers that mixing reduced graphene oxide (rGO) with the catalyst powder increases the catalyst's efficiency by facilitating charge transfer within the catalyst composite as well as through synergistic effect. For example, Su-Hong Yu et al reported Mn₃O₄/ CoSe₂ hybrid and CoSe₂ nanobelts anchored on nitrogen-doped reduced graphene oxides as electrocatalysts which showed optimized performance in oxygen electrocatalysis.^{39,40} The groups of Bell⁴¹ and Dai⁴² reported the greatly enhanced OER activity of Co₃O₄ nanocrystals by anchoring them on Au and graphene support, respectively. Such an enhancement in activity for the above mentioned hybrid catalyst was believed to be due to the synergistic chemical coupling effects between the metals and the support matrix. Furthermore, there has been reports where metal free graphene oxide doped with N,O and P functioned as OER electrocatalysts and showed an overpotential of 430 mV to achieve 10 mA cm⁻².⁴³ Hence, in our research, we have applied both of the above-mentioned approaches (i.e. lowering the overpotential through transition

metal doping, and increasing current density through facilitating charge transfer within the matrix) to design a high efficiency OER electrocatalyst from a ternary Ni-based selenide. Accordingly, in this article we have reported the synthesis of FeNi₂Se₄-NrGO nanocomposite and have shown their exceptionally good catalytic performance for OER in alkaline medium. This catalyst shows excellent activity for OER in alkaline medium reaching a current density of 10 mA cm⁻² at an overpotential of 170 mV, which is one of the lowest overpotentials that has been reported till date. Interestingly, this catalyst composite also shows high activity of ORR in alkaline medium with an onset potential close to that of Pt.⁴² It must be noted that this is one of the first examples of a Ni-Fe-based OER electrocatalyst which contains Ni(III) in the starting composition. Notably, the Ni pre-oxidation peak is absent in all the LSV plots for OER supporting the claim that this catalyst indeed contains Ni(III), which has also been confirmed through detailed XPS analysis. We have also shown the positive effect of NrGO on the catalyst's performance, whereby it reduces the overpotential significantly possibly due to synergistic effects between the catalyst and NrGO. Apart from reporting highly efficient OER-ORR bifunctional catalyst, this study also provides more proof for the effect of anion coordination on the catalyst performance, as well as the synergistic role of nanoscale interactions between the catalyst particles and graphene matrix to enhance catalytic activity. The findings reported here presents a new direction for the selenide based hybrid catalysts, which may be extended to investigate other ternary selenide based hybrid nanocomposites for a broad range of energy-related applications.

2. RESULT AND DISCUSSION

2.1. COMPOSITION AND MORPHOLOGY CHARACTERIZATION

The FeNi₂Se₄ catalysts were synthesized by hydrothermal technique (Experimental details provided in supporting information). Pure FeNi₂Se₄ nanoparticles (hereafter referred to as nanoparticles) and FeNi₂Se₄-NrGO nanocomposite containing FeNi₂Se₄ nanoparticles intermixed with *in situ* generated NrGO (characterization details have been provided in Methods and Supporting information) were recovered as blackish powder from the autoclave. The NrGO was synthesized and characterized following standard procedure as described in the Supporting information (Figure S1). Figure 1 shows the powder X-ray diffraction (pxrd) pattern of *as-synthesized* blackish products. As can be seen from the Figure, the pxrd pattern matched very well with FeNi₂Se₄ standard pattern (PDF # 04-006-5240) indicating high degree of crystallinity and purity of the product. Interestingly, the crystallinity of the product was preserved in the FeNi₂Se₄-NrGO nanocomposite, which showed nearly identical pxrd pattern.

Several ternary iron nickel selenides has been reported till date and a notable feature of this class of compounds lies in their structure and magneto-optic properties.⁴⁴ Mixed metal selenides, FeNi₂Se₄ (or NiFe₂Se₄) belong to a specific structure type, AB₂X₄, containing a hexagonal close packing of the chalcogenide anion (X), while the metal atoms (A and B) occupy octahedral holes above and below the chalcogen layers. The structure is derived from the stoichiometric end-member NiSe (NiAs structure type)⁴⁵ by replacing every alternate metal layer with half-filled metal layer such that 50% of the metal sites in every alternate layer are vacant and the formulation leads to Ni₃Se₄. If every alternate metal

layer is removed completely, it results in the NiSe₂ structure. Among the metals *A* and *B*, *A* is a divalent cation occupying the partially occupied metal layer, while *B* is a trivalent cation occupying the fully occupied metal layers. A series of ternary metal selenides with the generic formula *AB*₂Se₄ has been reported in the literature where *A* and *B* can be Ti, Cr, Mn, Fe, Co, Ni, and so on.⁴⁶ Hence, in this structure type it might be possible to achieve +3 oxidation state of Ni in a formulation such as *MNi*₂Se₄. Interestingly, it has been observed that in the Cr₃Se₄ structure type, Fe has a preference for occupying the *A* sub-

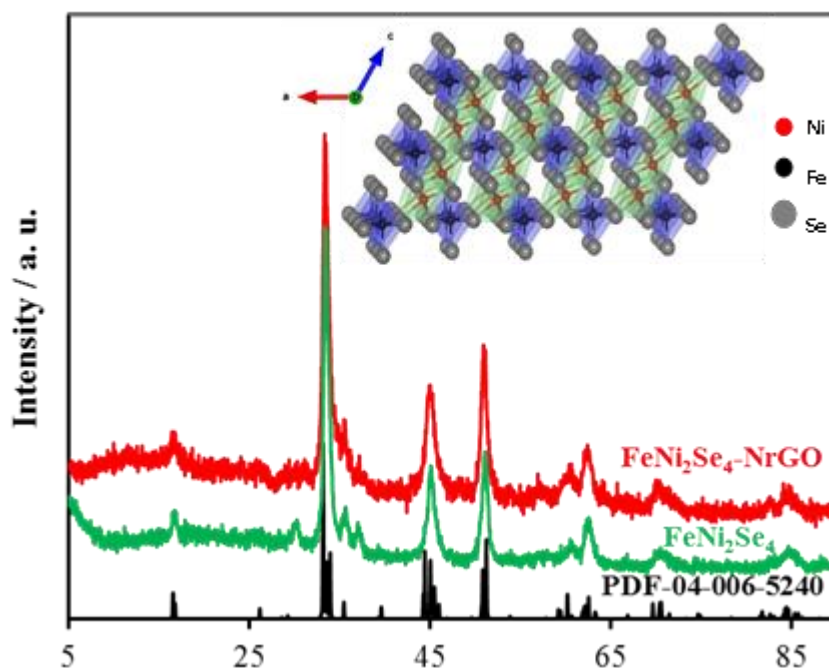


Figure 1. PXRD pattern of FeNi₂Se₄-NrGO nanocomposite and FeNi₂Se₄ nanoparticles along with reference FeNi₂Se₄ (PDF # 04-006-5240). Inset shows the crystal structure of FeNi₂Se₄ created from structure files corresponding to PDF # 04-006-5240. Color coded: black – Fe, red – Ni, grey – Se.

lattice thereby, suggesting that FeNi_2Se_4 should contain Ni^{3+} . In the current context it is also important to understand the difference between NiFe_2Se_4 and FeNi_2Se_4 . Although NiFe_2Se_4 and FeNi_2Se_4 are both generically referred to as AB_2Se_4 , and both of them.

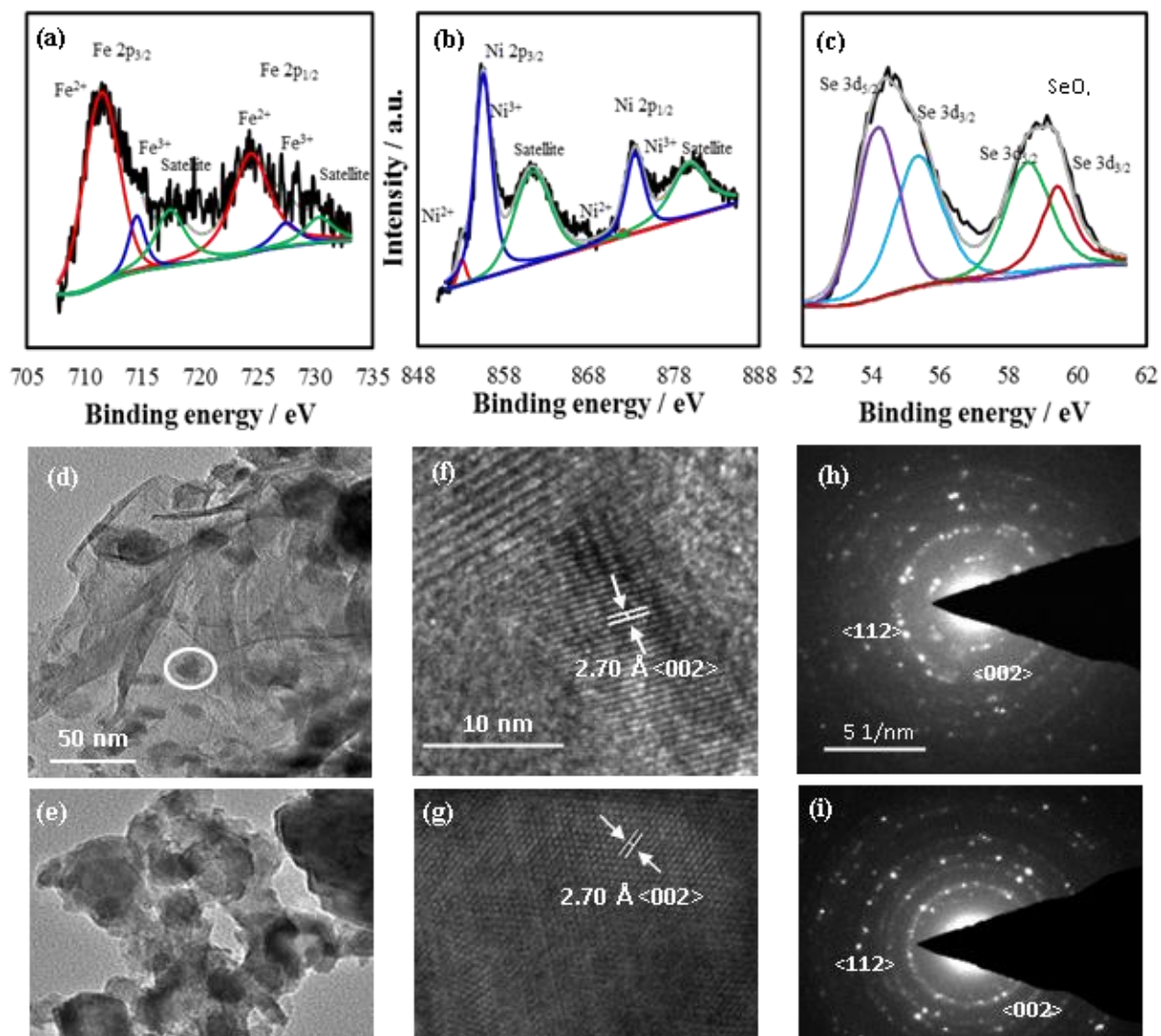


Figure 2. Deconvoluted XPS spectra of the as prepared FeNi_2Se_4 -NrGO nanocomposite showing the (a) Fe 2p, (b) Ni 2p and (c) Se 3d signals. (d, e) TEM images of FeNi_2Se_4 -NrGO and FeNi_2Se_4 , respectively. White circular mark is a visual guide to notice the nanoparticle in the NrGO matrix. (f, g) HRTEM images of FeNi_2Se_4 -NrGO nanocomposite and FeNi_2Se_4 nanoparticles. (h, i) SAED patterns collected from FeNi_2Se_4 -NrGO nanocomposite and FeNi_2Se_4 nanoparticle ensemble.

crystallize in the spinel structure-type, there are subtle differences between these two compositions. Specifically, the occupancy of the *A* and *B* sites, interchange between these two compositions. In FeNi_2Se_4 , Ni is in +3 oxidation state while Fe occupies the divalent cation site.

A good indication of the oxidation states can be obtained from X-ray photoelectron spectroscopy (XPS). Accordingly, the surface composition of as-prepared FeNi_2Se_4 -NrGO was investigated through XPS. The electronic states of Ni, Fe and Se in as prepared FeNi_2Se_4 nanoparticles were estimated from the deconvoluted XPS spectra as presented in Figure 2 (a, b, c). The deconvoluted Fe 2p and Ni 2p peaks reveal the presence of variable oxidation states of $\text{Fe}^{2+}/\text{Fe}^{3+}$ and $\text{Ni}^{2+}/\text{Ni}^{3+}$, respectively. The Fe 2p XPS spectrum in Figure 2a shows peaks at 711.4 and 724.4 eV corresponding to $\text{Fe}^{2+} 2p_{3/2}$ & $\text{Fe}^{2+} 2p_{1/2}$; while peaks at 714.5 and 727.4 eV correspond to $\text{Fe}^{3+} 2p_{3/2}$ & $\text{Fe}^{3+} 2p_{1/2}$, respectively. The obvious satellite peaks of Fe 2p can be found at 717.4 and 730.4 eV.⁴⁷ Similarly, the deconvoluted Ni 2p spectra is shown in Figure 2b, where the binding energies at 853.1 and 872.0 eV belong to $\text{Ni}^{2+} 2p_{3/2}$ & $\text{Ni}^{2+} 2p_{1/2}$ and peaks at 855.6 and 873.4 eV are for $\text{Ni}^{3+} 2p_{3/2}$ & $\text{Ni}^{3+} 2p_{1/2}$, respectively. The shakeup satellite peak of Ni 2p was observed at 861.3 and 879.7 eV.⁴⁸ Figure 2c, shows the Se 3d spectra where the peaks of $3d_{5/2}$ and $3d_{3/2}$ at the binding energies of 54.1 and 55.3 eV confirm the presence of Se^{2-} and the peak at ~ 59 eV indicates the existence of SeO_x species which might due to the surface oxidation of selenide. It should be noted that there was no evidence of metal oxides on the surface from XPS analysis. Since the catalyst is composed of variable oxidation states of metals we have calculated approximate percentage of $\text{Fe}^{2+/3+}$ and $\text{Ni}^{2+/3+}$, based on the area under the peaks in the deconvoluted XPS spectra. The *as-synthesized* catalyst contained 23% Fe^{2+} , 6% Fe^{3+}

and 3% Ni²⁺, 68% Ni³⁺. From the XPS fitting analysis, composition of the catalyst can be written as Fe_{1-x}Ni_x(Ni_{2-y}Fe_y)Se₄, where x = 0.1 and y = 0.15 leading to the ratio between the metals to be Fe:Ni = 1.05:1.95 which is in close agreement with the value obtained from EDS (Table S1). It should be noted that the trivalent cationic site in the fully occupied layer (*B*-site) was predominantly occupied by Ni³⁺ with some Fe³⁺ substitution, while the divalent cationic site (*A*- site) was majorly Fe²⁺. A similar XPS spectra was observed for FeNi₂Se₄ nanoparticles. High resolution N 1s XPS spectrum collected from the the FeNi₂Se₄-NrGO composite revealed pyridinic and pyrrolic N peaks at 398.7 and 400.2 eV, respectively as shown in Figure S2a. The high-resolution XPS spectrum of C 1s (Figure S2b) showed a broad peak at 280-288 eV⁴⁹ which can be attributed to different organic functional groups such as hydroxyl (-C-OH) and carboxyl (-COOH), C-C, C=O and nitrogen containing groups like C-N, and C=N on the rGO sheets. These functional groups might interact with FeNi₂Se₄ and enable the direct growth of FeNi₂Se₄ on NrGO sheets. It should be noted that the XPS spectra from FeNi₂Se₄ and FeNi₂Se₄-NrGO did not show evidence of any oxidic phase corresponding to either of the metal oxides indicating high purity of the sample.

Detailed transmission electron microscopy (TEM) confirmed the formation of FeNi₂Se₄- NrGO nanocomposite (Figure 2d) as well as formation of the FeNi₂Se₄ nanoparticles (Figure 2e). The average particle size for the bare nanoparticles was estimated to be 10 – 15 nm. HRTEM seen in Figure 2f and 2g confirmed the crystalline nature of the hybrid nanocomposite and the lattice fringes can be assigned to <002> spacing of FeNi₂Se₄. Selected area electron diffraction (SAED) patterns shown in the Figures 2h and 2i, further confirms the crystallinity of the as prepared nanocomposite and

nanoparticles, and the diffraction spots could be indexed to $\langle 002 \rangle$ and $\langle 112 \rangle$ lattice planes of FeNi_2Se_4 crystal structure. The FeNi_2Se_4 nanoparticles were agglomerated because of high surface energy which leads to irregular morphology. SEM images (Figure S3) show the randomly distributed catalyst particles with high surface roughness for FeNi_2Se_4 -NrGO and FeNi_2Se_4 . The presence of NrGO was observed as a hazy layer around the particles as seen in Figure S3a. Elemental composition analysis was done from energy dispersive X-ray spectroscopy (EDS) confirmed the presence of C, N (from reduced graphene oxide) along with Fe, Ni and Se with a relative ratio 1: 2: 4 (Fe:Ni:Se) for the nanocomposite as shown in Figure S4a. The Fe:Ni:Se relative ratio remained same for bare nanoparticles as seen in Figure S4b.

2.2. ELECTROCHEMICAL CHARACTERIZATION AND CATALYTIC ACTIVITIES

To assess the OER catalytic activity, our catalysts were drop casted onto commercially available carbon fiber paper (CFP) substrates with a typical loading of 0.55 mg cm^{-2} . Details of the electrode preparation has been provided in the supporting information. Electrochemically active surface area (ECSA) was measured in N_2 saturated 1 M KOH, making use of the double layer charging concept,⁵⁰ by varying scan rates from 20 to 160 mVs^{-1} as shown in Figure S5a and (b). By using equation S1, the ECSA was calculated to be 8.3 cm^2 for the nanocomposite while the bare nanoparticles showed an ECSA of 5.3 cm^2 . Correspondingly, a roughness factor (RF) of the composite and nanoparticle film was estimated to be 17.53 and 11.27, respectively, which indicates that the NrGO composite has a more textured morphology. Typically larger RF induces better catalytic activity due to larger exposure of the active sites on the catalyst surface.

Linear sweep voltammetry (LSV) measurements were conducted in N_2 saturated 1 M KOH solution (pH 13.6), at a scan rate of 10 mV s^{-1} . Calibrated Ag|AgCl and Pt mesh were used as reference electrode and counter electrode, respectively. The measured potentials using Ag|AgCl are converted to reversible hydrogen electrode (RHE) using the Nernst equation (according to equation S2). For comparison, a RuO_2 film was also electrodeposited following standard procedures (see Supporting Information) and the LSV was measured under identical conditions as mentioned above. The nanocomposite $FeNi_2Se_4$ -NRGO catalyst showed a low onset potential of 1.38 V vs RHE for OER and a

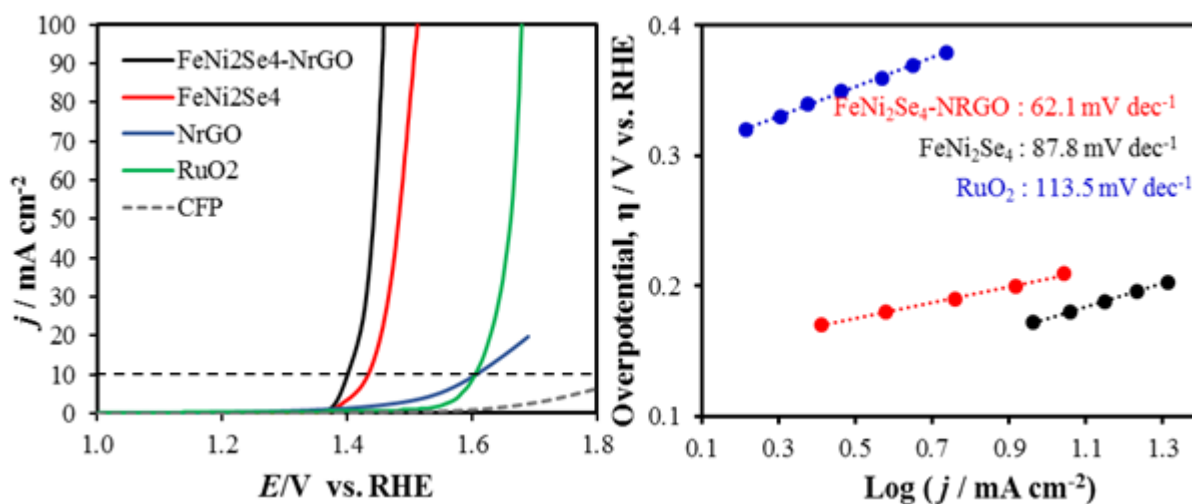


Figure 3. (a) LSVs measured for different catalysts coated on CFP substrate in N_2 saturated 1.0 M KOH solution at a scan rate of 10 mV s^{-1} . (b) Tafel plots of $FeNi_2Se_4$ -NrGO.

small overpotential of 170 mV to achieve the current density of 10 mA cm^{-2} as shown in Figure 3a. The onset and overpotential for $FeNi_2Se_4$ -NrGO nanocomposite was also confirmed from the cyclic voltammogram (CV) plot (as shown in Figure S6) which

provides a more accurate way of determining these potentials from the reverse cycle of the CV, which is unaffected by the oxidation peak corresponding to Ni^{2+} oxidation (if any). The CV plot also shows that the $\text{FeNi}_2\text{Se}_4\text{-NrGO}$ nanocomposite had a very a high current density at low applied potential surpassing most of the conventional electrocatalysts. FeNi_2Se_4 nanoparticles without NrGO also was catalytically active showing an onset of 1.38V and required 210 mV to achieve the current density of 10 mA cm^{-2} . Similar onset potential for catalytic activity but more sluggish rise of current density in absence of NrGO in the catalytic film is another indication of the synergistic effect in the catalyst-NrGO composite. On the other hand, NrGO by itself showed very less OER activity, while RuO_2 required 360mV to achieve 10 mA cm^{-2} current density. It was observed that the overpotential at 10 mA cm^{-2} for this selenide based hybrid catalyst is lower than most of the previously reported OER catalysts based on nickel-oxides, nickel iron hydroxides, layered double hydroxides and nickel selenides on nickel foam (Table 1).⁵¹⁻⁵³ In fact, as per our knowledge, this overpotential is the second lowest^[23] amongst all the reported overpotential for OER electrocatalysts active in alkaline medium. It should be noted that our catalyst is supported on CFP, which in contrast to Ni foam has very less or no catalytic activity by itself and does not have extensive porous network as the foam. This implies that the high catalytic activity observed from the FeNi_2Se_4 nanoparticles and $\text{FeNi}_2\text{Se}_4\text{-NrGO}$ composite is from the catalyst alone. The OER kinetics of the above catalysts was probed further by analyzing their Tafel plots as given by the equation S4, and shown in Figure 3b. The resulting Tafel slopes were found to be 62.1 mV dec^{-1} , 87.8 mV dec^{-1} and $113.5 \text{ mV dec}^{-1}$ for $\text{FeNi}_2\text{Se}_4\text{-NrGO}$ composite, FeNi_2Se_4 and RuO_2 , respectively. It should be noted here that the $\text{FeNi}_2\text{Se}_4\text{-NrGO}$ composite exhibits the smaller Tafel slope among the

catalysts reported in this study, confirming faster charge transfer and synergistic effect between FeNi₂Se₄ nanoparticles and NrGO. The turnover frequency (TOF) was calculated at an overpotential of 250 mV, assuming that all the metal sites of the catalyst are catalytically active. The TOF value was found to be 0.050 s⁻¹ for FeNi₂Se₄-NrGO, which is higher than IrO_x (0.0089 s⁻¹)⁵⁴ indicating better OER activity of the hybrid catalyst.

2.3. EFFECT OF NANOSCOPIC INTERACTION BETWEEN GRAPHENE AND FeNi₂Se₄ NANOPARTICLES ON OER CATALYTIC ACTIVITY

The improved OER activity with low overpotential and higher current density of FeNi₂Se₄-NrGO composite possibly originated from the synergistic effect between highly conducting NrGO matrix and electrocatalytic FeNi₂Se₄. Such synergistic effects has been observed previously by other groups, where activity of CoSe₂ and Co₃O₄ was enhanced by doping with NrGO.^{40, 42} The synergistic effect of NrGO on the catalytic activity was further confirmed by the observed dependence of catalytic activity on the relative ratio of FeNi₂Se₄ and NrGO. It was observed that lowering the FeNi₂Se₄ loading to 1:1 ratio with NrGO led to systematic reduction in OER activity (Figure S7). This suggests that the active reaction sites in our hybrid materials are the transition metal ions, Ni³⁺ species at the interface with NrGO. It is believed that N groups on the reduced GO can also serve as favorable nucleation and anchor sites for the mixed metal nanoparticles, which leads to a strong coupling between Fe/Ni and rGO.

2.4. EFFECT OF STRUCTURE AND COVALENCY ON OER CATALYTIC ACTIVITY

While the FeNi_2Se_4 and $\text{FeNi}_2\text{Se}_4\text{-NrGO}$ showed high catalytic activity, interestingly it was observed that there was no pre-oxidation peak visible in the LSV, that has been typically observed with Ni-based OER electrocatalysts.⁵⁵ Such pre-oxidation peaks have been attributed to the conversion of $\text{Ni}^{2+} \rightarrow \text{Ni}^{3+}$, whereby Ni^{3+} is the actual catalytically active species. The absence of such pre-oxidation peaks further confirms the proposition that Ni is majorly present as Ni^{3+} in this reported catalytic composite. We have analyzed this further by studying the oxidation-reduction process for several cycles through cyclic voltammetry (CV). As shown in Figure S8, initial anodic cycle was marked by stark absence of the pre-oxidation peak before the onset of OER. On the contrary, during the reverse cathodic sweep, reduction peak corresponding to $\text{Ni}^{3+} \rightarrow \text{Ni}^{2+}$ was observed. During subsequent anodic potential sweep, the electrochemically generated Ni^{2+} was seen to be oxidized to Ni^{3+} exhibiting the characteristic $\text{Ni}^{2+} \rightarrow \text{Ni}^{3+}$ oxidation peak, which gradually intensified with subsequent cycling. This further confirms that the as-prepared catalyst indeed contained Ni^{3+} . However this Ni^{3+} could be electrochemically reduced to Ni^{2+} during the electrochemical catalytic process, and the generated Ni^{2+} could subsequently be oxidized to Ni^{3+} in the anodic sweep. This is one of the first examples of OER catalyst which has Ni^{3+} in the as-prepared catalyst composition, which might be one of the reasons for the very low onset potential and overpotential at 10 mA cm^{-2} for OER.

Fe plays a critical role in enhancing the activity of Ni based oxygen evolution electrocatalysts, and the synergistic effect between Fe and Ni in mixed metal based OER electrocatalyst has been previously studied by several researchers. Boettcher *et al*, has extensively studied the effect of Fe incorporation in $\text{Ni}(\text{OH})_2$ and $\text{Ni}(\text{OOH})_2$ on the OER

activity.⁵⁶ The functional role of the Fe dopant was also investigated, and Stahl *et al.* suggested formation of Fe⁴⁺ in NiFe-hydroxides by performing Mossbauer spectroscopic studies *in operando*.^[57] On the contrary no such Fe⁴⁺ species was detected in only Fe oxide based catalysts. According to these researchers, the presence of Fe⁴⁺ is induced by the neighboring Ni ions, which in turn will influence the electron density around the Ni-center thereby affecting the activity of NiFe hydroxide. However, the active site for catalytic activity is still Ni³⁺ and Fe⁴⁺ is not kinetically competent as the active site. On the other hand, Corrigan *et al*⁵⁸ proposed that partial-charge transfer between the metal sites (Fe and Ni^{3+/4+}), can also enhance the catalytic activity. We believe that in the present case, the presence of Fe²⁺ in the neighboring vacancy-ordered layer enhances charge transfer from Ni³⁺ thereby facilitating the catalytic activity by redistributing and reducing the electron density near Ni-site. The absence of pre-oxidation peaks as observed in the LSV curves of FeNi₂Se₄ and FeNi₂Se₄-NrGO indicates that Ni³⁺ available in the pristine state is still the active site for catalyzing OER.

As has been explained earlier changing the anion composition from highly electronegative oxide to less electronegative selenide, increases covalency in the lattice. Effect of covalency on the OER catalytic activity has been explained for transition metal oxides very clearly by Shao-Horn *et al.* on the basis of the molecular orbital model.⁵⁹ According to that model, the interaction between oxygen and metal *d* states is responsible for the OER activity, whereby, the *e_g* orbital of surface transition metal ions participates in σ -bonding interaction with the anion adsorbate. The *d*-electron filling in *e_g* orbitals can thus influence bond strength of oxygen-related intermediate species on catalytic surface thereby optimizing catalyst performance. The model also predicts that increasing covalency in the

metal-oxygen bond results in the higher OER activity. Hence to highlight the direct effect of increased covalency on the OER catalytic performance of these ternary chalcogenides, we have compared the catalytic activity between the pure oxide (FeNi_2O_4) and the selenide (FeNi_2Se_4) phases. Such comparison also clarifies the doubts regarding presence and/or influence of surface oxidic phases on the catalytic activity. Accordingly, we have synthesized FeNi_2O_4 -NrGO by hydrothermal methods (experimental details in supporting information) and the phase identification was confirmed by pXRD (Figure 4a). Electrochemical studies of this catalyst was performed in 1 M KOH by preparing the electrode with similar loading as the selenide phase. The onset potential for OER catalytic activity with FeNi_2O_4 -NrGO was 1.41 V while overpotential at 10 mA cm^{-2} was obtained at 260 mV as seen in Figure 4b. While this overpotential by itself was better than the previously reported Ni-Fe double hydroxides, highlighting the importance of crystal structure and packing on catalytic activities, it was still significantly higher than the corresponding selenide. The overpotential measured for FeNi_2Se_4 -NrGO under similar conditions was only 170 mV. This ~ 90 mV difference between the overpotentials of the selenide and oxide based hybrid OER catalysts indicate that the selenide coordination indeed enhances catalytic activity of the Ni^{3+} center due to increased covalency of Ni-Se bonds compared to Ni-O bonds, which effectively changes the chemical environment around Ni^{3+} and lowers the oxidation potential. Hence the higher catalytic activity in FeNi_2Se_4 and FeNi_2Se_4 -NrGO hybrid nanocomposite can be attributed to increased covalency of the lattice, exchange interaction with Fe and synergistic effect of NrGO.

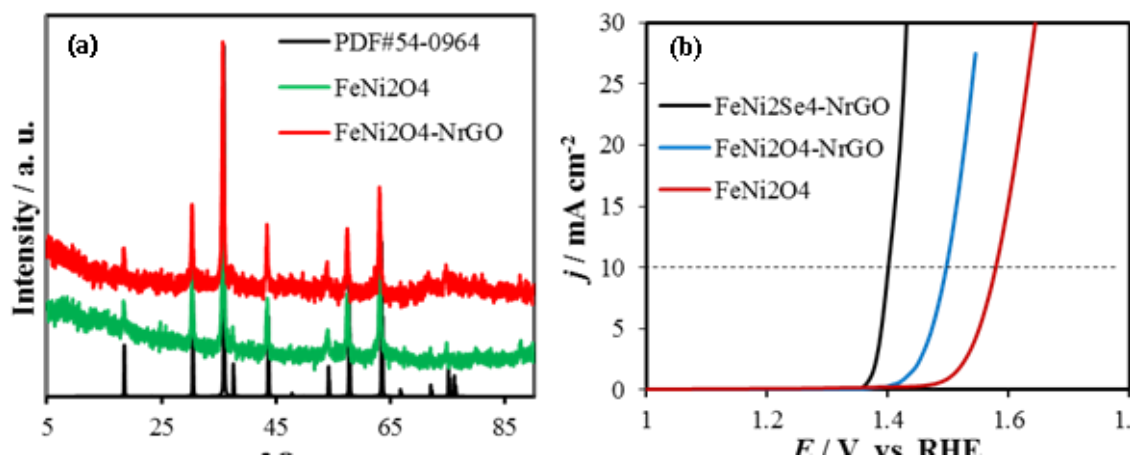


Figure 4. (a) Pxd of as-synthesized FeNi_2O_4 and $\text{FeNi}_2\text{O}_4\text{-NrGO}$ compared with standard FeNi_2O_4 (PDF# 54-0964). (b) Comparison of LSV of $\text{FeNi}_2\text{Se}_4\text{-NrGO}$, $\text{FeNi}_2\text{O}_4\text{-NrGO}$ and FeNi_2O_4 showing the enhanced OER catalytic activity of the ternary selenide.

2.5. ANALYZING THE EVOLVED GAS AND ESTIMATION OF FARADAIC EFFICIENCY

In order to confirm the composition of the evolved gas and to calculate the Faradaic efficiency, we have designed a OER-ORR combined experiment in a bipotentiostat mode with rotating ring disk electrode, wherein, OER takes place at GC disk electrode coated with $\text{FeNi}_2\text{Se}_4\text{-NrGO}$ composite, while simultaneous oxygen reduction reaction (ORR) was performed at the Pt ring electrode maintained at a constant voltage of 0.2 V vs RHE. Before the experiment, electrolyte solution (1 M KOH) was degassed with N_2 for 30 mins and the whole experiment was performed under a blanket of N_2 gas. The concept was that the Pt ring electrode will show a ring current corresponding to ORR if and only if the gas evolved in the disk electrode is oxygen. The electrode was rotated at 1600 rpm and OER activity at the anode (maintained at 1.38 V) was characterized by increasing disk current density. As shown in the Figure S9a, the cathodic current at the Pt ring electrode showed a

simultaneous increase as soon as the disk voltage passed the onset potential indicating that the gas evolved indeed was O₂.

The Faradaic efficiency was determined according to equation S6 using similar bipotentiostat experiment involving GC disk electrode and Pt ring electrode. Details of the experimental procedure has been reported previously.^[24] The disk electrode was maintained for 1 min at a constant potential from 1.41 V to 1.45 V *vs* RHE, while being rotated at 1600 rpm under continuous N₂ bubbling. At 1.41 V the highest Faradaic efficiency was obtained which was 99.8% and the lowest Faradaic efficiency was at 1.45 V (*vs* RHE) to be 51.9%. This decrease in the Faradaic efficiency can be attributed to the limitation of the Pt ring's collection efficiency, which cannot reduce the large amounts of O₂ produced by the disk electrode.

2.6. INVESTIGATING STABILITY OF THE CATALYSTS AND POST-CATALYTIC CHARACTERIZATION

The stability of the hybrid nanocomposite for continuous oxygen evolution was carried out through chronoamperometric measurements (*j vs. t*) for 12 hours as shown in Figure 5a, at an applied potential of 1.40 V *vs* RHE, where the catalyst achieved current density of 10 mA cm⁻² in 1 M KOH solution. The catalyst composite was prepared with 2% Nafion, which showed excellent durability without any decrease in the current density.

As can be seen from Figure 5a, there was no degradation of current density even after 12 h. The stability of the catalyst was further confirmed through LSV (inset Figure 5a) studies which showed that the catalyst has similar onset potential and overpotential at 10 mA cm⁻² even after 12 hours of chronoamperometry.

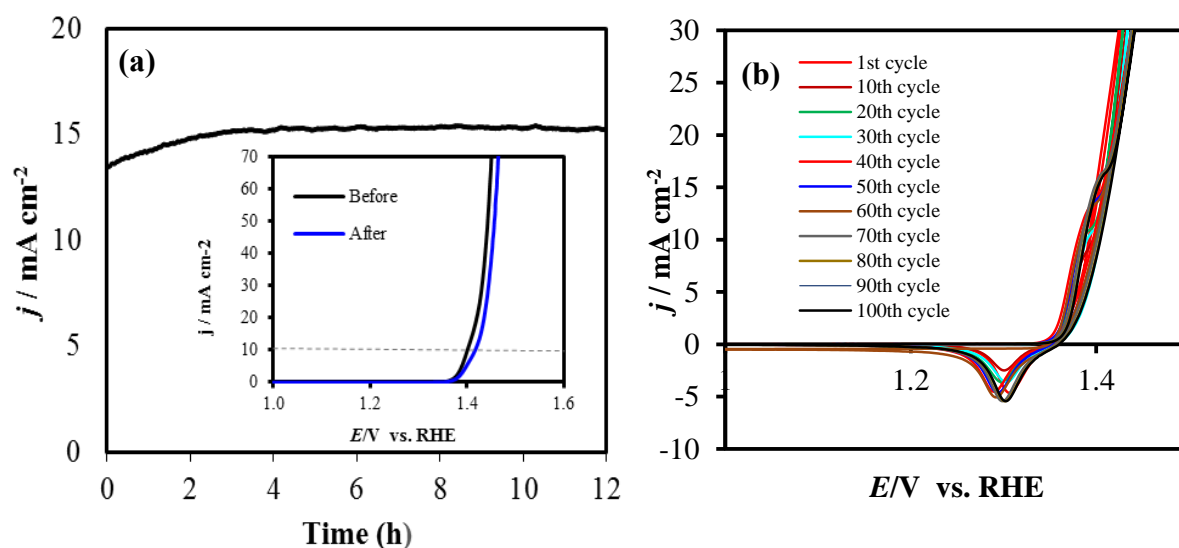


Figure 5. (a) Chronoamperometric stability study for FeNi₂Se₄-NrGO nanocomposite under continuous O₂ evolution for 12 h. Inset shows comparison of LSVs of the catalyst before and after chronoamperometry for 12 h. (b) 100 CV cycles of FeNi₂Se₄-NrGO in N₂ saturated 1.0 M KOH.

The surface chemistry of the catalyst composite was also probed electrochemically based on the idea that a change of anion coordination around the transition metal center (Ni) will be accompanied by a shift in the oxidation-reduction peak potential of the Ni²⁺/Ni³⁺ species, as has been shown earlier. Specifically, if the surface is coated with layers of the mixed metal oxide (FeNi₂O₄, NiO_x or Ni(Fe)OOH), then it is expected that the oxidation-reduction peak of Ni²⁺/Ni³⁺ couple will shift towards more anodic potentials. Through CV cycling studies for 100 cycles (Figure 5b), it was observed that the CV plots of FeNi₂Se₄ catalyst composite were almost superimposable, with the reduction peak and gradually intensifying oxidation peak lying at 1.30 and 1.36 V respectively. In FeNi₂O₄ however, the corresponding oxidation-reduction peaks were observed at 1.28 and 1.38 V respectively (Figure S10). It should also be mentioned here that surface

corrosion/degradation happens during the initial cycles itself, therefore, a scan for over 100 cycles can be considered as a proper reflection of the surface changes. While the oxidation-reduction peak potentials did not show a shift, there was a slight decrease in the current density may be due to loss of material from the electrode due to evolution of O₂ from the surface. The electrochemical cycling test thus confirmed that the surface coordination was still majorly selenide even after 100 cycles. The surface composition was further characterized through XPS and pXRD collected after 12 h of chronoamperometric measurements. For such studies, the hybrid catalyst was drop-casted onto Au substrate which was subjected to 12 h of continuous O₂ evolution in 1 M KOH. PXRd of the catalyst composites on Au-glass after chronoamperometry showed that the structural integrity was maintained as shown in Figure 6a. XPS spectra collected after chronoamperometry showed the Ni 2p and Fe 2p peaks were unchanged as shown in Figure 6b & c), and Se 3d peaks are shown in Figure 6d. More importantly, there was no evidence of formation of metal oxides such as Ni-oxide and Fe-oxide (confirmed by the absence of characteristic XPS peaks) after extensive periods of continuous oxygen evolution.

A comparison of FeNi₂Se₄ and FeNi₂Se₄-NrGO composite with other Ni-chalcogenide based OER electrocatalysts, revealed that FeNi₂Se₄-NrGO actually showed the second lowest overpotential in the series (Tables 1 and Table S2). The higher activity can be attributed to the combination of several favorable factors: (i) increased covalency in the lattice that lowers the oxidation potential of the transition metal at the catalytically active site thereby facilitating anion adsorption and onset of catalytic activity; (ii) nanostructuring which leads to higher surface roughness and better exposure of active sites to the electrolyte;

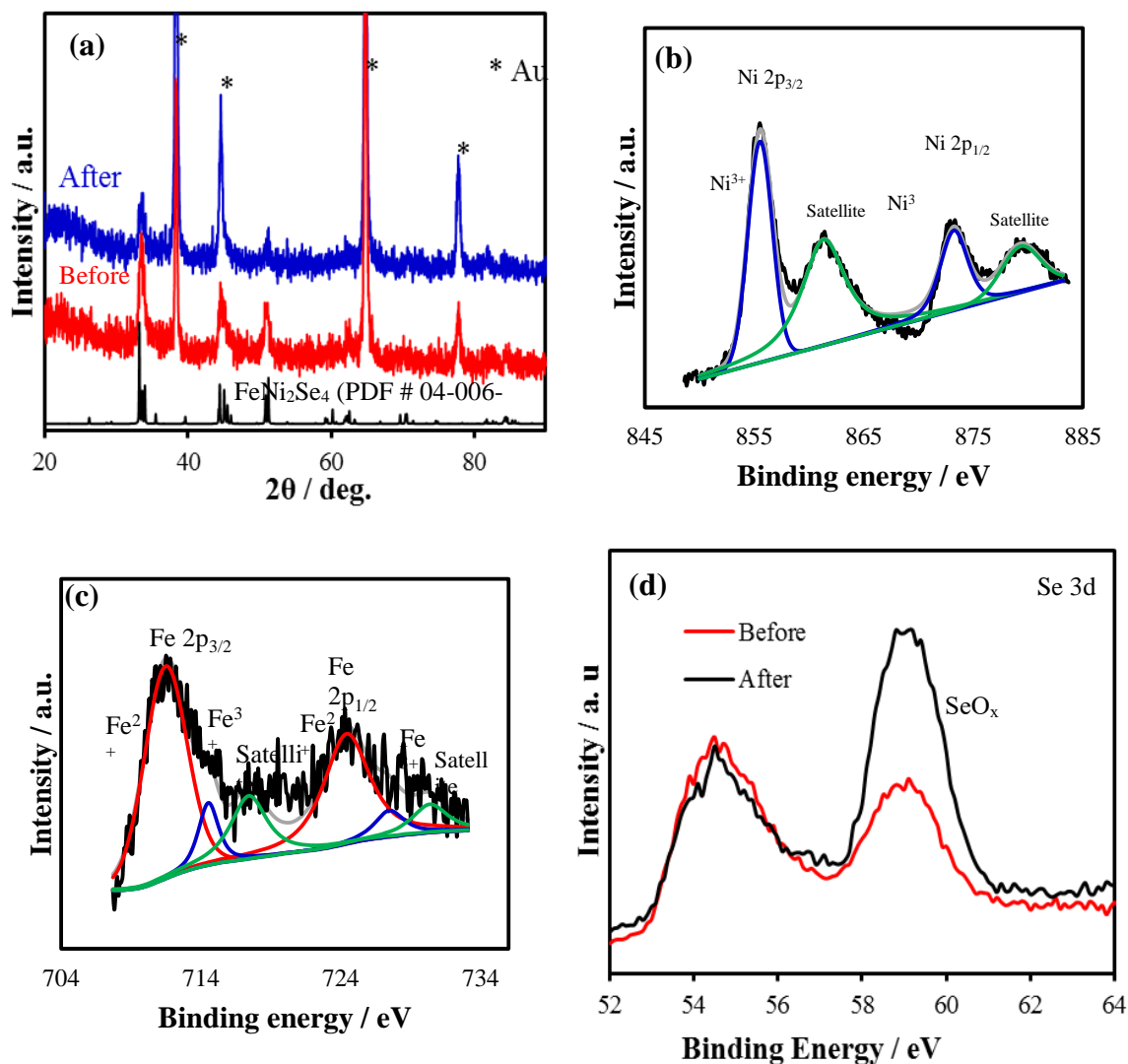


Figure 6. (a) Pxrds spectra of FeNi₂Se₄ before and after 12 h of chronoamperometry on Au-glass. (b) Ni and (c) Fe XPS signal after chronoamperometry for 12 h. (d) XPS spectra of Se before and after chronoamperometry study.

(iii) the preferable charge transfer between Fe and Ni centers reducing the local electron density around Ni which further enhances the catalytic activity; (iv) the synergistic effect between N-center of NrGO and the anchored metal (Ni/Fe) atoms in the NrGO hybrid composite which leads to favorable nanoscale interactions and facilitated charge transport

within the catalyst composite. The remarkably high catalytic activity, favorable kinetics, and strong durability suggests that FeNi₂Se₄-NrGO can be one of the most promising candidate for OER in alkaline electrolyte.

2.7. FeNi₂Se₄- NrGO AS AN ORR CATALYST

Recently carbon nanostructures and transition metal chalcogenides have been shown to exhibit catalytic activity for ORR in alkaline medium.⁶⁰⁻⁶² Accordingly, the ORR catalytic activity of FeNi₂Se₄-NrGO nanocomposite was investigated using a RRDE setup in O₂ saturated 1 M KOH at a scan rate of 10 mV s⁻¹. The nanocomposite catalyst was dropcasted onto glassy carbon disk electrode and the ring current was monitored with Pt ring electrode. All the measurements were performed with mass loading of 0.45 mg/cm². The ORR hydrodynamic voltammograms of the FeNi₂Se₄-NrGO hybrid catalyst at different rotation rates was shown in Figure 7a. It was observed that the hybrid catalyst was indeed active for ORR and showed an onset potential of 0.93 V, comparable to that of Pt in alkaline medium.⁶³ High conductivity of the NrGO matrix has an important influence in increasing current density of the hybrid catalytic composite and the half-wave potential ($E_{1/2}$) was observed at 0.61 V vs RHE, which is comparable with the best chalcogenide-based ORR catalysts that has been reported.⁶⁴ The kinetics of the ORR catalytic activity along with the number of electrons involved in the process were determined from Koutecky - Levich plots (K-L plots, equation S9) as shown in Figure 7b.

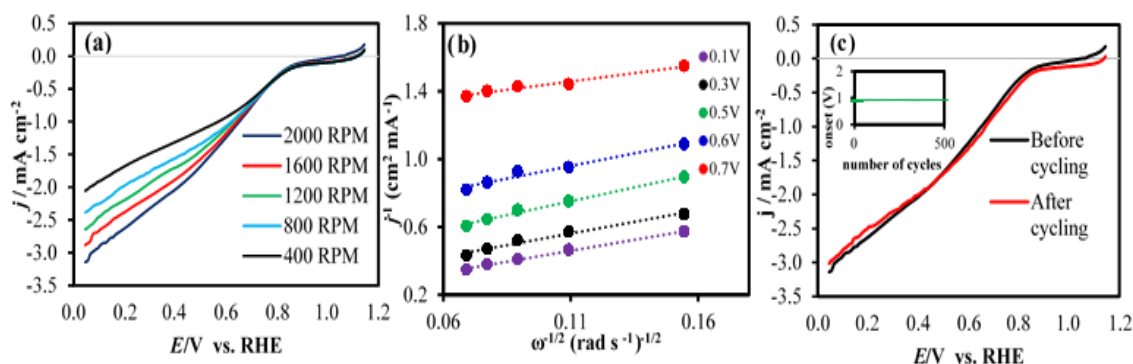


Figure 7. ORR catalytic activity of FeNi₂Se₄-NrGO nanocomposite. (a) Linear sweep voltammograms of FeNi₂Se₄-NrGO nanocomposite at different rotation rates. (b) K-L plots at different potentials. (c) LSVs of nanocomposite before and after 500 cycles of ORR activity. Inset shows stability of the ORR onset potential for 500 cycles.

The linear and parallel behavior of the K-L plots at various potentials suggest identical electron transfer involved throughout the ORR process and first order reduction kinetic with respect to dissolved oxygen.⁴² The slopes of the K-L plots of (j_i^{-1} versus $\omega^{-1/2}$) at various potentials were similar to that expected for four-electron ORR, and the value of n was calculated to be 3.94 for the FeNi₂Se₄-NrGO surface similar to that observed for commercially available Pt/C catalyst. The exclusive 4e⁻ reduction process was also confirmed from the ratio of ring and disk currents using equation S7. Additionally RRDE experiments were also used to estimate the percentage of H₂O₂ produced (equation S8). It was observed that less than 10 % H₂O₂ was generated during the ORR process (Figure S11). The enhanced ORR catalytic activity for the nanocomposite suggests synergistic coupling between FeNi₂Se₄ and NrGO, similar to that observed in case of OER.

The stability of the ORR activity was investigated through cycling studies, wherein the catalyst was cycled for 500 cycles in O₂ saturated 1 M KOH solution at 1200 rpm. As

can be seen from the the LSV plots measured before and after 500 cycles (Figure 7c), there was no change in the ORR onset potential, current density, and half-wave potential. Monitoring the onset potential also showed that it was pretty much constant throughout 500 cycles as shown in the inset of Figure 7c. Such cycling study ascertained that the catalyst has high stability and durability for ORR during an extended period of time.

3. CONCLUSION

In summary, we have successfully grown FeNi₂Se₄ nanoparticles and FeNi₂Se₄-NrGO nanocomposite by using a simple hydrothermal technique. This inexpensive and easily reproducible electrocatalyst shows highly efficient bifunctional OER-ORR catalytic activity in alkaline medium. The exceptional OER activity is characterized by a small η of 170 mV at the current density of 10 mA cm⁻² and a Tafel slope down to 62.1 mV dec⁻¹. The low onset potential required for O₂ evolution as well as overpotential required to reach 10 mA cm⁻², is one of the lowest that has been reported so far, making this hybrid composite a very promising OER electrocatalyst. The ORR activity is also better than the other chalcogenide based electrocatalysts and is comparable to Pt. Hence, this novel hybrid composite has exhibited significantly enhanced OER-ORR catalytic performances with high catalytic activity, favorable kinetics, and extended stability. The synergistic coupling between the N-doped reduced graphene oxide and FeNi₂Se₄ nanoparticles is believed to boost the excellent OER performance. The simple synthetic method, earth abundance of the constituent elements, and low overpotential makes this bifunctional catalyst a front runner for various energy related applications.

SUPPORTING INFORMATION

Materials and Methods

Materials. Nickel chloride hexahydrate [NiCl₂ · 6H₂O] from J T Baker Chemical Co, Iron sulfate heptahydrate [FeSO₄ · 7H₂O] from Fisher Scientific, Selenium dioxide [SeO₂] from Acros chemicals, Hydrazine monohydrate from Acros chemicals and KOH from Fisher chemicals. All chemicals were of analytical grade and were used as received without further purification.

Synthesis of Graphene Oxide (GO)

Graphene oxide was synthesized by modified Hummers method.¹ Typically, 1 g of graphite and 0.5 g of sodium nitrate were mixed together followed by the addition of 23 ml of conc. sulfuric acid under constant stirring. After 1 h, 3 g of KMnO₄ was added gradually to the above solution while keeping the temperature less than 20°C to prevent overheating. The mixture was stirred at 35 °C for 12 h and the resulting solution was diluted by adding 500 ml of water under vigorous stirring. To ensure the completion of reaction with KMnO₄, the suspension was further treated with 30% H₂O₂ solution (5 ml). The resulting mixture was washed with HCl and H₂O respectively and allowed to stand for 48 hrs, followed by centrifugation and drying.

Synthesis of NrGO

0.5 g of GO was stirred in 5 ml water followed by addition of 0.1 ml hydrazine monohydrate and 0.1 ml of ammonium hydroxide. The solution was stirred for 10 mins before transferring to 23 ml Teflon lined hydrothermal bomb. The reaction was carried out

at 145°C for 12 hrs. The solid was washed with DI water and ethanol several time and dried in vacuum oven at 40°C overnight.

Synthesis of FeNi₂Se₄

FeNi₂Se₄ nanoparticles was synthesized by hydrothermal method. In a typical procedure, 5 mmol of FeSO₄.7H₂O, 10 mmols of NiCl₂.6H₂O and 20 mmols of SeO₂ were mixed in 10 ml of deionized water. The solution was stirred on a magnetic stirrer. About 5 mins later 0.25 ml of hydrazine monohydrate was added. The solution of stirred for another 5 mins and then transferred to 23 ml Teflon - lined autoclave, which was sealed and maintained at 145°C for 24 h and then naturally cooled to room temperature. The resulting black solid was then washed several times with DI water and ethanol. The solid was dried in an oven maintained at 40°C overnight.

Synthesis of FeNi₂Se₄ -Nitrogen Doped Reduced Graphene Oxide Nanocomposite

Firstly, Graphene oxide is taken 30% by weight in 5 ml DI water. This mixture was sonicated for 15 mins. GO-water mixture is added to FeNi₂Se₄ nanoparticles (from the above procedure) while stirring. 0.25 ml hydrazine monohydrate is added and this solution is sonicated for 30 mins. 0.5ml NH₄OH in 0.7 ml water is added. This solution is transferred to 23 ml Teflon - lined autoclave, which was sealed and maintained at 145°C for 24 h and then naturally cooled to room temperature. The cleaning procedure remains same as above. FeNi₂Se₄ – NrGO was synthesized similar to the procedures reported to synthesize other graphene oxide based materials.² Hydrazine monohydrate was used as reducing agent, which reduces the Se⁴⁺ to Se²⁻ and chemically reduces graphene oxide to reduced graphene oxide (rGO) to a certain extent. An additional step of sonicating the above solution for 30 mins was introduced. Sonication of a FeNi₂Se₄ - NrGO dispersion in the presence of

reducing agent like hydrazine monohydrate results in high-coverage of metal nanoparticle on rGO sheets. An additional benefit of sonication includes the induced reduction in the exfoliation of individual rGO sheets. This increases the likelihood of metal nanoparticle deposition on single-layer rGO sheets. Hydrothermal treatment at 145°C for 24 h gave FeNi₂Se₄-NrGO powder. During the hydrothermal treatment, crystallization of FeNi₂Se₄ and further reduction of GO to rGO were achieved simultaneously. We also added NH₄OH in our synthesis steps to obtain an N-doped hybrid catalyst denoted as FeNi₂Se₄-NrGO.

Synthesis of FeNi₂O₄-NrGO by Hydrothermal Method

FeNi₂O₄ -NrGO was synthesized by hydrothermal method. In a typical procedure, 1 mmol of Fe(NO₃)₃·9H₂O, 2 mmols of Ni(NO₃)₃·6H₂O and 40 mmols of urea were mixed in 5 ml of deionized water. The solution was stirred on a magnetic stirrer. Graphene oxide which was synthesized by modified Hummers method was taken 30% by weight in 5 ml DI water. This mixture was sonicated for 15 mins. About 5 mins later this 5ml of graphene oxide was added to the metal precursor solution. 0.5ml NH₄OH in 0.7 ml water is added. The solution of stirred for another 5 mins and then transferred to 20 ml Teflon - lined autoclave, which was sealed and maintained at 185°C for 12 h and then naturally cooled to room temperature.^{3,4} The resulting black solid was then washed several times with DI water and ethanol. The solid was dried in a vacuum oven maintained at 40°C overnight.

Electrodeposition of RuO₂ on GC

Electrodeposition of RuO₂ on GC substrate was carried out from a mixture of RuCl₃ (0.452 g) and KCl (2.952 g) in 40 ml of 0.01M HCl by using cyclic voltammetry from 0.015 to 0.915 V (vs. Ag|AgCl) for 100 cycles at a scan rate of 50 mV s⁻¹. Finally heated at 200°C for 3 h in presence of Air.

Electrode Preparation

The preparation method of the working electrodes is as follows. 2.5 mg of catalyst powder was dispersed in 300 μL of ethanol mixed with 0.8 μL of Nafion (5wt %). This mixture was ultra-sonicated for about 30 mins to generate a homogeneous ink. 20 μL of the ink was drop casted onto carbon fiber paper, leading to the catalyst loading $\sim 0.55 \text{ mg cm}^{-2}$. The as prepared catalyst was dried at room temperature for 12 h. For comparison, bare carbon fiber paper which was cleaned and dried for electrochemical measurement was also measured.

Characterizations

Powder X-ray Diffraction. The electrodeposited substrates were studied as such without any further treatment. The product was characterized through powder X-ray diffraction (PXRD) using Philips X-Pert using CuK α (1.5418 \AA) radiation. The PXRD pattern was collected from 5° to 90° .

The average catalyst particle size was calculated from the XRD diffraction peak width using the Scherrer equation

$$L = \frac{K\lambda}{\beta \cos\theta} \quad (1)$$

where L is the particle size, λ is the X-ray wavelength in nanometer (0.15418 nm), β is the peak width of the diffraction peak profile at half maximum height in radians and K is a constant, normally taken as 0.9. The value of β in 2θ axis of diffraction profile must be in radians. The FeNi₂Se₄-NrGO composite showed an average size of 22. In comparison, FeNi₂O₄-NrGO showed an average size of 20 nm.

Transmission Electron Microscopy (TEM). High resolution TEM images and selected area electron diffraction (SEAD) was obtained using FEI Tecnai F20. The probe current is 1.2 nA with a spot size of less than 2 nm. STEM mode in the TEM was also used for dark field imaging where the convergence angle was 13 mrad and the camera length was 30 mm. This scope is equipped using an Oxford ultra-thin (UTW) window EDS detector, which allows detection of the elements.

X-ray Photoelectron Spectroscopy (XPS). XPS measurements of the catalysts were performed using a Kratos Axis 165 X-ray Photoelectron Spectrometer using the monochromatic Al X-ray source. The spectra were collected as is and after sputtering with Ar for 30 sec which removes approximately >1 nm from the surface.

Electrochemical Measurements. Electrochemically active surface area (ECSA) for FeNi₂Se₄-NrGO and FeNi₂Se₄ was determined by double layer capacitance in the non-faradaic region according to the equation

$$ECSA = C_{DL} / C_s \quad (2)$$

where C_{DL} is the double layer capacitance and C_s is the specific capacitance. For this work the $C_s = 0.04 \text{ mFcm}^{-2}$. By plotting the capacitive current (i_{DL}) versus the scan rate (ν) according to the equation $i_{DL} = C_{DL} \nu$, we obtain a straight line where the slope of this line will give the C_{DL} value. Cyclic voltammograms were recorded in N₂ saturated 1M KOH solution from -0.3 V to 0.08 V vs Ag|AgCl, with varying scan rates from 20 to 160 mVs⁻¹. FeNi₂Se₄-NrGO has a higher value of ECSA compared to FeNi₂Se₄ which suggest that the hybrid nanocomposite has a catalytically active sites.

Electrochemical measurements were performed at room temperature in a standard three-electrode glass cell using IviumStat potentiostat. Note that the current density was

normalized to the geometrical area and the measured potentials vs Ag/AgCl were converted to a reversible hydrogen electrode (RHE) scale according to the Nernst equation

$$E_{\text{RHE}} = E_{\text{Ag/AgCl}} + 0.059 \text{ pH} + E^{\circ}_{\text{Ag/AgCl}} \quad (3)$$

The overpotential (η) was calculated according to the following formula

$$\eta \text{ (V)} = E_{\text{RHE}} - 1.23 \text{ V} \quad (4)$$

The electrolyte was prepared using DI water and KOH pellets (99.99% weight). All measurements were conducted under N_2 saturation. Linear sweep voltammograms (LSV) and cyclic voltammetry (CV) were conducted with scan rates in the range of 10 mV s^{-1} .

Tafel Plots. The catalytic performance of the hybrid catalyst for OER is carried out by measuring the Tafel slopes according to the equation given below.

$$\eta = a + 2.3 \frac{RT}{\alpha n F} \log(j) \quad (5)$$

where η is the overpotential, j is the current density and the other symbols have their usual meanings.

TOF. The turnover frequency (TOF) was calculated from the following equation

$$TOF = \frac{I}{4Fm} \quad (6)$$

where I is the current in Amperes, F is the Faraday constant and m is the number of moles of the active catalyst.

Faradaic efficiency was calculated using the following equation

$$\text{Faradaic efficiency} = \frac{2i_r}{i_d N} \quad (7)$$

where, i_d and i_r are the disk and ring currents, respectively and N is the collection efficiency (0.24).

The percentage of the electrogenerated hydrogen peroxide ($X_{\text{H}_2\text{O}_2}$) and the number of electron transferred (n) during the ORR were also calculated using Eqs. (S8) and (9):

$$X_{\text{H}_2\text{O}_2} = \frac{\frac{200I_{\text{R}}}{N}}{I_{\text{D}} + \frac{I_{\text{R}}}{N}} \quad (8)$$

$$n = \frac{4I_{\text{D}}}{I_{\text{D}} + \frac{I_{\text{R}}}{N}} \quad (9)$$

where I_{D} and I_{R} are the disk and ring currents, respectively and N is the collection efficiency (0.24).

K-L Plots. The number of electrons transferred per oxygen molecule involved in the ORR at the $\text{FeNi}_2\text{Se}_4\text{-NrGO@GC}$ electrode was determined by the Koutecky-Levich equation.

$$\frac{1}{j} = \frac{1}{j_k} + \frac{1}{B\omega^{1/2}} \quad (10)$$

where j_k is the kinetic current density B is the so-called B-factor and equal to $0.62nFC_bD_o^{2/3}v^{-1/6}$ k is the rate constant, n is number of electrons transferred for per oxygen molecule, F is the Faraday constant ($96\,485\text{ C mol}^{-1}$), A is geometric area of electrode (0.196 cm^2), D_{O_2} is the diffusion coefficient of O_2 ($1.9 \times 10^{-5}\text{ cm}^2\text{ s}^{-1}$), ν is the kinetic viscosity of the solution ($1.009 \times 10^{-2}\text{ cm}^2\text{ s}^{-1}$), and C_{O_2} is the concentration of dissolved O_2 in solution ($1.2 \times 10^{-6}\text{ mol cm}^{-3}$). A plot of $1/j$ vs. $\omega^{-1/2}$ should yield a straight line having a slope equal to B . The values of B allow us to assess the number of electrons involved in the ORR. From an experimental data set where the current is measured at different rotation rates, it is possible to extract the kinetic current from a so-called K-L plot. In a K-L plot the inverse measured current is plotted versus the inverse square root of the rotation rate.

Characterization of GO & NrGO

Formation of NrGO was confirmed by Raman, XRD (1) and TEM studies. Figure S1(a) gives the TEM image of the as prepared NrGO film. Raman spectroscopy is an important tool to understand the defects and disorders in the NrGO sample. The Raman spectra shows to significant peaks at 1319 cm^{-1} and 1591 cm^{-1} for NrGO as shown in Figure S1(c). NrGO has been reported to have higher I_D/I_G ratio which leads to the defective nature of material which will have a direct impact on the porosity and the activation sites for the metal atoms to reside.

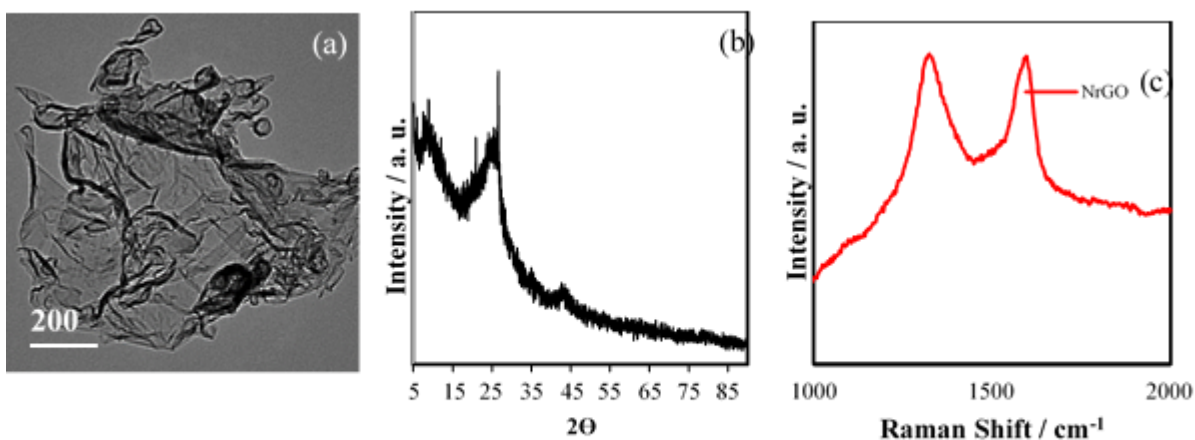


Figure S1. (a) TEM image of nitrogen doped reduced graphene oxide (b) PXRD spectra of graphene oxide and reduced graphene oxide. (c) Raman spectra recorded for GO and NrGO.

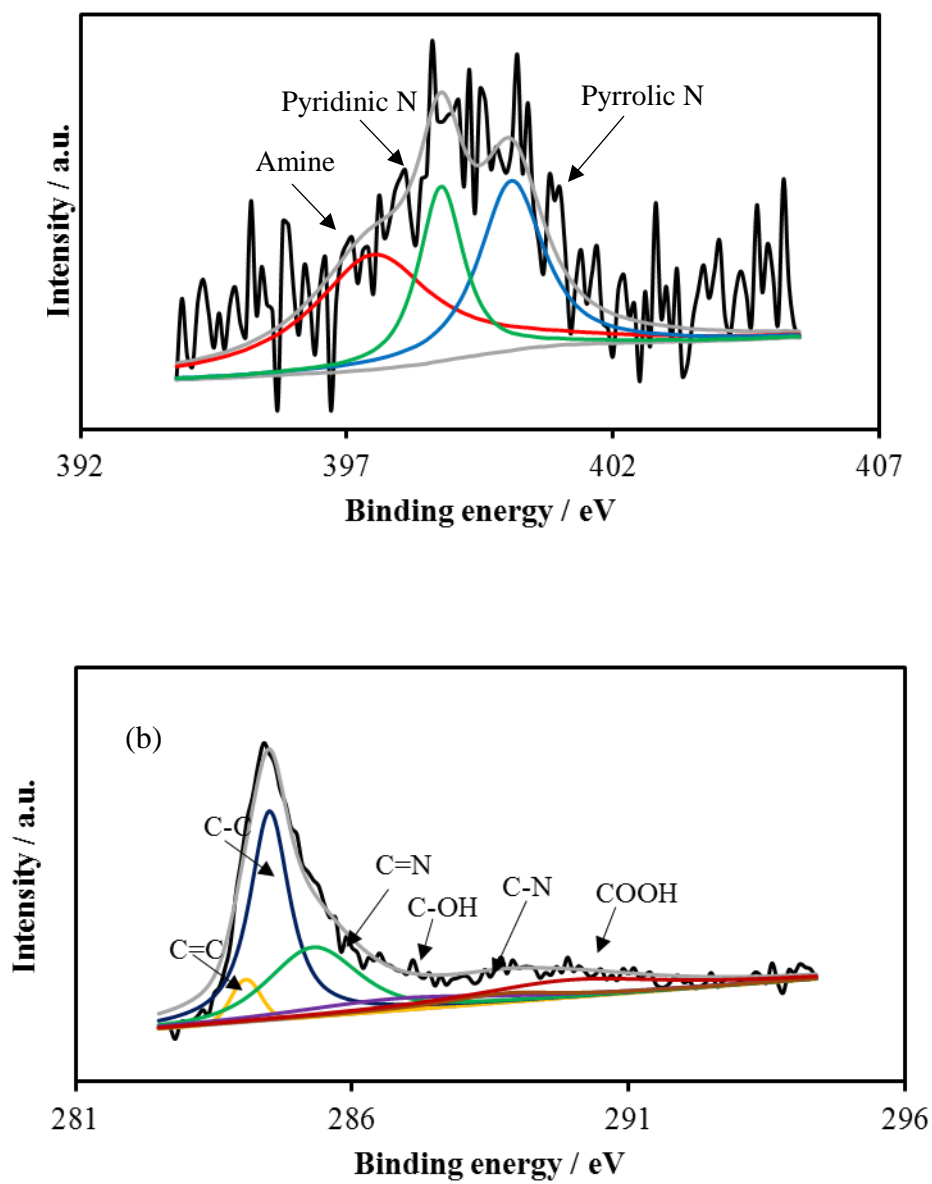


Figure S2. (a) Deconvoluted XPS spectrum of N1s (b) C1s.

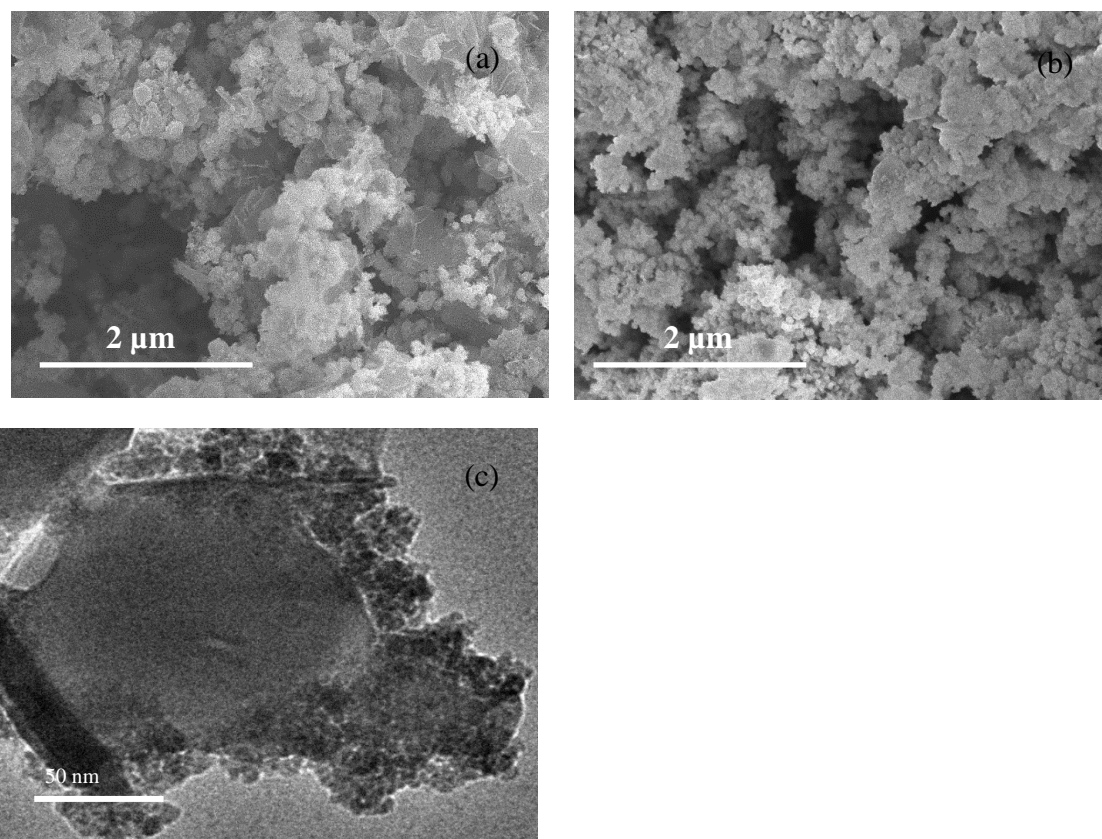


Figure S3. SEM image of the as-synthesized (a) powder of $\text{FeNi}_2\text{Se}_4\text{-NrGO}$ (b) FeNi_2Se_4 (c) TEM image of $\text{FeNi}_2\text{O}_4\text{-NrGO}$.

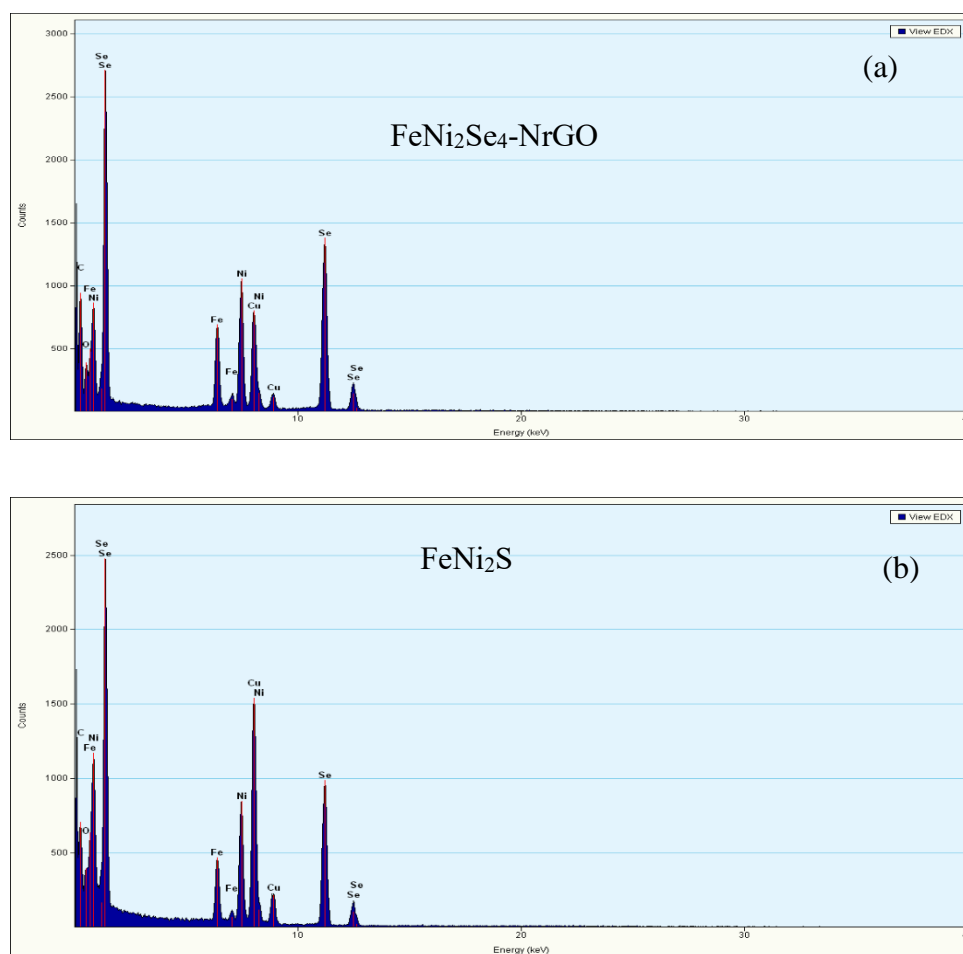


Figure S4. EDS pattern of (a) FeNi₂Se₄-NrGO (b) FeNi₂Se₄.

Table S1. Table for atomic % collected by EDS from Techni F20 (TEM).

Element	Atomic %
C(K)	23.92
O(K)	8.08
Fe(K)	4.02
Ni(K)	10.85
Cu(K)	35.48
Se(K)	17.65

Element	Atomic %
C(K)	44.52
O(K)	7.89
Fe(K)	4.34
Ni(K)	8.73
Cu(K)	16.99
Se(K)	17.51

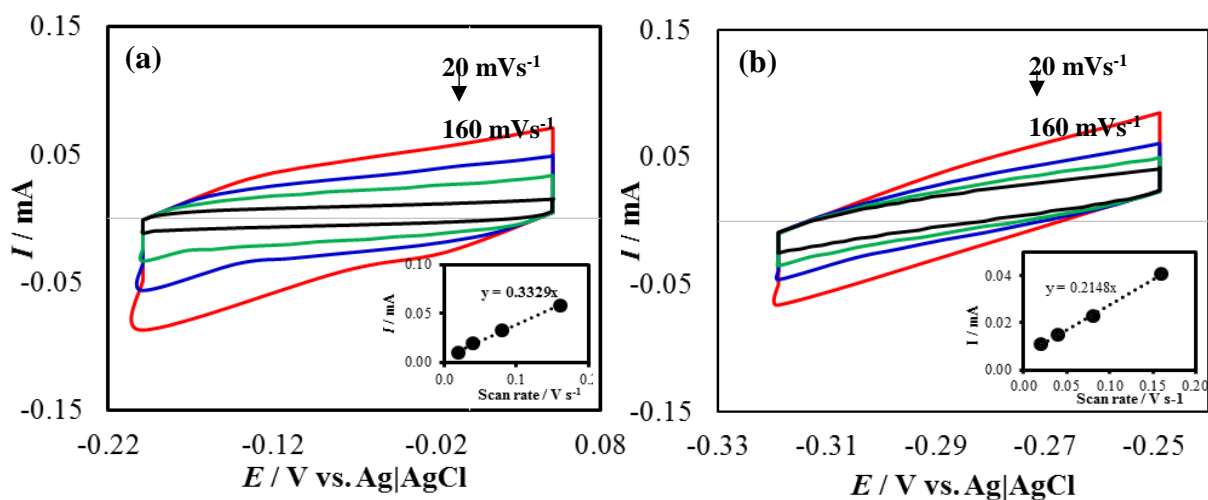


Figure S5. Cyclic voltammograms measured for the (a) FeNi₂Se₄-NrGO nanocomposite, and (b) FeNi₂Se₄ in N₂ saturated 1.0 M KOH solution at different scan rates from 20 to 160 mV s⁻¹. Insets show plots of anodic current measured at -0.14 V for FeNi₂Se₄-NrGO and -0.30 V for FeNi₂Se₄ as a function of scan rate.

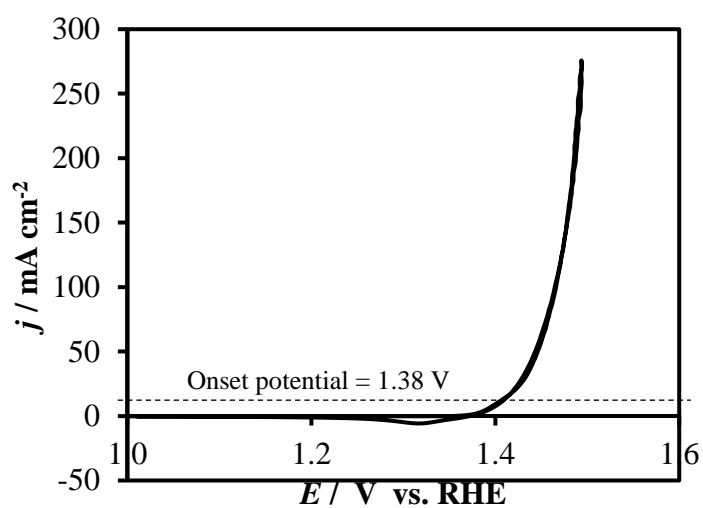


Figure S6. CV to calculate onset potential and overpotential to achieve 10 mA cm^{-2} from $\text{FeNi}_2\text{Se}_4\text{-NrGO}$ composite.

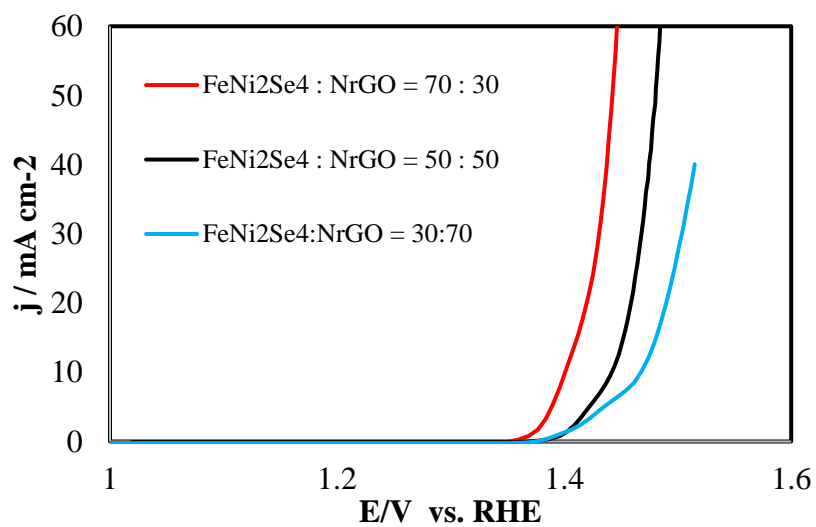


Figure S7. LSV comparison of different ratios of $\text{FeNi}_2\text{Se}_4\text{:NrGO}$.

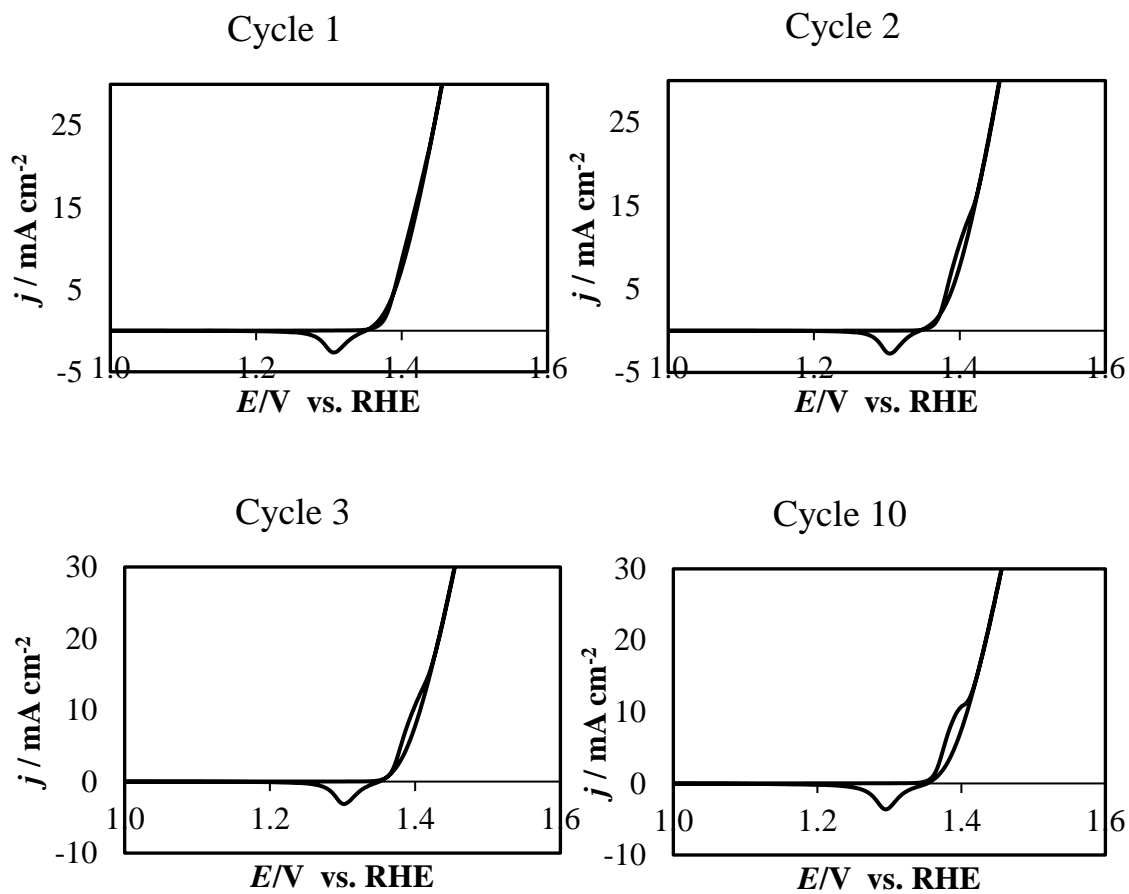


Figure S8. Ni oxidation peak experiment. (a) cycle 1- no $\text{Ni}^{2+} \rightarrow \text{Ni}^{3+}$ oxidation observed; (b) Cycle 2 – very small Ni^{2+} oxidation peak; Cycle 3 (c) and cycle 10 (d) shows growing intensity of the Ni^{2+} oxidation peak.

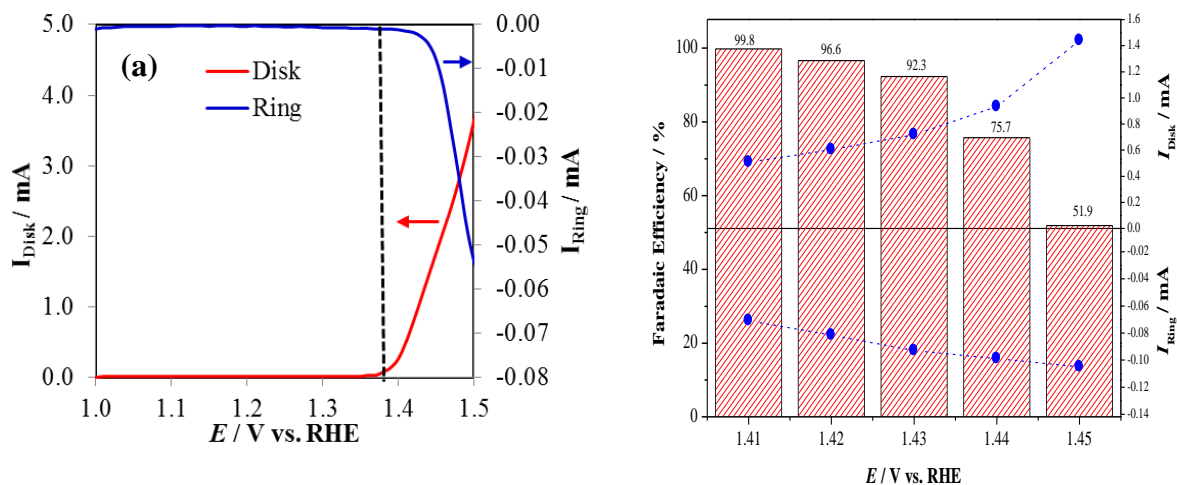


Figure S9. a) OER-ORR combined LSV plots showing OER at the FeNi₂Se₄-NrGO/GC disk electrode in N₂-saturated 1.0 M KOH and ORR ring current at the Pt ring electrode which was held at 0.2 V vs. RHE in the same electrolyte. The black dash line shows the onset of OER at the disk electrode which coincides with the onset of increasing ring current indicating onset of ORR at the Pt ring electrode. b) Faradaic efficiency of FeNi₂Se₄-NrGO nanocomposite.

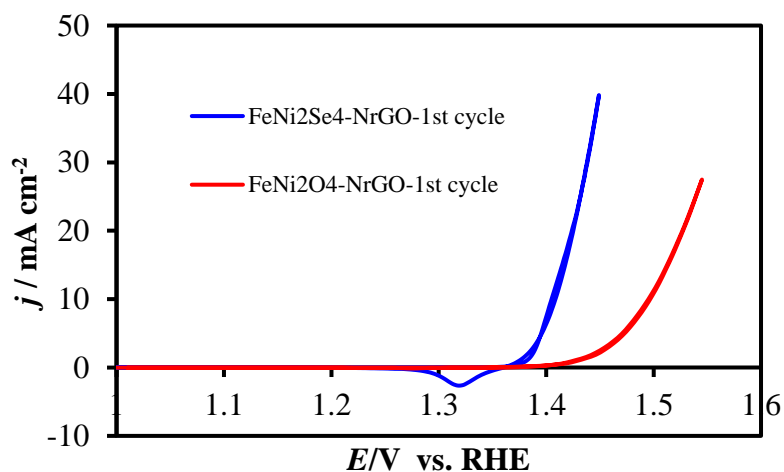


Figure S10. CV comparison of 1st cycle of FeNi₂Se₄-NrGO and FeNi₂O₄-NrGO.

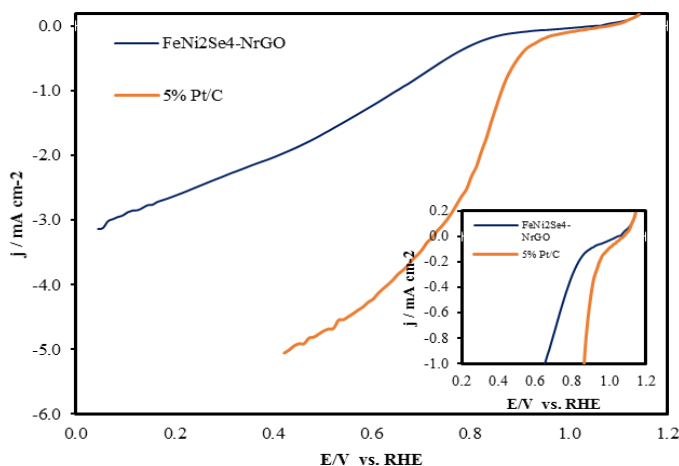


Figure S11. ORR catalytic activity of FeNi₂Se₄-NrGO nanocomposite. Linear sweep voltammograms of FeNi₂Se₄-NrGO nanocomposite at different rotation rates, and 5% Pt/C as standards at a rotation of 2000 RPM. (inset) shows the onset of the FeNi₂Se₄-NrGO nanocomposite compared with Pt standard.

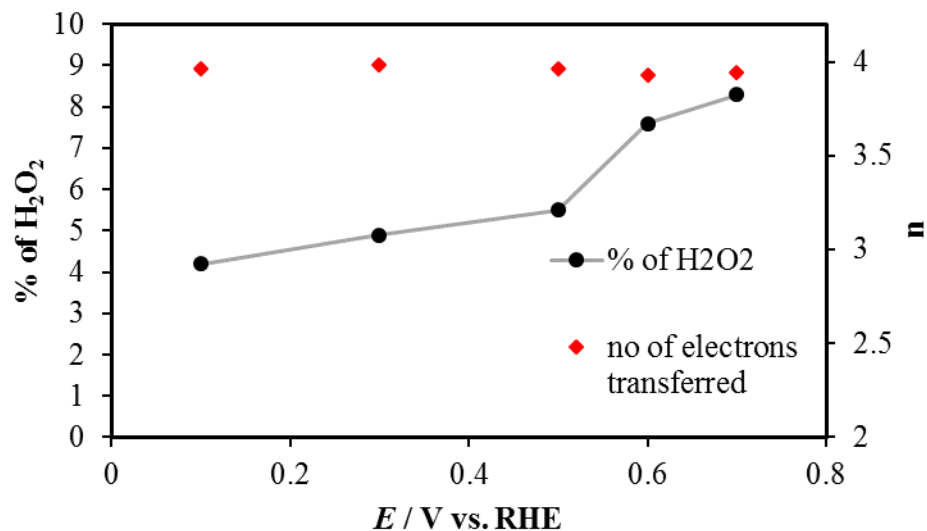


Figure S12. Percentage of peroxide (solid line) and the electron transfer number (n) of nanocomposite at various potentials, based on the corresponding RRDE data in Figure 7a.

Table S2. Comparison of overpotential for different transition metal chalcogenides based OER electrocatalysts.

Electrocatalyst composition	Catalyst Loading	Electrolyte	Overpotential (mV vs. RHE) @ 10 ^a , 20 ^b or 50 ^c mA cm ⁻²	Reference
FeNi ₂ Se ₄ -NrGO@CFP	0.55 mg cm ⁻²	1 M KOH	170 ^a	This work
FeNi ₂ O ₄ -NrGO@CFP	0.55 mg cm ⁻²	1 M KOH	260 ^a	This work
NiCo ₂ S ₄ NA/CC	4.0 mg cm ⁻²	1 M KOH	340 mV (100 mA cm ⁻²)	<i>Nanoscale</i> 2015 , <i>7</i> , 15122–15126
NiCo ₂ S ₄ NW/NF	-	1 M KOH	260 ^a	<i>Adv. Funct. Mater.</i> 2016 , <i>26</i> , 4661–4672
NiCo ₂ O ₄ hollow microcuboids	~1 mg cm ⁻²	1 M NaOH	290 ^a	<i>Angew. Chem. Int. Ed.</i> 2016 , <i>55</i> , 6290–6294
Ni-Co-O@Ni-Co-S NA	-	1 M KOH	300 ^b	<i>Phys. Chem. Chem. Phys.</i> 2014 , <i>16</i> , 20402–20405
NiCo ₂ O ₄	-	1 M KOH	391 ^b	<i>Adv. Energy Mater.</i> 2015 , <i>5</i> , 1402031-1402038
(a-CoSe/Ti)	3.8 mg cm ⁻²	1 M KOH	292 ^a	<i>Chem. Commun.</i> 2015 , <i>51</i> , 16683
Co _{0.85} Se	-	1 M KOH	324 ^a	<i>Adv. Mater.</i> 2016 , <i>28</i> , 77–85
(Ni,Co) _{0.85} Se	-	1 M KOH	255 ^a	<i>Adv. Mater.</i> 2016 , <i>28</i> , 77–85
Co _{0.13} Ni _{0.87} Se ₂ /Ti	1.67 mg cm ⁻²	1 M KOH	320 mV (100 mA cm ⁻²)	<i>Nanoscale</i> 2016 , <i>8</i> , 3911- 3915
NiSe ₂ /Ti	-	1 M KOH	350 mV (100 mA cm ⁻²)	<i>Nanoscale</i> 2016 , <i>8</i> , 3911- 3915
NiSe ₂	1 mg cm ⁻²	1 M KOH	250 ^a	<i>ACS Appl. Mater. Interfaces.</i> 2016 , <i>8</i> , 5327–5334
CoSe ₂	1 mg cm ⁻²	1 M KOH	430 ^a	<i>ACS Appl. Mater. Interfaces.</i> 2016 , <i>8</i> , 5327–5334

REFERENCES

1. N. S. Lewis and D. G. Nocera, *Proceedings of the National Academy of Sciences*, 2006, **103**, 15729-15735.
2. A. J. Bard and M. A. Fox, *Accounts of Chemical Research*, 1995, **28**, 141-145.
3. M. Winter and R. J. Brodd, *Chemical Reviews*, 2004, **104**, 4245-4270.
4. A. A. Gewirth and M. S. Thorum, *Inorganic Chemistry*, 2010, **49**, 3557-3566.
5. W. T. Hong, M. Risch, K. A. Stoerzinger, A. Grimaud, J. Suntivich and Y. Shao-Horn, *Energy & Environmental Science*, 2015, **8**, 1404-1427.
6. L. Trotochaud and S. W. Boettcher, *Scripta Materialia*, 2014, **74**, 25-32.
7. K. Zhu, M. Li, X. Li, X. Zhu, J. Wang and W. Yang, *Chemical Communications*, 2016, **52**, 11803-11806.
8. G. M. Whitesides and G. W. Crabtree, *Science*, 2007, **315**, 796-798.
9. C. C. L. McCrory, S. Jung, J. C. Peters and T. F. Jaramillo, *Journal of the American Chemical Society*, 2013, **135**, 16977-16987.
10. E. Fabbri, A. Habereder, K. Waltar, R. Kötz and T. J. Schmidt, *Catalysis Science & Technology*, 2014, **4**, 3800-3821.
11. H. Tang, C. M. Hessel, J. Wang, N. Yang, R. Yu, H. Zhao and D. Wang, *Chemical Society Reviews*, 2014, **43**, 4281-4299.
12. Q. Jia, E. Liu, L. Jiao, J. Li and S. Mukerjee, *Current Opinion in Electrochemistry*, 2018, **12**, 209-217.
13. Y. Gorlin, C.-J. Chung, J. D. Benck, D. Nordlund, L. Seitz, T.-C. Weng, D. Sokaras, B. M. Clemens and T. F. Jaramillo, *Journal of the American Chemical Society*, 2014, **136**, 4920-4926.
14. S. W. Lee, C. Carlton, M. Risch, Y. Surendranath, S. Chen, S. Furutsuki, A. Yamada, D. G. Nocera and Y. Shao-Horn, *Journal of the American Chemical Society*, 2012, **134**, 16959-16962.
15. T. Hamann, *Science*, 2014, **345**, 1566-1567.

16. J. Luo, J.-H. Im, M. T. Mayer, M. Schreier, M. K. Nazeeruddin, N.-G. Park, S. D. Tilley, H. J. Fan and M. Grätzel, *Science*, 2014, **345**, 1593-1596.
17. W. Zhou, X.-J. Wu, X. Cao, X. Huang, C. Tan, J. Tian, H. Liu, J. Wang and H. Zhang, *Energy & Environmental Science*, 2013, **6**, 2921-2924.
18. J. Masud, A. T. Swesi, W. P. R. Liyanage and M. Nath, *ACS Applied Materials & Interfaces*, 2016, **8**, 17292-17302.
19. M. Liao, G. Zeng, T. Luo, Z. Jin, Y. Wang, X. Kou and D. Xiao, *Electrochimica Acta*, 2016, **194**, 59-66.
20. X. Xu, F. Song and X. Hu, *Nature Communications*, 2016, **7**, 12324.
21. M.-R. Gao, Z.-Y. Lin, T.-T. Zhuang, J. Jiang, Y.-F. Xu, Y.-R. Zheng and S.-H. Yu, *Journal of Materials Chemistry*, 2012, **22**, 13662-13668.
22. A. T. Swesi, J. Masud and M. Nath, *Energy & Environmental Science*, 2016, **9**, 1771-1782.
23. A. T. Swesi, J. Masud, W. P. R. Liyanage, S. Umaphathi, E. Bohannan, J. Medvedeva and M. Nath, *Scientific Reports*, 2017, **7**, 2401.
24. M. Gong and H. Dai, *Nano Research*, 2015, **8**, 23-39.
25. L. Trotochaud, S. L. Young, J. K. Ranney and S. W. Boettcher, *Journal of the American Chemical Society*, 2014, **136**, 6744-6753.
26. K. Fan, H. Chen, Y. Ji, H. Huang, P. M. Claesson, Q. Daniel, B. Philippe, H. Rensmo, F. Li, Y. Luo and L. Sun, *Nature Communications*, 2016, **7**, 11981.
27. F. M. Sapountzi, J. M. Gracia, C. J. Weststrate, H. O. A. Fredriksson and J. W. Niemantsverdriet, *Progress in Energy and Combustion Science*, 2017, **58**, 1-35.
28. O. Mabayoje, A. Shoola, B. R. Wygant and C. B. Mullins, *ACS Energy Letters*, 2016, **1**, 195-201.
29. Y. Zhan, M. Lu, S. Yang, Z. Liu and J. Y. Lee, *ChemElectroChem*, 2016, **3**, 615-621.
30. J. Masud, P.-C. Ioannou, N. Levesanos, P. Kyritsis and M. Nath, *ChemSusChem*, 2016, **9**, 3128-3132.
31. E. Ebsworth, J. Lewis, J. Burgess, A. Downs, J. Turner, F. Mabbs, D. Machin and F. Kohl, *Annu. Rep. Prog. Chem.*, 1966, **63**, 129-238.

32. B. Zheng, F. Tang, J. Luo, J. W. Schultz, N. P. Rath and L. M. Mirica, *Journal of the American Chemical Society*, 2014, **136**, 6499-6504.
33. K. S. Novoselov, A. K. Geim, S. V. Morozov, D. Jiang, Y. Zhang, S. V. Dubonos, I. V. Grigorieva and A. A. Firsov, *Science*, 2004, **306**, 666-669.
34. K. S. Novoselov, A. K. Geim, S. V. Morozov, D. Jiang, M. I. Katsnelson, I. V. Grigorieva, S. V. Dubonos and A. A. Firsov, *Nature*, 2005, **438**, 197-200.
35. Y. Zhang, Y.-W. Tan, H. L. Stormer and P. Kim, *Nature*, 2005, **438**, 201-204.
36. Y. Zhang, J. P. Small, M. E. S. Amori and P. Kim, *Physical Review Letters*, 2005, **94**, 176803.
37. G. Wu, K. L. More, C. M. Johnston and P. Zelenay, *Science*, 2011, **332**, 443-447.
38. R. Kou, Y. Shao, D. Wang, M. H. Engelhard, J. H. Kwak, J. Wang, V. V. Viswanathan, C. Wang, Y. Lin, Y. Wang, I. A. Aksay and J. Liu, *Electrochemistry Communications*, 2009, **11**, 954-957.
39. M.-R. Gao, Y.-F. Xu, J. Jiang, Y.-R. Zheng and S.-H. Yu, *Journal of the American Chemical Society*, 2012, **134**, 2930-2933.
40. M.-R. Gao, X. Cao, Q. Gao, Y.-F. Xu, Y.-R. Zheng, J. Jiang and S.-H. Yu, *ACS Nano*, 2014, **8**, 3970-3978.
41. B. S. Yeo and A. T. Bell, *Journal of the American Chemical Society*, 2011, **133**, 5587-5593.
42. Y. Liang, Y. Li, H. Wang, J. Zhou, J. Wang, T. Regier and H. Dai, *Nature Materials*, 2011, **10**, 780-786.
43. J. Lai, S. Li, F. Wu, M. Saqib, R. Luque and G. Xu, *Energy & Environmental Science*, 2016, **9**, 1210-1214.
44. K. Kojima, S. Murase, K. Sato and K. Adachi, *Journal of the Physical Society of Japan*, 1970, **29**, 1642-1642.
45. A. Kjekshus and W. B. Pearson, *Progress in Solid State Chemistry*, 1964, **1**, 83-174.
46. A. Hayashi, K. Imada, K. Inoue, Y. Ueda and K. Kosuge, 1986.
47. R. Tang, C. Jiang, W. Qian, J. Jian, X. Zhang, H. Wang and H. Yang, *Scientific Reports*, 2015, **5**, 13645.

48. C. Xia, Q. Jiang, C. Zhao, M. N. Hedhili and H. N. Alshareef, *Advanced Materials*, 2016, **28**, 77-85.
49. H. Nolan, B. Mendoza-Sanchez, N. Ashok Kumar, N. McEvoy, S. O'Brien, V. Nicolosi and G. S. Duesberg, *Physical Chemistry Chemical Physics*, 2014, **16**, 2280-2284.
50. *Russian Journal of Electrochemistry*, 2002, **38**, 1364-1365.
51. H. B. Yang, J. Miao, S.-F. Hung, J. Chen, H. B. Tao, X. Wang, L. Zhang, R. Chen, J. Gao, H. M. Chen, L. Dai and B. Liu, *Science Advances*, 2016, **2**, e1501122.
52. L.-A. Stern and X. Hu, *Faraday Discussions*, 2014, **176**, 363-379.
53. Y. Qiu, L. Xin and W. Li, *Langmuir*, 2014, **30**, 7893-7901.
54. L. Trotochaud, J. K. Ranney, K. N. Williams and S. W. Boettcher, *Journal of the American Chemical Society*, 2012, **134**, 17253-17261.
55. X. Li, F. C. Walsh and D. Pletcher, *Physical Chemistry Chemical Physics*, 2011, **13**, 1162-1167.
56. J. Y. C. Chen, L. Dang, H. Liang, W. Bi, J. B. Gerken, S. Jin, E. E. Alp and S. S. Stahl, *Journal of the American Chemical Society*, 2015, **137**, 15090-15093.
57. D. A. Corrigan, R. S. Conell, C. A. Fierro and D. A. Scherson, *The Journal of Physical Chemistry*, 1987, **91**, 5009-5011.
58. J. Suntivich, K. J. May, H. A. Gasteiger, J. B. Goodenough and Y. Shao-Horn, *Science*, 2011, **334**, 1383-1385.
59. H. Wang, Y. Liang, Y. Li and H. Dai, *Angewandte Chemie International Edition*, 2011, **50**, 10969-10972.
60. Z.-S. Wu, S. Yang, Y. Sun, K. Parvez, X. Feng and K. Müllen, *Journal of the American Chemical Society*, 2012, **134**, 9082-9085.
61. Q. Liu, J. Jin and J. Zhang, *ACS Applied Materials & Interfaces*, 2013, **5**, 5002-5008.
62. L. Geniès, R. Faure and R. Durand, *Electrochimica Acta*, 1998, **44**, 1317-1327.
63. L. Zhu, D. Susac, M. Teo, K. C. Wong, P. C. Wong, R. R. Parsons, D. Bizzotto, K. A. R. Mitchell and S. A. Campbell, *Journal of Catalysis*, 2008, **258**, 235-242.

64. I. H. Kwak, H. S. Im, D. M. Jang, Y. W. Kim, K. Park, Y. R. Lim, E. H. Cha and J. Park, *ACS Applied Materials & Interfaces*, 2016, **8**, 5327-5334.
65. W. Ma, R. Ma, C. Wang, J. Liang, X. Liu, K. Zhou and T. Sasaki, *ACS Nano*, 2015, **9**, 1977-1984.

III. HIGH-EFFICIENCY ELECTROCHEMICAL DOPAMINE SENSOR BASED ON TRANSITION METAL SELENIDES

Siddesh Umapathi¹, Jahangir Masud¹, Holly Coleman², Manashi Nath^{1}*

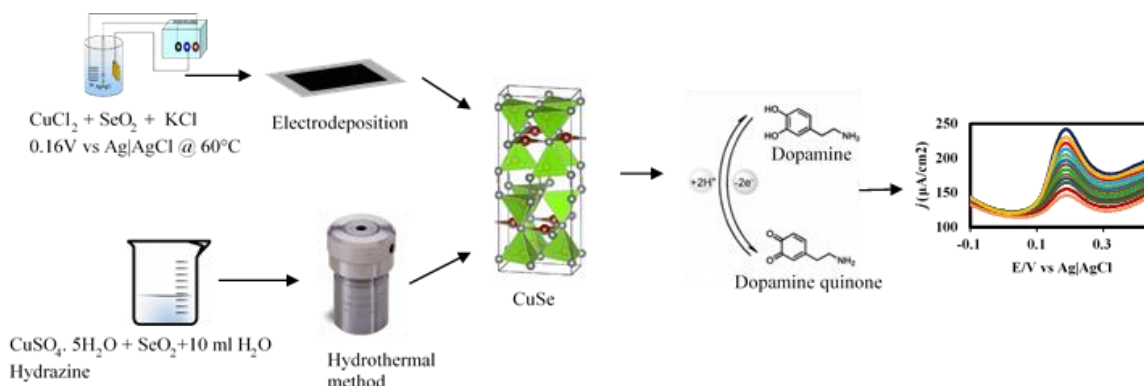
1. Department of Chemistry, Missouri University of Science & Technology, Rolla, MO 65409, USA.
2. Department of Chemical Engineering, Missouri University of Science & Technology, Rolla, MO 65409, USA.

ABSTRACT

Dopamine sensing has gained considerable attention in recent years due to its relation to neurological health and possible link to progression and development of neurodegenerative diseases including depression and PTSD. A continuous monitoring of dopamine levels in the brain fluid can lead to significant advancement in understanding the role of these biomarkers in signaling progression and development of the neurodegenerative diseases. In this article we have reported a dopamine biosensor comprising simple binary copper selenide, showing high sensitivity for dopamine detection with low limit of detection. A sensitivity of $26 \mu\text{A}/\mu\text{M}\cdot\text{cm}^2$ was obtained with this biosensor which typically indicates that this will be ideal to detect even small fluctuations in the transient dopamine concentration. Apart from high sensitivity and low LOD, the dopamine oxidation on the catalyst surface also occurred at a low applied potential ($<0.18 \text{ V vs Ag|AgCl}$), thereby significantly increasing selectivity of the process specifically with

respect to ascorbic and uric acids, which are considered to be the most prominent interferents for dopamine detection. This is the first report of dopamine sensing with a simple binary selenide comprising earth-abundant elements and can have large significance in designing efficient biosensors that can be transformative for understanding neurodegenerative diseases further.

Keywords: *Dopamine Sensor, CuSe, Transitions metal chalcogenides, DA electrooxidation, Square Wave Voltammetry*



1. INTRODUCTION

In recent years there has been an increasing demand for understanding the function and activity of the neurochemicals and its influence on various neurodegenerative diseases. Among the various neurochemicals, catecholamines such as dopamine (DA) and norepinephrine (NE) have received special attention since these are considered to be important neurobiomarkers and their levels are indicative of presence and extent of stress-

related disorders such as post-traumatic stress disorder (PTSD), sleep deprivation, and depression. The abnormal levels of DA in the brain are also associated with other neurological and psychiatric disorders including Parkinson's disease, schizophrenia, and the use of substance abuse^{1,2}. Recent research also suggests that characteristic dormant levels of DA and NE in an individual might influence response towards trauma and trigger subsequent development of PTSD. Hence there is an urgent need not only to detect the levels of DA in an individual, but also to monitor the fluctuation in DA level over a considerable period of time, which can lead to early detection of neurodegenerative stress-related disorders. However, detection of DA in physiological fluids is not straightforward as its concentration in central nervous system as well as peripheral fluids such as blood and the renal system is very low (0.01–1 μM for healthy people)^{3,4} which limits their detection by standard analytical methods. The conventional way to determine DA in clinical setup has been carried out by using analytical techniques including fluorescence⁵, surface-enhanced Raman scattering^{6,7}, colorimetric sensor⁸, self-powered triboelectric nanosensor⁹, NMR relaxation method¹⁰, capillary electrophoresis¹¹, spectrophotometry¹², and electrochemical methods¹³⁻¹⁵. Moreover, the detection of DA needs to be carried out reliably at the point of sample collection to reduce patient anxiety and discomfort, especially for the aging population and those with social stress. Hence electrochemical detection of dopamine seems to be more attractive for developing portable dopamine sensor and continuous monitoring system and has been employed in the clinical analysis to determine the concentration of DA owing to ease of operation and cost effectiveness. It also provides enough sensitivity, unlike other biological molecules, such as glucose¹⁶⁻¹⁸. However, electrochemical detection of dopamine under physiological conditions is

challenging, as its presence in the biological fluids is extremely low compared to other interferents such as ascorbic acid, uric acid and glucose which significantly affects selectivity of the biosensors¹⁹⁻²³. The elimination of interference caused by these biomolecules is very critical and numerous efforts have been devoted to nullify the fouling effects and improve sensor's selectivity. To address this issue, it is highly recommended to develop quick, reliable and selective techniques to determine dopamine concentration. The electrochemical oxidation of dopamine has been explored on carbon based electrodes²⁴⁻²⁹. However, the large overpotential required for electrochemical oxidation at carbon electrode, typically around 0.3 V vs Ag|AgCl³⁰, makes the quantitative estimation of dopamine difficult, since other analytes present in the physiological system also undergoes electrochemical oxidation a major interferent for dopamine estimation is ascorbic acid owing to its presence of similar functional groups. One promising approach for reducing the applied voltage is to use chemically modified electrodes, which uses redox mediator on the surface which can enhance electron-transfer kinetics between the electrode and analyte (DA) and thus decrease the operating potential. Several of such modifier materials such as polymers^{31,32} metal nanoparticles^{33,34}, carbon materials^{35,36}, and metal oxides^{37,38} have been used to overcome the problem of interference. For instance, Oshaka *et al.* reported dopamine oxidation in the presence of ascorbic acid at an electropolymerized film of N,N-dimethylaniline, coated on a glassy carbon electrode³⁹. This electrode showed a significant stability without being poisoned by the adsorption of the oxidized product of ascorbic acid on the electrode surface. Another study showed the oxidation peak separation of dopamine and ascorbic acid occurred when a graphite electrode was modified with ultrafine TiO₂ nanoparticles⁴⁰. Dopamine can undergo electrochemical oxidation by following either a 1-

electron or 2-electron pathway yielding a semiquinone or quinone form, respectively as shown in Fig. 1. Based on the molecular structure, dopamine electrooxidation essentially can be viewed as oxidation of the hydroxyl functionality to a ketonic group. Recently, transition metal chalcogenides (TMCs) have shown good electrocatalytic activity for oxidizing hydroxyl functional groups. High lattice conductivity and better electrochemical activity of the transition metal center makes these materials perform as efficient electrocatalysts with lower input energy requirement⁴¹⁻⁴⁵. Although TMCs have been used extensively as water oxidation electrocatalysts (Masud et al. 2018; Swesi et al. 2017; Umapathi et al. 2017), and some for biosensors⁴⁶⁻⁵⁰, however, there has been limited report on using transition metal chalcogenides for non-enzymatic dopamine sensing⁵¹⁻⁵³.

In this article, we have reported a simple binary transition metal selenide, *viz.* CuSe nanostructures for efficient dopamine sensing at extremely low applied potential for the first time. The CuSe nanostructures has been synthesized by hydrothermal and electrodeposition techniques and characterized by diffraction, spectroscopic methods and electron microscopy. The as-synthesized CuSe catalyst exhibits an exceptional performance for dopamine oxidation at low applied potential of 0.18 V vs. Ag|AgCl with superior sensitivity of 26.80 and 8.80 $\mu\text{A mM}^{-1} \text{cm}^{-2}$ for electrodeposited CuSe and hydrothermally synthesized CuSe respectively. This electrocatalyst also exhibits high selectivity for dopamine oxidation in the presence of interfering species, and excellent long-term stability and repeatability.

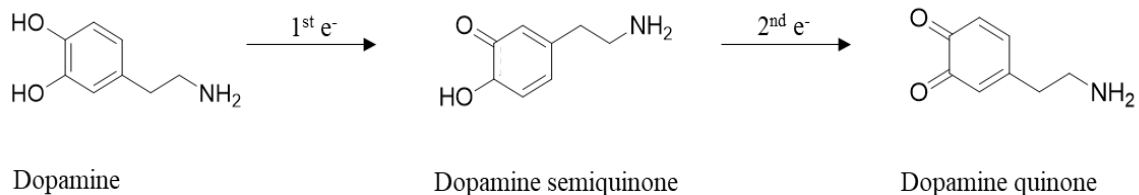


Figure 1. Schematic of dopamine electrooxidation at CuSe electrode surface.

2. MATERIALS AND METHODS

2.1. REAGENTS AND CHEMICALS

All reagents were of analytical grade and were purchased from Fischer Scientific ($\text{CuSO}_4 \cdot 6\text{H}_2\text{O}$, $\text{CuCl}_2 \cdot 6\text{H}_2\text{O}$, KH_2PO_4 , and K_2HPO_4) Acros Organics (SeO_2 , Dopamine, Ascorbic Acid, Glucose and Uric acid), and Alfa Aesar (Hydrazine monohydrate). All chemicals were used as received without further purification. All solutions were prepared by appropriate dilution with deionized water.

2.2. CHARACTERIZATION

Structural analysis was performed using Philip X Pert powder X-Ray diffractometer (pXrd), having a $\text{CuK}\alpha$ (1.5418 Å) radiation source. The average particle size of copper selenide was calculated from the pXrd diffraction peak using the Scherrer equation:

$$L = K\lambda / \beta \cos\theta \quad (1)$$

where L is the particle size, λ is the X-ray wavelength in nanometer (0.15418 nm), β is the peak full width at half maxima of the diffraction peak in radians and K is a constant, normally taken as 0.9.

Morphology of the product was analyzed using FEI Helios Nanolab 600 electron microscope with an accelerating voltage of 10kV and working distance of 5 mm. To obtain high resolution TEM images (HRTEM) and selected area electron diffraction (SAED) the sample was electrodeposited directly on the Cu grid and characterized with Tecnai F20. Energy dispersive spectroscopy was performed to characterize the elemental composition. Additionally, to analyze the surface chemical composition, X-ray Photoelectron spectroscopy (XPS) was performed using KRATOS AXIS 165 spectrometer with an Al X-ray source. All electrochemical measurements were carried out with the Iviumstat workstation. All electrochemical characterizations were performed with a conventional three-electrode electrochemical cell where catalyst on carbon cloth, a graphite rod and Ag|AgCl_(KCl saturated) were used as the working, counter, and reference electrode, respectively.

2.3. SYNTHESIS OF CuSe BY HYDROTHERMAL METHOD

The CuSe nanostructures were synthesized by hydrothermal techniques following a typical procedure as outlined below. CuSO₄·5H₂O (10 mmol), and SeO₂ (5 mmol) were mixed in DI water (10 ml) and the solution was stirred on a magnetic stirrer. About 5 mins later hydrazine monohydrate (0.25 ml) was added. The solution of stirred for another 5 mins and then transferred to 23 ml Teflon – lined steel autoclave, which was sealed and maintained at 145°C for 43 h and then naturally cooled to room temperature. The resulting

black solid was then filtered and washed several times with DI water and ethanol. The solid was dried in an oven maintained at 60°C overnight.

2.4. SYNTHESIS OF CuSe BY ELECTRODEPOSITION

For electrodeposition of CuSe film, the electrolyte was prepared by dissolving CuCl₂·2H₂O (2 mM), SeO₂ (4.5 mM) and KCl (99%)(0.1 M) in deionized water. The pH of the solution was adjusted to 2.5 by using 0.2M HCl solution and the electrolyte was stirred at 300 rpm during deposition. The electrodeposition was carried out in a conventional three-electrode electrochemical cell as mentioned in the apparatus section. To obtain high quality thin film, deposition was carried out at -0.16V vs Ag|AgCl for 10 mins at 60°C. The as-obtained thin film was thoroughly washed with DI water and allowed to dry at room temperature.

2.5. ELECTROCHEMICAL MEASUREMENTS

The effective electrode surface area is critical factor for analyte, i.e. DA adsorption, which in turn shows the electrochemical response. To assess the electrochemical active surface area (ECSA) of CuSe, a double layer capacitance measurement was performed in N₂ saturated 1 M KOH as electrolyte. As shown in Figure. S1, the potential region was selected in non-Faradaic region, where the current corresponds only to the double layer capacitance. A series of current-voltage plots was performed by varying the scan rates from 2.5 – 20 mVs⁻¹. Double layer capacitance, C_{dl} was calculated using the equation (2) and ECSA was obtained from equation (3)

$$I_{dl} = C_{dl} \times v \quad (2)$$

$$\text{ECSA} = C_{\text{dl}} / C_s \quad (3)$$

where C_s is the specific capacitance of the catalyst or the capacitance of the smooth surface of the material per unit area under identical electrolyte conditions. For our studies we have considered the value of C_s to be 0.04 mF cm^{-2} in 1 M KOH solution. Thus the ECSA of the ED-CuSe was estimated to be 1059.74 cm^{-2} and for HT-CuSe it was 890.45 cm^{-2} .

Square wave voltammetry and chronoamperometric measurements were done in 0.1 M phosphate buffer solution at pH 7.0, under continuous stirring in a three electrode setup to measure the oxidation current corresponding to dopamine electro-oxidation. The analytical calculations such as limit of detection (LOD) of the CuSe based DA sensor was calculated according to previously reported equation,^{54, 55}

$$\text{LOD} = S/N \times S_b/m \quad (4)$$

where S/N is the signal to noise ratio, S_b refers to the blank standard deviation and m is the slope of the calibration curve. For this study S/N value was selected as 3.

The CuSe nanostructures were also used for analyzing dopamine content in urine samples collected from voluntary healthy individuals using standard addition methods⁵⁶. Typically, the urine sample was diluted 10 times with 0.1 M PBS to overcome the unnecessary interference of waste materials. To do the recovery study, the urine solution was spiked with a known concentration of DA. In order to ascertain the reproducibility, two batches of urine samples with same concentration of DA were prepared. Control solution of different concentrations of DA ranging from $10 \mu\text{M}$ to $50 \mu\text{M}$ was prepared and the current-voltage response of the known concentrations of DA along with the urine samples was recorded. This procedure was repeated twice to check the robustness and reliability of the catalyst.

3. RESULT AND DISCUSSION

To confirm the structure and composition of the product, pXRD analysis for both electrodeposited and hydrothermally synthesized CuSe was carried out as shown in the Fig. 2A. The hydrothermally synthesized CuSe shows higher degree of crystallinity and, all the diffraction peaks can be assigned to CuSe phase, which is consistent with standard pattern (PDF: 00-006-0427). The average crystallite size of the as-synthesized CuSe was calculated to be 10-20 nm by Scherrer's equation (1). On the other hand, pXRD pattern for electrodeposited CuSe on Au-glass (Figure. S2) indicated lesser degree of crystallinity. It has been reported previously that electrodeposition often yield poorly crystalline or even amorphous products. Other researchers have reported that electrodeposited CuSe shows amorphous nature, where the crystallinity was greatly affected by the deposition potential and time in the same electrolyte composition ⁵⁷.

The crystal structure for CuSe is analogous to a mineral named *Klockmannite* showing a lattice structure as shown in the inset of Figure. 2A. It crystallizes in a hexagonal $P6_3/mmc$ space group where Cu atoms (brown spheres in Figure. 2A inset) are present in two different coordinations, trigonal planar forming $CuSe_3$ moieties and tetrahedral $CuSe_4$ species. The trigonal planar $CuSe_3$ layers are sandwiched between the $CuSe_4$ tetrahedral layers, while the tetrahedral layers are connected through formation of Se-Se bonds along the *c*-axis. The Cu(1)-Se has a bond length of 2.275 Å in the trigonal planar coordination, while Cu(2)-Se has a bond length of 2.408 Å in the tetrahedral coordination. As expected from the coordination geometry, the Cu(1)-Se are shorter compared to Cu(2)-Se suggesting that Cu(1)-Se might have higher bond strength. The availability of different coordination

geometry around the Cu center and more importantly presence of lower coordination geometry can enhance the availability of additional coordination sites and formation of reaction intermediates through oxidative insertion of hydroxyl (OH^-) anion along with coordination expansion. Such factors will be very critical for the adsorption of dopamine through its OH functional group and subsequent oxidation to dopamine quinone on the catalyst surface.

The surface elemental composition of the CuSe catalyst was studied through X-ray photoelectron spectroscopy (XPS) as presented in Figure. 2B and C. Deconvoluted high resolution Cu 2p spectrum of ED-CuSe can be fitted to peaks at 932.2 and 952.3 eV corresponding to Cu^+ $2p_{3/2}$ and $2p_{1/2}$ and 934.4 and 954.6 eV for Cu^{2+} $2p_{3/2}$ and $2p_{1/2}$, respectively, which also confirmed the presence of mixed oxidation states for Cu. The satellite peaks were observed at 942.4 and 962.6 eV possibly due to overlapping between the Cu and Se. Similarly, oxidation states of Cu in HT-CuSe could be assigned at 932.3 and 952.2 for Cu^+ $2p_{3/2}$ and $2p_{1/2}$ and 934.0 and 954.4 for Cu^{2+} $2p_{3/2}$ and $2p_{1/2}$ respectively. The shakeup satellite peaks of Cu 2p was observed at 943 and 963.4 eV. From the XPS spectra it was evident that Cu was present in mixed oxidation states of +1 and +2 in both sample preparations. Presence of such mixed oxidation states for Cu has been reported previously in electrodeposited and CVD synthesis of copper selenide ⁴¹. The percentage of $\text{Cu}^{+1}/\text{Cu}^{2+}$ ratio was calculated by integrating the area under the peaks of the deconvoluted XPS spectra. The as synthesized catalyst consisted of 75:25 of Cu^+ and Cu^{2+} , respectively. The deconvoluted Se 3d XPS spectra for ED-CuSe and HT-CuSe has been shown in the inset of Figure. 2B and C. Both samples showed peaks at 54.1 and 55.0 eV for Se $3d_{3/2}$ and $3d_{5/2}$ respectively. A weak shoulder was also visible at 56.8 eV for ED-CuSe due to

the surface oxidation of Se to SeO_2 . These values are in accordance to the previously reported XPS of CuSe ⁴¹.

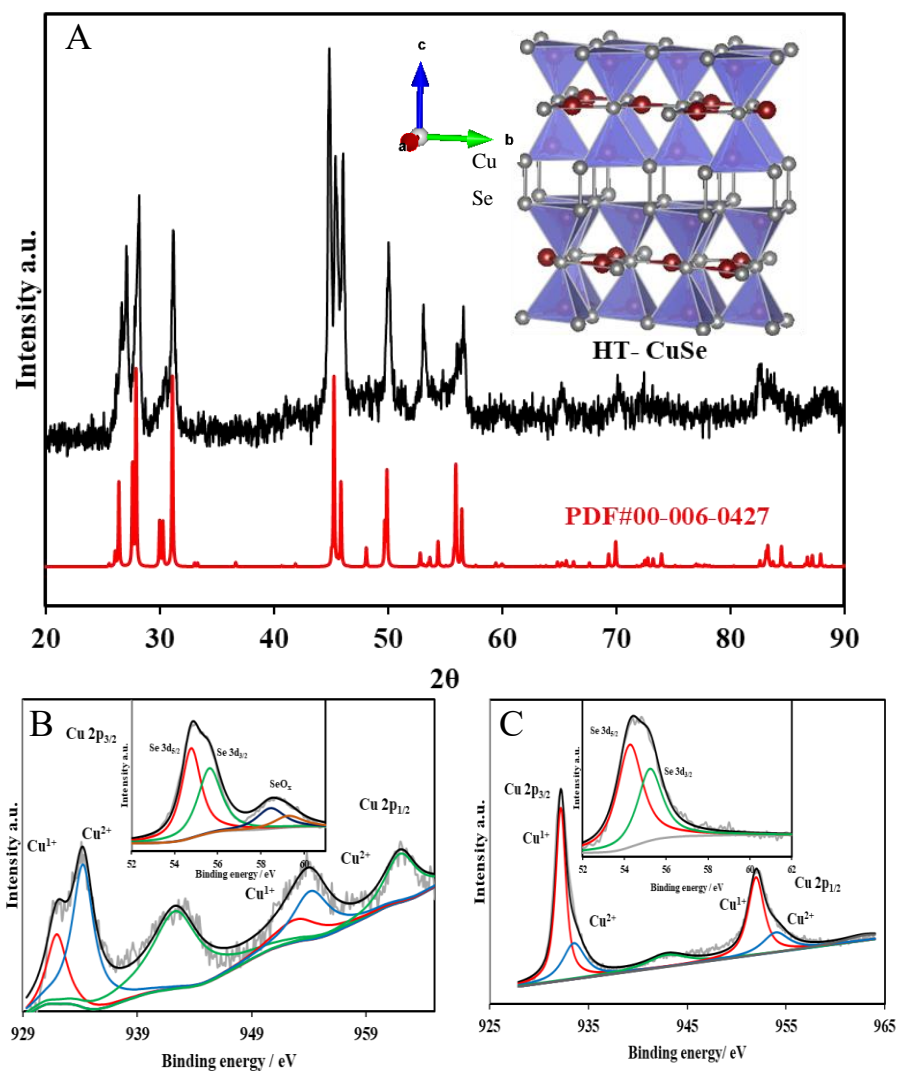


Figure 2. (a) PXRD pattern and deconvoluted XPS spectra of Cu 2p from (b) electrodeposited and (c) hydrothermally synthesized CuSe.

The morphology of ED-CuSe and HT-CuSe samples were studied by scanning electron microscopy (SEM) as shown in Figure. 3A and 3C. It is clearly seen that ED-CuSe exhibits a nanoflake like morphology where the surface of the flakes are wrinkled and crumpled. On closer inspection it was observed that most of the nanoflakes had a hexagonal cross-section. Such polygonal shape of the nanoflakes can be related to the crystallographic structure by considering possibilities of oriented growth along a preferred lattice direction. The inset of Figure. S3A shows an illustration of the evolving cross-section for a crystallite growing along the *c*-direction. As can be seen from the inset, if CuSe nanocrystallite grows along the *c*-direction, the resulting nanoflakes can have a hexagonal cross-section. However, to properly identify the preferred direction of growth, one needs to do a texturing study on a thin film deposited on a single crystalline substrate. To support our claim for high efficiency of this catalyst, we have also calculated the roughness factor using ECSA and the geometric area. The ED-CuSe samples have high roughness factor of 1630.36, which is essential for a better exposure of the catalytically active sites to the electrolyte. The HT-CuSe powder on the other hand also showed nanostructured morphology with a variable size ranging from 8 nm to 40 nm and a mean particle size of 22 nm. These granular shaped nanoparticles have a roughness factor of 1369.94, which is very close in value to that obtained for ED-CuSe. The elemental composition of the nanostructures was also confirmed through energy dispersive x- ray spectra (EDS) taken at several regions of the sample to confirm uniformity of the composition. EDS data reveals that the atomic ratio between Cu:Se to be close to 0.48:0.52 and 0.47:0.53 for ED and HT-CuSe, respectively, confirming the composition to be CuSe. The elemental mapping of ED-CuSe also revealed uniform distribution of Cu and Se throughout the film, further confirming that the CuSe

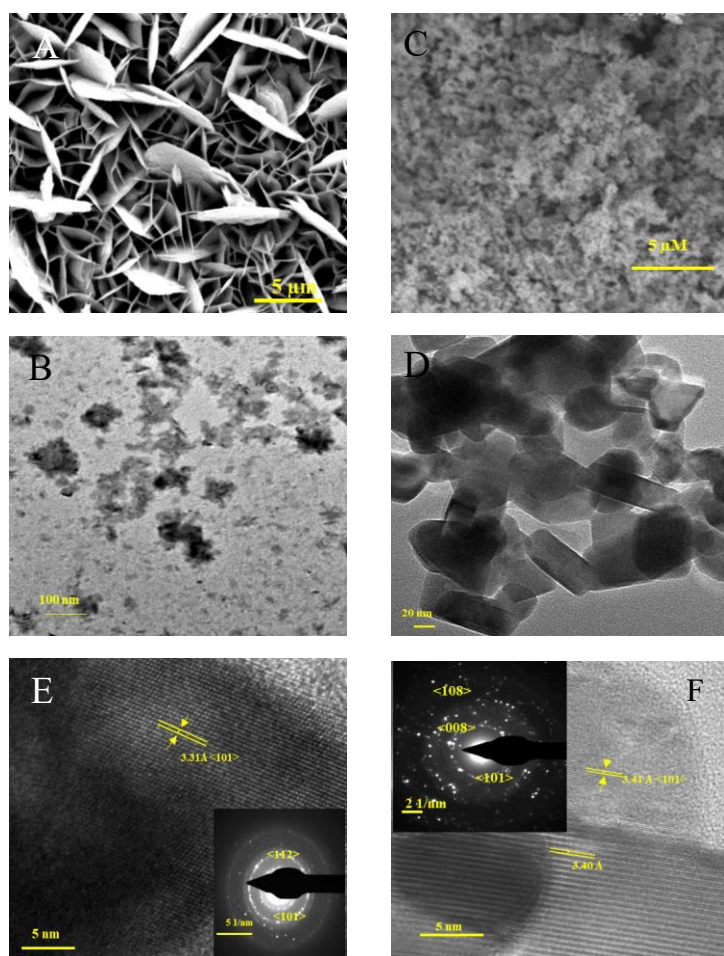


Figure 3. SEM images of (a) ED-CuSe and (c) HT-CuSe. TEM images of (b) ED-CuSe and (d) HT-CuSe. HR-TEM images of (e) ED-CuSe and (f) HT-CuSe.

confirming the composition to be CuSe. The elemental mapping of ED-CuSe also revealed uniform distribution of Cu and Se throughout the film, further confirming that the composition was indeed CuSe which was critical characterization given the amorphous nature of the deposit (Figure. S3B).

Transmission electron microscopy (TEM) was also performed to investigate the microstructural details as shown in Figure. 3B and D. It can be seen from Figure. 3B, that

ED- CuSe nanoparticles had a smooth surface with nearly circular shapes with a particle size ranging from 10-20 nm. Alternatively, HT-CuSe (Figure. 3D) showed agglomeration of nanostructures due to high surface energy. These nanoparticles have well defined morphology with a particle size varying from 25-50 nm. High resolution TEM (HRTEM) of ED-CuSe (Figure. 3E) showed clear lattice fringes with a d -spacing of 3.31 Å which corresponds to (101) lattice spacing of CuSe. The crystalline nature of HT-CuSe was also confirmed with HRTEM which showed lattice fringes with a d -spacing of 3.41 Å corresponding to (101) lattice planes as shown in Figure. 3F. The crystallinity of these nanostructures was further confirmed through selected area electron diffraction (SAED) patterns as shown in insets of Figure. 3E and F. The SAED patterns revealed polycrystalline nature of both ED-CuSe and HT-CuSe where the diffraction spots could be indexed to (101), (112), and (108) lattice planes for ED-CuSe and HT- CuSe, respectively.

3.1. ELECTROCHEMICAL OXIDATION OF DOPAMINE

As illustrated in Figure. 1 above, dopamine can undergo partial or full oxidation following one electron or two electron oxidation pathway to form semi-quinone or quinone, respectively. The CuSe samples synthesized above was tested for electrocatalytic dopamine oxidation in 0.1M phosphate buffer solution (PBS). The modified electrode containing ED-CuSe or HT-CuSe was used as electrode and cyclic voltammograms (CVs) were measured in N₂ saturated PBS in presence of 0.1 mM dopamine (DA). Figure. S4 shows the electrocatalytic response under various scan rates. When the scan rate was increased from 5 mV . s⁻¹ to 75 mV . s⁻¹, the oxidation peak currents for ED-CuSe and HT-CuSe showed a gradual increase as expected, which can be observed as a positive shift in

the anodic region and an equivalent negative shift in the cathodic region. The corresponding calibration plots derived from the peak currents vs the scan rate showed a linear correlation ($R^2= 0.9954$ and 0.9986 for ED-CuSe and HT-CuSe respectively) which confirms that the electrooxidation/reduction of DA is indeed a diffusion controlled process for both ED-CuSe (Figure. S4A) and HT-CuSe (Figure. S4B). Interestingly, ED-CuSe showed a higher oxidation peak current compared to HT-CuSe which may be attributed to the growth of the active catalyst directly on the electrode surface, larger surface area with porous network, high surface energy and enhanced electron transfer between ED-CuSe surface and the electrolyte.

Square wave voltammetry (SWV) is one of the best techniques for testing sensing efficiencies and can provide better sensitivity and peak resolution. Figure. 4A and 4B shows the SWV curves measured for different concentrations of DA ranging from $1 \mu\text{M}$ – $640 \mu\text{M}$ of DA on ED-CuSe and HT-CuSe respectively. From the CV and SWV plots it can be observed that the oxidation of DA occurs at 0.18 V vs Ag|AgCl which is 200 mV less than earlier reports^{58,59}. The corresponding anodic peak potential vs DA concentration plots show two linear regions, $0.25 \mu\text{M} - 10 \mu\text{M}$ and $20 \mu\text{M}$ to $320 \mu\text{M}$ with the linear regression equations of $I_{\text{pa}} (\mu\text{A}) = 6.06 + 254.74 C_{\text{DA}} (\mu\text{M})$ and $I_{\text{pa}} (\mu\text{A}) = 0.507 + 361.59 C_{\text{DA}} (\mu\text{M})$ [where, I_{pa} = anodic peak current, C_{DA} = concentration of DA added to the electrolyte] for ED-CuSe (Figure. S5A), respectively. Similarly the linear regression equations of $I_{\text{pa}} (\mu\text{A}) = 5.629 + 152.67 C_{\text{DA}} (\mu\text{M})$ and $I_{\text{pa}} (\mu\text{A}) = 0.415 + 193.34 C_{\text{DA}} (\mu\text{M})$, was observed for HT-CuSe (Figure. S5C) for the two linear regions.

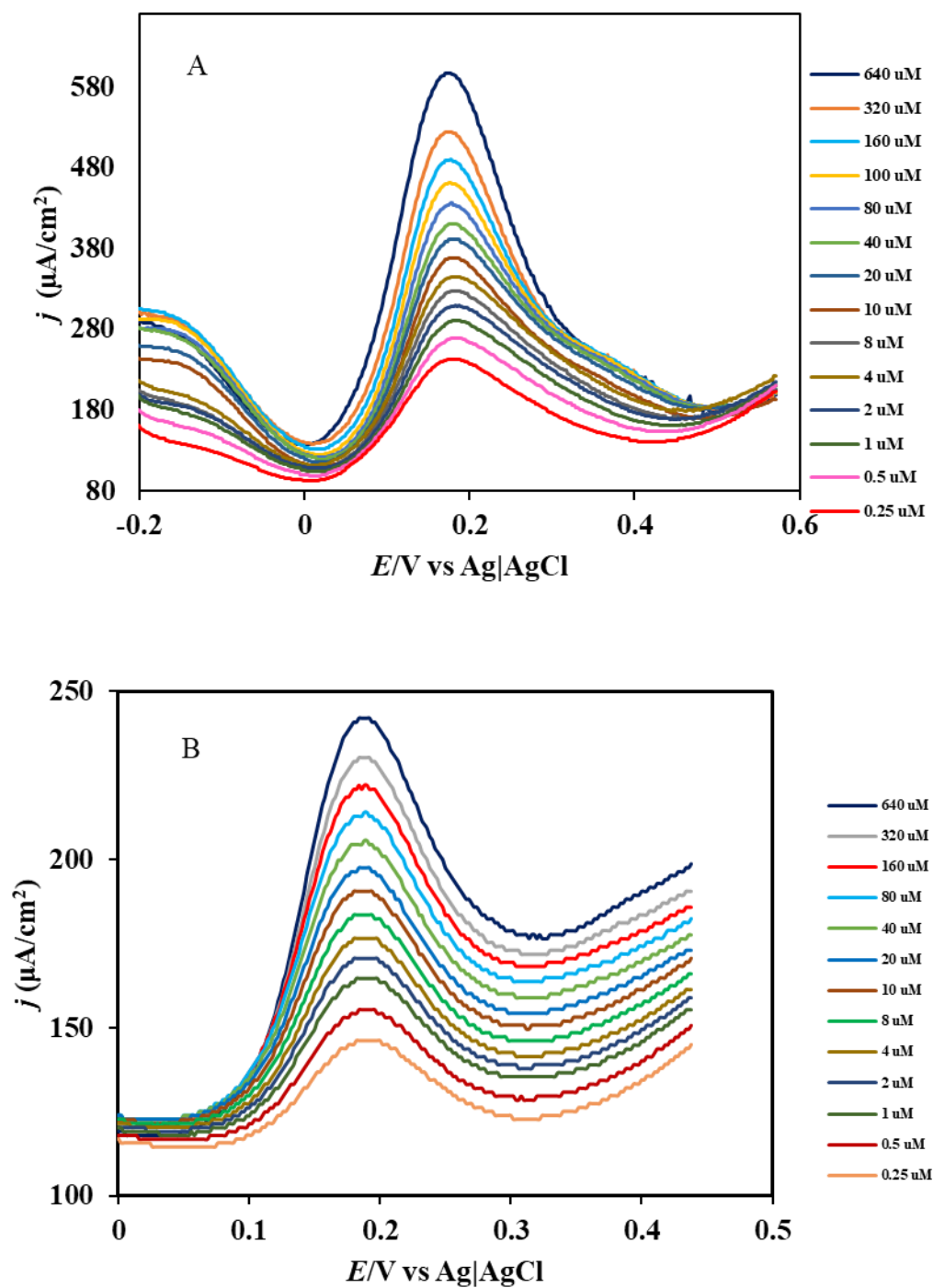


Figure 4. SWV plots of (a) ED-CuSe and (b) HT-CuSe in 0.1 M PBS solution in the presence of increasing concentrations of DA.

The higher slopes illustrates faster increase of oxidation current and the high sensitivity of these electrocatalyst towards dopamine oxidation. While both ED-CuSe and HT-CuSe shows strong response to wide range of concentrations of DA, the ED-CuSe however, exhibits a more well-defined oxidation peak even at lowest concentration of DA. This difference between the HT-CuSe and ED-CuSe modified electrodes might be attributed to the electrode preparation. In HT-CuSe, the hydrothermally synthesized powder is assembled on the electrode with the help of Nafion solution. Such treatment reduces the exposure of active sites of the material as well as introduces contact resistance between the physically adhered catalytic powder and electrode ⁶⁰.

To further confirm and quantify the sensitivity of our catalyst, chronoamperometric detection of DA was performed by adding different concentration of DA to the electrolyte at a constant applied potential of 0.18 V vs Ag|AgCl. Figure. 5A and B shows the representative chronoamperometric *i* vs *t* curve showing response of CuSe to successive addition of various concentrations of DA. Figure. 5C and D shows the calibration plot obtained from the linear fit of the extracted peak current vs concentration of DA in the range 50 pM to 20 μM with a regression equation of $I_{pa} (\mu A) = 26.80 + 84.05 C_{DA} (\mu M)$ with a correlation coefficient of 0.9987 for ED-CuSe and 50 nM to 20 μM $I_{pa} (\mu A) = 8.80 + 21.71 C_{DA} (\mu M)$ with a correlation coefficient of 0.99767 for HT-CuSe (Figure. S6 shows the linear range of 40- 320 μM ED-CuSe and 40- 640 μM HT-CuSe). The sensitivity (S) could be estimated from the linear fit in the low concentration region, and it was calculated to be 26.80 $\mu A \mu M^{-1} cm^{-2}$ and 8.80 $\mu A \mu M^{-1} cm^{-2}$ for electrodeposited and hydrothermally synthesized CuSe, respectively.

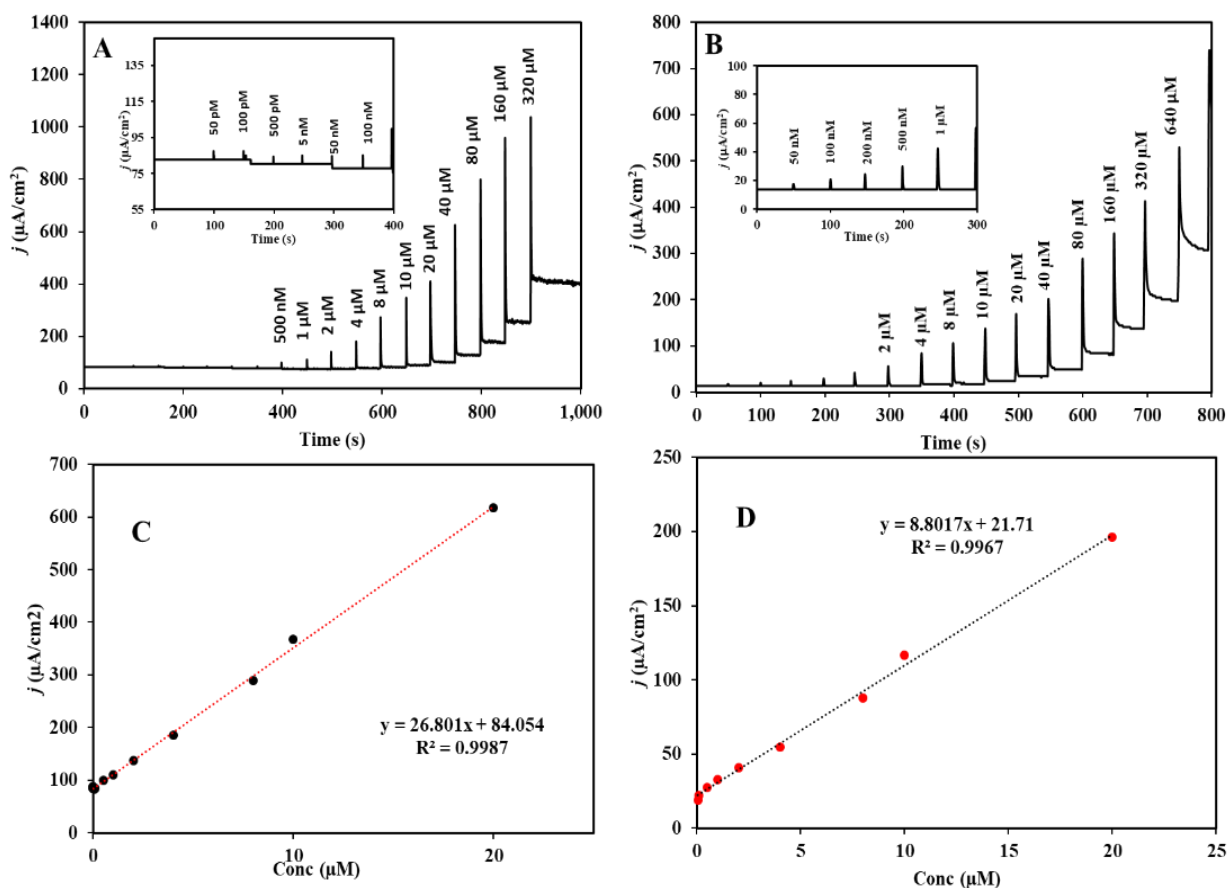


Figure 5. Chronoamperometric responses of the (a) ED-CuSe and (b) HT-CuSe to successive additions of DA into stirring 0.1M PBS electrolyte. The working potential was set at 0.18 V vs Ag|AgCl, and the DA concentrations ranged from 50 pM to 320 μM for ED-CuSe and 50 nM to 1 mM for HT-CuSe for sequential addition. Inset shows magnified portion of the amperometric response for lower concentrations. (c) and (d) shows the peak current vs concentration of dopamine for ED and HT-CuSe respectively, leading to estimation of sensitivity of the device.

The limit of detection (LOD) could be estimated by considering a signal to noise ratio (S/N) of 3, and a LOD of 98 nM and 68 nM was obtained for ED-CuSe and HT-CuSe, respectively. It must be noted here that these are the lowest LOD reported for DA sensors making these the most efficient. The detection and quantification of dopamine in

pathological samples suffer from the challenge that the level of dopamine vary within a wide range and from person to person. Specifically, in patients suffering from mental health disorder can have excessively low amounts of dopamine or fluctuating dopamine levels making it harder to detect with standard analytical techniques. Hence a low LOD for dopamine sensor is critical for rapid diagnosis of mental health condition in susceptible individuals. Furthermore, on comparing the performance of the two catalysts, it was observed that ED-CuSe has higher sensitivity while HT-CuSe has lower LOD. Again this may be due the presence of Nafion binder in HT-CuSe modified electrode which can interfere and lower the sensing capability of nanoparticle composite.⁶⁰ However, electrodeposited CuSe is free of any binder and surface is more sensitive towards DA adsorption and subsequent oxidation. Table 1 compares the LOD values for the most sensitive catalyst reported towards electrochemical oxidation of DA with the performance of CuSe reported in this article. It can be clearly seen that the CuSe reported here is one of the most efficient dopamine sensors irrespective of the method of synthesis. As shown in the amperometric increase of current upon successive addition of various concentrations of DA, a significant and fast current response is observed at low applied potential of 0.18 V vs Ag|AgCl. The current reached 98% of steady state current density in 1 sec for both ED and HT CuSe (Figure. S7) showing that the response time is very fast with these sensors. Such fast response time and high sensitivity with low LOD makes these sensors highly applicable for onsite detection and real-time monitoring of dopamine levels.

It should be noted that the sensitivity and LOD of the CuSe based sensor reported here is superior to other non-enzymatic based catalytic sensors reported previously.^{61, 62}

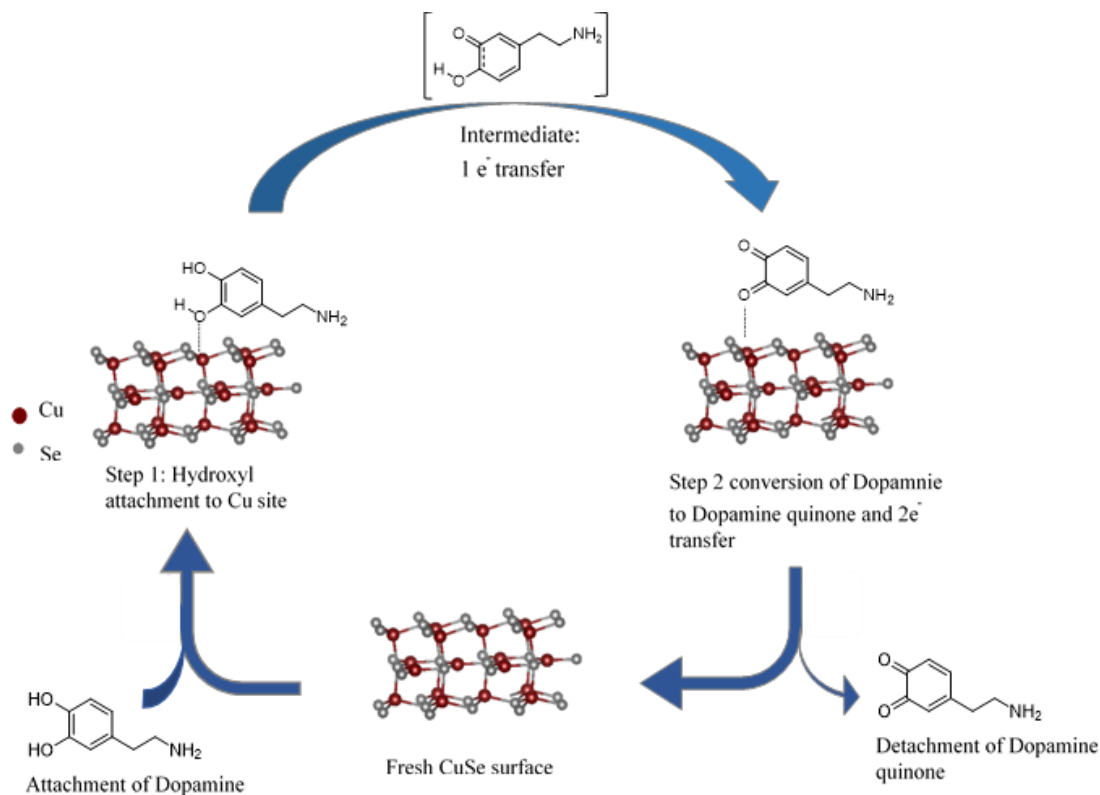


Figure 6. Scheme illustrating catalytic conversion of dopamine to dopamine quinone on CuSe substrate.

The highly efficient dopamine sensing on the surface of CuSe can be possibly understood by following the mechanism of dopamine oxidation on the catalyst surface. As shown in Figure. 1, the dopamine oxidation involves conversion of the hydroxyl (-OH) functional group to ketonic (=O) group. It can be expected that such conversion is initiated by the adsorption of the analyte (DA) on the catalyst surface through the coordination of -OH functional group of the molecule (Figure. 6) to the catalytically active transition metal site, i.e. Cu. The transition metal site can undergo local site oxidation to accommodate attachment of such electron rich Lewis base, and hence it can be envisioned that the redox potential of the transition metal site will have a large influence on the ease of -OH group

attachment on the surface, which is also reflected in the applied potential needed for dopamine oxidation. Typically, the -OH group attachment on the active site will occur at lower applied potential if the local site oxidation can occur at low potential. Previously it has been shown that the local site oxidation and adsorption of -OH groups to the transition metal sites can be altered by changing the ligand coordination around the active site.⁶³ Typically reducing the electronegativity and increasing covalency around the active site leads to reduction of the local site oxidation potential, and more facile attachment of the -OH group on the surface at low applied potential.^{43, 64} Hence it can be expected that the reduced electronegativity and increased covalency of Se compared to O can make the analyte adsorption on the selenide-based catalyst surface occur at a lower anodic potential compared to the oxides, thereby lowering the operating potential of the sensor. Electron transfer between the electrode (catalyst)-electrolyte occurs following the analyte adsorption on the surface leading to oxidation of dopamine to the dopamine quinone form as shown in Scheme 2. Such electron transfer will be facilitated by the higher conductivity of the catalyst composite. The increased covalency of the anionic ligand also helps in increasing the conductivity by reducing the bandgap in the selenides. The oxidized molecule can readily desorb from the catalyst surface while the active site is regenerated. Furthermore, the coordination geometry around the catalytically active site (Cu) can also facilitate analyte adsorption. As described above, the crystal structure of CuSe contains two coordination environments for Cu, namely a trigonal and tetrahedral coordination. Such lower coordination numbers along with a layered geometry can lead to facile attachment of molecules such as dopamine. Lastly, higher surface area of the CuSe nanostructure-based films revealing thin edges of nanoflakes enhances exposure of the

active sites to the analyte leading to higher efficiency of analyte sensing through direct oxidation of dopamine to dopamine-quinone. Therefore, the combined effect of morphology, porosity, coordination geometry and higher conductivity of the catalyst composite along with increased anion covalency leads to oxidation of dopamine on the catalyst surface occur at lower applied potential producing higher current density which increases the sensitivity of the catalyst, while lowering the detection limit. It must also be noted that ED-CuSe shows significantly higher sensitivity which can be explained by the fact that the electrodeposited sample is directly grown on the catalyst surface which reduces the contact resistance, as has been observed previously.⁶⁵

One of challenges in detection of DA is the interference from other chemical compounds commonly found in bodily fluids such as ascorbic acid (AA), uric acid (UA), glucose (GC) and sodium chloride (NaCl). All of these compounds can oxidize near the oxidation potential of DA. Hence to evaluate the selectivity of CuSe towards dopamine oxidation at low applied potential, an amperometric experiment was conducted at a constant applied potential of +0.18 V vs Ag|AgCl in 0.1 M PBS solution, where the DA and other interfering compounds were added successively to the same electrolyte. As shown in Figure. 7A and B, ED-CuSe and HT-CuSe modified electrodes shows a higher current response upon addition of 0.05 mM DA while successive additions of 0.5 mM UA, GC and NaCl did not show any change in current output. However, addition of 0.5 mM ascorbic acid showed a small current response. It should be noted the concentration of AA was 10 times higher than the DA concentration.

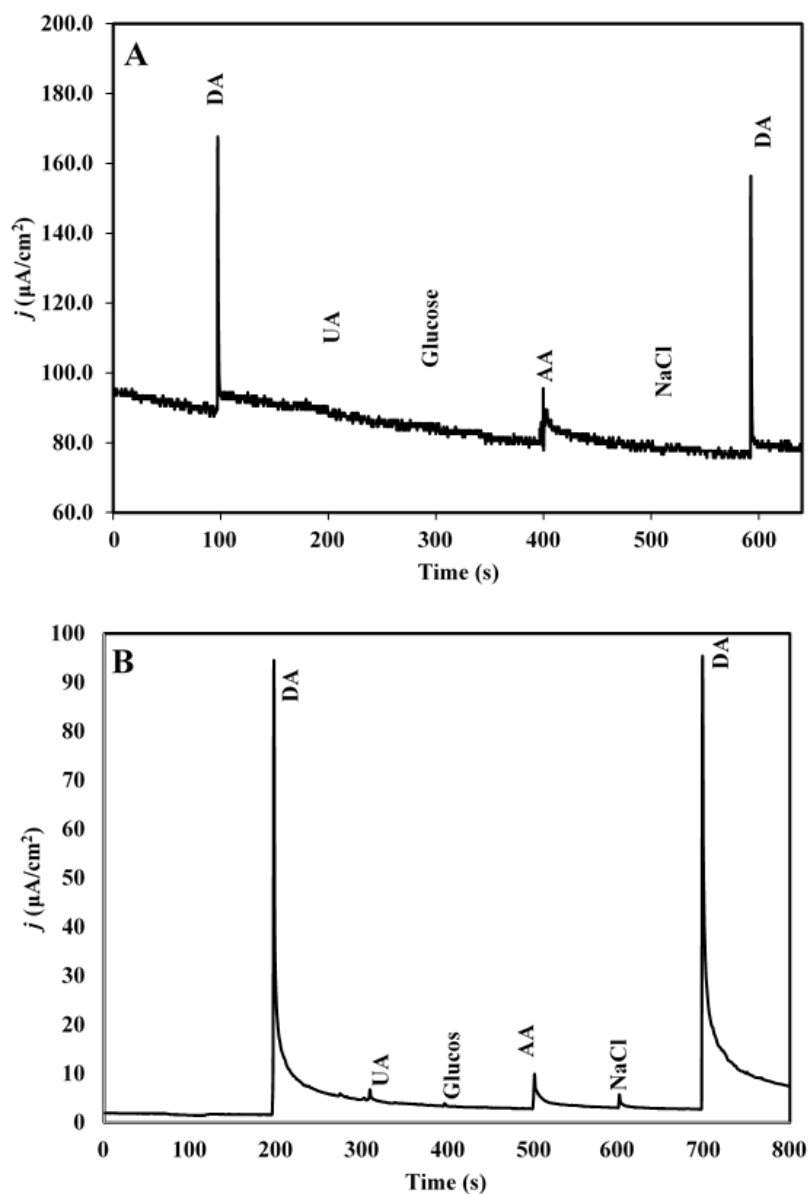


Figure 7. Amperometric responses of the (a) ED-CuSe and (b) HT-CuSe in various interferents.

Further addition of DA continues to emulate a response, indicating the robustness of the catalyst towards selectivity at a lower applied potential and in the presence of higher concentrations of interfering chemicals. In order to investigate the selectivity of this sensor

towards dopamine oxidation further, we attempted to understand the oxidation profile of dopamine in presence of ascorbic acid and uric acid. Since ascorbic acid and dopamine has similar -OH functionalities, the selectivity of a catalyst is also reflected by its ability to spatially separate the oxidation peaks of DA and AA in the SWV plot. Hence, the oxidation potentials of DA, AA and UA in a mixture was determined with ED-CuSe on carbon cloth where the concentrations was 40 μM for DA, and 300 μM for AA and UA each (Figure. S8). Three anodic peaks at 0.032, 0.185 and 0.405 V vs Ag|AgCl were observed for the oxidation of AA, DA and UA, respectively. It was observed that the oxidation potential of ascorbic acid was lower than the oxidation potential of DA as has been previously reported⁵⁹. A separation of the oxidation peak potentials of DA and AA by 0.153 V as observed on CuSe surface is significant for selective detection of these biomolecules. This observation of DA and AA oxidation was similar to other reports⁶⁶⁻⁶⁸. The potential difference between DA and UA oxidation is even larger (0.220 V) signifying that the CuSe surface indeed offers higher selectivity for dopamine sensing even in the presence of higher concentrations of other biomolecules with similar structure. Moreover, it also shows that CuSe can be also used to detect ascorbic acid and uric acid, *albeit* at different applied potential, thus increasing the versatility of this sensor.

The reproducibility and consistency tests were performed for four different batches of electrodes synthesized under similar conditions. All these electrodes exhibited high sensitivity of 26.70, 26.72, 26.87 and 26.85 $\mu\text{A } \mu\text{M}^{-1} \text{cm}^{-2}$ for electrodeposited CuSe and 8.78, 8.75, 8.89 and 8.79 $\mu\text{A } \mu\text{M}^{-1} \text{cm}^{-2}$ for the hydrothermally synthesized CuSe. The calculated standard deviation for the sensitivity is 0.08% and 0.06% for ED-CuSe and HT-CuSe, which proves the high reliability and reproducibility of these sensors toward DA

detection (Figure. S9). The long term stability was evaluated by CV plots measured for 100 cycles at a scan rate of 50 mVs^{-1} in presence of 0.1 mM DA in 0.1 M PBS electrolyte. As shown in Figure. S10, the DA oxidation showed similar current density for 100 cycles, where 89% of the peak current intensity was retained, however upon addition of freshly prepared DA of the same concentration the catalyst showed an almost identical CV (inset of Figure. S10) with identical current density compared to the pristine CuSe electrode. This CV test verified that there is no surface poisoning of the catalyst with repeated sensing events or decline in the activity for long term application.

3.2. DOPAMINE DETECTION IN PHYSIOLOGICAL SAMPLE

To check the practical application of CuSe towards dopamine sensing in real physiological samples, the DA levels were estimated using urine samples from healthy individuals following protocols reported earlier.⁶⁹ Specifically, 10 ml of urine was collected and diluted 10 times with 0.1 M PBS to overcome the interference from unwanted organic molecules. SWV was measured in the potential range from -0.2 to 0.6 V vs Ag|AgCl with the CuSe-modified electrode setup as described above. Since no noticeable oxidation peaks were detected, to evaluate the accuracy of the method, a known concentration ($35 \text{ }\mu\text{M}$) of standard DA solution was added to the electrolyte and was detected by calibrating the measured current density against the sensitivity of the sensor. The recovery percentages were calculated based on determined DA concentrations which is summarized in Table 2. The calculated results show good recovery ($\sim 100\%$) and respectable standard deviation which is less than 1% , confirming the promising potential for practical application of this CuSe-based sensor for DA detection.

4. CONCLUSION

CuSe nanostructures has been identified as a highly efficient electrocatalyst for dopamine oxidation. CuSe nanostructures were synthesized by two methods, namely direct electrodeposition on carbon cloth and hydrothermal technique. Interestingly, the synthesis method does not affect the activity of CuSe to oxidize and sense dopamine. The high sensitivity ($26.8 \mu\text{A } \mu\text{M}^{-1} \text{cm}^{-2}$ for ED and $8.80 \mu\text{A } \mu\text{M}^{-1} \text{cm}^{-2}$ for HT) at a low applied potential of $+0.18 \text{ V vs Ag|AgCl}$, low detection limit (98 nM for ED and 68 nM of HT), short response time (1 s), makes these sensors lucrative for practical applications in real-time continuous dopamine monitoring systems as well as point-of-care detection units. The CuSe based non-enzymatic dopamine sensor has impressive selectivity for dopamine sensing, long-term stability and repeatability. Since dopamine is being an important neurochemical, its detection and monitoring has become the center of attraction for diagnosis of mental health diseases this research can pave the path to designing portable dopamine sensing modules and will help to understand the correlation between dopamine as a biomarker and progression of neurodegenerative disorder.

Table 1. Comparison of analytical performance of ED and HT CuSe with previously reported carbon and metal nanoparticles based dopamine electrochemical sensors.

Electrode	Limit of Detection (μM)	Linear Range(μM)	Sensitivity ($\mu\text{A } \mu\text{M}^{-1} \text{ cm}^{-2}$)	Peak potential (V vs Ag AgCl)	Reference
ED-CuSe	0.068	50 pM – 20; 40-320	26.80	0.18	This work
HT-CuSe	0.098	0.050-20; 40-640	8.80	0.18	This work
AuNS/GCE	0.28	2–298	-	0.22	70
TC8A/Au	0.5	1–100	-	0.2	71
F-CuInS ₂ QDs	0.2	0.5–40	-	-	72
AgNP/SiO ₂ /GO/GC	0.26	2–80	-	0.2	73
Fe ₃ O ₄ /Chit	0.006	0.02 – 75	-	-	74
TiO ₂ /CeO ₂ / sol-gel/CF	0.04	0.1-180	-	-	75
Au/GO/ITO	1.28	0.1–30	0.53	0.24	76
NiO-RGO/ITO	1	1–60	1.04	0.2	77
N-rGO/MnO/GCE	3	10–180	0.09	0.51	78
PABSA-rMoS ₂	1	1–50	0.22	0.15	79
Graphene	2.64	4-100	-	-	80
Graphene-LDH	0.3	1-199	-	0.195	81

Table 2. DA determination in urine samples with ED-CuSe.

Sample	Initial DA	Added DA	Detected DA	Recovery	Std Deviation (3 runs)
Individual 1	Not detected	35	34.85	99.44	0.64
Individual 2	Not detected	35	35.22	100.23	0.86

SUPPORTING INFORMATION

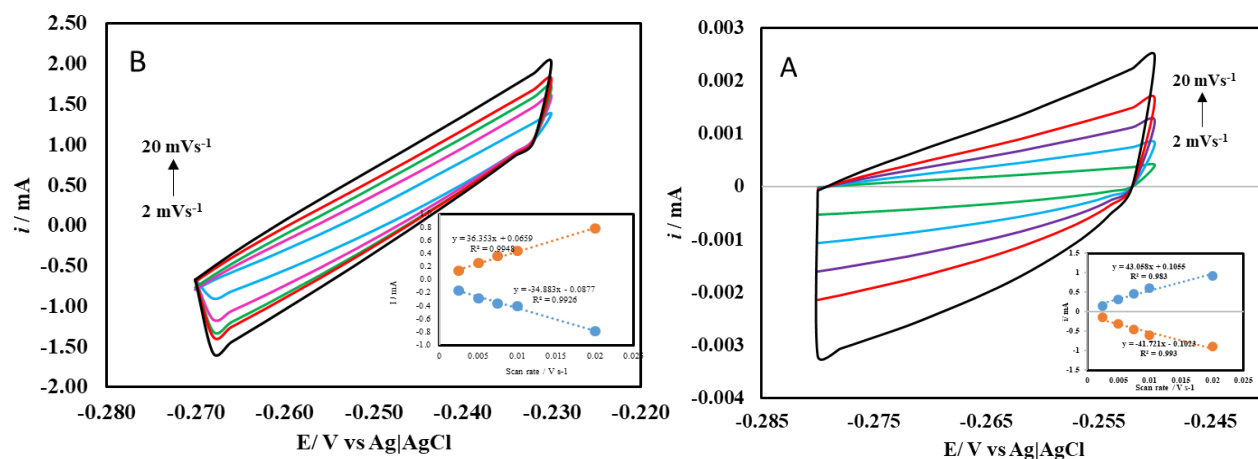


Figure S1. Electrochemically active surface area analysis of (A) ED-CuSe and (B) HT-CuSe at different scan rates. Inset in (A) and (B) linear fitting of capacitive currents vs. scan rate.

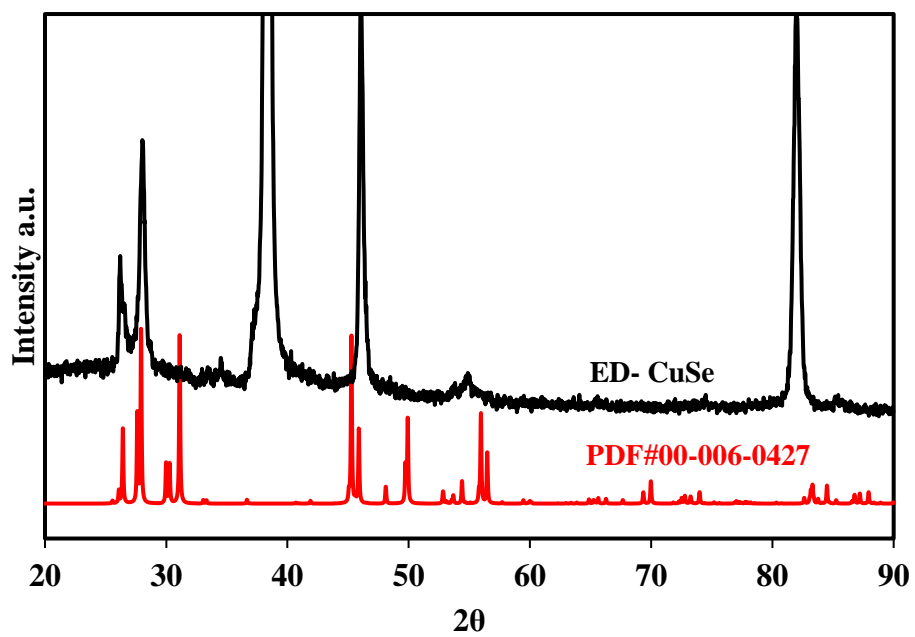


Figure S2. PXRD pattern of electrodeposited, ED-CuSe along with the reference CuSe (PDF#00-006-0427).

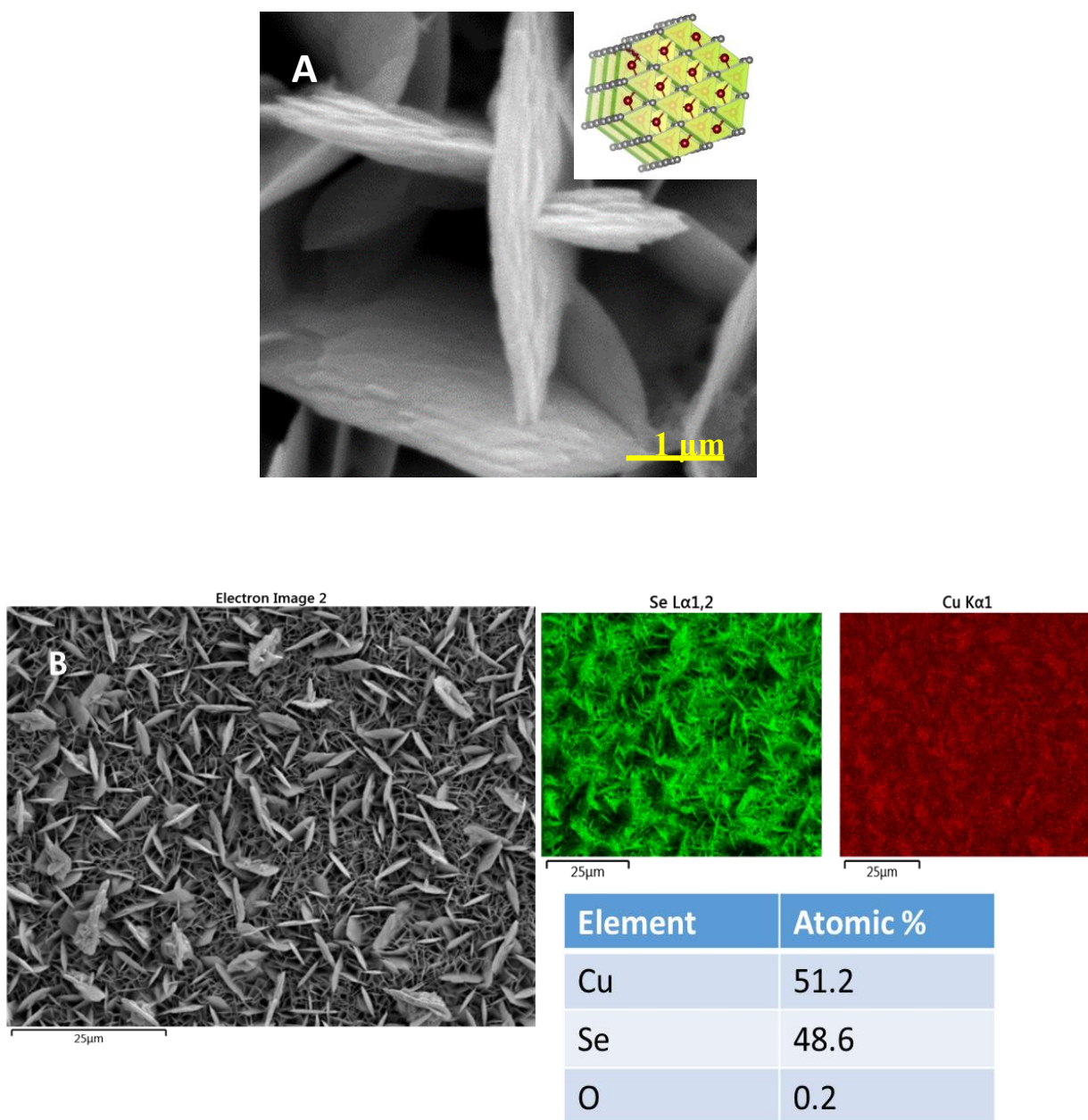


Figure S3. (A) SEM image of ED-CuSe at 1 μm magnification. Inset shows possible layer stacking along c axis following preferred direction of growth [gray – Se, red - Cu]. (B) Elemental mapping of ED-CuSe with atomic percentage distribution.

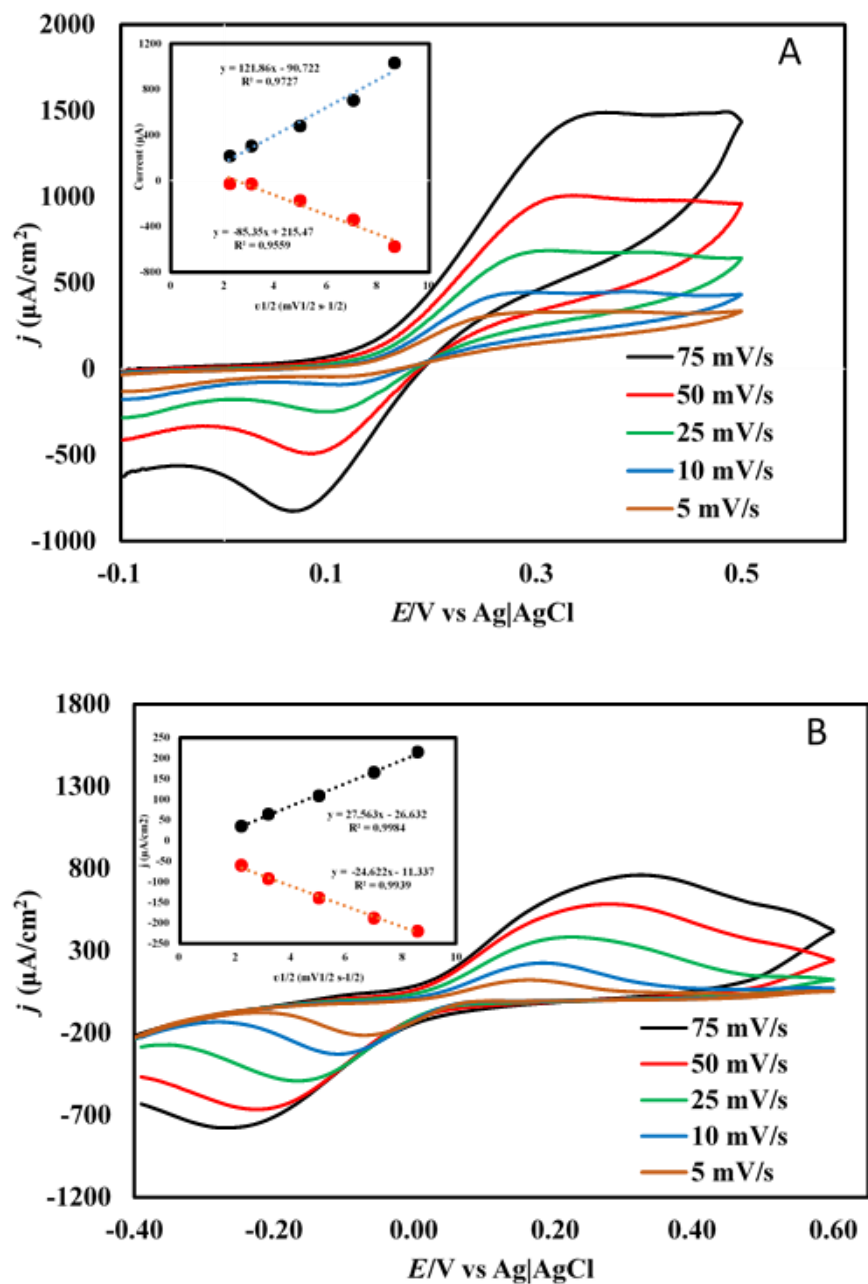


Figure S4. (A). CV curves of ED-CuSe with scan rates ranging from 5 to 75 mV/s. Inset shows the calibration plots of the redox peak currents (I_{pa} & I_{pc}) from ED-CuSe with the square root of the scan rates. (B) CV curves of HT-CuSe with scan rates ranging from 5 to 75 mV/s. Inset shows the calibration plots of the redox peak currents (I_{pa} & I_{pc}) from HT-CuSe with the square root of the scan rates.

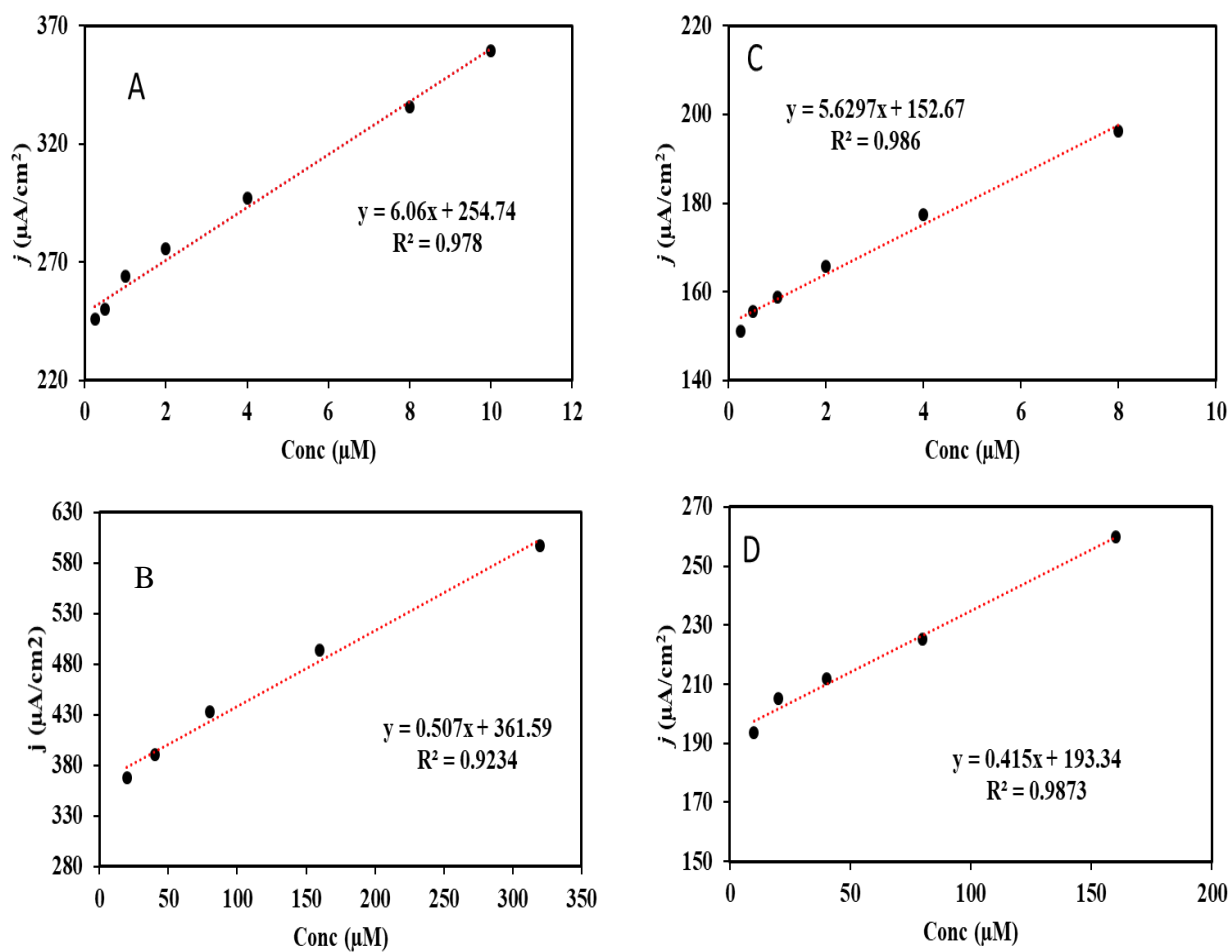


Figure S5. (A) and (B) Low and high concentration of ED-CuSe peak current vs the concentration of dopamine and (C) and (D) HT-CuSe nanoparticles from the SWV technique.

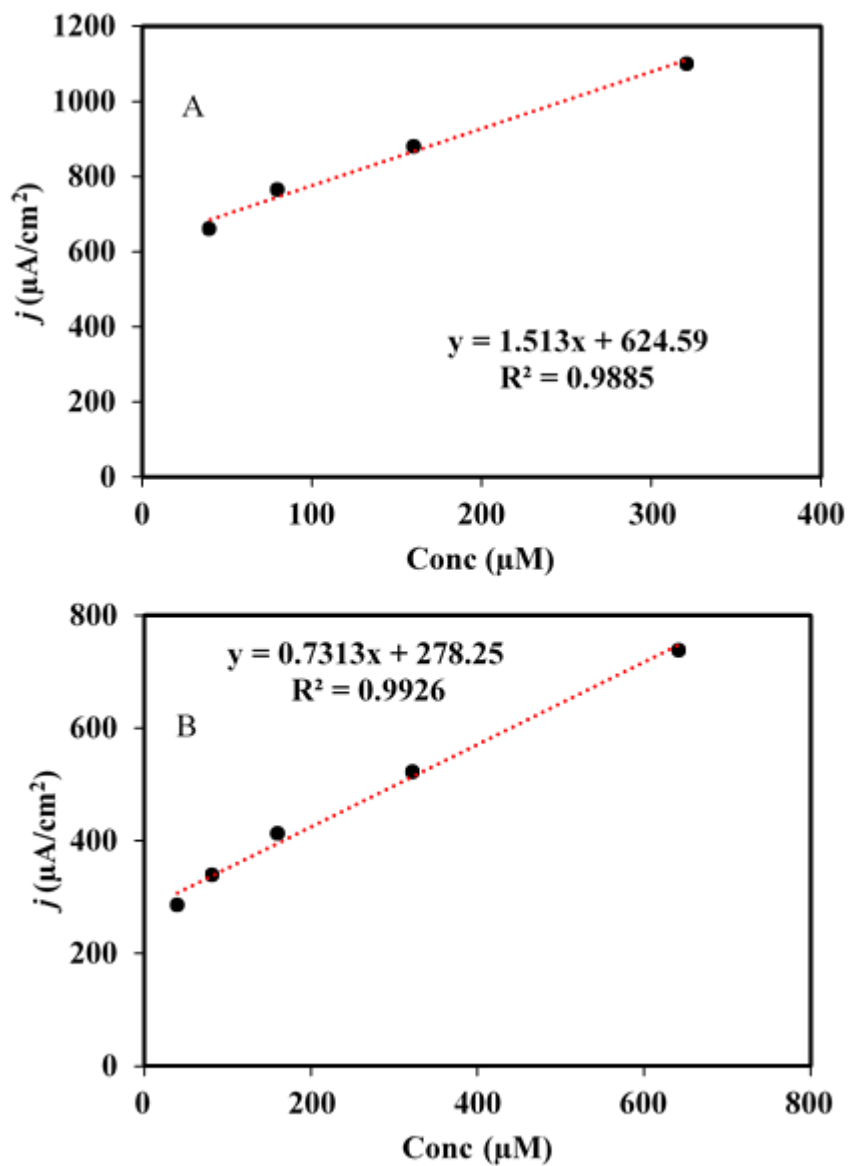


Figure S6. Variation of peak current vs the concentration of dopamine at higher concentration range from (A) ED-CuSe and (B) HT- CuSe.

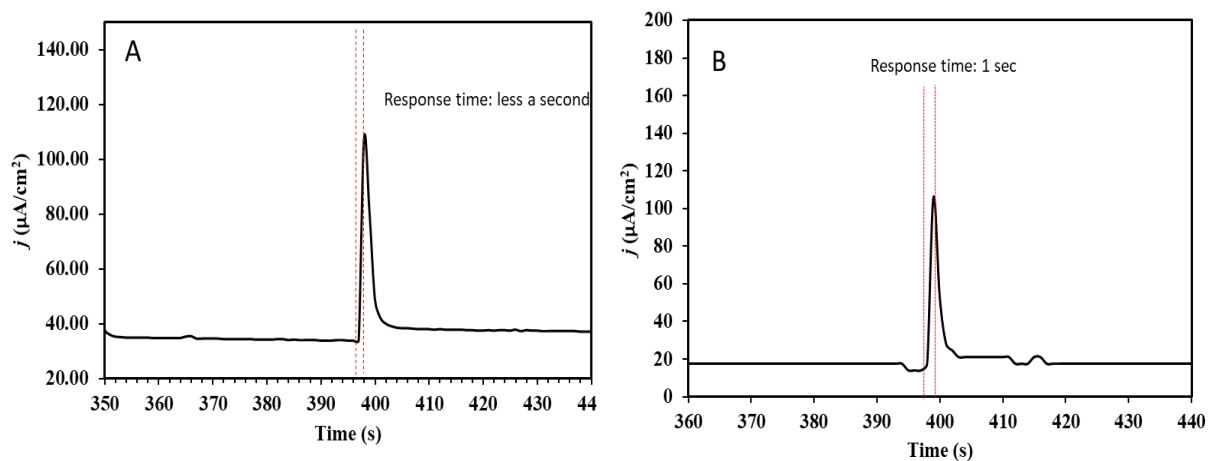


Figure S7. Response time to reach the steady-state current for (A) ED-CuSe and (B) HT-CuSe.

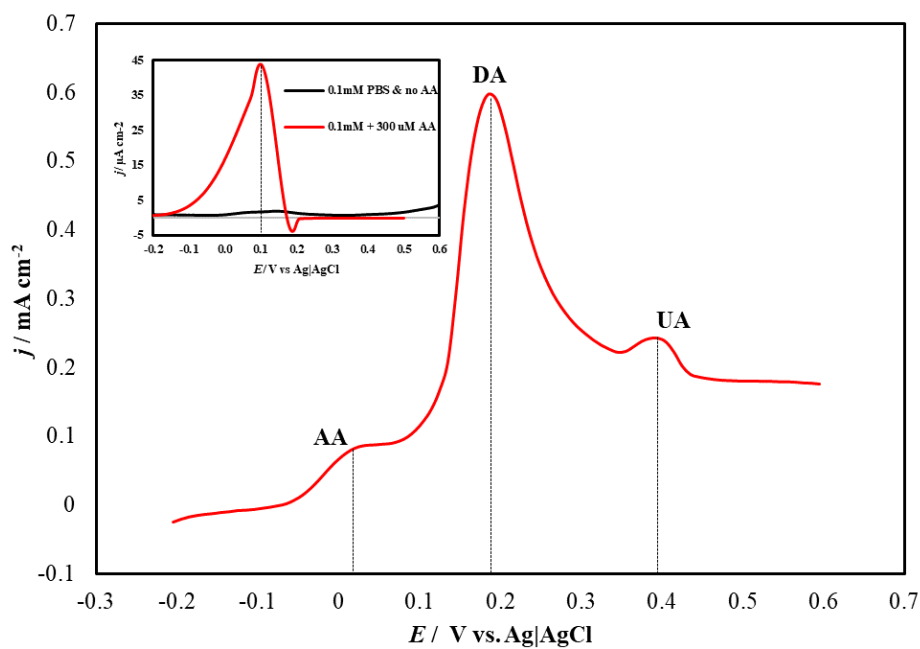


Figure S8. SWV of a mixed electrolyte containing 40 μM DA, 300 μM AA and UA at ED-CuSe in pH 7 PBS electrolyte. Inset shows SWV plot of 300 μM AA in 0.1 M PBS solution.

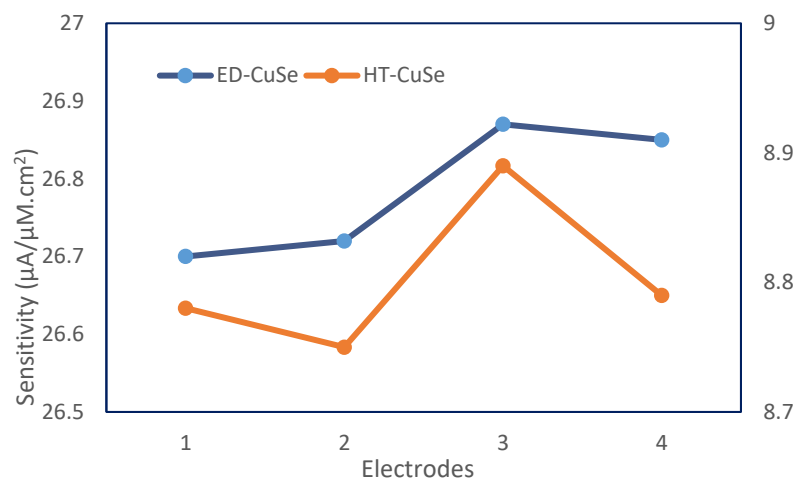


Figure S9. Sensitivity of different batches of ED-CuSe and HT-CuSe modified electrodes showing the error bars.

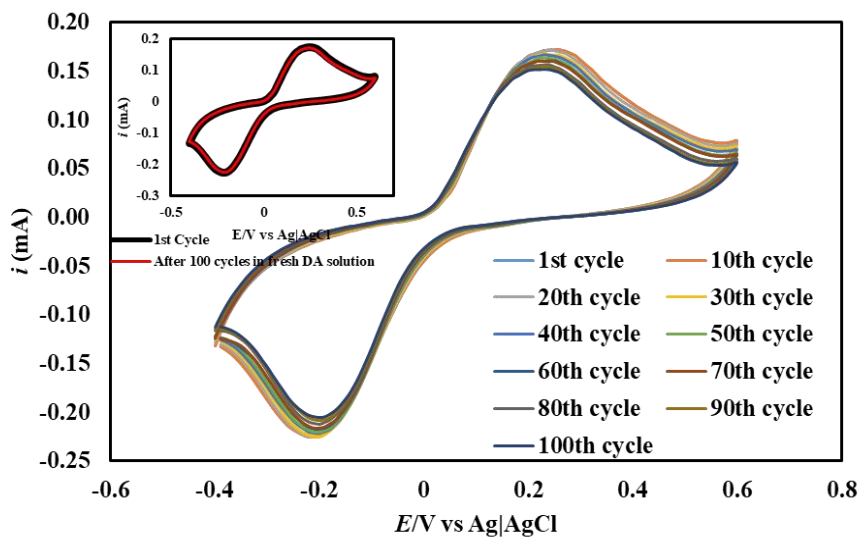


Figure S10. CV plots of HT-CuSe in 0.1M PBS + 0.005 mM DA at scan rate of 50 mV/s for 100 cycles.

REFERENCES

1. X. Xia, X. Shen, Y. Du, W. Ye and C. Wang, *Sensors and Actuators B: Chemical*, 2016, **237**, 685-692.
2. R. N. Goyal, V. K. Gupta, N. Bachheti and R. A. Sharma, *Electroanalysis*, 2008, **20**, 757-764.
3. A. Celebanska, D. Tomaszewska, A. Lesniewski and M. Opallo, *Biosensors and Bioelectronics*, 2011, **26**, 4417-4422.
4. J. Salamon, Y. Sathishkumar, K. Ramachandran, Y. S. Lee, D. J. Yoo, A. R. Kim and G. Gnana kumar, *Biosensors and Bioelectronics*, 2015, **64**, 269-276.
5. Y. Mao, Y. Bao, D. Han, F. Li and L. Niu, *Biosensors and Bioelectronics*, 2012, **38**, 55-60.
6. V. Ranc, Z. Markova, M. Hajduch, R. Prucek, L. Kvitek, J. Kaslik, K. Safarova and R. Zboril, *Analytical Chemistry*, 2014, **86**, 2939-2946.
7. M. Kaya and M. Volkan, *Analytical Chemistry*, 2012, **84**, 7729-7735.
8. Y. Tao, Y. Lin, J. Ren and X. Qu, *Biosensors and Bioelectronics*, 2013, **42**, 41-46.
9. Y. Jie, N. Wang, X. Cao, Y. Xu, T. Li, X. Zhang and Z. L. Wang, *ACS Nano*, 2015, **9**, 8376-8383.
10. T. O. Ahmadov, P. Joshi, J. Zhang, K. Nahan, J. A. Caruso and P. Zhang, *Chemical Communications*, 2015, **51**, 11425-11428.
11. S. Wang, *Chromatographia*, 2009, **v. 70**, pp. 1467-1471-2009 v.1470 no.1469-1410.
12. M. Mamiński, M. Olejniczak, M. Chudy, A. Dybko and Z. Brzózka, *Analytica Chimica Acta*, 2005, **540**, 153-157.
13. D.-S. Kim, E.-S. Kang, S. Baek, S.-S. Choo, Y.-H. Chung, D. Lee, J. Min and T.-H. Kim, *Scientific Reports*, 2018, **8**, 14049.
14. S. Schindler and T. Bechtold, *Journal of Electroanalytical Chemistry*, 2019, **836**, 94-101.
15. Q. He, J. Liu, X. Liu, G. Li, D. Chen, P. Deng and J. Liang, *Electrochimica Acta*, 2019, **296**, 683-692.

16. M. Labib, E. H. Sargent and S. O. Kelley, *Chemical Reviews*, 2016, **116**, 9001-9090.
17. K. Jackowska and P. Krysinski, *Anal Bioanal Chem*, 2013, **405**, 3753-3771.
18. H. Devnani, N. Rashid and P. P. Ingole, *ChemistrySelect*, 2019, **4**, 633-643.
19. A. Pandikumar, G. T. Soon How, T. P. See, F. S. Omar, S. Jayabal, K. Z. Kamali, N. Yusoff, A. Jamil, R. Ramaraj, S. A. John, H. N. Lim and N. M. Huang, *RSC Advances*, 2014, **4**, 63296-63323.
20. X. Niu, M. Lan, H. Zhao, C. Chen, *Analytical Chemistry*, **2013**, **85**, 3561-3569.
21. Y. Li and X. Lin, *Sensors and Actuators B: Chemical*, 2006, **115**, 134-139.
22. A. Liu, I. Honma and H. Zhou, *Biosensors and Bioelectronics*, 2007, **23**, 74-80.
23. J. N. Tiwari, V. Vij, K. C. Kemp and K. S. Kim, *ACS Nano*, 2016, **10**, 46-80.
24. H. Muguruma, Y. Inoue, H. Inoue and T. Ohsawa, *The Journal of Physical Chemistry C*, 2016, **120**, 12284-12292.
25. Y. Wu, Z. Dou, Y. Liu, G. Lv, T. Pu and X. He, *RSC Advances*, 2013, **3**, 12726-12734.
26. L. Jiang, G. W. Nelson, J. Abda and J. S. Foord, *ACS Applied Materials & Interfaces*, 2016, **8**, 28338-28348.
27. A. Oleinick, I. Álvarez-Martos, I. Svir, E. E. Ferapontova and C. Amatore, *Journal of The Electrochemical Society*, 2018, **165**, G3057-G3065.
28. I. Gualandi, D. Tonelli, F. Mariani, E. Scavetta, M. Marzocchi and B. Fraboni, *Scientific Reports*, 2016, **6**, 35419.
29. C. Lin, L. Chen, E. E. L. Tanner and R. G. Compton, *Physical Chemistry Chemical Physics*, 2018, **20**, 148-157.
30. A. Savk, B. Özdil, B. Demirkan, M. S. Nas, M. H. Calimli, M. H. Alma, Inamuddin, A. M. Asiri and F. Şen, *Materials Science and Engineering: C*, 2019, **99**, 248-254.
31. D. Lakshmi, A. Bossi, M. J. Whitcombe, I. Chianella, S. A. Fowler, S. Subrahmanyam, E. V. Piletska and S. A. Piletsky, *Analytical Chemistry*, 2009, **81**, 3576-3584.

32. Y. Wu, L. Cui, Y. Liu, G. Lv, T. Pu, D. Liu and X. He, *Analyst*, 2013, **138**, 1204-1211.
33. Y. Oztekin, M. Tok, E. Bilici, L. Mikoliunaite, Z. Yazicigil, A. Ramanaviciene and A. Ramanavicius, *Electrochimica Acta*, 2012, **76**, 201-207.
34. C.-S. Lee, S. H. Yu and T. H. Kim, *Nanomaterials*, 2018, **8**, 17.
35. Y. Wang, Y. Li, L. Tang, J. Lu and J. Li, *Electrochemistry Communications*, 2009, **11**, 889-892.
36. D. Han, T. Han, C. Shan, A. Ivaska and L. Niu, *Electroanalysis*, 2010, **22**, 2001-2008.
37. B. Fang, G. Wang, W. Zhang, M. Li and X. Kan, *Electroanalysis*, 2005, **17**, 744-748.
38. R. Nurzulaikha, H. N. Lim, I. Harrison, S. S. Lim, A. Pandikumar, N. M. Huang, S. P. Lim, G. S. H. Thien, N. Yusoff and I. Ibrahim, *Sensing and Bio-Sensing Research*, 2015, **5**, 42-49.
39. P. R. Roy, T. Okajima and T. Ohsaka, *Bioelectrochemistry*, 2003, **59**, 11-19.
40. Q. Li, Y. Wang and G. Luo, *Materials Science and Engineering: C*, 2000, **11**, 71-74.
41. J. Masud, W. P. R. Liyanage, X. Cao, A. Saxena and M. Nath, *ACS Applied Energy Materials*, 2018, **1**, 4075-4083.
42. S. Umapathi, J. Masud, A. T. Swesi and M. Nath, *Advanced Sustainable Systems*, 2017, **1**, 1700086.
43. A. T. Swesi, J. Masud, W. P. R. Liyanage, S. Umapathi, E. Bohannan, J. Medvedeva and M. Nath, *Scientific Reports*, 2017, **7**, 2401.
44. J. Luxa, V. Mazánek, D. Bouša, D. Sedmidubský, M. Pumera and Z. Sofer, *ChemElectroChem*, 2016, **3**, 565-571.
45. X. Wu, S. Han, D. He, C. Yu, C. Lei, W. Liu, G. Zheng, X. Zhang and L. Lei, *ACS Sustainable Chemistry & Engineering*, 2018, **6**, 8672-8678.
46. M. Ma, W. Zhu, D. Zhao, Y. Ma, N. Hu, Y. Suo and J. Wang, *Sensors and Actuators B: Chemical*, 2019, **278**, 110-116.
47. Y.-H. Wang, K.-J. Huang and X. Wu, *Biosensors and Bioelectronics*, 2017, **97**, 305-316.

48. S. Mani, S. Ramaraj, S.-M. Chen, B. Dinesh and T.-W. Chen, *Journal of Colloid and Interface Science*, 2017, **507**, 378-385.
49. P. K. Kannan, D. J. Late, H. Morgan and C. S. Rout, *Nanoscale*, 2015, **7**, 13293-13312.
50. Y. Li, X. He, M. Guo, D. Lin, C. Xu, F. Xie and X. Sun, *Sensors and Actuators B: Chemical*, 2018, **274**, 427-432.
51. X. Li, *International Journal of Electrochemical Science*, 2019, DOI: 10.20964/2019.05.68, 4327-4337.
52. X. Chia, A. Y. S. Eng, A. Ambrosi, S. M. Tan and M. Pumera, *Chemical Reviews*, 2015, **115**, 11941-11966.
53. S. Ramki, *International Journal of Electrochemical Science*, 2019, DOI: 10.20964/2019.01.58, 1069-1081.
54. Ö. Ertekin, S. Öztürk and Z. Z. Öztürk, *Sensors*, 2016, **16**, 1274.
55. T. Dayakar, K. Venkateswara Rao, K. Bikshalu, V. Rajendar and S.-H. Park, *Materials Science and Engineering: C*, 2017, **75**, 1472-1479.
56. A. Hammami, R. Sahli and N. Raouafi, *Microchimica Acta*, 2016, **183**, 1137-1144.
57. M. Dhanam, P. K. Manoj and R. R. Prabhu, *Journal of Crystal Growth*, 2005, **280**, 425-435.
58. P. Yadav, S. Manivannan, H.-S. Kim, K. Pandey, K. Kim and J. Kim, *Electroanalysis*, 2017, **29**, 2106-2113.
59. Z.-H. Sheng, X.-Q. Zheng, J.-Y. Xu, W.-J. Bao, F.-B. Wang and X.-H. Xia, *Biosens Bioelectron*, 2012, **34**, 125-131.
60. S. Hou, M. L. Kasner, S. Su, K. Patel and R. Cuellari, *The Journal of Physical Chemistry C*, 2010, **114**, 14915-14921.
61. Y. Chen and T. C. Tan, *Biosensors and Bioelectronics*, 1994, **9**, 401-410.
62. W.-C. Lee, K.-B. Kim, N. G. Gurudatt, K. K. Hussain, C. S. Choi, D.-S. Park and Y.-B. Shim, *Biosensors and Bioelectronics*, 2019, **130**, 48-54.
63. J. Masud, P.-C. Ioannou, N. Levesanos, P. Kyritsis and M. Nath, *ChemSusChem*, 2016, **9**, 3128-3132.

64. U. De Silva, J. Masud, N. Zhang, Y. Hong, W. P. R. Liyanage, M. Asle Zaeem and M. Nath, *Journal of Materials Chemistry A*, 2018, **6**, 7608-7622.
65. Y. Zhang, Y. Ji, Z. Wang, S. Liu and T. Zhang, *RSC Advances*, 2015, **5**, 106307-106314.
66. H. Wang, F. Ren, C. Wang, B. Yang, D. Bin, K. Zhang and Y. Du, *RSC Advances*, 2014, **4**, 26895-26901.
67. S. P. Kumar, R. Manjunatha, T. V. Venkatesha and G. S. Suresh, *Russian Journal of Electrochemistry*, 2013, **49**, 299-306.
68. Q. Lian, Z. He, Q. He, A. Luo, K. Yan, D. Zhang, X. Lu and X. Zhou, *Analytica Chimica Acta*, 2014, **823**, 32-39.
69. A. Manbohi and S. H. Ahmadi, *Sensing and Bio-Sensing Research*, 2019, **23**, 100270.
70. Q.-L. Zhang, J.-X. Feng, A.-J. Wang, J. Wei, Z.-Y. Lv and J.-J. Feng, *Microchimica Acta*, 2015, **182**, 589-595.
71. G. Zheng, M. Chen, X. Liu, J. Zhou, J. Xie and G. Diao, *Electrochimica Acta*, 2014, DOI: DOI:10.1016/j.electacta.2014.05.086, 301-309.
72. S. Liu, F. Shi, X. Zhao, L. Chen and X. Su, *Biosensors and Bioelectronics*, 2013, **47**, 379-384.
73. F. H. Cincotto, T. C. Canevari, A. M. Campos, R. Landers and S. A. S. Machado, *Analyst*, 2014, **139**, 4634-4640.
74. Y. Wang, X. Zhang, Y. Chen, H. Xu, Y. Tan and S. Wang, *American Journal of Biomedical Sciences*, 2010, DOI: 10.5099/aj100300209, 209-216.
75. J. Njagi, M. M. Chernov, J. C. Leiter and S. Andreescu, *Analytical Chemistry*, 2010, **82**, 989-996.
76. S.-S. Choo, E.-S. Kang, I. Song, D. Lee, J.-W. Choi and T.-H. Kim, *Sensors*, 2017, **17**, 861.
77. H. Y. Yue, H. J. Zhang, S. Huang, X. Gao, S. S. Song, Z. Wang, W. Q. Wang and E. H. Guan, *Journal of Materials Science: Materials in Electronics*, 2019, **30**, 5000-5007.
78. D. Zhao, G. Yu, K. Tian and C. Xu, *Biosensors and Bioelectronics*, 2016, **82**, 119-126.

79. T. Yang, H. Chen, C. Jing, S. Luo, W. Li and K. Jiao, *Sensors and Actuators B: Chemical*, 2017, **249**, 451-457.
80. Y.-R. Kim, S. Bong, Y.-J. Kang, Y. Yang, R. K. Mahajan, J. S. Kim and H. Kim, *Biosensors and Bioelectronics*, 2010, **25**, 2366-2369.
81. Y. Wang, W. Peng, L. Liu, M. Tang, F. Gao and M. Li, *Microchimica Acta*, 2011, **174**, 41-46.

IV. NANOSTRUCTURED COPPER SELENIDE AS AN ULTRASENSITIVE AND SELECTIVE NON ENZYMATIC GLUCOSE BIOSENSOR

*Siddesh Umapathi, Jahangir Masud† and Manashi Nath**

Department of Chemistry, Missouri University of Science & Technology, Rolla,
MO 65409

ABSTRACT

Copper selenide (CuSe) nanostructures with highly porous surface topology was synthesized by one step electrodeposition method directly on carbon cloth electrode. The electrocatalytic performance of CuSe was estimated towards electro-oxidation of glucose which is the primary reaction for non-enzymatic detection of glucose. The electrocatalytic performance of this glucose biosensor was estimated using detailed electrochemical measurements in both added glucose solutions as well as physiological samples. The CuSe modified electrode showed a sensitivity of $19.419 \text{ mA mM}^{-1} \text{ cm}^{-2}$ for glucose detection at a very low applied potential of $+0.15 \text{ V vs Ag|AgCl}$, low detection limit of $0.196 \text{ }\mu\text{M}$ and a linear range of glucose detection from 100 nM - $40 \text{ }\mu\text{M}$. Furthermore, it was observed that CuSe was selective towards glucose oxidation and the other interfering species such as ascorbic acid, lactose and uric acid showed no significant response at the applied potential. This simple and inexpensive way of detecting glucose at ultralow concentrations at low working potential using binder-free copper selenide film directly grown on the electrodes makes it a novel biosensor. The CuSe-modified electrodes also showed good

reproducibility and stability for electrochemical glucose detection over prolonged periods of time.

1. INTRODUCTION

Diabetes caused by the imbalance of glucose level in blood has been of severe concern lately, leading to 1.5 million deaths across the globe according to World Health organization reports. It has also been predicted that diabetes will become 7th leading cause of mortality by 2030.¹⁻⁴ Diabetes is a silent killer where the symptoms may not be expressed until a very advanced stage leading to more fatality. Hence, continuous monitoring of blood glucose levels in susceptible as well as healthy individuals is very important to detect onset of diabetes at an early stage and minimize progression of the disease by taking preventive measures. While commercially available enzyme-based glucose sensing strips are widely used for measuring blood glucose levels, their limited shelf life, low sensitivity, non-reusability, and high cost, makes it desirable to seek alternate solutions for glucose sensing.⁵⁻⁷ Moreover, non-enzymatic glucose sensors are also lucrative for long-term continuous blood glucose monitoring systems that can be implanted in peripheral tissue including sub-dermis or tooth enamel. Electrochemical glucose sensors work on the principle of direct glucose oxidation on the electrocatalytic surface, and can be categorized into two types: the enzymatic and non-enzymatic glucose sensors.⁸⁻¹⁰ Among these the non-enzymatic glucose sensors have attracted considerable attention over the last few years attributed to their advantages such as high stability and sensitivity, low cost, and simple preparation.¹¹⁻

Over the last several years various non-enzymatic glucose sensors based on different kinds of materials have been reported, such as metal nanoparticles and carbon materials, where polymer binders have been used to immobilize these nanoparticles. Such non-conductive polymeric binders add inactive component in the catalytic composite which may hinder the ability for quick electron transfer within the catalytic composite and reduce sensitivity.¹⁴⁻¹⁷ On the other hand, transition metals consisting of Ni, Co and Fe have been demonstrated as promising materials towards glucose oxidation which also have the advantage of being earth abundant, low cost and environmental friendly.¹⁸⁻²² Multi metal alloy and multi metallic compounds such as Co-Ni, Ni-Fe and Ni-Cu have also shown good electrochemical glucose sensing.²³⁻²⁶

In recent years, transition metal chalcogenides has gained considerable attention in electrochemical devices such as water electrolyzer, fuel cells, and as supercapacitors, owing to their unprecedented high electrocatalytic activity. This improvement of electrochemical activity of TMC is primarily caused by reduced anion electronegativity and high degree of covalency in the lattice which leads to better electrochemical tunability and reduced bandgap in the materials. While the electrochemical tunability aids in adsorption of reactive intermediates on the catalyst surface through local oxidation/reduction of the transition metal active site, a reduced bandgap also enhances the charge transport at the catalyst-electrolyte interface as well as through the catalyst composite.²⁷⁻²⁹ The effect of decreasing anion electronegativity on the electrocatalytic activity has been recently observed in a series of Ni-chalcogenide water oxidation catalysts where it was observed that the catalytic efficiency progressively improves from Ni-oxide to Ni-telluride.³⁰⁻³² Copper has been studied recently for its electrochemical activity in

various systems, and presents as attractive case for further expansion attributed to its abundancy on earth's surface, and low-cost.³³⁻³⁵ These attributes has led to the usage of Cu in various catalytic processes.³⁶ However, reports of copper chalcogenides in electrochemical devices are still limited. As explained above, decreasing anion electronegativity is expected to improve the electrochemical tunability of the catalytically active transition metal center leading to better electrocatalytic activity.

In this communication, we have reported a high efficiency, non-enzymatic, direct glucose electrochemical sensor based on CuSe synthesized by one step electrodeposition directly on the electrode surface. Such direct growth on the electrode surface avoids the use of any adhesive or polymeric binder which can reduce sensing performance. The as-prepared CuSe shows excellent sensitivity and low limit of detection for detection of glucose. The developed sensor was also applied successfully for the detection of glucose in human blood samples.

2. RESULT AND DISCUSSION

D-Glucose, copper chloride, selenium oxide and NaOH were purchased from Arcos chemicals. Uric acid (UA), l-ascorbic acid (AA), dopamine (DA), NaCl and KCl were obtained from Alfa Aesar. All chemicals were used as received without any further purification. Deionized water was used in all experiments.

The CuSe thin film was prepared directly on a carbon cloth electrode through direct electrodeposition using a conventional three electrode set-up, where Ag|AgCl was used as the reference electrode, graphite rod as the counter electrode and commercial carbon cloth

as the working electrode. The deposition area of CuSe was pre-defined by using a masking tape exposing a 0.08 cm^2 hole on the electrode surface. The electrolyte contained 2 mM of copper chloride, 4.5 mM SeO_2 and 0.1 M of KCl in deionized water. The pH of the electrolyte was adjusted to 2 using dilute HCl. This solution was purged with N_2 gas for 20 minutes prior to electrodeposition to reduce amount of dissolved air. Electrodeposition was carried out at an applied voltage of -0.16 V vs Ag|AgCl for 300 seconds. Following electrodeposition, the substrate was mildly washed with DI water and dried naturally.

The composition, phase, and morphology of the electrodeposited film was identified through powder X-ray diffraction (pxrd), scanning electron microscopy (SEM) (FEI Helios Nanolab 600) using 10kV accelerated voltage, and Energy dispersive spectroscopy (EDS). Composition of the film was also analyzed through X-ray photoelectron spectroscopy (XPS) using KRATOS AXIS 165 spectrometer with Al source. Transmission electron microscopy (Tecnai F20 with an accelerating voltage of 200 kV) was also performed to investigate nanostructure details of the morphology. Electrochemical measurements were performed using Iviumstat electrochemical workstation using a three-electrode system with CuSe on carbon cloth as working electrode, saturated Ag|AgCl as reference electrode and a graphite rod served as counter electrode.

The pxrd pattern was collected from a CuSe film deposited on Au substrate, which was used to obtain better background for the diffraction pattern. Figure 1a shows the pxrd pattern of as-deposited thin film on Au-substrate. It was observed that the film was weakly crystalline and the diffraction pattern could be matched with the standard diffraction pattern for CuSe (PDF# 00-006-0427). CuSe crystallizes in a hexagonal structure with Cu in two different coordination geometries, trigonal planar and tetrahedral. Such low

coordination geometries around the active sites are expected to enhance adsorption of oxygenated reactive intermediates on the surface through coordination expansion leading to improved electrocatalytic performance. The composition of the as-deposited film was confirmed through XPS, which also provides details of local bonding environment and oxidation states of the elements. As shown in Figure 1b the Cu 2p spectrum shows peaks centered at 932.2 and 952.3 eV for Cu^+ $2p_{3/2}$ and $2p_{1/2}$ and 934.4 and 954.6 eV for Cu^{2+} $2p_{3/2}$ and $2p_{1/2}$ respectively. This also suggested that Cu was present in mixed oxidation states, while the satellite peaks are observed at 942.4 and 962.6 eV. The deconvoluted Se 3d spectra of electrodeposited CuSe (inset of Figure 1b) shows peaks at 54.4 and 55.4 for Se $3d_{5/2}$ and $3d_{3/2}$ respectively which is in accordance to previously reported copper selenide.³⁷

The SEM images of as-deposited CuSe thin film as depicted in Figure 1c showed that CuSe had a rough surface topology comprising nanoflake like morphology. The nanoflakes are randomly oriented leading to a porous film which provides high surface area for the glucose adsorption. The elemental mapping through EDS showed uniform distribution of Cu and Se throughout the composite, while quantification of the EDS data yielded an elemental ratio of 1: 1 for Cu: Se (Figure S1). TEM studies (Figure 1d) showed similar flake-like nanostructures while HRTEM images showed the lattice fringes corresponding to a d- spacing of 3.31 Å which could be matched to 101 lattice spacing of CuSe (Figure S2).

The electrocatalytic performance of CuSe thin film towards oxidation of glucose was studied by cyclic voltammogram (CV). Figure 2a shows the CV of CuSe thin film on carbon cloth measured in presence and absence of 0.1 mM glucose in 0.1 M NaOH

electrolyte at 10 mV/s scan rate. While the current response was moderate in a blank 0.1 M NaOH electrolyte, upon addition of 0.1 mM of glucose into the alkaline electrolyte,

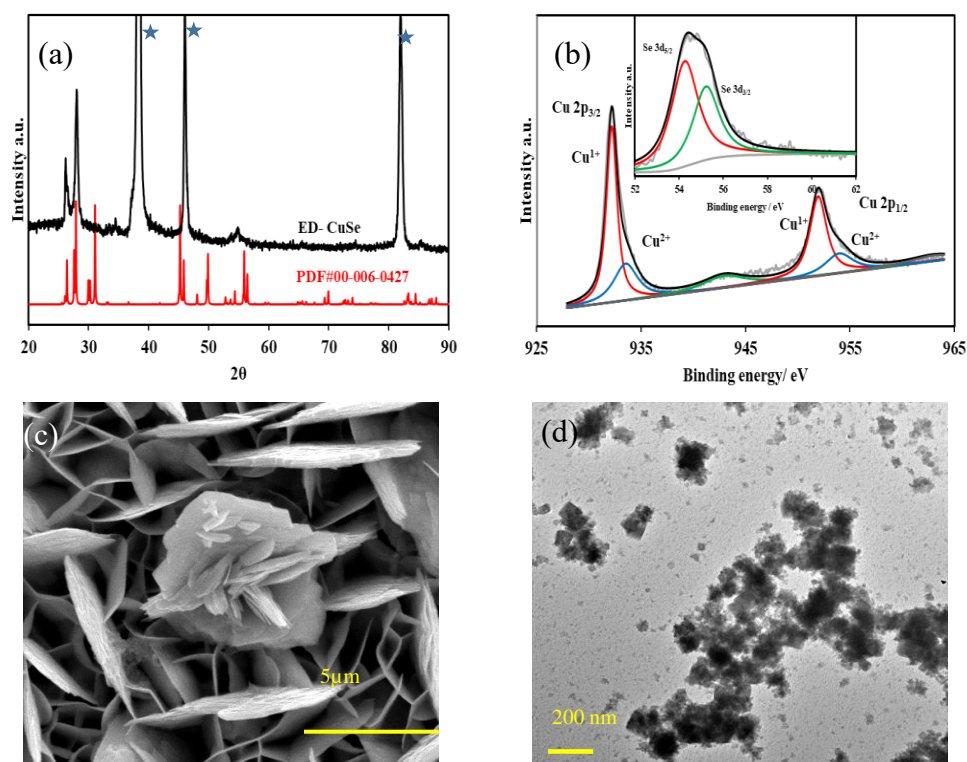


Figure 1. (a) PXRD pattern of electrodeposited CuSe, compared with the reference pattern (PDF#00-006-0427) star denotes Au peaks. (b) Deconvoluted XPS spectra of Cu 2p CuSe. Inset in (b) shows the corresponding Se 3d signals (c) SEM images of CuSe and (d) TEM images of CuSe.

there was a substantial increase in the anodic current, indicating oxidation of glucose on the CuSe-coated electrode. This oxidation was also observed in the reverse sweep of CV, which further confirmed the process to be analyte, i.e. glucose oxidation on the electrode surface. To further evaluate the electrocatalytic performance of CuSe towards glucose

oxidation, the scan rates were varied from 5 mV/s to 75 mV/s as shown in Figure 2b. The glucose oxidation peaks shows obvious trend in the increase of current with respect to the scan rate in addition to a positive shift of the anodic potential. The redox peak current

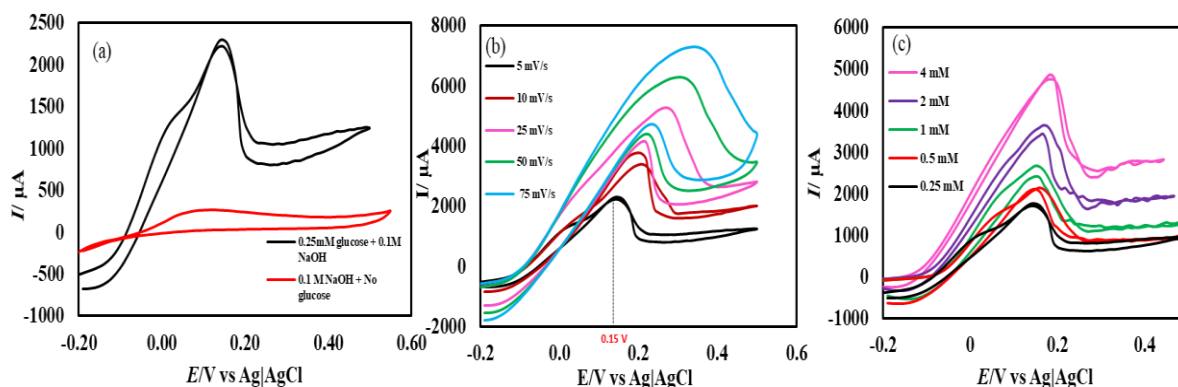


Figure 2. (a) CV curves of CuSe with 0.25 mM glucose and no glucose in 0.1 M NaOH solution (b) with scan rates ranging from 5 to 75 mV/s. (c) CV curves of CuSe with varying concentrations of glucose ranging from 0.25 mM to 4 mM.

showed a linear correlation ($R^2 = 0.9965$) with square root of the scan rate, which is typical for a diffusion controlled process for any electrochemical oxidation. On addition of 0.25, 0.5, 1, 2 and 4 mM of glucose to 0.1 M NaOH solution, CuSe composite electrode showed an increase in the current density corresponding to the increase in glucose concentration (Figure 2c), indicating that the oxidation current is mainly due to the availability of increased glucose content in the electrolyte.

In order to determine the optimal applied potential for glucose sensing, the oxidation current was measured by scanning the potential ranging from 0.05 V to 0.3 V vs Ag|AgCl using amperometric technique with successive addition of 0.1 mM glucose to the

0.1 M NaOH electrolyte under constant stirring. Figure S3 shows that the ratio of oxidation current vs the potential range from 0.05 V to 0.30 V, where the highest oxidation current was achieved at 0.15 V, after which it begins to decay. Hence, the ideal working potential for oxidation of glucose at electrodeposited CuSe thin film was selected to be +0.15 V vs Ag|AgCl for the rest of the study.

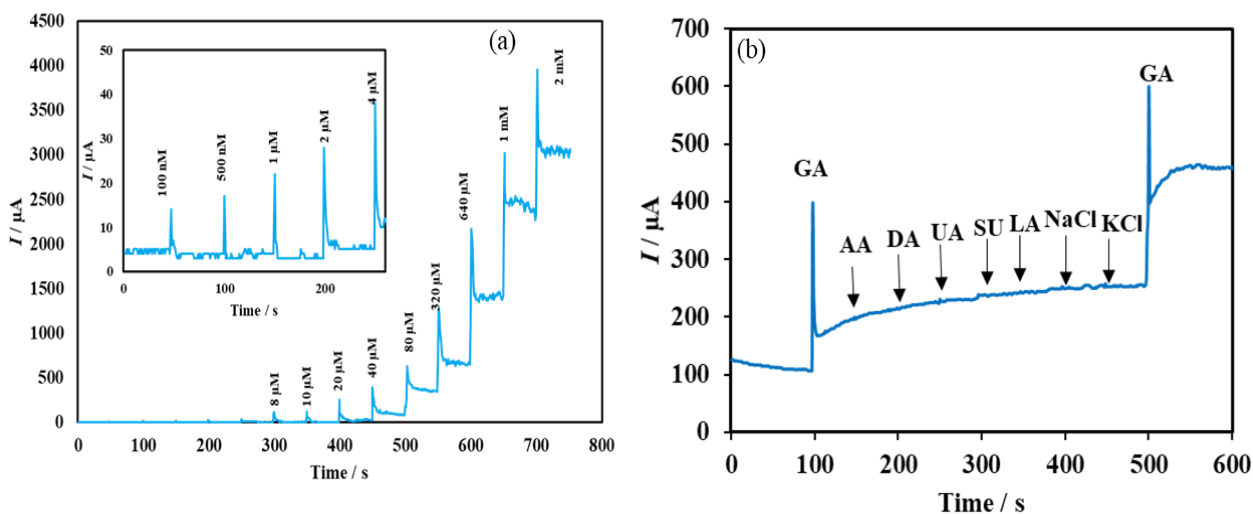


Figure 3. (a) Chronoamperometric responses of the CuSe to successive additions of glucose into stirring 0.1M NaOH electrolyte. The working potential was set at +0.15 V vs Ag|AgCl, and the glucose concentrations ranged from 100 nM to 2 mM for sequential addition. Inset shows magnified portion of the amperometric response for lower concentrations. (b) Amperometric responses of CuSe 0.1M NaOH with successive addition of glucose (0.1 mM), AA (0.5 mM), DA (0.5 mM), UA (0.5 mM), Sucrose (0.1 mM), Lactose (0.1 mM), NaCl (0.5 mM), KCl (0.5 mM) and glucose (0.1 mM) at an applied potential of +0.15 V vs Ag|AgCl.

Chronoamperometric technique was used to measure the response of CuSe composite electrode upon successive injections of glucose in a homogeneously stirred NaOH solution. The limit of detection and linear range were also determined using the

above method. As shown in Figure 3a, a constant potential of +0.15 V vs Ag|AgCl was applied, when CuSe-modified electrodes showed a rapid and significant response of increasing anodic current upon addition of glucose ranging from 100 nM to 2 mM, which indicates the high sensitivity of CuSe towards glucose sensing. The calibration curve was obtained by plotting the peak anodic current vs concentration of glucose from the amperometric experiment described above. Figure S4 shows the calibration curve from 100 nM to 2 mM where the corresponding regression equation can be described as $I \text{ (mA)} = 19.419C \text{ (mM)} + 0.0231$ ($R^2 = 0.9998$) having a high sensitivity of $19.419 \text{ mA mM}^{-1} \text{ cm}^{-2}$. Further the linear detection range of CuSe towards glucose was 100 nM to 40 μM and a second linear region for higher concentrations from 80 μM to 2 mM, with a limit of detection of 196 nM. Figure S5 shows the response time of CuSe upon addition of glucose. The catalyst achieves steady state current within 2 sec of glucose addition, which shows that these CuSe-modified electrodes is capable of real time monitoring of glucose in the body.

Several biomolecules with similar oxidation profiles are known to interfere in detection of glucose which makes the development of nonenzymatic glucose sensors very challenging. Species such as ascorbic acid (AA), dopamine (DA), lactose, NaCl and KCl commonly available in lower concentration in bodily fluids can exhibit interference by undergoing electro-oxidation. Therefore, the selectivity of CuSe towards glucose oxidation was confirmed by measuring amperometric response of CuSe composite electrode upon consecutive injection of glucose and other interferents as mentioned above. A constant potential of +0.15 v vs Ag|AgCl was applied to an evenly stirred 0.1 M NaOH solution wherein, addition of 0.1 mM of glucose showed rapid increase of anodic current. Addition

of sucrose and lactose (0.1 mM) and AA, DA, LC, NaCl, KCl (0.5 mM) did not show any appreciable oxidation current. However, the second addition of 0.1 mM glucose showed similar jump in anodic current density as observed from the 1st addition which validated the functionality and selectivity of the CuSe based composite electrode was (Figure 3b). Thus it was confirmed that CuSe exhibits high sensitivity and selectivity for non-enzymatic glucose sensing at an extremely low working potential.

The practical applicability of the fabricated non-enzymatic glucose sensor was investigated by the determination of glucose in human blood samples using a known method³⁸ and comparing it with the commercially available enzymatic glucometer kit (ReliOn). Specifically, the experiment comprised of first stabilizing current response of the electrode by adding 1mM of glucose two times. The blood sample was then injected directly to the NaOH electrolyte in the vicinity of the CuSe-modified electrode. 1mM of glucose was added again and the current response was recorded. The glucose level in the blood samples was measured from linear fit of the plot obtained by plotting the current density vs glucose concentration of standard glucose additions. Table 2 lists the glucose concentration as detected by a standard glucometer and the CuSe based sensor. Each sample was tested three times and the calculated relative standard deviation of less than 3% suggests the robustness and reliability of CuSe towards glucose sensing in physiological samples.

Owing to its high sensitivity, short response time and low detection limit electrodeposited CuSe is a potential candidate for continuous glucose monitoring system for commercial applications. Additionally, CuSe has a low working potential and selectivity to sense glucose and not the other biomolecules commonly present in bodily

fluids which is an advantage to use in wearable biosensors. Other than biosensing, CuSe has also been reported for electrochemical energy conversion.³⁹ The superior electrochemical performance of CuSe especially towards glucose oxidation can be attributed to several factors. The initial step of glucose oxidation is the activation of the catalyst achieved by attachment of the molecule on the electrode surface through the coordination of the -OH functional group on the catalytically active transition metal site (Cu). Such -OH attachment proceeds through local site oxidation of the active site. Previously we have shown the -OH adsorption can be facilitated by controlling the ligand environment, typically by decreasing anion electronegativity,³¹ which reduces the required potential for catalyst activation, thereby increasing efficiency.⁴⁰ Moreover, Cu in copper selenide has mixed oxidation states. In case of Cu^+ and Se^{2-} we can expect a certain degree of polarization due to charge imbalance. However in case of Cu^{2+} there is increase in the covalency between Cu-Se bonds. This mixed oxidation states leads to inductive effect and redistribution of electron density at metal sites through *d-d* interactions, which is favorable for -OH groups to adsorb. Additionally, replacing oxides with less electronegative selenides also leads to increased covalency in the lattice and enhances the redox activity at Cu site which consequently has an effect on the reversible electrochemical response. The low potential required for glucose oxidation is advantageous for making affordable and energy efficient non-enzymatic glucose sensors.

3. CONCLUSION

In conclusion simple, binary copper selenide has been identified as a highly efficient, non-enzymatic, electrochemical glucose biosensor with low limit of detection and high sensitivity. The CuSe was synthesized directly on the electrodes by electrodeposition producing a porous morphology comprising flake-like nanostructures. The electrocatalytic activity for glucose oxidation was studied in alkaline conditions. Electrodeposited CuSe exhibited superior efficiency for glucose oxidation with a sensitivity of $19.419 \text{ mA mM}^{-1} \text{ cm}^{-2}$ and a low detection limit of $0.196 \text{ }\mu\text{M}$, has a wide linear range $100 \text{ nM} - 40 \text{ }\mu\text{M}$ and fast response time of less than 2 s, long term stability and excellent selectivity. These attributes ensure that this system will be able to reliably detect very small fluctuation in glucose level in even bodily fluids such as urine, sweat, tears, tissue fluids etc., which has very low concentration of glucose. Additionally, the glucose oxidation at CuSe-modified electrodes occurs at very low working potential of $+0.15 \text{ V vs Ag|AgCl}$ which increases the energy efficiency of the system. These results reveal a great potential of electrodeposited CuSe as a high-efficiency glucose sensor with practical applicability.

Table 1. Results of glucose detection human blood.

Sample	Glucometer (mM)	CuSe (mM)	RSD (% , n=3)
1 st glucose	6.37	6.39	1.4
2 nd glucose	4.72	4.84	3.59
3d glucose	5.7	5.55	2.4
Blood 1	5.45	5.56	2.6
Blood 2	5.48	5.5	2.1

Table 2. Comparison of performance of various copper based nonenzymatic glucose sensors.

Electrode	Applied potential (/V vs Ag AgCl)	Sensitivity (mA mM ⁻¹ cm ⁻²)	Linear range	LOD (μM)	Ref
CuSe	0.15	19.41	100 nM-80μM; 100μM-2mM	0.196	This work
CuO NWA/CF	0.50	32.33	0.10 mM–0.50 mM	0.02	41
Cu ₂ Se SPS/CF	0.50	18.66	0.25 μM –0.237 mM	0.25	35
CuNi/C Nanosheet	0.54	17.12	0.2 μM –2.72 mM	0.066	42
Cu@porous carbon	0.55	10.1	1μM–6.0 mM	0.6	43
CuS/RGO/CuS/Cu	0.65	22.67	0.001–0.655 mM	0.5	44
CuO nanowires	0.55	0.648	-	2	12
CuO NPs	0.50	1430	0.04–6.0 mM	5	45
CuCo ₂ O ₄ NWAs /CC	0.55	3930	0.001–0.93 mM	0.5	46
CuO/rGO/CNT	0.60	9278	0.01–1 mM	1	47
CuO/NiO/PANI/GCE	0.60	3402	20 μM –2.5 mM	2	48
CuO–ZnO NRs/FTO	0.62	2961.7	Up to 8.45 mM	0.4	49

SUPPORTING INFORMATION

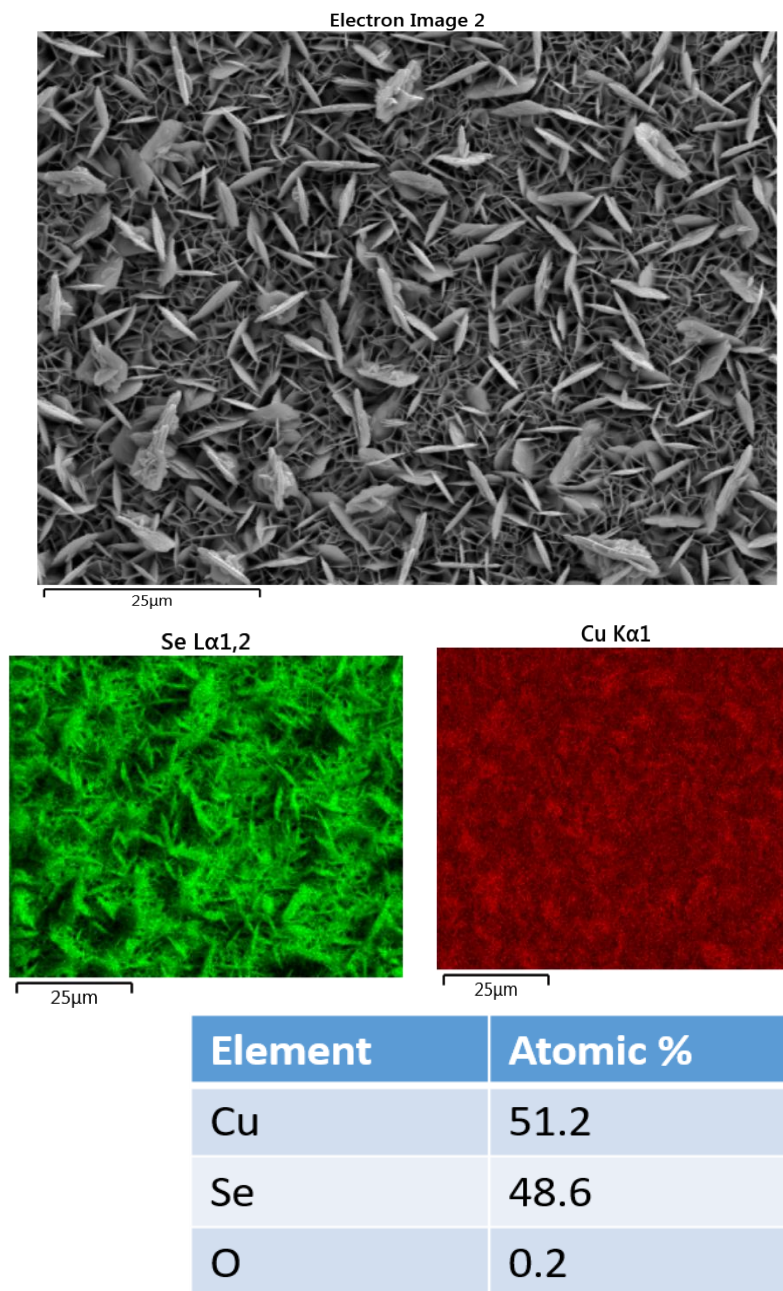


Figure S1. SEM image of CuSe at 1 μ M magnification, and elemental mapping of CuSe with atomic percentage distribution.

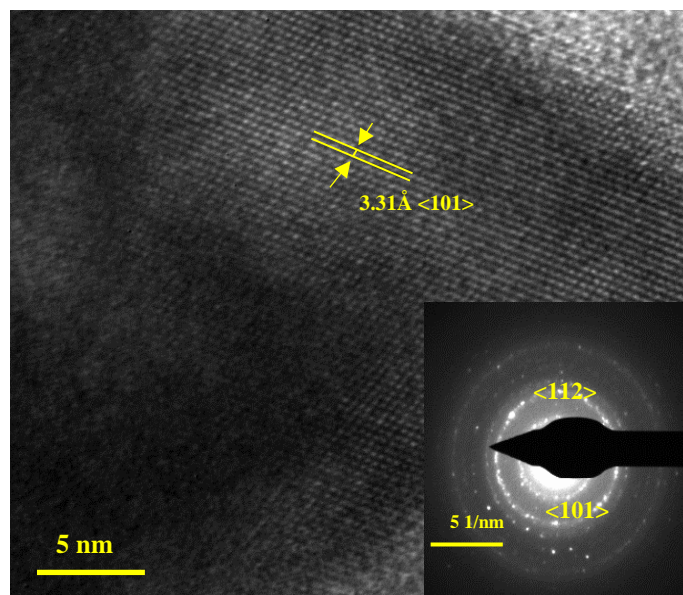


Figure S2. HR-TEM images ED- CuSe.

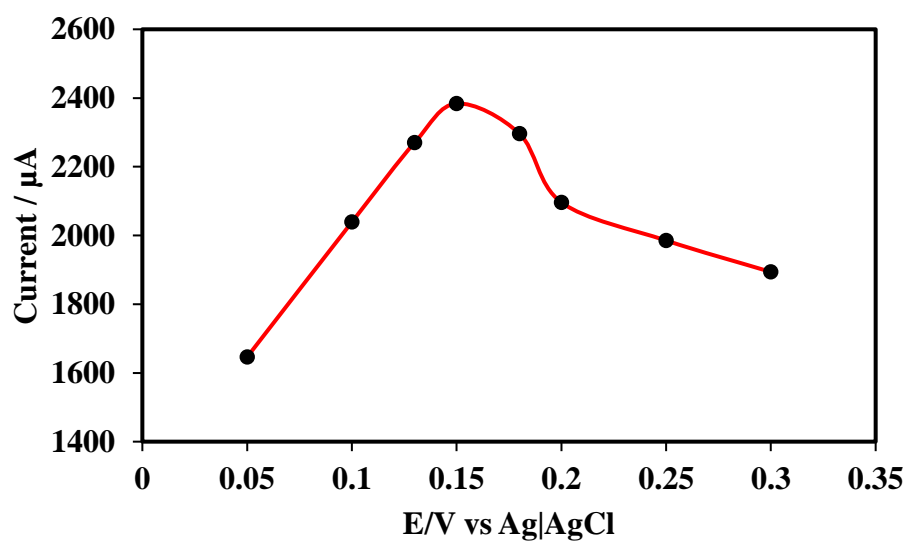


Figure S3. i vs V curve to determine the ideal working potential for glucose oxidation. +0.15 V vs Ag|AgCl shows the highest current and this potential is used for the rest of amperometric experiments.

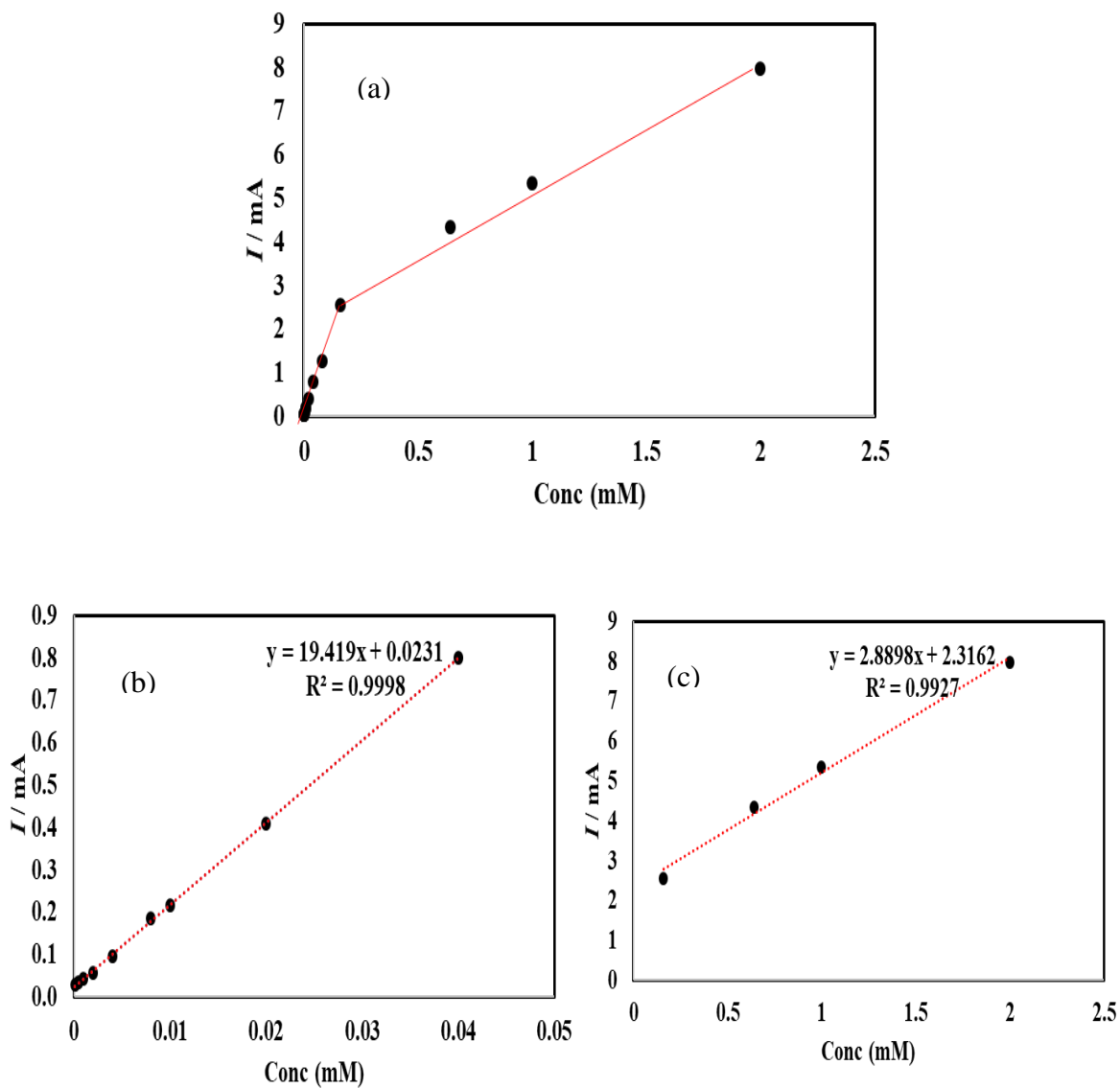


Figure S4. (a) Low and high concentration of CuSe peak current versus the concentration of glucose (b) linear range from 100 nM to 40 μ M and (c) linear range from 100 μ M to 2 mM.

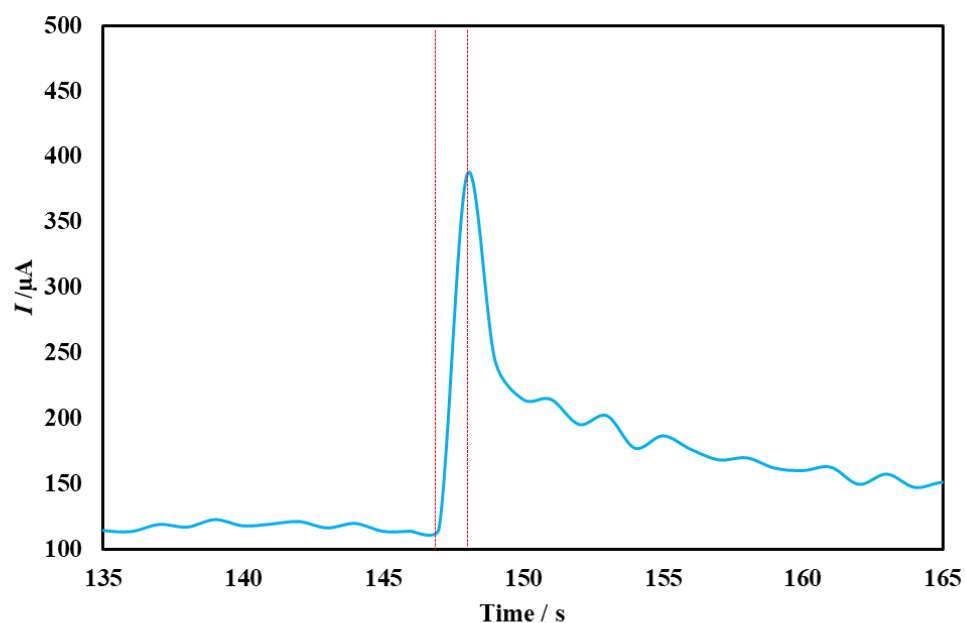


Figure S5. Plot of the response time to reach the steady-state current for CuSe.

REFERENCES

1. K. M. Bullard, C. C. Cowie, S. E. Lessem, S. H. Saydah, A. Menke, L. S. Geiss, T. J. Orchard, D. B. Rolka and G. Imperatore, *MMWR Morb Mortal Wkly Rep*, 2018, **67**, 359-361.
2. A. L. Galant, R. C. Kaufman and J. D. Wilson, *Food Chemistry*, 2015, **188**, 149-160.
3. A. T. Kharroubi and H. M. Darwish, *World J Diabetes*, 2015, **6**, 850-867.
4. A. Stokes and S. H. Preston, *PLoS One*, 2017, **12**, e0170219-e0170219.
5. G. Rocchitta, A. Spanu, S. Babudieri, G. Latte, G. Madeddu, G. Galleri, S. Nuvoli, P. Bagella, M. I. Demartis, V. Fiore, R. Manetti and P. A. Serra, *Sensors*, 2016, **16**, 780.

6. R. Gaia, S. Angela, B. Sergio, L. Gavinella, M. Giordano, G. Grazia, N. Susanna, B. Paola, D. Maria Ilaria, F. Vito, M. Roberto and S. Pier Andrea, *Sensors*, 2016, **16**, 780-780.
7. R. Wilson and A. P. F. Turner, *Biosensors and Bioelectronics*, 1992, **7**, 165-185.
8. E.-H. Yoo and S.-Y. Lee, *Sensors (Basel)*, 2010, **10**, 4558-4576.
9. J. Wang, *Chemical Reviews*, 2008, **108**, 814-825.
10. A. Harper and M. R. Anderson, *Sensors*, 2010, **10**, 8248-8274.
11. P. Si, Y. Huang, T. Wang and J. Ma, *RSC Advances*, 2013, **3**, 3487-3502.
12. Y. Zhang, Y. Liu, L. Su, Z. Zhang, D. Huo, C. Hou and Y. Lei, *Sensors and Actuators B: Chemical*, 2014, **191**, 86-93.
13. Y. Mu, D. Jia, Y. He, Y. Miao and H.-L. Wu, *Biosensors and Bioelectronics*, 2011, **26**, 2948-2952.
14. A. A. Saei, J. E. N. Dolatabadi, P. Najafi-Marandi, A. Abhari and M. de la Guardia, *TrAC Trends in Analytical Chemistry*, 2013, **42**, 216-227.
15. J. Luo, S. Jiang, H. Zhang, J. Jiang and X. Liu, *Analytica Chimica Acta*, 2012, **709**, 47-53.
16. H.-X. Wu, W.-M. Cao, Y. Li, G. Liu, Y. Wen, H.-F. Yang and S.-P. Yang, *Electrochimica Acta*, 2010, **55**, 3734-3740.
17. Z. Zhu, L. Garcia-Gancedo, A. J. Flewitt, H. Xie, F. Moussy and W. I. Milne, *Sensors*, 2012, **12**, 5996-6022.
18. Y. Zhang, Y. Wang, J. Jia and J. Wang, *Sensors and Actuators B: Chemical*, 2012, **171-172**, 580-587.
19. P. Vennila, D. J. Yoo, A. R. Kim and G. G. kumar, *Journal of Alloys and Compounds*, 2017, **703**, 633-642.
20. T. Chen, D. Liu, W. Lu, K. Wang, G. Du, A. M. Asiri and X. Sun, *Analytical Chemistry*, 2016, **88**, 7885-7889.
21. P. K. Kannan and C. S. Rout, *Chemistry – A European Journal*, 2015, **21**, 9355-9359.
22. X. Niu, M. Lan, H. Zhao and C. Chen, *Analytical Chemistry*, 2013, **85**, 3561-3569.

23. K. Ramachandran, T. Raj kumar, K. J. Babu and G. Gnana kumar, *Scientific Reports*, 2016, **6**, 36583.
24. J. Yang, X. Liang, L. Cui, H. Liu, J. Xie and W. Liu, *Biosensors and Bioelectronics*, 2016, **80**, 171-174.
25. M. Ranjani, Y. Sathishkumar, Y. S. Lee, D. Jin Yoo, A. R. Kim and G. Gnana kumar, *RSC Advances*, 2015, **5**, 57804-57814.
26. P. V. Suneesh, V. Sara Vargis, T. Ramachandran, B. G. Nair and T. G. Satheesh Babu, *Sensors and Actuators B: Chemical*, 2015, **215**, 337-344.
27. A. T. Swesi, J. Masud, W. P. R. Liyanage, S. Umapathi, E. Bohannan, J. Medvedeva and M. Nath, *Scientific reports*, 2017, **7**, 2401-2401.
28. M. Pumera, Z. Sofer and A. Ambrosi, *Journal of Materials Chemistry A*, 2014, **2**, 8981-8987.
29. M.-R. Gao, J. Jiang and S.-H. Yu, *Small*, 2012, **8**, 13-27.
30. S. Umapathi, J. Masud, A. T. Swesi and M. Nath, *Advanced Sustainable Systems*, 2017, **1**, 1700086.
31. U. De Silva, J. Masud, N. Zhang, Y. Hong, W. P. R. Liyanage, M. Asle Zaeem and M. Nath, *Journal of Materials Chemistry A*, 2018, **6**, 7608-7622.
32. J. Masud, P.-C. Ioannou, N. Levesanos, P. Kyritsis and M. Nath, *ChemSusChem*, 2016, **9**, 3128-3132.
33. J. Masud, W. P. R. Liyanage, X. Cao, A. Saxena and M. Nath, *ACS Applied Energy Materials*, 2018, **1**, 4075-4083.
34. Y. Wang, S. Liu, Y. Lai, Y. Zhu, R. Guo, Y. Xia, W. Huang and Z. Li, *Sensors and Actuators B: Chemical*, 2018, **262**, 801-809.
35. W. Zhu, J. Wang, W. Zhang, N. Hu, J. Wang, L. Huang, R. Wang, Y. Suo and J. Wang, *Journal of Materials Chemistry B*, 2018, **6**, 718-724.
36. M. B. Gawande, A. Goswami, F.-X. Felpin, T. Asefa, X. Huang, R. Silva, X. Zou, R. Zboril and R. S. Varma, *Chemical Reviews*, 2016, **116**, 3722-3811.
37. X. Liu, X. Duan, P. Peng and W. Zheng, *Nanoscale*, 2011, **3**, 5090-5095.
38. X. Liu, W. Yang, L. Chen and J. Jia, *Electrochimica Acta*, 2017, **235**, 519-526.

39. L. Zhang, C. Ye, X. Li, Y. Ding, H. Liang, G. Zhao and Y. Wang, *Nano-Micro Letters*, 2017, **10**, 28.
40. X. Zhang, J. Luo, P. Tang, J. R. Morante, J. Arbiol, C. Xu, Q. Li and J. Fransaer, *Sensors and Actuators B: Chemical*, 2018, **254**, 272-281.
41. C. Zhao, X. Wu, X. Zhang, P. Li and X. Qian, *Journal of Electroanalytical Chemistry*, 2017, **785**, 172-179.
42. F. Huang, Y. Zhong, J. Chen, S. Li, Y. Li, F. Wang and S. Feng, *Analytical Methods*, 2013, **5**, 3050-3055.
43. X. Luo, M. Huang, L. Bie, D. He, Y. Zhang and P. Jiang, *RSC Advances*, 2017, **7**, 23093-23101.
44. C. Lee, S. H. Lee, M. Cho and Y. Lee, *Microchimica Acta*, 2016, **183**, 3285-3292.
45. K. Ghanbari and Z. Babaei, *Analytical Biochemistry*, 2016, **498**, 37-46.
46. R. Ahmad, N. Tripathy, M.-S. Ahn, K. S. Bhat, T. Mahmoudi, Y. Wang, J.-Y. Yoo, D.-W. Kwon, H.-Y. Yang and Y.-B. Hahn, *Scientific Reports*, 2017, **7**, 5715.
47. K. G. Schick, V. G. Magearu and C. O. Huber, *Clinical Chemistry*, 1978, **24**, 448-450.
48. X. Cao, E. Johnson and M. Nath, *ACS Sustainable Chemistry & Engineering*, 2019, **7**, 9588-9600.
49. X. Cao, Y. Hong, N. Zhang, Q. Chen, J. Masud, M. A. Zaeem and M. Nath, *ACS Catalysis*, 2018, **8**, 8273-8289.

V. FeCo₂Se₄ – FUNCTIONALIZED ONION LIKE CARBON AS AN EFFICIENT CATALYST FOR OXYGEN EVOLUTION AND OXYGEN REDUCTION REACTION

*Siddesh Umapathi and Manashi Nath**

Department of Chemistry, Missouri University of Science & Technology,
Rolla, MO 65409, USA.

*Email: nathm@mst.edu

ABSTRACT

Construction of highly efficient and stable catalyst for water splitting is of high importance for wide variety of application. In this communication we report a bifunctional hybrid electrocatalyst FeCo₂Se₄ with functionalized onion like carbon (OLC-PhNH₂) for oxygen evolution reaction with a small overpotential of 270 mV to reach 10 mAcm⁻² and oxygen reduction reaction with an onset potential of 0.85 V and E_{1/2} of 0.75 V proceeds through a 4 electron process.

1. INTRODUCTION

The demand for clean and sustainable energy is one of the top priorities across the globe. Generation of hydrogen and oxygen through catalyst-aided water splitting which

has immense applications in metal air batteries, PEM fuel cells and solar to fuel energy production.^{1,2} IrO_x and RuO_x are known as the state-of-the-art oxygen evolution reaction (OER) and Pt /C is the best oxygen reduction reaction (ORR) catalysts which are mostly comprised of precious metals that hindered the commercialization of renewable energy technologies.^{3,4} Designing efficient and cost-effective water splitting catalysts remains the Holy Grail for large scale, affordable energy production from sustainable energy inputs, such as solar and wind.⁵

Several new catalysts based on first row transition metals has been reported in the recent past.^{6,7,8} Among these, Co based electrocatalyst takes a special mention as it has been reported for both OER and ORR applications.^{9,10} On the other hand transition metal selenides often generates O₂ at low overpotentials and also having a stability outperforming the state of the art catalysts.¹¹ Mixed metal selenides with ordered spinel structure having a general formula AB₂X₄ (A and B – metal; X - chalcogen) is proved to show better catalytic activity. Li et al. reported MFe₂O₄ (M = Co, Cu, Mn, Ni) nanofibers synthesized by electrospinning and thermal treatment. Among these compositions CoFe₂O₄ showed the best activity for OER.¹² This may be possibly due to the incorporation of iron in cobalt based system which can be understood as (i) The electrical conductivity of the system is increased (ii) Due to the d-d overlap within the crystal lattice. However, changing from CoFe₂X₄ to FeCo₂X₄ will allow half of the low spin Fe³⁺ to occupy the B site increases the Lewis acidity which gives ample catalytic sites for the hydroxyl groups for further OER process.¹³ This effect is also observed in Fe doped CoOOH which has shown improvement in OER catalytic activity by many folds.¹⁴

Incorporating the conducting carbon matrix such as graphene,¹⁵ reduced graphene oxide¹⁶ and carbon nanotubes¹⁷ has shown to increase the current density, and efficiency of the catalyst. In here, we have used onion like carbon (OLC) as the conducting carbon matrix, which consists of several fullerene like carbon shell enclosed within one another which have certain degree of disorder. The advantages of OLC are its high conductivity ($\sim 4 \text{ Scm}^{-1}$), high surface area and disordered nature which is makes it attractive for electrochemical applications.¹⁸ Further we have introduced a redox active surface species like phenylenediamine group on to OLC's through diazotization reaction, to incorporate the nitrogen content in the catalyst where the edge pyridinic and pyrrolic N are believed to be the hot spots for the energy conversion reactions.¹⁹

For the first time we report a P-Phenylenediamne (-PhNH₂) functionalized onion like carbon (OLCPhNH₂) combined with vacancy ordered spinel FeCo₂Se₄ to obtain a hybrid catalyst FeCo₂Se₄- OLCPhNH₂ (FCS-OLC PhNH₂) synthesized by simple insitu hydrothermal method, which is active for both oxygen evolution and oxygen reduction reactions. The OER catalytic activity shows a low overpotential of 270 mV to achieve 10 mA cm⁻² in alkaline solution with a small Tafel slope of 72 mV dec⁻¹. In addition, the catalyst is also active for ORR with an onset potential of 0.87 V vs RHE and having a 3.98 e⁻ process and a low H₂O₂ content of ~10-12 %. Electrodes prepared from the FCS-OLCPhNH₂ catalyst also shows excellent stability with retention of activity even after 12 h of constant current electrolysis for OER and 1000 cycles CV for ORR.

2. RESULT AND DISCUSSION

The synthesis of FCS- OLCPhNH₂ catalyst was carried out in a two-step strategy. First the nanoions were functionalized with –PhNH₂ group by a reported procedure. In the second step, stoichiometric quantities of Fe, Co and Se precursors were added along with the functionalized OLC in a Teflon lined hydrothermal bomb for 12 h at 185°C. The as obtained black product was washed several times using water and ethanol followed by drying overnight in an oven at 60°C. The as-synthesized catalyst was characterized by using powder X-ray diffraction (PXRD) patterns and compared with reference spectrum (PDF #04-006-5242). It was evident from PXRD that the as-synthesized hybrid catalyst was a good match with the reference diffraction pattern and all the peaks was indexed with almost no detectable impurities (Figure 1a). The average particle size was estimated to be ~50 nm calculated using the Scherrer equation.¹⁶ The morphological details of the hybrid catalyst was done using TEM, where the particles were nicely dispersed with OLC-PhNH₂ acting as a filling agent which increases the particle –particle contact and surrounds the FCS surface (Figure 1b). Due to the high surface energy the FCS particles are agglomerated, having a spherical morphology with ~100 nm particle size. The hybrid catalyst shows the FCS is monodispersed with OLCPhNH₂ surrounding each FCS particles (Figure 1c). TEM shows the surface of the hybrid catalyst has rough surface where the particle size of OLCPhNH₂ was approximately 5-8 nm. HRTEM patterns obtained from FCS- OLCPhNH₂ showed diffuse diffraction rings corresponding to the $\langle 311 \rangle$ and $\langle 110 \rangle$ lattice planes of FeCo₂Se₄, which also confirmed the presence of nanocrystalline FeCo₂Se₄

phase in the catalysts (Figure S1a). HRTEM images clearly shows the lattice fringes with a d spacing of 2.2 Å which corresponds to <311> facets of FeCo₂Se₄ (Figure S1b).

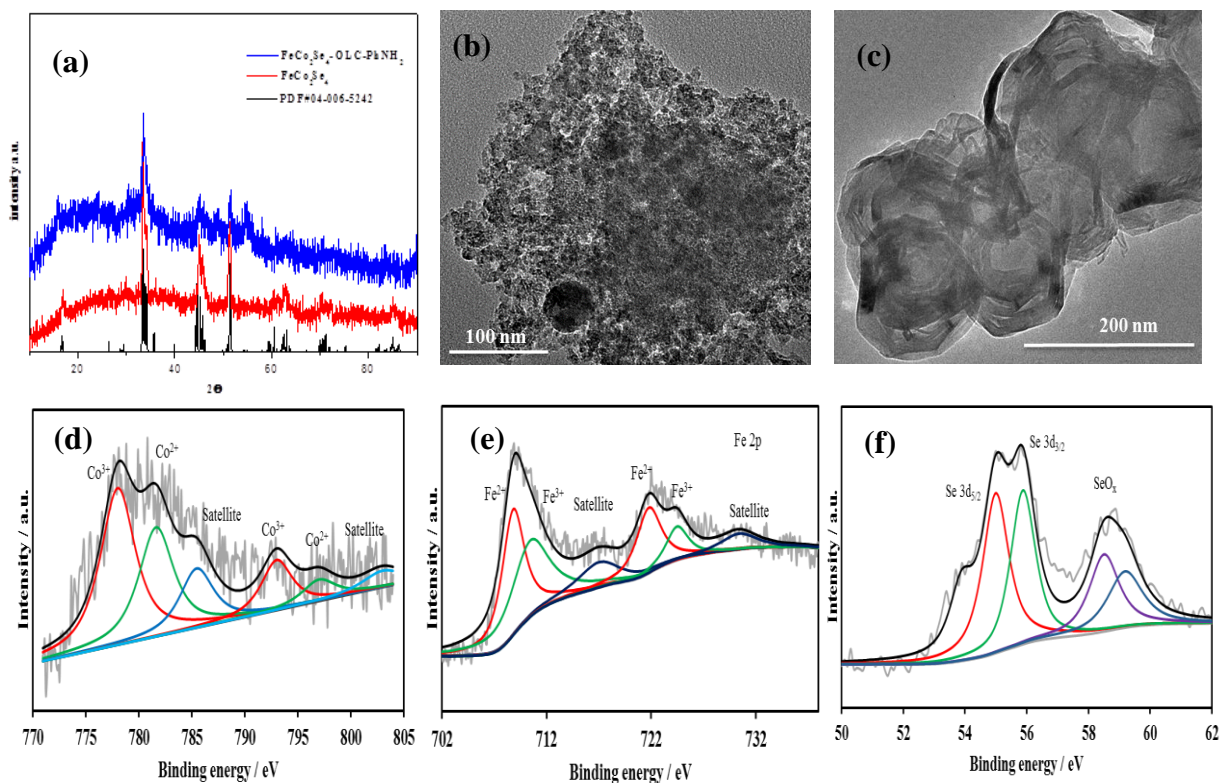


Figure 1. (a) XRD of FeCo₂Se₄- OLCPhNH₂ (b) TEM images of FeCo₂Se₄- OLCPhNH₂ (c) FeCo₂Se₄. Deconvoluted XPS spectra of (d) Co 2p (e) Fe 2p and (f) Se 3d.

The FTIR spectra of pristine carbon nano-onions and functionalized carbon nanonions comparing with diazonium salt are shown in Figure S2. The spectrum of pristine nano-onions shows peaks relating to C-H stretching to aldehyde and alkane at 2656 and 2957 cm⁻¹ respectively along with the OH stretching at 3482cm⁻¹ due to physisorbed water,

indicating presence of IR-active functional groups in the CNO sample. After the diazotization reaction, the spectra of functionalized carbon nanoions peaks about 1603 and 2876 cm^{-1} appear which originates to N-H bending (amine group) and N-H stretching respectively.

The chemical composition of the as synthesized hybrid catalyst was analyzed by X-ray photoelectron spectroscopy (XPS). All binding energies for Fe, Co and Se were calibrated with respect to C 1s (284.5 eV) as a reference binding energy. The chemical composition and the oxidation state of the catalyst were investigated from the deconvoluted XPS spectra, and the corresponding results are presented in (Figure 1d-1f). The deconvoluted Fe 2p and Co 2p confirmed the presence of mixed valence of metal ions which might play a significant role in their catalytic activity. As shown in Figure. 1d, the binding energies are 778.34 and 793.44 eV of Co 2p are assigned to Co^{3+} and of 780.66 and 795.64 eV are attributed to Co^{2+} with its shake-up satellite peaks at 785.47 and 802.52 eV.²⁰ Similarly, in the Fe 2p spectra (Figure. 1d), the peaks at 708.82 and 721.76 eV correspond to Fe^{2+} while those at 710.59 and 724.48 eV corroborate with Fe^{3+} .²⁰ In the Se 3d XPS spectrum in Figure. 1e, the peaks at 53.76 and 55.45 eV correspond to Se $3d_{5/2}$ and Se $3d_{3/2}$, respectively, which were comparable with the binding energies commonly observed in the transition metal selenides. SeO_x peaks are observed at 58.5 and 59.43 eV due to the surface oxidation.²¹

All the catalytic activities have been measured in 1 M KOH alkaline solution and the results were compared with state-of-the-art OER catalyst RuO_2 , which was prepared in by electrodeposition. Calibrated silver-silver chloride ($\text{Ag}|\text{AgCl}|\text{KCl}_{(\text{sat.})}$) and GC plate were used as reference electrode and counter electrode respectively. The catalyst was drop

casted on commercially available carbon fiber paper (CFP). Loading of the FCS-OLCPhNH₂ was calculated to be 0.6 mg cm⁻². Electrochemically active surface area (ECSA) was calculated by using the double layer capacitance current in the non-Faradaic region similar to the previous reports (SI Figure S3).²⁷² The ECSA of the hybrid catalyst and FCS was found to be 61 cm² and 42 cm² respectively, which is 19 times higher than the FCS. Figure 2a shows the linear sweep voltammograms (LSV) of the catalysts in 1 M KOH at a scan rate of 10 mV s⁻¹. Interestingly, hybrid catalyst (FCS-OLCPhNH₂) requires very low overpotential (270 mV) to achieve 10 mA cm⁻² current density compared to catalyst (FCS) without adding any OLCPhNH₂ (320 mV needs to get 10 mA cm⁻²). It is to be noted that the ratio between the FCS to OLCPhNH₂ was 80:20, which gave the best OER activity. On the other hand, by increasing the OLCPhNH₂ content to catalyst, activity was decreased substantially. For instance, 50:50 ratio of FCS to OLCPhNH₂ increased the overpotential to 310 mV and 30:70 ratio of FCS to OLCPhNH₂ of addition further increased to 315 mV to get the current density of 10 mA cm⁻². This trend of reduction in the OER activity suggests that the active center is the structurally ordered FeCo₂Se₄ and OLCPhNH₂ acts as the conducting matrix surrounding the active center for better charge transfer and faster kinetics. With the increase in FCS content, the OER activity increases firstly and reaches the maximum value when the FCS content is 80 wt%. It declines sharply thereafter, indicating that the synergistic effect is dependent on the loading amount of OLCPhNH₂ is neither too low nor too high. In order to know the OER kinetic of these catalysts, Tafel plots have been derived from the OER polarization curves and presented in Figure S4. The hybrid catalyst exhibited the lower value (72 mV s⁻¹) of Tafel slopes than that of the others. The low value in Tafel supports the faster OER kinetics of the catalysts. These values are

superior to the noble metal based state of art catalyst RuO_2 and also noteworthy considering the facile synthetic approach. Table 1 provides the comparison of our synthesized the different catalysts and reported cobalt chalcogen-based OER catalysts where FCS-OLCPhNH₂ showed the better OER catalytic activity. Chronoamperometric study was conducted to understand the stability of hybrid catalyst at a constant potential of 1.53 V for 12 h as shown in Figure 2b. There was no degradation of current during the continuous oxygen evolution process suggesting that the catalyst is quite stable. The OER polarization curves exhibit the similar activity before and after stability for 12 h. This exceptional stability of the hybrid catalyst is achieved by the suitable combination of the FCS and the OLCPhNH₂. The compositional stability of catalyst was further checked by XPS after stability for 12 h. The XPS binding energies of Fe 2p, Co 2p and Se 3d (Figure. S5) of the catalyst after stability showed the similar values that of as prepared catalyst.

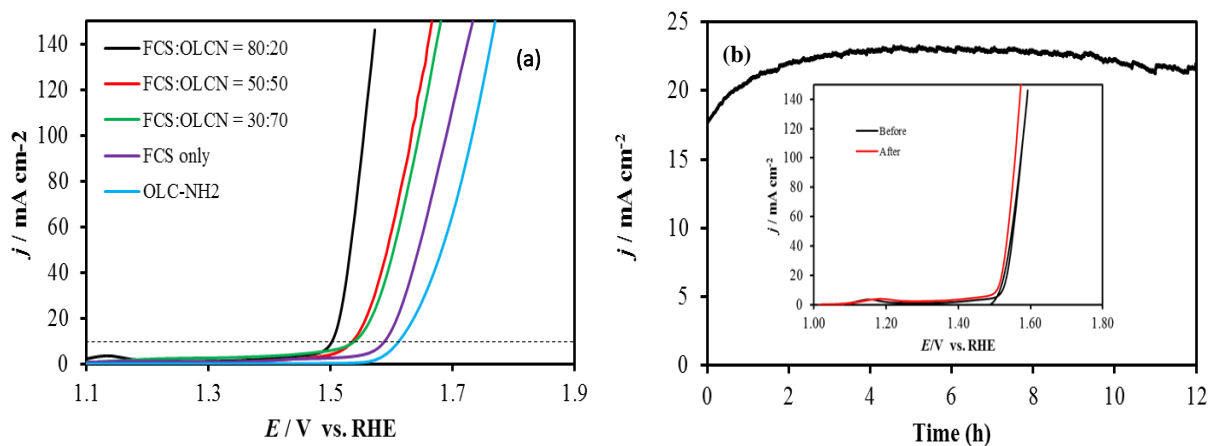


Figure 2. (a) OER comparison and (b) chronoamperometry at 1.53 V for 12 h, LSV before and after of 12 h stability (inset).

We extended our study of the hybrid catalyst to oxygen reduction reaction (ORR) which is the main reaction taking place in the fuel cell technology. ORR was performed using the RRDE setup with O₂ saturated 1M KOH solution. The ORR hydrodynamic voltammograms of the FCS-OLCPhNH₂ hybrid catalyst (mass loading of 0.55 mg cm⁻²) were carried out at a scan rate of 10 mVs⁻¹ with different rotation rates as shown in Figure 3a. It is evident that FCS- OLCPhNH₂ has better ORR onset (0.87 V vs RHE) than the FCS (0.84 V vs RHE). The ORR activity of this hybrid catalyst was compared with the commercial Pt/C (5 wt % of Pt) that shows an onset potential of 0.96 V vs RHE. FCS-OLCH has a positive onset potential and higher limiting current density than FCS and OLCPhNH₂, suggesting that synergistic effect plays a pivotal role in the overall performance. The half wave potential (E_{1/2}) of FCS- OLCPhNH₂ 0.7 V vs RHE which is less than compare to 5% Pt (0.82 V vs RHE), but better than FCS (E_{1/2}=0.67 vs. RHE) and OLCPhNH₂ (E_{1/2}=0.68 V vs. RHE) A positive onset potential, E_{1/2} and a higher limiting current density makes FCS- OLCPhNH₂ superior to FCS and OLCPhNH₂. To obtain further information about ORR kinetics, the Koutecky–Levich plots (j⁻¹ vs. ω^{-1/2}) of hybrid catalyst are obtained from LSVs at various potentials, which showed good linearity at various rotation speed (Figure 3c). Using the KL plot electron transfer number (n) of FCS-OLCPhNH₂ and Pt/C were calculated to be 4 at a wide potential range, which suggests a four-electron pathway for oxygen reduction. In addition the %H₂O₂ was calculated to 10-12% using the formula in given SI.

We evaluate the kinetic parameters Tafel plots of FCS- OLCPhNH₂ and Pt/C derived from LSVs data are compared as shown in Figure. S6, the Tafel slope of FCS-OLCPhNH₂ is 91.3 mV per decade, which is close to the 82.8mV per decade of the Pt/C,

indicating that the FCS- OLCPhNH₂ has good kinetic current for ORR. To better understanding the role of OLCPhNH₂ in the enhancing the catalytic activity for the ORR of FCS, the loading of OLCPhNH₂ was increased to 50% by weight and the catalytic performance of FCS: OLCPhNH₂= 50:50 was examined using the RRDE (Figure. 3a). The different mass loading of OLCPhNH₂ in the hybrid can be obtained by varying the concentration of the OLCPhNH₂ solution in the hydrothermal process. It is found that only an appropriate ratio of OLCPhNH₂ gives the best ORR activity. The highest ORR activity is obtained at FCS: OLCPhNH₂ ratio of 70:30. More theoretical analysis and experimental characterization are still necessary to unravel the detailed mechanism of the ORR process of the hybrid.

To investigate the stability of the catalyst continues CV was performed for 1000 cycles in 1M KOH solution under constant supply of oxygen at 1200 RPM. Figure 3d shows the LSV of FCS- OLCPhNH₂ before and after 1000 cycles where the catalyst retained the onset, half wave potential and current density proving the excellent stability in alkaline solution. We believe that it may be due to the unique properties of OLCPhNH₂, which could act as an oxygen buffer and feed the adjacent FCS with additional oxygen.

Therefore, the experimental results shows the hybrid FeCo₂Se₄-OLCPhNH₂ demonstrates best OER and ORR activity as compared to the activity of the spinel or the carbonaceous material alone. This can be attributed to cobalt in the low spin configuration with $t_{2g}^6e_g^1$ electronic configuration where e_g has one electron, which is high optimal for OER catalytic activity.²² Further the presence of iron increases the affinity for oxygen species and with cobalt in the system it significantly promotes the 4e⁻ process in ORR process. This phenomenon also improves the OER process by reducing the overpotential

close to 1.23 V. Additionally as previously stated that replacing oxides with selenides can bring the band gap closer to water oxidation levels enhancing the redox activity at the metal site and consequently lowering the overpotential in OER and improved onset and $E_{1/2}$ in case of ORR. The synergistic effect between iron and cobalt on highly conductive functionalized onion like carbons may contribute in enhancing intrinsic property of FeCo_2Se_4 .

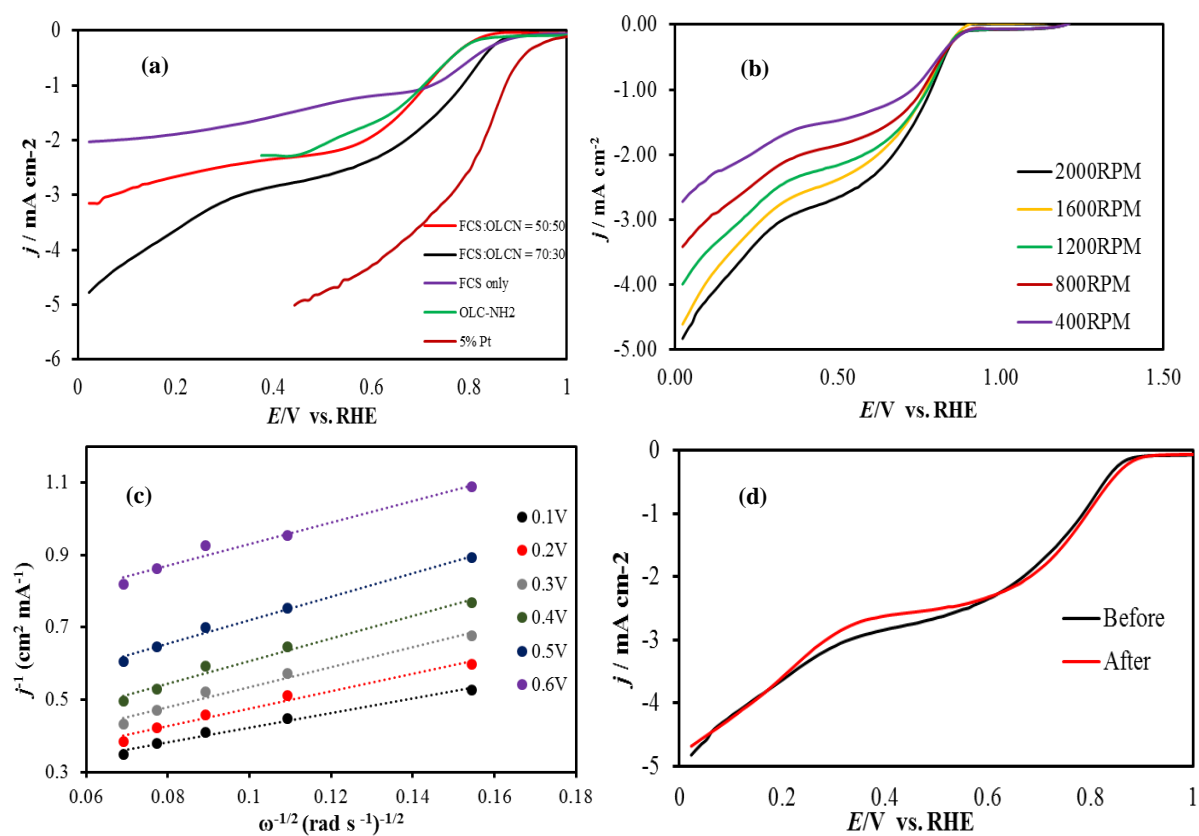


Figure 3. (a) ORR comparison of FCS- OLCPhNH₂ with different ratios, FCS, OLCPhNH₂ and 5% Pt (b) ORR polarization curves of FCS- OLCPhNH₂ at different rotations (c) K-L plots at different potential (d) LSV comparison of FCS- OLCPhNH₂ for before and after 1000 cycles.

3. CONCLUSION

In conclusion, we have reported an earth abundant and carbon based FeCO₂Se₄-OLCPhNH₂ bifunctional hybrid catalyst for OER and ORR with high energy efficiency. For OER the catalyst requires a low overpotential of 270 mV to achieve 10 mA cm⁻² with a Tafel slope of 72 mV dec⁻¹. The catalyst is also active for ORR with an onset potential of 0.87 V and undergoes a 4 electron process with a low H₂O₂ production of 10-12%. Additionally, the catalyst shows an excellent stability with for both of OER and ORR for extended period of time. Overall with high efficiency and catalytic activity combined with stability this system makes it an important member for sustainable future.

SUPPORTING INFORMATION

Materials and Methods

Materials. Cobalt Sulfate heptahydrate (CoSO₄ · 7H₂O) from Acros Chemicals, Iron sulfate heptahydrate (FeSO₄ · 7H₂O) from Fisher Scientific, Selenium dioxide [SeO₂] from Acros chemicals, Hydrazine monohydrate from Acros chemicals and KOH from Fisher chemicals. All chemicals were of analytical grade and were used as received without further purification.

Synthesis of Functionalized Carbon Nanooxions (OLC-PhNH₂). The carbon nanooxions (23.1 mg), p-Penylenediamine (23.1 mg, 0.2136 mmol), sodium nitrite (1.05 equivalent mol of p-penylenediamine, 15.48 mg), and 5 mL of deionized water were added to a 20 mL glass vial and sonicated for 20 minutes at room temperature. After sonication

the vial was putted in ice-salt bath with stirring until temperature achieve 0-5°C and add deionized water at 0°C to a volume 10 mL. For initiation reaction the hydrochloric acid was added dropwise until pH of solution equals 2-3. The reaction was carried out for an hour controlling the temperature (0-5°C). After the reaction, washing and centrifugation (8000 rpm, 15 minutes for each time) were performed until pH = 5-6 and the resulting sediment was dried in vacuum oven at 60°C.

Synthesis of FeCo₂Se₄. FeCo₂Se₄ nanoparticles was synthesized by hydrothermal method. In a typical procedure, FeSO₄·7H₂O (5 mmol), CoSO₄·7H₂O (10 mmols) and SeO₂ (20 mmols) were mixed in DI water (10 ml). The solution was stirred on a magnetic stirrer. About 5 mins later hydrazine monohydrate (0.25 ml) was added. The solution of stirred for another 5 mins and then transferred to 23 ml Teflon - lined autoclave, which was sealed and maintained at 185°C for 12 h and then naturally cooled to room temperature. The resulting black solid was then washed several times with DI water and ethanol. The solid was dried in an oven maintained at 40°C overnight.

Synthesis of FeCo₂Se₄ – OLCPhNH₂. Firstly, OLC-PhNH₂ is taken 20% by weight in DI water (5 ml). This mixture was sonicated for 15 mins. OLC-PhNH₂-water mixture is added to FeCo₂Se₄ nanoparticles (from the above procedure) while stirring. Hydrazine monohydrate (0.25 ml) is added and this solution is sonicated for 30 mins. This solution is transferred to 23 ml Teflon - lined autoclave, which was sealed and maintained at 185°C for 12 h and then naturally cooled to room temperature. The cleaning procedure remains same as above. Hydrazine monohydrate was used as reducing agent, which reduces the Se⁴⁺ to Se²⁻. An additional step of sonicating the above solution for 20 mins was introduced. Sonication of a FeCo₂Se₄ - OLC-PhNH₂ dispersion in the presence of

reducing agent like hydrazine monohydrate results in high-coverage of OLC on the surface of metal nanoparticles. This increases the likelihood of metal nanoparticle fill on single-layer rGO sheets. Hydrothermal treatment at 185°C for 12 h gave FeCo₂Se₄-NrGO powder. During the hydrothermal treatment, crystallization of FeCo₂Se₄ and further attachment of OLC-PhNH₂ around the nanoparticles was achieved simultaneously.

Tafel plots. The catalytic performance of the hybrid catalyst for OER is carried out by measuring the Tafel slopes according to the equation given below:

$$\eta = a + \frac{2.3 RT}{\alpha n F} \log(j) \quad (1)$$

where η is the overpotential, j is the current density and the other symbols have their usual meanings.

The percentage of the electrogenerated hydrogen peroxide ($X_{\text{H}_2\text{O}_2}$) and the number of electron transferred (n) during the ORR were also calculated using Eqs. (2) and (3):

$$X_{\text{H}_2\text{O}_2} = \frac{\frac{200I_{\text{R}}}{N}}{I_{\text{D}} + \frac{I_{\text{R}}}{N}} \quad (2)$$

$$n = \frac{4I_{\text{D}}}{I_{\text{D}} + \frac{I_{\text{R}}}{N}} \quad (3)$$

where I_{D} and I_{R} are the disk and ring currents, respectively and N is the collection efficiency (0.24).

K-L Plots. The number of electrons transferred per oxygen molecule involved in the ORR at the FeNi₂Se₄-NrGO@GC electrode was determined by the Koutecky-Levich equation.

$$\frac{1}{j} = \frac{1}{j_k} + \frac{1}{B\omega^{1/2}} \quad (4)$$

where j_k is the kinetic current density B is the so-called B-factor and equal to $0.62nFC_bD_o^{2/3}v^{-1/6}$ k is the rate constant, n is number of electrons transferred for per oxygen molecule, F is the Faraday constant (96 485 C mol⁻¹), A is geometric area of electrode (0.196 cm²), D_{O2} is the diffusion coefficient of O₂ (1.9×10^{-5} cm² s⁻¹), v is the kinetic viscosity of the solution (1.009×10^{-2} cm² s⁻¹), and C_{O2} is the concentration of dissolved O₂ in solution (1.2×10^{-6} mol cm⁻³). A plot of j_k vs. C_{O_2} should yield a straight line having a slope equal to B. The values of B allow us to assess the number of electrons involved in the ORR.

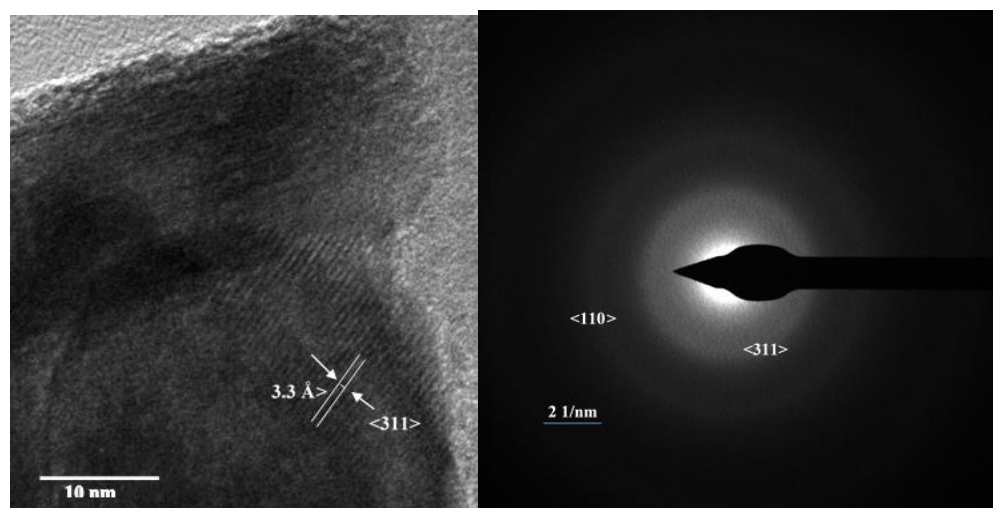


Figure S1. HRTEM and SAED of FeCo₂Se₄.

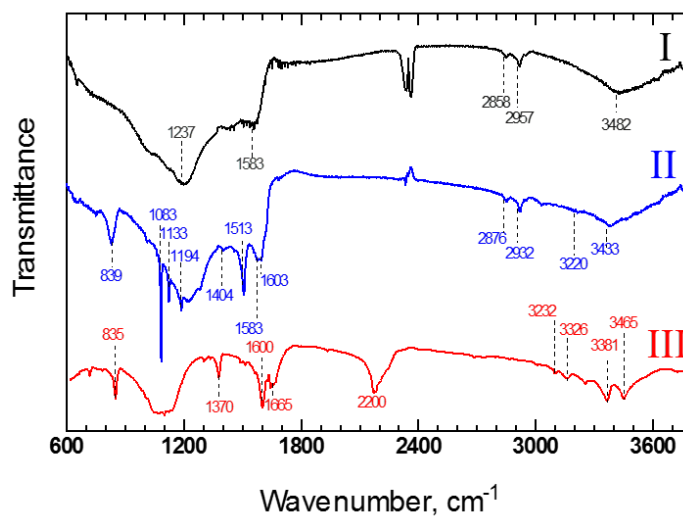


Figure S2. Characterization of OLC-PhNH₂ by IR spectroscopy I – Carbon nanoions, II – Functionalized carbon nanoions III – Diazonium salt.

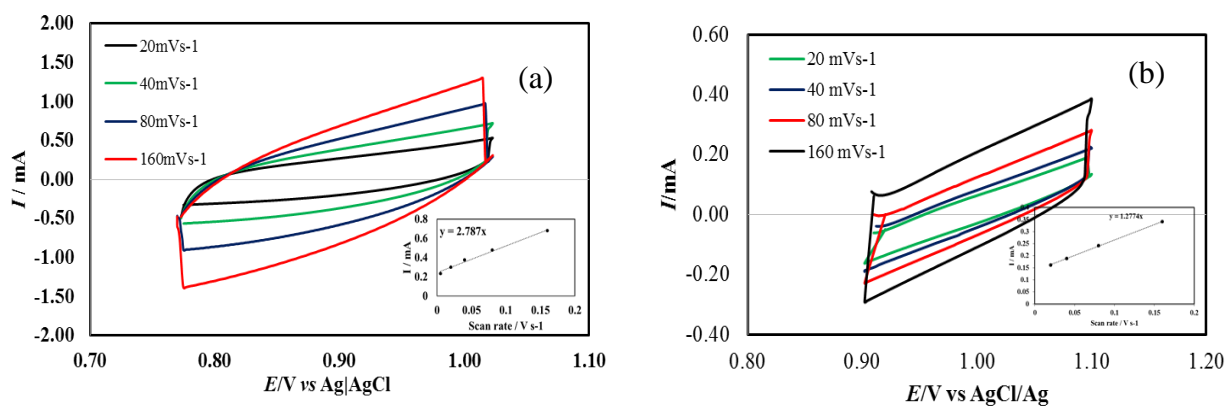


Figure S3. (a) ECSA for FCS-OLCPhNH₂ (b) ECSA for FCS.

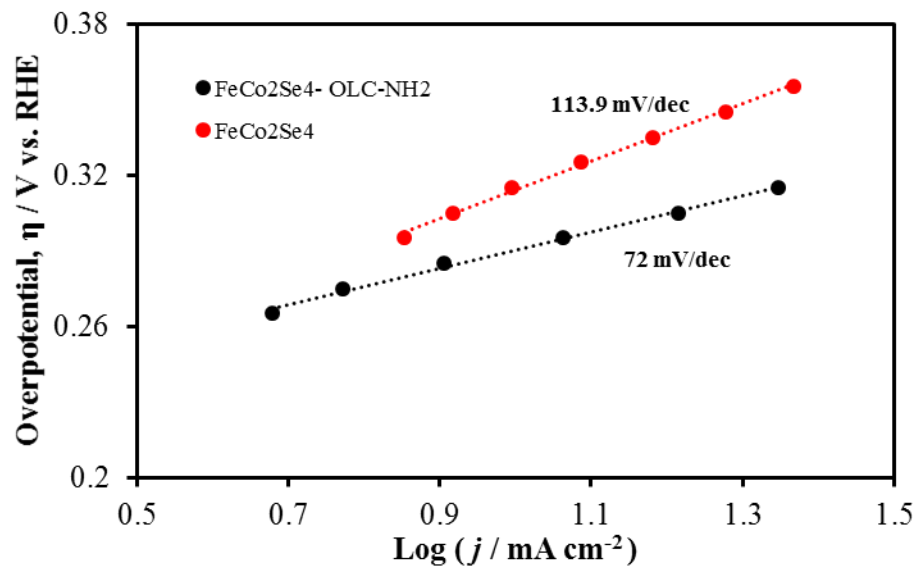


Figure S4. Tafel plot for OER.

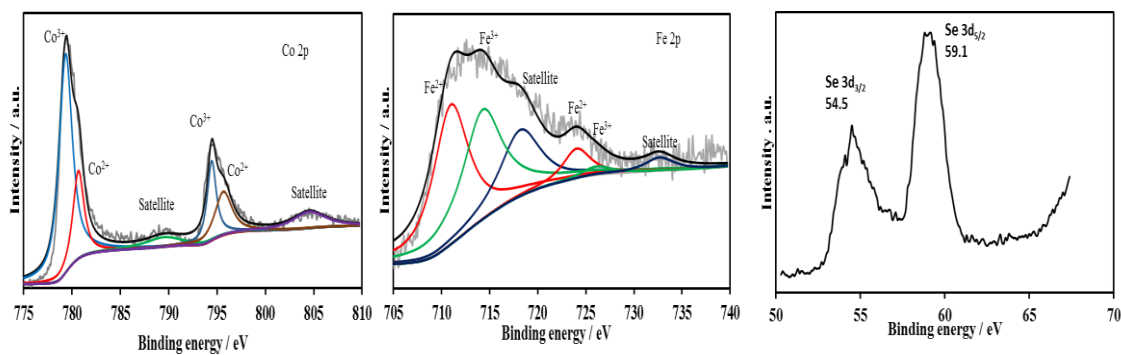


Figure S5. XPS after activity.

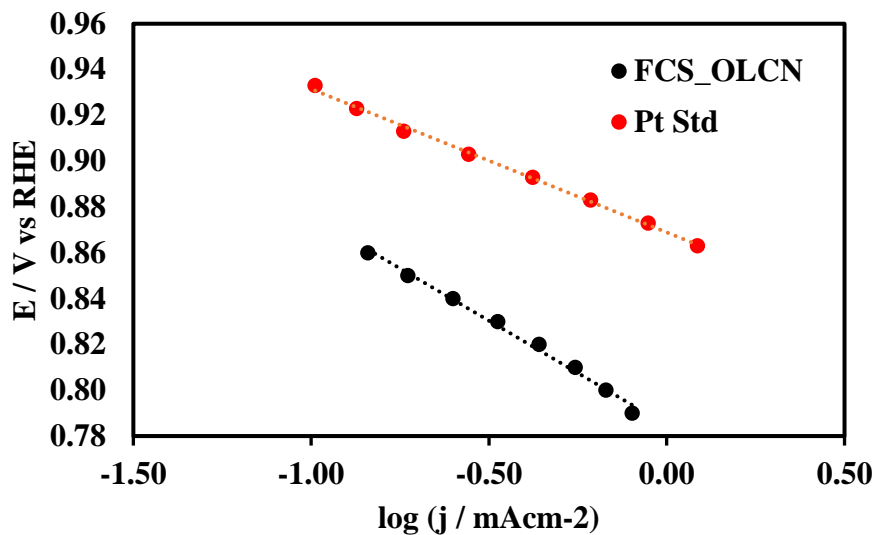


Figure S6. Tafel plot of FCS- OLCPhNH₂ comparing with Pt/C for ORR.

REFERENCES

1. J. R. McKone, N. S. Lewis and H. B. Gray, *Chemistry of Materials*, 2013, **26**, 407-414.
2. N. Armaroli and V. Balzani, *Angew Chem Int Ed Engl*, 2007, **46**, 52-66.
3. E. Slavcheva, U. Schnakenberg and W. Mokwa, *Applied Surface Science*, 2006, **253**, 1964-1969.
4. S. Henning, L. Kuhn, J. Herranz, J. Durst, T. Binniger, M. Nachttegaal, M. Werheid, W. Liu, M. Adam, S. Kaskel, A. Eychmuller and T. J. Schmidt, *J Electrochem Soc*, 2016, **163**, F998-F1003.
5. A. J. Bard and M. A. Fox, *Accounts Chem Res*, 1995, **28**, 141-145.
6. C. C. McCrory, S. Jung, J. C. Peters and T. F. Jaramillo, *J Am Chem Soc*, 2013, **135**, 16977-16987.

7. G. Liu, K. Wang, X. Gao, D. He and J. Li, *Electrochim Acta*, 2016, **211**, 871-878.
8. H. Zhang, H. Li, H. Wang, K. He, S. Wang, Y. Tang and J. Chen, *J Power Sources*, 2015, **280**, 640-648.
9. Y. Liang, Y. Li, H. Wang, J. Zhou, J. Wang, T. Regier and H. Dai, *Nat Mater*, 2011, **10**, 780-786.
10. Y. Liu, H. Cheng, M. Lyu, S. Fan, Q. Liu, W. Zhang, Y. Zhi, C. Wang, C. Xiao, S. Wei, B. Ye and Y. Xie, *J Am Chem Soc*, 2014, **136**, 15670-15675.
11. J. Masud, A. T. Swesi, W. P. Liyanage and M. Nath, *ACS Appl Mater Interfaces*, 2016, **8**, 17292-17302.
12. M. Li, Y. Xiong, X. Liu, X. Bo, Y. Zhang, C. Han and L. Guo, *Nanoscale*, 2015, **7**, 8920-8930.
13. T. A. S. Ferreira, J. C. Waerenborgh, M. H. R. M. Mendonça, M. R. Nunes and F. M. Costa, *Solid State Sciences*, 2003, **5**, 383-392.
14. M. S. Burke, M. G. Kast, L. Trotochaud, A. M. Smith and S. W. Boettcher, *J Am Chem Soc*, 2015, **137**, 3638-3648.
15. S. Chen and S.-Z. Qiao, *Acs Nano*, 2013, **7**, 10190-10196.
16. S. Umapathi, J. Masud, A. T. Swesi and M. Nath, *Advanced Sustainable Systems*, 2017, **1**, 1700086.
17. Y. Cheng and S. P. Jiang, *Progress in Natural Science: Materials International*, 2015, **25**, 545-553.
18. M. Zeiger, N. Jackel, V. N. Mochalin and V. Presser, *J Mater Chem A*, 2016, **4**, 3172-3196.
19. X. Ge, A. Sumboja, D. Wu, T. An, B. Li, F. W. T. Goh, T. S. A. Hor, Y. Zong and Z. Liu, *Acs Catal*, 2015, **5**, 4643-4667.
20. J.-Y. Zhang, L. Lv, Y. Tian, Z. Li, X. Ao, Y. Lan, J. Jiang and C. Wang, *Acs Appl Mater Inter*, 2017, **9**, 33833-33840.
21. C. Xia, Q. Jiang, C. Zhao, M. N. Hedhili and H. N. Alshareef, *Adv Mater*, 2016, **28**, 77-85.
22. L. Liang, H. Cheng, F. Lei, J. Han, S. Gao, C. Wang, Y. Sun, S. Qamar, S. Wei and Y. Xie, *Angewandte Chemie International Edition*, 2015, **54**, 12004-12008.

SECTION

2. CONCLUSIONS

Transition metal chalcogenides synthesized by hydrothermal and electrodeposition techniques were studied for electrochemical applications in this study. These transition metal chalcogenides have combined with various conductive carbon matrix such as reduced graphene oxide, onion like carbons and carbon nanotubes to improve the properties. Also these hybrid nanostructuring of the electrocatalyst increases the electrocatalytic efficiency manifold by increasing the functional surface area. The aim of this research is to synthesize high efficiency electrocatalysts from transition metal selenides using the principles of materials chemistry to particularly tune the redox potential of the centre metal site by redistributing the electron density and therefore influencing the activity.

Paper I introduces the solution based method of synthesizing FeP nanoparticles and further making a hybrid catalyst by introducing reduced graphene oxide as a conducting carbon matrix. This catalyst requires comparatively lower overpotential to achieve 10 mA cm⁻² which is significantly lower than the state-of-the-art IrOx catalysts and is one of the lowest for phosphide based electrocatalyst. Importantly, the FeP nanoparticles can be combined with reduced graphene oxide sheets which results in significantly improved catalytic activity owing to the synergistic effect. High catalytic activity along with the ease of synthesis of the nanoparticles, makes this system have high technological importance.

Paper II introduces one pot hydrothermal method of synthesizing FeNi₂Se₄-rGO hybrid catalyst in nanometer range for energy conversion application. The exceptional OER activity is characterized by a small η of 170 mV at the current density of 10 mV cm⁻² and a Tafel slope down to 62.1 mV dec⁻¹. The low onset potential required for O₂ evolution as well as overpotential required to reach 10 mA cm⁻², is one of the lowest that has been reported so far, making this hybrid composite a very promising OER electrocatalyst. The ORR activity is also better than the other chalcogenide based electrocatalysts and is comparable to Pt. Hence, this novel hybrid composite has exhibited significantly enhanced OER-ORR catalytic performances with high catalytic activity, favorable kinetics, and extended stability. The synergistic coupling between the N-doped reduced graphene oxide and FeNi₂Se₄ nanoparticles is believed to boost the excellent OER performance.

Paper III similarly shows the importance of carbon matrix to improve the performance of hybrid catalyst. FeCo₂Se₄ – OLCPhNH₂ was synthesized by hydrothermal method and thoroughly characterized to know the structure and morphology. This hybrid catalyst similarly shows bifunctional capabilities towards OER and ORR. For OER the catalyst requires a low overpotential of 270 mV to achieve 10 mA cm⁻² with a Tafel slope of 72 mV dec⁻¹. The catalyst is also active for ORR with an onset potential of 0.87 V and undergoes a 4 electron process with a low H₂O₂ production of 10-12%. Additionally, the catalyst shows an excellent stability with for both of OER and ORR for extended period of time. The simple synthetic method, earth abundancy of the constituent elements, and low overpotential makes this bifunctional catalyst a front runner for various energy related applications.

Paper IV explains the use of transition metal selenides as sensor material to detect dopamine for the first time. CuSe was synthesized by two methods namely hydrothermal and electrodeposition. Irrespective of the material synthesis CuSe sensed dopamine at nanomolar range. The high sensitivity ($26.8 \mu\text{A } \mu\text{M}^{-1} \text{cm}^{-2}$ for ED and $8.80 \mu\text{A } \mu\text{M}^{-1} \text{cm}^{-2}$ for HT) at a low applied potential of $+0.18 \text{ V vs Ag|AgCl}$, low detection limit (98 nM for ED and 68 nM of HT), short response time (1 s), makes these sensors lucrative for practical applications in real-time continuous dopamine monitoring systems as well as point-of-care detection units. The CuSe based non-enzymatic dopamine sensor has impressive selectivity for dopamine sensing, long-term stability and repeatability.

Paper V exhibits CuSe as a non enzymatic glucose sensor which was synthesized by simple electrodeposition producing a flake like nanostructures. The electrocatalytic activity for glucose oxidation was studied in alkaline conditions. Electrodeposited CuSe exhibited superior efficiency for glucose oxidation with a sensitivity of $19.419 \text{ mA mM}^{-1} \text{cm}^{-2}$ and a low detection limit of $0.196 \mu\text{M}$, has a wide linear range $100 \text{ nM} - 40 \mu\text{M}$ and fast response time of less than 2 s , long term stability and excellent selectivity at very low applied potential of $+0.15 \text{ V vs Ag|AgCl}$. These results reveal a great potential of electrodeposited CuSe as a high-efficiency glucose sensor with practical applicability.

REFERENCES

1. G. Gahleitner, *International Journal of Hydrogen Energy*, 2013, **38**, 2039-2061.
2. S. H. Jensen, P. H. Larsen and M. Mogensen, *International Journal of Hydrogen Energy*, 2007, **32**, 3253-3257.
3. M. Balat, *International Journal of Hydrogen Energy*, 2008, **33**, 4013-4029.
4. M. N. Manage, D. Hodgson, N. Milligan, S. J. R. Simons and D. J. L. Brett, *International Journal of Hydrogen Energy*, 2011, **36**, 5782-5796.
5. O. Bičáková and P. Straka, *International Journal of Hydrogen Energy*, 2012, **37**, 11563-11578.
6. S. Anantharaj, S. R. Ede, K. Sakthikumar, K. Karthick, S. Mishra and S. Kundu, *ACS Catalysis*, 2016, **6**, 8069-8097.
7. F. M. Sapountzi, J. M. Gracia, C. J. Weststrate, H. O. A. Fredriksson and J. W. Niemantsverdriet, *Progress in Energy and Combustion Science*, 2017, **58**, 1-35.
8. N.-T. Suen, S.-F. Hung, Q. Quan, N. Zhang, Y.-J. Xu and H. M. Chen, *Chemical Society Reviews*, 2017, **46**, 337-365.
9. D. K. Niakolas, M. Daletou, S. G. Neophytides and C. G. Vayenas, *Ambio*, 2016, **45** Suppl 1, S32-S37.
10. C. C. L. McCrory, S. Jung, I. M. Ferrer, S. M. Chatman, J. C. Peters and T. F. Jaramillo, *Journal of the American Chemical Society*, 2015, **137**, 4347-4357.
11. W. T. Hong, M. Risch, K. A. Stoerzinger, A. Grimaud, J. Suntivich and Y. Shao-Horn, *Energy & Environmental Science*, 2015, **8**, 1404-1427.
12. A. T. Swesi, J. Masud and M. Nath, *Energy & Environmental Science*, 2016, **9**, 1771-1782.
13. X. Ge, A. Sumboja, D. Wu, T. An, B. Li, F. W. T. Goh, T. S. A. Hor, Y. Zong and Z. Liu, *ACS Catalysis*, 2015, **5**, 4643-4667.
14. S. Umapathi, J. Masud, A. T. Swesi and M. Nath, *Advanced Sustainable Systems*, 2017, **1**, 1700086.
15. H. Dau, C. Limberg, T. Reier, M. Risch, S. Roggan and P. Strasser, *ChemCatChem*, 2010, **2**, 724-761.

16. J. O. Bockris and T. Otagawa, *The Journal of Physical Chemistry*, 1983, **87**, 2960-2971.
17. G. Bronoel and J. Reby, *Electrochimica Acta*, 1980, **25**, 973-976.
18. A. J. Tkalych, H. L. Zhuang and E. A. Carter, *ACS Catalysis*, 2017, **7**, 5329-5339.
19. Z. Chen, D. Higgins, A. Yu, L. Zhang and J. Zhang, *Energy & Environmental Science*, 2011, **4**, 3167-3192.
20. Y. Feng, A. Gago, L. Timperman and N. Alonso-Vante, *Electrochimica Acta*, 2011, **56**, 1009-1022.
21. F. A. Rasmussen and K. S. Thygesen, *The Journal of Physical Chemistry C*, 2015, **119**, 13169-13183.
22. S. Lauer, A. X. Trautwein and F. E. Harris, *Physical Review B*, 1984, **29**, 6774-6783.
23. J. Suntivich, K. J. May, H. A. Gasteiger, J. B. Goodenough and Y. Shao-Horn, *Science*, 2011, DOI: 10.1126/science.1212858.
24. M.-R. Gao, Z.-Y. Lin, T.-T. Zhuang, J. Jiang, Y.-F. Xu, Y.-R. Zheng and S.-H. Yu, *Journal of Materials Chemistry*, 2012, **22**, 13662-13668.
25. Z. Pu, Y. Luo, A. M. Asiri and X. Sun, *ACS Applied Materials & Interfaces*, 2016, **8**, 4718-4723.
26. W. Zhu, X. Yue, W. Zhang, S. Yu, Y. Zhang, J. Wang and J. Wang, *Chemical Communications*, 2016, **52**, 1486-1489.
27. J. Luo, J.-H. Im, M. T. Mayer, M. Schreier, M. K. Nazeeruddin, N.-G. Park, S. D. Tilley, H. J. Fan and M. Grätzel, *Science*, 2014, **345**, 1593-1596.
28. X. Xu, F. Song and X. Hu, *Nat Commun*, 2016, **7**, 12324.
29. C. Tang, N. Cheng, Z. Pu, W. Xing and X. Sun, *Angewandte Chemie International Edition*, 2015, **54**, 9351-9355.
30. H. Zhu, P. Zhang and S. Dai, *ACS Catalysis*, 2015, **5**, 6370-6385.
31. J. H. Montoya, M. Garcia-Mota, J. K. Nørskov and A. Vojvodic, *Physical Chemistry Chemical Physics*, 2015, **17**, 2634-2640.

32. B. Song, K. Li, Y. Yin, T. Wu, L. Dang, M. Cabán-Acevedo, J. Han, T. Gao, X. Wang, Z. Zhang, J. R. Schmidt, P. Xu and S. Jin, *ACS Catalysis*, 2017, **7**, 8549-8557.
33. Y.-R. Zheng, M.-R. Gao, Z.-Y. Yu, Q. Gao, H.-L. Gao and S.-H. Yu, *Chemical Science*, 2015, **6**, 4594-4598.
34. W. Zhou, X.-J. Wu, X. Cao, X. Huang, C. Tan, J. Tian, H. Liu, J. Wang and H. Zhang, *Energy & Environmental Science*, 2013, **6**, 2921-2924.
35. Y. R. Zheng, M. R. Gao, Q. Gao, H. H. Li, J. Xu, Z. Y. Wu and S. H. Yu, *Small*, 2015, **11**, 182-188.
36. J. Kibsgaard, Z. Chen, B. N. Reinecke and T. F. Jaramillo, *Nat Mater*, 2012, **11**, 963-969.
37. D. Jasion, J. M. Barforoush, Q. Qiao, Y. Zhu, S. Ren and K. C. Leonard, *ACS Catalysis*, 2015, **5**, 6653-6657.
38. J. Rosen, G. S. Hutchings and F. Jiao, *Journal of the American Chemical Society*, 2013, **135**, 4516-4521.
39. Z. Zhuang, W. Sheng and Y. Yan, *Adv Mater*, 2014, **26**, 3950-3955.
40. L. Hu, H. S. Kim, J.-Y. Lee, P. Peumans and Y. Cui, *ACS Nano*, 2010, **4**, 2955-2963.
41. T.-B. Song, Y. Chen, C.-H. Chung, Y. Yang, B. Bob, H.-S. Duan, G. Li, K.-N. Tu, Y. Huang and Y. Yang, *ACS Nano*, 2014, **8**, 2804-2811.
42. Z. Yu, Q. Zhang, L. Li, Q. Chen, X. Niu, J. Liu and Q. Pei, *Adv Mater*, 2011, **23**, 664-668.
43. B. Bob, T.-B. Song, C.-C. Chen, Z. Xu and Y. Yang, *Chemistry of Materials*, 2013, **25**, 4725-4730.
44. F. Rosalbino, S. Delsante, G. Borzone and G. Scavino, *International Journal of Hydrogen Energy*, 2013, **38**, 10170-10177.
45. B. Hammer and J. K. Nørskov, in *Advances in Catalysis*, Academic Press, 2000, vol. 45, pp. 71-129.
46. J. K. Nørskov, T. Bligaard, J. Rossmeisl and C. H. Christensen, *Nature Chemistry*, 2009, **1**, 37-46.

47. D. A. Corrigan, R. S. Conell, C. A. Fierro and D. A. Scherson, *The Journal of Physical Chemistry*, 1987, **91**, 5009-5011.
48. F. Song, M. M. Busch, B. Lassalle-Kaiser, C.-S. Hsu, E. Petkucheva, M. Bensimon, H. M. Chen, C. Corminboeuf and X. Hu, *ACS Central Science*, 2019, **5**, 558-568.
49. E. L. M. a. R. E. Rocheleau, *J. Electrochem. Soc.*, 1997, **144**, 3072-3077.
50. F. Song and X. Hu, *Nat Commun*, 2014, **5**, 4477.
51. H. Wang, H. W. Lee, Y. Deng, Z. Lu, P. C. Hsu, Y. Liu, D. Lin and Y. Cui, *Nat Commun*, 2015, **6**, 7261.
52. F. Cheng, J. Shen, B. Peng, Y. Pan, Z. Tao and J. Chen, *Nature Chemistry*, 2011, **3**, 79-84.
53. F. Jiao and H. Frei, *Angewandte Chemie International Edition*, 2009, **48**, 1841-1844.
54. Y. Sun, J. P. Bigi, N. A. Piro, M. L. Tang, J. R. Long and C. J. Chang, *Journal of the American Chemical Society*, 2011, **133**, 9212-9215.
55. T. Faunce, S. Styring, M. R. Wasielewski, G. W. Brudvig, A. W. Rutherford, J. Messinger, A. F. Lee, C. L. Hill, H. deGroot, M. Fontecave, D. R. MacFarlane, B. Hankamer, D. G. Nocera, D. M. Tiede, H. Dau, W. Hillier, L. Wang and R. Amal, *Energy & Environmental Science*, 2013, **6**, 1074-1076.
56. D. G. Nocera, *Accounts of Chemical Research*, 2012, **45**, 767-776.
57. Y. Yang, J. Liu, B. Zhang and F. Liu, *Journal of Hazardous Materials*, 2017, **321**, 154-161.
58. Q. Zhao, Z. Yan, C. Chen and J. Chen, *Chemical Reviews*, 2017, **117**, 10121-10211.
59. D. G. Papageorgiou, I. A. Kinloch and R. J. Young, *Progress in Materials Science*, 2017, **90**, 75-127.
60. M. Gong, Y. Li, H. Wang, Y. Liang, J. Z. Wu, J. Zhou, J. Wang, T. Regier, F. Wei and H. Dai, *Journal of the American Chemical Society*, 2013, **135**, 8452-8455.
61. T. Zhan, Y. Zhang, X. Liu, S. Lu and W. Hou, *Journal of Power Sources*, 2016, **333**, 53-60.
62. I. H. Kwak, H. S. Im, D. M. Jang, Y. W. Kim, K. Park, Y. R. Lim, E. H. Cha and J. Park, *ACS Applied Materials & Interfaces*, 2016, **8**, 5327-5334.

63. J. Masud, A. T. Swesi, W. P. Liyanage and M. Nath, *ACS Appl Mater Interfaces*, 2016, **8**, 17292-17302.
64. D. Kong, J. J. Cha, H. Wang, H. R. Lee and Y. Cui, *Energy & Environmental Science*, 2013, **6**, 3553-3558.
65. X. Zhong, H. Yu, X. Wang, L. Liu, Y. Jiang, L. Wang, G. Zhuang, Y. Chu, X. Li and J.-g. Wang, *ACS Applied Materials & Interfaces*, 2014, **6**, 13448-13454.
66. L. Liu, G. Samjeske, S.-i. Nagamatsu, O. Sekizawa, K. Nagasawa, S. Takao, Y. Imaizumi, T. Yamamoto, T. Uruga and Y. Iwasawa, *The Journal of Physical Chemistry C*, 2012, **116**, 23453-23464.
67. J. Du, T. Zhang, F. Cheng, W. Chu, Z. Wu and J. Chen, *Inorganic Chemistry*, 2014, **53**, 9106-9114.
68. L. Geniès, R. Faure and R. Durand, *Electrochimica Acta*, 1998, **44**, 1317-1327.
69. I. Srejjic, Z. Rakocevic, M. Nenadovic and S. Strbac, *Electrochimica Acta*, 2015, **169**, 22-31.
70. F. H. B. Lima, J. Zhang, M. H. Shao, K. Sasaki, M. B. Vukmirovic, E. A. Ticianelli and R. R. Adzic, *The Journal of Physical Chemistry C*, 2007, **111**, 404-410.
71. H. Erikson, A. Sarapuu, N. Alexeyeva, K. Tammeveski, J. Solla-Gullón and J. M. Feliu, *Electrochimica Acta*, 2012, **59**, 329-335.
72. Y. Liang, Y. Li, H. Wang, J. Zhou, J. Wang, T. Regier and H. Dai, *Nat Mater*, 2011, **10**, 780-786.
73. P. W. Menezes, A. Indra, D. González-Flores, N. R. Sahraie, I. Zaharieva, M. Schwarze, P. Strasser, H. Dau and M. Driess, *ACS Catalysis*, 2015, **5**, 2017-2027.
74. G. Zhang, C. Li, J. Liu, L. Zhou, R. Liu, X. Han, H. Huang, H. Hu, Y. Liu and Z. Kang, *Journal of Materials Chemistry A*, 2014, **2**, 8184-8189.
75. E. Lee, J.-H. Jang and Y.-U. Kwon, *Journal of Power Sources*, 2015, **273**, 735-741.
76. X. Tong, S. Chen, C. Guo, X. Xia and X.-Y. Guo, *ACS Applied Materials & Interfaces*, 2016, **8**, 28274-28282.
77. H. Zhu, S. Zhang, Y.-X. Huang, L. Wu and S. Sun, *Nano Letters*, 2013, **13**, 2947-2951.
78. R. Ning, J. Tian, A. M. Asiri, A. H. Qusti, A. O. Al-Youbi and X. Sun, *Langmuir*, 2013, **29**, 13146-13151.

79. K. Mohanraju, V. Sreejith, R. Ananth and L. Cindrella, *Journal of Power Sources*, 2015, **284**, 383-391.
80. Z.-S. Wu, S. Yang, Y. Sun, K. Parvez, X. Feng and K. Müllen, *Journal of the American Chemical Society*, 2012, **134**, 9082-9085.
81. X. Zhai, W. Yang, M. Li, G. Lv, J. Liu and X. Zhang, *Carbon*, 2013, **65**, 277-286.
82. J. Liu, J. Liu, W. Song, F. Wang and Y. Song, *Journal of Materials Chemistry A*, 2014, **2**, 17477-17488.
83. L. Qiao, H. Y. Xiao, H. M. Meyer, J. N. Sun, C. M. Rouleau, A. A. Puretzky, D. B. Geohegan, I. N. Ivanov, M. Yoon, W. J. Weber and M. D. Biegalski, *Journal of Materials Chemistry C*, 2013, **1**, 4628-4633.
84. Y. Liang, Y. Li, H. Wang, J. Zhou, J. Wang, T. Regier and H. Dai, *Nature materials*, 2011, **10**, 780-786.
85. Y. Liang, H. Wang, P. Diao, W. Chang, G. Hong, Y. Li, M. Gong, L. Xie, J. Zhou, J. Wang, T. Z. Regier, F. Wei and H. Dai, *Journal of the American Chemical Society*, 2012, **134**, 15849-15857.
86. M. Wang, J. Huang, M. Wang, D. Zhang, W. Zhang, W. Li and J. Chen, *Electrochemistry Communications*, 2013, **34**, 299-303.
87. Y. Wang, X. Cui, L. Chen, C. Wei, F. Cui, H. Yao, J. Shi and Y. Li, *Dalton Transactions*, 2014, **43**, 4163-4168.
88. L. Hu, L. Wu, M. Liao, X. Hu and X. Fang, *Advanced Functional Materials*, 2012, **22**, 998-1004.
89. Z.-Q. Liu, Q.-Z. Xu, J.-Y. Wang, N. Li, S.-H. Guo, Y.-Z. Su, H.-J. Wang, J.-H. Zhang and S. Chen, *International Journal of Hydrogen Energy*, 2013, **38**, 6657-6662.
90. Y. Xiao, C. Hu, L. Qu, C. Hu and M. Cao, *Chemistry – A European Journal*, 2013, **19**, 14271-14278.
91. H. Zhang, H. Li, H. Wang, K. He, S. Wang, Y. Tang and J. Chen, *Journal of Power Sources*, 2015, **280**, 640-648.
92. Z. Yang, H. Nie, X. a. Chen, X. Chen and S. Huang, *Journal of Power Sources*, 2013, **236**, 238-249.
93. L. Lai, J. R. Potts, D. Zhan, L. Wang, C. K. Poh, C. Tang, H. Gong, Z. Shen, J. Lin and R. S. Ruoff, *Energy & Environmental Science*, 2012, **5**, 7936-7942.

94. T. Sharifi, G. Hu, X. Jia and T. Wågberg, *ACS Nano*, 2012, **6**, 8904-8912.
95. M. Gerloch, J. H. Harding and R. G. Woolley, Berlin, Heidelberg, 1981.
96. S. F. A. Kettle, in *Physical Inorganic Chemistry: A Coordination Chemistry Approach*, Springer Berlin Heidelberg, Berlin, Heidelberg, 1996, DOI: 10.1007/978-3-662-25191-1_7, pp. 121-155.
97. U. De Silva, J. Masud, N. Zhang, Y. Hong, W. P. R. Liyanage, M. Asle Zaeem and M. Nath, *Journal of Materials Chemistry A*, 2018, **6**, 7608-7622.
98. R. R. Adzic, J. Zhang, K. Sasaki, M. B. Vukmirovic, M. Shao, J. X. Wang, A. U. Nilekar, M. Mavrikakis, J. A. Valerio and F. Uribe, *Topics in Catalysis*, 2007, **46**, 249-262.
99. J. Masud and M. Nath, *ACS Energy Letters*, 2016, **1**, 27-31.
100. D. Zhao, S. Zhang, G. Yin, C. Du, Z. Wang and J. Wei, *Journal of Power Sources*, 2012, **206**, 103-107.
101. B. Yu, J. Jin, H. Wu, S. Wang, Q. Xia and H. Liu, *International Journal of Hydrogen Energy*, 2017, **42**, 236-242.
102. D. Zhao, S. Zhang, G. Yin, C. Du, Z. Wang and J. Wei, *Electrochimica Acta*, 2013, **91**, 179-184.
103. P. Ganesan, M. Prabu, J. Sanetuntikul and S. Shanmugam, *ACS Catalysis*, 2015, **5**, 3625-3637.
104. A. Rabis, P. Rodriguez and T. J. Schmidt, *ACS Catalysis*, 2012, **2**, 864-890.
105. P. Damborský, J. Švitel and J. Katrlík, *Essays Biochem*, 2016, **60**, 91-100.
106. J. Wang, in *Perspectives in Bioanalysis*, eds. E. Paleček, F. Scheller and J. Wang, Elsevier, 2005, vol. 1, pp. 175-194.
107. G. Wang, X. He, L. Wang, A. Gu, Y. Huang, B. Fang, B. Geng and X. Zhang, *Microchimica Acta*, 2013, **180**, 161-186.
108. R. M. Wightman, L. J. May and A. C. Michael, *Analytical Chemistry*, 1988, **60**, 769A-779A.
109. H.-F. Cui, J.-S. Ye, Y. Chen, S.-C. Chong and F.-S. Sheu, *Analytical Chemistry*, 2006, **78**, 6347-6355.
110. R. N. Adams, *Analytical Chemistry*, 1976, **48**, 1126A-1138A.

111. K. P. Troyer, M. L. A. V. Heien, B. J. Venton and R. M. Wightman, *Current Opinion in Chemical Biology*, 2002, **6**, 696-703.
112. J. B. Justice, *Journal of Neuroscience Methods*, 1993, **48**, 263-276.
113. R. D. O'Neill, *Analyst*, 1994, **119**, 767-779.
114. S. Alwarappan, G. Liu and C.-Z. Li, *Nanomedicine: Nanotechnology, Biology and Medicine*, 2010, **6**, 52-57.
115. D. P. Quan, D. P. Tuyen, T. D. Lam, P. T. N. Tram, N. H. Binh and P. H. Viet, *Colloids and Surfaces B: Biointerfaces*, 2011, **88**, 764-770.
116. C.-L. Sun, C.-T. Chang, H.-H. Lee, J. Zhou, J. Wang, T.-K. Sham and W.-F. Pong, *ACS Nano*, 2011, **5**, 7788-7795.
117. C.-F. Tang, S. A. Kumar and S.-M. Chen, *Analytical Biochemistry*, 2008, **380**, 174-183.
118. J. Huang, Y. Liu, H. Hou and T. You, *Biosensors and Bioelectronics*, 2008, **24**, 632-637.
119. M.-S. Hsu, Y.-L. Chen, C.-Y. Lee and H.-T. Chiu, *ACS Applied Materials & Interfaces*, 2012, **4**, 5570-5575.
120. J. Du, R. Yue, F. Ren, Z. Yao, F. Jiang, P. Yang and Y. Du, *Gold Bulletin*, 2013, **46**, 137-144.
121. C.-L. Sun, H.-H. Lee, J.-M. Yang and C.-C. Wu, *Biosensors and Bioelectronics*, 2011, **26**, 3450-3455.
122. M. Hadi and A. Rouhollahi, *Analytica Chimica Acta*, 2012, **721**, 55-60.
123. S. Palanisamy, *Materials Research Express*, 2014, **1**, 045020.
124. H. Filik, A. Avan, S. Aydar and R. Arpaci, *International journal of electrochemical science*, 2014, **9**, 2775-2789.
125. D. Han, T. Han, C. Shan, A. Ivaska and L. Niu, *Electroanalysis*, 2010, **22**, 2001-2008.
126. L. M. Niu, K. Q. Lian, H. M. Shi, Y. B. Wu, W. J. Kang and S. Y. Bi, *Sensors and Actuators B: Chemical*, 2013, **178**, 10-18.
127. H. Filik, A. A. Avan and S. Aydar, *Arabian Journal of Chemistry*, 2016, **9**, 471-480.

128. *Russian Journal of Electrochemistry*, 2002, **38**, 1364-1365.
129. Q. Liu, X. Zhu, Z. Huo, X. He, Y. Liang and M. Xu, *Talanta*, 2012, **97**, 557-562.
130. S. Hou, M. L. Kasner, S. Su, K. Patel and R. Cuellari, *The Journal of Physical Chemistry C*, 2010, **114**, 14915-14921.
131. Y.-R. Kim, S. Bong, Y.-J. Kang, Y. Yang, R. K. Mahajan, J. S. Kim and H. Kim, *Biosensors and Bioelectronics*, 2010, **25**, 2366-2369.
132. M. Pumera, A. Ambrosi, A. Bonanni, E. Chng and H. Poh, *TrAC Trends in Analytical Chemistry*, 2010, **29**, 954-965.
133. L. Tan, K.-G. Zhou, Y.-H. Zhang, H.-X. Wang, X.-D. Wang, Y.-F. Guo and H.-L. Zhang, *Electrochemistry Communications*, 2010, **12**, 557-560.
134. Z. Wang, J. Xia, L. Zhu, X. Chen, F. Zhang, S. Yao, Y. Li and Y. Xia, *Electroanalysis*, 2011, **23**, 2463-2471.
135. P. Si, H. Chen, P. Kannan and D.-H. Kim, *Analyst*, 2011, **136**, 5134-5138.
136. E. Katz, I. Willner and J. Wang, *Electroanalysis*, 2004, **16**, 19-44.
137. D. Hernández-Santos, M. B. González-García and A. C. García, *Electroanalysis*, 2002, **14**, 1225-1235.
138. A. Stoyanova and V. Tsakova, *Journal of Solid State Electrochemistry*, 2010, **14**, 1957-1965.
139. Ş. Ulubay and Z. Dursun, *Talanta*, 2010, **80**, 1461-1466.
140. S. Mahshid, C. Li, S. S. Mahshid, M. Askari, A. Dolati, L. Yang, S. Luo and Q. Cai, *Analyst*, 2011, **136**, 2322-2329.
141. Y. Liu, W. Zhu, D. wu and Q. Wei, *Measurement*, 2015, **60**, 1-5.
142. S.-O. Enfors, *Enzyme and Microbial Technology*, 1981, **3**, 29-32.
143. S. Park, H. Boo and T. D. Chung, *Analytica Chimica Acta*, 2006, **556**, 46-57.
144. T. T. Ngo, *International Journal of Biochemistry*, 1980, **11**, 459-465.
145. A. E. G. Cass, G. Davis, G. D. Francis, H. A. O. Hill, W. J. Aston, I. J. Higgins, E. V. Plotkin, L. D. L. Scott and A. P. F. Turner, *Analytical Chemistry*, 1984, **56**, 667-671.

146. A. Heller, *Accounts of Chemical Research*, 1990, **23**, 128-134.
147. Y. Degani and A. Heller, *The Journal of Physical Chemistry*, 1987, **91**, 1285-1289.
148. P. N. Bartlett and K. F. E. Pratt, *Journal of Electroanalytical Chemistry*, 1995, **397**, 53-60.
149. S. Park, T. D. Chung and H. C. Kim, *Analytical Chemistry*, 2003, **75**, 3046-3049.
150. A. Turner, I. Karube and G. S. Wilson, eds., *Biosensors : Fundamentals and Applications*, Oxford University Press, Oxford, New York, 1987.
151. N. Mano, F. Mao and A. Heller, *Journal of the American Chemical Society*, 2003, **125**, 6588-6594.
152. M.-J. Shao, X.-K. Xing and C.-C. Liu, *Bioelectrochemistry and Bioenergetics*, 1987, **17**, 59-70.
153. S. Ernst, J. Heitbaum and C. H. Hamann, *Berichte der Bunsengesellschaft für physikalische Chemie*, 1980, **84**, 50-55.
154. J. Li, X. Wei and Y. Yuan, *Sensors and Actuators B: Chemical*, 2009, **139**, 400-406.
155. D. Mott, J. Luo, P. N. Njoki, Y. Lin, L. Wang and C.-J. Zhong, *Catalysis Today*, 2007, **122**, 378-385.
156. A. A. Saei, J. E. N. Dolatabadi, P. Najafi-Marandi, A. Abhari and M. de la Guardia, *TrAC Trends in Analytical Chemistry*, 2013, **42**, 216-227.
157. X. Ren, X. Meng and F. Tang, *Sensors and Actuators B: Chemical*, 2005, **110**, 358-363.
158. H. Wang, X. Wang, X. Zhang, X. Qin, Z. Zhao, Z. Miao, N. Huang and Q. Chen, *Biosensors and Bioelectronics*, 2009, **25**, 142-146.
159. Y. Fang, Y. Ni, G. Zhang, C. Mao, X. Huang and J. Shen, *Bioelectrochemistry*, 2012, **88**, 1-7.
160. J. Luo, S. Jiang, H. Zhang, J. Jiang and X. Liu, *Analytica Chimica Acta*, 2012, **709**, 47-53.
161. Q. Zeng, J.-S. Cheng, X.-F. Liu, H.-T. Bai and J.-H. Jiang, *Biosensors and Bioelectronics*, 2011, **26**, 3456-3463.

VITA

Siddesh Umapathi was born and raised in Bangalore, India. He received his bachelor (2007) and master's degree (2009) in Chemistry and Inorganic chemistry respectively from Bangalore University, India. During his undergraduate studies he was selected as Summer Fellow from Jawaharlal Nehru Center for Advanced Scientific Research (JNCASR). He worked on the magnetic properties of non magnetic nanomaterials for which he was awarded Rajiv Gandhi Young Talent Research Scholar. After his masters he worked for 5 years' as a R&D chemist at AkzoNobel, Bangalore. He joined MS&T in the Department of Chemistry of class 2015 under advising of Dr. Manashi Nath. His research interests are hybrid nanomaterials for energy conversion, storage and electrochemical sensors. As a PhD student he has been awarded Electrochemical Society (ECS) F.M. Beckett Summer Research Fellowship 2017 and won 1st place in three minute thesis (3MT) from Missouri S&T. He was awarded the Graduate Research Award from Department of Chemistry in 2018 and he was in cohort of 2016 Graduate Leadership Development Program offered by University of Missouri system. He received his PhD in Chemistry from Missouri University of Science & Technology in May 2020.